



Bournemouth University

**Defect Tolerance Assessment of Silicon Nitride
in Rolling Contact**

ABDUL WAHEED AWAN

BSc Mech Eng (Hons), MS, RE (PEC), AMIMechE

A thesis is submitted to Faculty of Science and Technology, Bournemouth University,
in partial fulfilment of the requirements for the degree of Doctor of Philosophy

2015

Faculty of Science and Technology

Bournemouth University, UK

In collaboration with SKF ERC, the Netherlands

Copyright Statement

This copy of the thesis has been supplied on the condition that anyone who consults it is understood to recognize that its copyright rests with its author and due acknowledgment must always be made of the use of any material contained in, or derived from this thesis.

In Memory of My Grandmother

In Memory of My Maternal Grandmother and Grandfather

In Memory of My Younger Brother, Zahid

To strive, To Seek, To Find and Not to Yield

Abstract

This thesis focuses on two relatively unexplored types of surface defects on silicon nitride balls – ‘star’ type defects and ‘missing material’. The main objective of this research is to determine failure modes and the critical or tolerable defect sizes for rolling bearing applications. This is achieved by means of both experimental and numerical techniques (for finding crack initiation location). A modified four-ball machine is used for the rolling contact fatigue experiments on star features and missing material defects (both during manufacturing process and artificially produced) on the surface of silicon nitride balls. Experiments are conducted at different loads (3.8-4.8GPa), lubrication types, specific speed (7500rpm) and temperature conditions (75°C) to find rolling contact fatigue limitations in relation to these defects. Laser micromachining is used to produce precise holes and trenches to simulate missing material. Two different types of bearing grade silicon nitride are tested to determine tolerance and failure modes in rolling contact fatigue. Scanning electron microscopy, light microscopy and white light interferometry are used for surface analysis and topography.

Post-experiment analysis in the star feature experiments has shown that star like radial cracks are prone to develop into missing material by internal fracture over the extent of the star in lubricated rolling contact. Lubrication quality or film thickness and orientation of the pre-existing cracks to the rolling direction influenced the damage process and severity. In the case of missing material experiments, samples with different diameters (50-100 μ m), depths (5-50 μ m) and shape (right cylindrical, conical and oblique cylindrical) were tested. It has been confirmed that, apart from the main experimental parameters like applied pressure, cavity diameter and depth, parameters such as cavity base profile, shape and cavity location and orientation on the contact track are important for rolling contact fatigue of silicon nitride material. Replica produced cavity base profiles to investigate failure reasons. Cross-sectioning also gave very good insight of surface and subsurface features both before and after testing (including un-failed specimens). Incipient spalls on tested samples provided the information to understand the failure mechanism (mainly spalling) in the material.

FEM is used for finding stress fields at surface and sub-surface positions and ultimately predicting the location and position of crack initiation. 2D (Axi-symmetric and plane strain) and 3D models are developed to compare the results, whereas static versus quasi static analysis is presented to examine the effect of rolling. Models are verified using classical contact theory. Hydrostatic pressure effects are also successfully modeled using the finite element analysis approach. Fluid elements modeling on the solid interface of the cavity produced a different stress field and have indicated the location of crack initiation.

Publications resulting from this research

International Conferences

1. Abdul Waheed Awan, Mark Hadfield, Ben Thomas, Charlotte Vieillard, Junbiao Lai, Yuri Kadin and Robin Cundill, “Modeling of surface defects in silicon nitride rolling element in lubricated rolling contact”, Oral presentation at 69th STLE Conference, May 18-22, 2014, Florida, USA.
2. Abdul Waheed Awan, Mark Hadfield, Ben Thomas, Charlotte Vieillard, and Robin Cundill, “Surface star defect tolerance assessment on finished silicon nitride balls in rolling contact”, Oral presentation at 40th Leeds-Lyon Conference, September 04-06, 2013, Lyon, France. (Extended abstract : <http://tribo-lyon2013.sciencesconf.org/18116/document>)
3. Abdul Waheed Awan, Mark Hadfield, Ben Thomas, Charlotte Vieillard, and Robin Cundill, “An experimental investigation of rolling contact failure within silicon nitride subject to micro surface defects”, Oral presentation at 5th World Tribology Congress, September 08-13, 2013, Torino, Italy. (Extended abstract-ISBN: 9788890818509)
4. Abdul Waheed Awan, Mark Hadfield, Charlotte Vieillard, Ben Thomas, Robin Cundill and Jelena Sekulic, “Defect Tolerance Assessment of Silicon Nitride in Rolling Contact subjected to star defects”, Abstract accepted for 4th International Conference on Tribology and Design, September 03-05, 2012, Kos, Greece.

Poster Conferences (Bournemouth University)

1. Abdul Waheed Awan, Mark Hadfield, Ben Thomas and Robin Cundill, “Hydrostatic pressure effect in silicon nitride under rolling contact: A FEA study”, 5th Annual Bournemouth University Postgraduate Research Conference, April 29, 2013.
2. Abdul Waheed Awan, Mark Hadfield, Ben Thomas and Robin Cundill, “Lubrication effects on the star surface defects within silicon nitride under rolling contact”, 4th Annual Bournemouth University Postgraduate Research Conference, June 28, 2012.

-
3. Abdul Waheed Awan, Mark Hadfield, Ben Thomas and Robin Cundill, “Silicon Nitride in Rolling Contact subject to surface star defects”, 5th Annual DEC Postgraduate Research Poster Conference, May 23, 2012.
 4. Abdul Waheed Awan, Mark Hadfield, Ben Thomas and Robin Cundill, “Defect Tolerance Assessment of Silicon Nitride in Rolling Contact”, 4th Annual DEC Postgraduate Research Poster Conference, May 18, 2011.

Reports

1. Abdul Waheed Awan, “Defect Tolerance assessment of silicon nitride in rolling contact”, SKF Internal Document, SKF Engineering and Research Centre, the Netherlands, March 2014
2. Abdul Waheed Awan, “Defect Tolerance assessment of silicon nitride in rolling contact fatigue subjected to surface defects”, SKF Internal Document, SKF Engineering and Research Centre, the Netherlands, February 2012.

Table of Contents

Copyright Statement	II
Abstract	IV
Publications resulting from this research	V
Table of Contents	VII
List of Figures	XI
List of Tables	XX
Acknowledgements	XXI
Author’s Declaration	XXIII
Abbreviations/Nomenclature	XXIV
Chapter 1 Introduction	1
1.1. Background	1
1.2. Scope and Objective of the Research	2
1.3. Literature Review	3
1.3.1. Rolling Bearings.....	3
1.3.2. Bearing Materials	4
1.3.3. Bearing Elements Life.....	5
1.3.4. Surface Defects	6
1.3.5. Experimental Techniques.....	8
1.3.6. Failure Modes in Silicon Nitride.....	10
1.3.7. Laser machining	13
1.3.8. Residual Stresses	14
1.3.9. Numerical Simulations	14
1.4. State-of-the-Art from Literature Survey	17
1.5. Outlines of Thesis	18
Chapter 2 Experimental Methodology	20
2.1. Materials Experimented	20
2.1.1. Silicon Nitride Balls	20
2.1.2. Steel Balls.....	21
2.2. Lubricants Used	21
2.3. Specimen preparation/pre-experiment study	21

2.3.1.	Fluorescent Penetrant Inspection	22
2.3.2.	Surface Inspection	23
2.4.	Rolling Contact Fatigue Experimenting	23
2.4.1.	Main Experiment Rig/Modified Four Ball Machine.....	23
2.4.2.	Defect Positioning Procedure.....	24
2.4.3.	RCF Experiment Procedure using modified 4-ball machine	25
2.5.	Surface Analysis	26
2.5.1.	Optical Microscopy	26
2.5.2.	White Light Interferometry	27
2.5.3.	Scanning Electron Microscopy	28
2.6.	Use of Replicas	30
2.6.1.	Replica Procedure	30
2.7.	Summary	31
Chapter 3	Experiments on stars features.....	32
3.1.	Natural Star Categorization	32
3.2.	RCF experiments on star features	34
3.2.1.	Experiments on category 1 Stars.....	35
3.2.2.	Experiments on category 5 Stars.....	46
3.2.3.	Experiments on Pit Size	52
3.3.	Star features – Discussion/Conclusions.....	58
3.4.	Artificial star Creation	60
3.4.1.	Artificial star feature using course diamond paste.....	60
3.4.2.	Artificial star using Vickers indenter	62
3.5.	Summary	62
Chapter 4	Laser Machining and Controlled Defects	65
4.1.	Non-Conventional Machining	65
4.1.1.	Ultrasonic Machining (USM)	65
4.1.2.	Electron Beam Machining (EBM)	66
4.1.3.	Laser Machining or Laser Beam Machining (LBM)	67
4.2.	Laser Machining of Missing Material Defects	68
4.2.1.	Laser Machining of Holes.....	69
4.2.2.	Laser Machining of Slots	71

4.3.	Summary	72
Chapter 5	Experiments on Missing Material.....	73
5.1.	Experiments on Shape I (Holes) – Material A.....	74
5.1.1.	Small Hole Experiments (50µm diameter)	74
5.1.2.	Medium Hole Experiments (75µm diameter)	93
5.1.3.	Large Hole Experiments (100µm diameter)	100
5.2.	Experiments on Shape I (Holes) – Material B	106
5.3.	Experiments on Shape I (Slot) – Material A.....	113
5.4.	Experiments on Shape II – Material A	114
5.5.	Shape performance experiments (Shape I, II and III) – Material A	116
5.6.	Contact pressure effect (contact vs. position).....	122
5.7.	Cavity base effect (Replica Study)	126
5.8.	EDS Analysis	127
5.9.	Failure Mechanism	127
5.9.1.	Unfailed Balls.....	127
5.9.2.	Spalled Balls.....	129
5.9.3.	Incipient Spalls	139
5.9.4.	Spalling Process	150
5.10.	Discussion and Conclusions	154
5.11.	Summary	154
Chapter 6	Finite Element Modeling of Missing Material.....	156
6.1.	Finite Element Modeling	156
6.2.	Model Verification.....	157
6.3.	2D Rolling Models.....	160
6.4.	3D Rolling Model	163
6.5.	Hydrostatic Pressure	167
6.6.	Hydrostatic Pressure Modeling in Abaqus	168
6.6.1.	Boundary Conditions	168
6.6.2.	Mesh.....	169
6.6.3.	Stress Field (Shape I/right cylindrical)	169
6.6.4.	Stress Field (Shape II/Conical)	171

6.7.	Results and Discussion (Shape I/Right Cylindrical).....	172
6.8.	Results and Discussion – Shape II (Shape I vs. Shape II)	179
6.9.	Theoretical Discussion.....	181
6.10.	Summary/Conclusions	182
Chapter 7	Discussion and Conclusions.....	183
7.1.	Discussion.....	183
7.1.1.	Experimental Work	183
7.1.2.	FE Modeling and Analysis.....	185
7.2.	Conclusions.....	185
7.3.	Design Guidelines	187
7.4.	Future Work.....	187
References	189
Bibliography	201
Appendices	203
Appendix A:	<i>Stress Factor and Load Calculations</i>	203
Appendix B:	<i>Calibration for TE92HS</i>	205
Appendix C :	<i>Replica Technical Data, Selection and Specifications</i>	206
Appendix D:	<i>Conductive Silver Paint – Technical Details</i>	208
Appendix E:	<i>Typical Surface Defects in Silicon Nitride</i>	209
Appendix F:	<i>Missing material (natural) shapes and depth</i>	210
Appendix G:	<i>Minimum Film Thickness</i>	211
Appendix H:	<i>Calculations for Diamond Tip Removal in Vickers Indentation</i>	212
Appendix I:	<i>Non-Conventional Machining Classifications</i>	214
Appendix J:	<i>Laser micromachining in Silicon Nitride</i>	215
Appendix K:	<i>Additional Features of CPA Series Micro Workstations</i>	218
Appendix L:	<i>Missing Material Experiments Classifications</i>	221
Appendix M:	<i>Contact Pressure variation from contact centre</i>	222
Appendix N:	<i>Tables for Corrected pressure</i>	223
Appendix O:	<i>EDS Analysis of Silicon Nitride Ball</i>	227
Appendix P:	<i>Calibration for SEM EDS</i>	228
Appendix Q :	<i>Finite Elements used in Missing Material Modeling</i>	229

List of Figures

Figure 1.1: Hybrid Ball Bearing (Courtesy: SKF)	2
Figure 2.1: Modified four ball machine (a) machine and control unit (b) 4-ball experimenter	24
Figure 2.2: Schematic drawing of defect positioning in modified four ball machine [Reproduced from Wang 2001].....	24
Figure 2.3: Olympus BX 60 Light Microscope (showing star feature-category 5).....	27
Figure 2.4: White Light Interferometer (Zygo Interferometer).....	28
Figure 2.5: Zeiss Supra 35 VP SEM (Courtesy: ETC Brunel University).....	29
Figure 2.6: (a) Sputter Coater for Gold Coating (b) Agar Turbo Carbon Coater for Carbon Coating	29
Figure 2.7: (a) Applying replicating material to sample surface using replicating system (b) Silver conductive paint for coating.....	31
Figure 3.1: Star feature category 1 (a) UV illumination (b) white light illumination	32
Figure 3.2: Star feature category 2 (a) UV illumination (b) white light illumination	33
Figure 3.3: Star feature category 3 (a) UV illumination (b) white light illumination	33
Figure 3.4: Star feature category 4 (a) UV illumination (b) white light illumination	33
Figure 3.5: Star feature category 5 (a) UV illumination (b) white light illumination	34
Figure 3.6: Experiment C1TF1 (a) Pre-experiment analysis using white light illumination (b) pre-experiment analysis using UV illumination (c) and (d) post-experiment (30million stress cycles) OM images (white light) (e) and (f) post-experiment SEM images.....	37
Figure 3.7: Experiment C1TF2 (a) pre-experiment OM image (b) post-experiment OM image (c) and (d) post experiment WLI images for surface deposition	38
Figure 3.8: Post-experiment (C1TF3) analysis of silicon nitride surface using microscopy (a) post 30million stress cycles (b) post-heat treatment at 500°C and dwell time of 1hour (c) and (d) post-heated at 500°C and dwell time of 1hour (interferometry 2D and 3D images)	39
Figure 3.9: Post-experiment (C1TF4) surface analysis of silicon nitride surface using microscopy (a) at 100x magnification (b) at 200x magnification	39
Figure 3.10: Experiment C1TM1 (a) pre-experiment UV illumination (b) pre-experiment white light illumination (c) and (d) post-experiment OM image	41
Figure 3.11: Experiment C1TM1 (a) and (b) post-experiment SEM images	41
Figure 3.12: Experiment C1TM2 (a) pre-experiment UV illumination (b) pre-experiment white light illumination (c) post-experiment OM image (d) post-experiment OM image at high magnification.....	42
Figure 3.13: Experiment C1TM2 (a) 2D and (b) 3D image interferometry.....	43
Figure 3.14: Experiment C1GR1 (a) pre-test UV illumination (b) post-test white light.....	44

Figure 3.15 Experiment C1GR2 (a) pre-test UV illumination (b) post-test white light	44
Figure 3.16: Experiment C1Grs1 (a) pre-experiment UV illumination (b) pre-experiment white light illumination (c) and (d) post-experiment OM images.....	45
Figure 3.17: Experiment C1Grs2 (a) pre-experiment UV illumination (b) pre-experiment white light illumination (c) and (d) post-experiment OM images.....	46
Figure 3.18: Experiment C5TM1 pre-test (a) white light illumination (b) UV illumination (c) and (d) surface mapping by interferometry	47
Figure 3.19: Experiment C5TM1 post-test- 100 million cycles (a) white light illumination (b) UV illumination (c) and (d) surface mapping by interferometry	48
Figure 3.20: Experiment C5TM2 pre-test (a) white light illumination (b) UV illumination (c) and (d) surface mapping by interferometry	49
Figure 3.21: Experiment C5TM2 post-test-20 million stress cycles (a) white light illumination (b) UV illumination (c) and (d) surface mapping by interferometry.....	50
Figure 3.22: Experiment C5TM3 post-test-60 million stress cycles (a) white light illumination (b) surface mapping by interferometry.....	50
Figure 3.23 Experiment C5TM4 pre-experiment (a) white light illumination (b) UV illumination (c) and (d) surface mapping by interferometry	51
Figure 3.24 Experiment C5TM4 post-test-100 million stress cycles (a) white light illumination (b) Surface mapping by interferometry	51
Figure 3.25 Experiment C5TM5 pre-experiment (a) white light illumination (b) UV illumination (c) and (d) surface mapping by interferometry	52
Figure 3.26: Experiment C5TM5 post-test-100 million stress cycles (a) surface analysis using white light illumination (b) Surface mapping by interferometry.....	53
Figure 3.27: Pre-experiment C1TM5 (a) light illumination (b) UV illumination.....	54
Figure 3.28: Post-experiment C1TM5 (Ball 18, Cat. = 1) (a) light illumination (b) UV illumination	54
Figure 3.29: Experiment C3TM1 pre-experiment (a) white light illumination (b) UV illumination (c) and (d) surface mapping by interferometry	55
Figure 3.30: Experiment C3TM1 post-experiment (a) white light illumination (b) UV illumination (c) and (d) surface mapping by interferometry	56
Figure 3.31: Experiment C5TM6 pre-experiment (a) white light illumination (b) UV illumination	56
Figure 3.32: Experiment C5TM6 pre-experiment (a) and (b) surface mapping by interferometry	57
Figure 3.33: Experiment C5TM6 post-test-100 million stress cycles (a) white light illumination (b) UV illumination.....	57
Figure 3.34: Experiment C5TM6 post-test-100 million stress cycles (a) and (b) surface mapping by interferometry	58

Figure 3.35: Comparison of different lubricants for star features category 1 experiments	59
Figure 3.36: Artificial star making using diamond paste (a) and (c) light illumination for sample 1 and 2 (b) and (d) UV illumination for sample 1 and 2 (Work done at ERC).....	61
Figure 3.37: Artificial star making using diamond paste (a) light illumination for sample 3 (b) UV illumination for sample 3 (Work done at ERC).....	61
Figure 3.38: Light microscopy for Vickers indentation (a) for 3kg _f (b) for 5kg _f (Work done at ERC).....	63
Figure 3.39: Artificial star - post polishing 3kg _f (a) indentation by light illumination (b) indentation by UV illumination (Work done at ERC).....	63
Figure 3.40: Artificial star - post polishing 5kg _f (a) indentation by light illumination (b) indentation by UV illumination (Work done at ERC).....	64
Figure 3.41: Artificial star-post polishing 10kg _f (a) indentation by light illumination (b) indentation by UV illumination (Work done at ERC).....	64
Figure 4.1: Typical Industrial Lasers used for different purposes [Karlicek 2011]	68
Figure 4.2: Laser Workstation (courtesy: Laser micromachining Limited, UK)	69
Figure 4.3: Proposed shapes for laser machining.....	70
Figure 4.4: Typical laser machined hole (a) Optical microscopy – top view (b) optical microscopy – cross-sectional view (c) Scanning electron microscopy	71
Figure 5.1: Experiment 01 (a) pre-experiment (b) post experiment (120M) (c) post-experiment- higher magnification OM image (d) post experiment SEM image	76
Figure 5.2: Experiment 02 (a) pre-experiment (b) post-experiment (30M) OM image	76
Figure 5.3: Pre-experiment (03) surface analysis using (a) microscopy (b) interferometry	77
Figure 5.4: Post-experiment (03, 100million stress cycles) surface analysis using microscopy (a) low magnification (b) higher magnification	77
Figure 5.5: Pre-experiment (04) surface analysis using (a) microscopy (b) interferometry	78
Figure 5.6: Post-experiment (04) analysis using (a) microscopy-dark field (b) 3D-surface mapping using interferometry	79
Figure 5.7: Surface analysis using microscopy (experiment 05) (a) pre-experiment (b) post-experiment.....	79
Figure 5.8: Surface analysis (experiment 06) (a) pre-experiment analysis using light interferometry (b) post-experiment analysis using light microscopy	80
Figure 5.9: Surface analysis (experiment 07) (a) post-experiment analysis using light microscopy-dark field (b) post-experiment analysis using light microscopy-dark field....	80
Figure 5.10: Surface mapping (experiment 08) using interferometry (a) pre-experiment (b) post-experiment	81
Figure 5.11: Surface analysis using microscopy (experiment 09) (a) pre-experiment (b) post-experiment.....	82

Figure 5.12: Pre-experiment surface analysis/mapping (experiment 10) (a) using light microscopy (b) using interferometry	82
Figure 5.13: Post-experiment surface analysis (experiment 10) using microscopy (a) low magnification (b) higher magnification.....	83
Figure 5.14: Pre-experiment surface analysis/mapping (experiment 11) (a) light microscopy (b) interferometry	83
Figure 5.15: Post-experiment surface analysis (experiment 11) using microscopy (a) low magnification light illumination (b) high magnification-light illumination.....	84
Figure 5.16: Pre-experiment surface analysis/mapping (experiment 12) (a) using light microscopy (b) using interferometry	84
Figure 5.17: Post-experiment surface analysis (experiment 12) using microscopy (a) low magnification light illumination (b) high magnification-light illumination.....	85
Figure 5.18: Post-experiment surface analysis (experiment 13) using light microscopy-dark field (a) lower magnification (b) higher magnification	85
Figure 5.19: Surface analysis/mapping (experiment 14) (a) and (b) pre-experiment using microscopy and interferometry respectively (c) and (d) post-experiment analysis by microscopy	86
Figure 5.20: Surface analysis/mapping (experiment 15) (a) and (b) pre-experiment using microscopy and interferometry respectively (c) and (d) post-experiment analysis by microscopy	87
Figure 5.21: Pre-exp. (16) surface analysis/mapping using (a) microscopy (b) interferometry	88
Figure 5.22: Post experiment (16) Surface analysis using microscopy.....	89
Figure 5.23: Surface analysis/mapping (experiment 17) (e)	89
Figure 5.24: Surface analysis (experiment 18) using microscopy (a) low magnification (b) higher magnification.....	90
Figure 5.25: Surface analysis (experiment 19) using microscopy (a) low magnification (b) higher magnification.....	90
Figure 5.26: Surface analysis (experiment 20) using microscopy (a) low magnification (b) higher magnification.....	91
Figure 5.27: Experiment (21) surface analysis (a) and (b) pre-experiment using interferometry (c) and (d) post-experiment microscopy.....	92
Figure 5.28: Post-experiment surface analysis (experiment 22) using microscopy (a) dark field illumination (b) light illumination (bright field).....	92
Figure 5.29: Post experiment surface analysis (experiment 23) using light microscopy (a) low magnification (b) higher magnifications	94
Figure 5.30: Pre-experiment surface analysis/mapping (experiment 24) using (a) microscopy (b) interferometry	94
Figure 5.31: Post-experiment surface analysis (experiment 24) using OM (a) at low magnification (b) at high magnification.....	95

Figure 5.32: Surface analysis/mapping (experiment 25) (a) Pre-experiment surface mapping of hole profile using interferometry (b) Post-experiment analysis using microscopy	95
Figure 5.33: Surface analysis/mapping (experiment 26) (a) and (b) pre-experiment using interferometry (c) and (d) post-experiment analysis by microscopy (dark field illumination)	96
Figure 5.34: Surface analysis/mapping (experiment 27) (a) and (b) pre-experiment using interferometry (c) and (d) post-experiment analysis by microscopy	97
Figure 5.35: Surface analysis/mapping (experiment 28) (a) pre-experiment using interferometry (b) post-experiment analysis by microscopy	97
Figure 5.36: Surface analysis/mapping (experiment 29) (a) and (b) pre-experiment using microscopy and interferometry respectively (c) and (d) post-experiment analysis by light microscopy	98
Figure 5.37: Surface analysis/mapping (experiment 30) (a) and (b) pre-experiment using microscopy and interferometry respectively (c) and (d) post-experiment analysis showing spall by microscopy and SEM respectively (e) and (f) SEM images showing cracks on trailing side and base of original cavity	99
Figure 5.38: Surface analysis/mapping (experiment 31) (a) and (c) pre and post-experiment analysis using microscopy, (b) and (d) pre and post-experiment surface mapping using interferometry	101
Figure 5.39: Surface analysis (experiment 32) using microscopy (a) pre-experiment (b) post-experiment	102
Figure 5.40: Surface analysis/mapping (experiment 33) (a) pre-experiment surface mapping using interferometry (b) post-experiment surface analysis using microscopy (c) and (d) post-experiment analysis using microscopy on leading and trailing side respectively	103
Figure 5.41: Surface analysis/mapping (experiment 34) (a) pre-experiment surface mapping using interferometry (b) post-experiment 3D surface profile (c) and (d) post-experiment surface analysis using microscopy	104
Figure 5.42: Surface analysis/mapping (experiment 35) (a) pre-experiment surface mapping using interferometry (b) post-experiment surface analysis using microscopy	104
Figure 5.43: Surface analysis/mapping (experiment 36) (a) pre-experiment surface mapping using interferometry (b) post-experiment surface analysis using microscopy	105
Figure 5.44: Surface analysis/mapping (experiment 37) (a) pre-experiment surface mapping using interferometry (b) post-experiment surface analysis using microscopy	105
Figure 5.45: Surface analysis/mapping (experiment B1) (a) pre-experiment surface mapping using interferometry (b) 3D cavity profile	107
Figure 5.46: Surface analysis/mapping (experiment B1) (a) and (b) Spall profile using microscopy and interferometry	107
Figure 5.47: Surface analysis (experiment B2) (a) and (b) post 100million stress cycles using microscopy	108

Figure 5.48: Surface analysis/mapping (experiment B3) (a) pre-experiment surface mapping using interferometry (b) post-experiment surface analysis using microscopy	108
Figure 5.49: Surface analysis/mapping (experiment B4) (a) pre-experiment surface mapping using interferometry (b) post-experiment surface analysis using microscopy	109
Figure 5.50: Surface analysis/mapping (experiment B5) (a) pre-experiment surface mapping using interferometry (b) post-experiment surface analysis using microscopy (c) spall profilometry (d) spall microscopy - darkfield	110
Figure 5.51: Surface analysis/mapping (experiment B6) (a) pre-experiment surface mapping using interferometry (b) post-experiment spall profile using interferometry and microscopy	111
Figure 5.52: Pre-experiment surface mapping (exp. B7) using interferometry.....	111
Figure 5.53: Spalled Surface analysis (experiment B7) using microscopy (a) light illumination (b) dark field illumination at high magnification	112
Figure 5.54: Surface analysis/mapping (exp. B8) (a) & (b) pre-experiment surface mapping using interferometry (c) and (d) post-experiment surface analysis using microscopy	112
Figure 5.55: Pre-experiment (38) analysis using (a) microscopy (b) interferometry	113
Figure 5.56: Post-experiment (38) analysis using microscopy (a) light illumination (b) dark field illumination	114
Figure 5.57: Surface analysis/mapping (experiment 39) (a) and (b) pre-experiment surface mapping using interferometry (c) and (d) post-experiment surface analysis using microscopy	115
Figure 5.58: Post-experiment (40) surface analysis using microscopy (a) low magnification - showing location on the contact track (b) higher magnification	116
Figure 5.59: Surface mapping using interferometry (Experiment 41) (a) Surface profile (b) 3D image of cavity	117
Figure 5.60: Post Experiment (41) surface analysis (a) and (b) post 30 and 35million using light microscopy (c) and (d) post 35million using SEM, showing spall and hole base....	118
Figure 5.61: Surface analysis (Experiment 42) (a) pre-experiment (b) post 0.15M (c) Spall image - SEM (d) Spall centre (original hole base) - SEM image.....	119
Figure 5.62: Surface analysis/mapping (experiment 43) (a) and (b) pre-experiment surface mapping using interferometry (c) and (d) post-experiment surface analysis using microscopy	120
Figure 5.63: Surface analysis/mapping (experiment 44) (a) pre-experiment surface mapping - interferometry (b) post-experiment surface analysis – microscopy	120
Figure 5.64: Surface analysis/mapping (experiment 45) (a) and (b) pre-experiment surface mapping using interferometry (c) & (d) post-experiment (0.1M) spall profile (OM and WLI).....	121
Figure 5.65: Surface analysis (experiment 46) using microscopy (a) Pre experiment (b) post 0.2million (c) and (d) post-experiment (0.45million stress cycles).....	122

Figure 5.66 Corrected contact pressure vs. hole depth for small diameter holes (50µm)	124
Figure 5.67 Corrected contact pressure vs. hole depth for medium diameter holes (75µm)..	124
Figure 5.68 Corrected contact pressure vs. hole depth for large diameter holes (100µm)	125
Figure 5.69 Corrected contact pressure vs. hole depth for shape I (right cylindrical) - small holes – Material A and B.....	125
Figure 5.70: Replica cavity profile using SEM (a) and (b) Shape I (c) and (d) Shape II.....	126
Figure 5.71: Replica cavity profile using SEM (a) and (b) Shape III	127
Figure 5.72: Small cracks near cavity base – Experiment 16 (successfully completed).....	128
Figure 5.73: Small cracks near cavity base – Experiment 20 (successfully completed).....	128
Figure 5.74: No cracks observed – Experiment 18 (successfully completed).....	129
Figure 5.75: No cracks observed – Experiment 19 (successfully completed).....	129
Figure 5.76: Experiment 13 spall profile (original hole : 50 µm diameter and 30 µm depth) (a) dark field illumination (b) UV illumination (original hole also can be seen in the Figure)	130
Figure 5.77: Typical spalling mechanism with Shape I profile.....	131
Figure 5.78: Spall analysis (exp. 13, Dia: 50µm, Depth: 30µm) of cross sectioned sample using microscopy (light illumination) - first finishing	133
Figure 5.79: Spall analysis (exp.13, Dia: 50µm, Depth: 30µm) of cross sectioned sample using microscopy (UV illumination) - first finishing.....	134
Figure 5.80: Spall analysis (exp.13, Dia: 50µm, Depth: 30µm) of cross sectioned sample using microscopy (light illumination) - second finishing	135
Figure 5.81: Spall analysis (exp.13, Dia: 50µm, Depth: 30µm) of cross sectioned sample using microscopy (light illumination) - 3 rd finishing	136
Figure 5.82: Spall analysis (exp.42, Dia: 100µm, Depth: 50µm) of cross sectioned sample using microscopy (light illumination) - 3 rd finishing.....	137
Figure 5.83: Spall analysis (exp.42, Dia: 100µm, Depth: 50µm) of cross sectioned sample using microscopy (UV illumination) - 3 rd finishing	138
Figure 5.84: Surface analysis (experiment 6, Dia: 50µm and Depth: 20µm) using microscopy (a) post 50million stress cycles (UV illumination) (b) post 50million stress cycles (dark field illumination).....	140
Figure 5.85: Sub-surface analysis (exp.6, Dia: 50µm, Depth: 20µm) using microscopy (light illumination) - First finishing	141
Figure 5.86: Sub-surface analysis (exp.6, Dia: 50µm, Depth: 20µm) using microscopy (UV illumination) - First finishing	142
Figure 5.87: Sub-surface analysis (exp.6, Dia: 50µm, Depth: 20µm) using microscopy (light illumination) - 2nd finishing.....	143
Figure 5.88: Sub-surface analysis (exp.6, Dia: 50µm, Depth: 20 µm) using microscopy (UV illumination) - 2nd finishing.....	144

Figure 5.89: Surface analysis (experiment 12, Dia: 50 μ m and Depth: 30 μ m) using microscopy (a) post-6million stress cycles (light illumination) (b) post-6million stress cycles (UV illumination) (c) post-6million stress cycles (dark field illumination).....	145
Figure 5.90: Sub-surface analysis (exp.12, Dia: 50 μ m, Depth: 30 μ m) using microscopy (light illumination) - 1st finishing.....	146
Figure 5.91: Sub-surface analysis (exp.12, Dia: 50 μ m, Depth: 30 μ m) using microscopy (UV illumination) - 1st finishing.....	147
Figure 5.92: Sub-surface analysis (exp.12, Dia: 50 μ m, Depth: 30 μ m) using microscopy (light illumination) - 2nd finishing.....	148
Figure 5.93: Sub-surface analysis (exp.12, Dia: 50 μ m, Depth: 30 μ m) sample using microscopy (UV illumination) - 2nd finishing.....	149
Figure 5.94: Failure mechanism schematic – Step 1 (Concluded from spalled and incipient spall samples)	151
Figure 5.95: Failure mechanism schematic – Step 2.....	152
Figure 5.96: Failure mechanism schematic – Step 3.....	153
Figure 6.1: 2D Mesh for ball-on-ball (without any hole).....	157
Figure 6.2: Maximum shear stress (MPa) for 2D static model ball-on-ball (without any hole)	158
Figure 6.3: Maximum principal stress (MPa) for 2D static model ball on ball (without any hole).....	158
Figure 6.4: Maximum shear stress (MPa) for 2D static model ball- on-ball (with hole)	159
Figure 6.5: Maximum principal stress (MPa) for 2D static model ball on ball (with hole)	160
Figure 6.6: 2D Rolling model mesh for ball on ball (with hole).....	161
Figure 6.7: Maximum principal stress (MPa) for 2D rolling model ball on ball (with hole) - at start of rolling (indent lies outside the contact)	161
Figure 6.8: Maximum principal stress (MPa) for 2D rolling model ball on ball (with hole) - almost at the centre of the contact (indent lies almost centre of contact).....	162
Figure 6.9: Maximum principal stress (MPa) for 2D rolling model ball-on-ball (with hole) - at the end of rolling (indent lies outside the contact)	162
Figure 6.10: Maximum shear stress (MPa) for 2D rolling model ball on ball (with hole) - at the almost centre of contact.....	163
Figure 6.11: 3D Model ball on ball (with hole) (a) 3D Model mesh (b) Closer view of the mesh on the lower ball with hole of 100 μ m diameter and 50 μ m depth	164
Figure 6.12: Maximum principal stress (MPa) during rolling (located close to leading edge)	165
Figure 6.13: Max. shear stress (Tresca-MPa) during rolling (located close to trailing edge) .	166
Figure 6.14: Max. von Mises stress (MPa) during rolling (located close to trailing edge)	166

Figure 6.15: Two rolling cases (a) contact centre exactly at hole's centre (b) contact centre far away from hole	167
Figure 6.16: Mesh for axi-symmetric fluid cavity problem	169
Figure 6.17: Von Mises (MPa) for larger diameter (100 μ m) and shallow depth (10 μ m)	170
Figure 6.18: Maximum PS (MPa) for larger diameter (100 μ m) and shallow depth (10 μ m) ..	170
Figure 6.19: Tresca (MPa) for large diameter hole (100 μ m) and shallow depth (10 μ m)	171
Figure 6.20: Tresca (MPa) for large diameter hole (100 μ m) and depth (50 μ m), Shape II	171
Figure 6.21: Max. PS (MPa) for large diameter hole (100 μ m) and depth (50 μ m), Shape II ..	172
Figure 6.22: Nodal positions - along the hole base	173
Figure 6.23: Nodal positions - along the hole top	173
Figure 6.24: Von Mises stresses (MPa) for small diameter hole (50 μ m) for three depth levels – along the hole base	174
Figure 6.25: Tresca (MPa) for small diameter hole (50 μ m) for three depth levels – along the hole base	174
Figure 6.26: Maximum principal stresses (MPa) for small diameter hole (50 μ m) for three depth levels – along hole base	175
Figure 6.27: von Mises stresses (MPa) for small diameter hole (located close to cavity corner) – along hole top	175
Figure 6.28: Maximum principal stresses (MPa) for small diameter hole - along hole top	176
Figure 6.29: Tresca (MPa) for small diameter hole (located close to cavity corner) along hole top	176
Figure 6.30: Tresca (MPa) comparison for small, medium and large diameters holes - along hole base	177
Figure 6.31: von Mises (MPa) comparison for small, medium and large diameters holes - along hole top	177
Figure 6.32: Maximum principal stresses (MPa) comparison for small, medium and large diameters holes - along hole top	178
Figure 6.33: von Mises (MPa) comparison for small, medium and large diameters holes - along hole top	178
Figure 6.34: Nodal positions - along the hole base and depth – Shape I (Figure 6.36).....	179
Figure 6.35: Nodal positions - along the hole depth – Shape II (Figure 6.36).....	180
Figure 6.36: Stress field comparison for shape I and Shape II (along hole depth – Figure 6.34-6.35).....	180

List of Tables

Table 2.1: Physical Properties comparison of Silicon Nitride and M-50 Steel	21
Table 2.2: Properties of different lubricants.	22
Table 3.1: Main experiments conducted on star feature category 1 using Traction Fluid.....	35
Table 3.2: Additional exp. conducted on star feature category 1 using Traction Fluid.....	35
Table 3.3: Main experiments conducted on star feature category 1 using TMO.....	40
Table 3.4: Additional experiments conducted on star feature category 1 using TMO	40
Table 3.5: Experiments conducted on natural star feature category 1 using Gearbox oil	43
Table 3.6: Details of experiments on Category 1 stars using Grease	44
Table 3.7: Details of experiments on Category 5 stars	47
Table 3.8: Details of experiments on pit size	53
Table 5.1: Experiments conducted on small diameter hole (Shape I/right cylindrical) at low and high contact pressures.....	75
Table 5.2: Experiments conducted on small diameter hole (Shape I/right cylindrical) at Intermediate Pressure (4.5GPa).....	88
Table 5.3: Experiments conducted on small diameter hole (Shape I/right cylindrical) at low and high contact pressures with sharp base corners	91
Table 5.4: Details of experiments on medium size holes (Shape I/right cylindrical).....	93
Table 5.5: Experiments conducted on large diameter hole (Shape I/right cylindrical)	100
Table 5.6: Experiment conducted on Shape I (Class B Material)	106
Table 5.7: Experiment conducted on Long Slot (Shape I/cylindrical)	113
Table 5.8: Experiment conducted on Shape II (Conical) – Material A	114
Table 5.9: Shape Performance Experiments (Shape I, II and III)	117

Acknowledgements

Many people helped and supported me in this research project and I am really indebted to all of them.

I am very grateful to my supervisor and mentor, Professor Mark Hadfield for his continuous support and encouragement throughout this research work. His scholarly guidance, positive criticism, visionary supervision, inspirational and friendly nature led me to this stage of success. He is also acknowledged for his support for the regular trips to Holland for attending project meetings, joint working and discussions, and to attend and participate in international conferences.

I am thankful to Dr. Ben Thomas for his support, advice and encouragement during course of this research. His help in experimental work at start is appreciated. I would take this opportunity to thank my Industrial Supervisor, Dr. Robin Cundill for his invaluable advice, help in thesis draft and vision regarding this project. His experience in ceramic materials was a big source of inspiration in my research.

Financial support for this project from SKF ERC is much appreciated. Many people from ERC helped and supported me during the completion of this research project. My special thanks and gratitude go to Charlotte Vieillard for her continuous support, encouragement and guidance. Her help in experimental work especially defect categorisation and cross sectioning is highly appreciated. She has been very supportive during my stay at ERC. Dr. Jelena Sekulic from ERC remained the contact person at the start of this joint project. Dr. Yuri Kadin, Dr. Junbiao Lai and Andriy Rychaahivskyy are much thanked for their support in FE modeling and analysis.

Graduate School, Bournemouth University, is acknowledged for financial support to travel Austria, Italy and USA to attend training courses and conferences.

I would also like to thank our research centre's director, Dr. Zulfiqar Khan for his support and help. Professor Jim Roach, Kelly Deacon-Smith, Naomi Bailey and Natalie Bates are acknowledged for their support during my stay at Bournemouth University. Brian Wright, Kevin Smith, Mike Day, and other members of BU workshops are acknowledged for their help in experimental work. Dr. Iakavos Tazankis is thanked for his help in surface analysis. Dr. Lorna Anguilano from ETC Brunel University is acknowledged for her help in SEM wok. Dr. Rizvi from Laser micromachining (LML

UK) and Dr. Clarke from Clark-MXR (USA) are thanked for their technical support in laser machine work during controlled defects machining.

Finally, last but not least, this work would have not been completed without the support and help from friends here at BU and family members back in Pakistan. My parents and other family members are acknowledged for all their support and prayers. Special thanks are for my fiancé; Sumaira Gulzar (and now my wife) for her patience and love during this research study.

Author's Declaration

This thesis contains the original work of the author except otherwise indicated.

Abbreviations/Nomenclature

<i>a</i>	Contact radius - Eq. A.4, 5.1
<i>AISI</i>	American Iron and Steel Institute
<i>ANSI</i>	American National Standard Institute
<i>BEASY</i>	Boundary Element Analysis System
<i>BEM</i>	Boundary Element Method
<i>CPA</i>	Chirped Pulse Amplifier (Laser)
<i>Crack broadening</i>	Crack mouth/face opening
<i>Crack growth</i>	Crack extension and growth in one direction
<i>Cracking</i>	Newly created cracks
<i>cSt</i>	centi Stoke ($1\text{mm}^2/\text{sec}$ or $10^{-6}\text{ m}^2/\text{sec}$)
<i>CTOD</i>	Crack Tip Opening Displacement
<i>DEC</i>	School of Design, Engineering and Computing (BU)
<i>DPSS</i>	Diode Pumped Solid State (Laser)
<i>E*</i>	Effective modulus of elasticity (Hybrid contact) – Eq. A.3-A.4
<i>EBM</i>	Electrical Beam Machining
<i>Edge wear</i>	Rounding and local wear at the edge of the features
<i>EDS</i>	Energy Dispersive x-ray Spectroscopy
<i>EHD</i>	Elasto-Hydrodynamic
<i>ERC</i>	Engineering and Research Centre (SKF)
<i>ETC</i>	Experimental Techniques Centre (Brunel University)
<i>Failure/Spall</i>	Large material loss triggering vibration sensor to shut down machine
<i>FEM</i>	Finite Element Modeling/Method
<i>FPI</i>	Fluorescent Penetrant Inspection
<i>FV</i>	Finite Volume
<i>GPa</i>	giga-pascal (10^9 N/m^2)
<i>GR</i>	Gearbox oil
<i>Grs</i>	Grease
<i>h</i>	Effective height – Eq. 2.1
<i>H_{min}</i>	Minimum film thickness – Eq. G.1

<i>HIP</i>	Hot Isostatically Pressed
<i>HV</i>	Vickers Hardness
<i>K_I, K_{II}, K_{III}</i>	Stress Intensity Factors
<i>K_{IC}</i>	Fracture Toughness
<i>ΔK_{th}</i>	Crack propagation threshold
<i>L</i>	Stress factor – Eq. A.1
<i>L</i>	Shaft load (modified four ball machine) – Eq. A.2
<i>LASER</i>	Light Amplification by Stimulated Emission of Radiation
<i>LBM</i>	Laser Beam Machining
<i>LEFM</i>	Linear Elastic Fracture Mechanics
<i>LML</i>	Laser Micromachining Limited
<i>LST</i>	Laser Surface Texturing
<i>Local loss</i>	Material loss within the confine of the original feature
<i>M</i>	Millions stress cycles
<i>Material loss</i>	Material loss within the confine of and extending outside the original feature
<i>Micro-slip</i>	Small relative tangential displacement in a contacting area at an interface
<i>Missing material</i>	Pits or holes typically originating during the densification stage of manufacturing on the rolling element bearing surface
<i>mm</i>	milli meter (10 ⁻³ m)
<i>Nd</i>	Neodymium doped
<i>NS</i>	Natural Star
<i>OM</i>	Optical/Light Microscope
<i>P</i>	Contact load – Eq. A.2
<i>P_o</i>	Maximum contact pressure – Eq. A.3, 5.1
<i>P_r</i>	Contact pressure at distance ‘r’ from contact centre – Eq. 5.1
<i>PS</i>	Pit Size (chapter 3) / Principal Stress (chapter 6)
<i>psi</i>	pound-force per square inch
<i>r</i>	Distance from contact centre – Eq. 5.1
<i>R*</i>	Effective radius (Hybrid contact) – Eq. A.3-A.4
<i>R_l</i>	Lower ball radius – Eq. A.1

R_u	Upper ball radius – Eq. A.1
R_a	Average surface roughness
<i>RCF</i>	Rolling Contact Fatigue
<i>rpm</i>	revolutions per minute
<i>SEM</i>	Scanning Electron Microscopy
<i>Stopped</i>	Test stopped (but with new features or due to ball rotation)
<i>Star feature</i>	Small radial crack patterns caused by over-rolling of diamond grit particles during ball lapping
<i>Suspended/ Completed</i>	No damage or no changes observed at predefined number of cycles (successfully completed)
<i>STLE</i>	Society of Tribologist and Lubrication Engineers (USA)
<i>TEM</i>	Transmission Electron Microscopy
<i>TF</i>	Traction Fluid
<i>TM/TMO</i>	Thin Mineral Oil
<i>Tribolayer</i>	Adherent surface layer to the surface of the contact track
<i>UMW</i>	Ultrafast Micromachining Workstation
<i>USM</i>	Ultrasonic Machining
<i>Uplift</i>	Raising of the material within the feature
<i>UV</i>	Ultra Violet
<i>WLI</i>	White Light Interferometer
<i>XFEM</i>	Extended Finite Element Method (FEM based technique used in Abaqus for modeling crack without changing mesh)
<i>YAG</i>	Yttrium Aluminium Garnet
<i>YLF</i>	Yttrium Lithium Fluoride
<i>Z</i>	No. of lower balls – Eq. A.1
β	Angle of chord of ring crack circle to contact centre line
φ	Angle in modified four ball machine (between top ball and lower balls) – Eq. A.2
φ_0	Half angle of ring crack arc
δ	Distance of centre of ring crack circle to contact centre line
μ	Coefficient of friction
μm	micro meter (micron – 10^{-6}m)

Chapter 1 Introduction

1.1. Background

Technical ceramics like silicon nitride, silicon carbide, alumina and zirconia (zirconium oxide) have shown improved performance in engineering applications like hybrid bearings, biomedical implants, aerospace and marine industry. However, not all such ceramics are suitable for rolling bearings and gears subjected to high repetitive contact stresses. The major limiting factors for ceramics in bearing applications are the low fracture toughness and difficulties in fabrication and high manufacturing costs compare to its counterpart steel. Silicon nitride has been proven to be the superior ceramic material for bearings [Miner et al. 1996, Tanimoto et al. 2000] particularly in hybrid bearings (steel races and ceramic rolling elements – Figure 1.1). Properties of low density, high stiffness and high corrosive and heat resistance give performance advantages in high speed bearings used in aircraft gas turbine engines [Hamburg et al. 1981, Miner et al. 1996] machine tool spindles [Aramki et al. 1988] and turbochargers [Tanimoto et al. 2000]. The non-conductive nature of silicon nitride allows it to be used in bearings for electrical traction motors as well as medical [Rahaman et al. 2007, Chevalier et al. 2009], nuclear and marine applications. Much work has been done on the development of the material's structure, properties, quality and manufacturing processes so that bearing grade silicon nitride is now widely available.

The main limiting factor of silicon nitride in hybrid ball bearing applications is the presence of surface defects and low fracture toughness [Piotrowske and O'Brien 2006]. These defects can decrease strength and performance and can shorten the life of bearing elements. Surface defects may be of different forms including cracks, inclusions, missing material (pits, holes) and contact marks. These defects may originate at various stages of manufacturing process from the original powder to final machining and polishing and can be very difficult to detect. Much work has been done regarding the rolling contact life of rings and balls with different defects in all-steel bearing applications. Major or severe defects, particularly cone or ring cracks, in silicon nitride balls in rolling contact applications also have been investigated extensively by different researchers [Hadfield 1993, Wang 2001, Zhao 2006]. Silicon nitride rolling element bearing with surface ring cracks were also used in refrigerated lubricated contacts [Khan 2006] and computational study was also conducted for critical flaw size for ring cracks [Levesque 2009].

Little, if any, work has been carried out on less severe surface defects on silicon nitride balls and their effect on performance. These defect types are missing material (pits or holes typically originating during the densification stage of manufacturing) and ‘star’ type features. These latter features are small radial crack patterns caused by over-rolling of diamond grit particles during ball lapping. Some star features also contain missing material. The main focus of this study has been to analyse the rolling contact fatigue behaviour of silicon nitride balls with missing material and star features, to determine failure mechanisms and to establish tolerable defect sizes in hybrid ball bearing application.



Figure 1.1: Hybrid Ball Bearing (Courtesy: SKF)

1.2. Scope and Objective of the Research

Scope of this study is to find out the effect of missing material and star features on the rolling contact fatigue performance of silicon nitride balls under rolling contact fatigue both experimentally as well as numerically. Research question is to find material tolerance and failure modes for surface star like features and missing material within silicon nitride in rolling contact.

The objectives of this research study can be summarized as;

- a. To understand the prevailing mechanisms of different surface defect geometries on rolling bearing elements

-
- b. To categorise surface star features and find their influence on the rolling contact fatigue characteristics of silicon nitride material
 - c. Simulate the precise missing material scenario by artificially producing surface defects using laser technology (micromachining)
 - d. Understand the failure mechanism of artificially produced missing materials that are aligned with natural surface defects
 - e. To generate numerical models with dry and lubricated contacts to determine stress fields and potential location and position of crack initiation and failure

1.3. Literature Review

1.3.1. Rolling Bearings

Rolling bearings are widely used to permit rotary motion of or about shafts and mainly used in aircraft gas turbines, rolling mills, machine spindles, gyroscopes, pumps and different drilling, power transmission and household appliances. These bearings are thought better than other bearings due to less frictional power loss, less amount of lubrication, requires shorter axial length and having variety of load and speed applications with excellent performance [Harris 1990].

Rolling bearing technology evolved over thousand years B.C. to present. Leonardo da Vinci was first who published manuscript on thrust ball bearing in 1490-1499. First ball bearing patent was issued to J.Rowe in 1734 but it was Coulomb who constructed the first prototype of modern ball bearing in 1760. Fischer (FAG) and Henry Timken (Timken) were the main manufacturers of rolling bearings in nineteenth century [Morton 1965]. Stresses between two elastic spheres in contact were first derived and calculated by Hertz [1882]. A Swedish engineer, Wingquist, was the first person who invented self-aligning ball bearing in 1907 at SKF. Talian [1969] classified the modern bearing era in three main domains i.e., classical, empirical and modern. Before the World War II, bearing were classified on the basis of art involved and after then these bearing are being designed on the basis of scientific knowledge. In 1970, Dee first proposed hot pressed silicon nitride for rolling element and journal bearing applications [Dee 1970].

1.3.2. Bearing Materials

Most rolling bearings throughout the world are made from 1% carbon, 1.5% chromium steel (BS 535A99, DIN 100Cr6, SAE 52100). This steel can be heat treated to a spheroidised annealed condition for ease of machining and then quenched and tempered to a hard martensitic or bainitic structure. Some bearings are also made from carburized low alloy steels. Tool steels such as M1, M2, M10 and T1 have been used for aeroengine mainshaft bearings. These steels have enough fatigue and wear resistance and adequate fracture toughness and so can be used in many special applications. Tool steels are particularly suited for gas turbine engine bearings as they have good temperature resistance and dimensional stability at higher operating temperatures which cannot be achieved with carbon-chromium steels. Recently, new steels, M50 and BG42, have been developed aerospace applications for long endurance and high temperature applications. BG42 has better corrosion resistance than other bearing steels. M50 and BG42 were found to be the most reliable and long endurance materials due to their reliable manufacturing (vacuum induction melted - vacuum arc remelted) techniques [Harris 1990].

Silicon nitride due to its lower density, lower mass moment of inertia and low coefficient of thermal expansion compared to its counterpart M50 Steel is feasible for gas turbine engines and aerospace applications [Hamburg et al. 1981]. With aircraft turbine mainshaft bearings, the main material property requirements are high temperature capability, high corrosion and fatigue resistance, high modulus of elasticity, low coefficient of thermal expansion and low density. Of the various carbide, oxide and nitride ceramics, silicon nitride has the best combination of these properties and has the lowest density which is important in reducing centrifugal moments in high speed bearings [Harris 1990]. It has been predicted that silicon nitride based hybrid bearings have 20 percent less frictional losses and 50 percent less wear rates than M50 steel bearings [Cento and Dareing 1999]. Wear rate of silicon nitride is predominantly depends on lubrication type and initial surface roughness [Chao et al. 1998]. Table 2.1 compares the physical properties of silicon nitride with M50 steel.

Silicon nitride based hybrid bearing can be used for extreme operating conditions [Bhushan and Sibley 1981, Takebayashi 2001]. Low density and low coefficient of thermal expansion are most important factors for high speed spindles for machine tools [Aramaki et al. 1988]. The use of silicon nitride hybrid bearings in machine spindles reduces the

centrifugal forces and gyroscopic moments which are very important for precise machining. Burrier [1996] done extensive testing to find best bearing grade silicon using 13 different type of materials from nine suppliers and concluded that hardness have more effect than density and elastic constant of the material for rolling contact fatigue. Cundill [1997] has conducted numerous experiments for finding the impact resistance of the silicon nitride balls with different manufacturing technique and additives. From the experiments, he concluded that hot isostatically pressed (HIP) or sintered + HIP materials had the maximum experimental and calculated strength [Zhao 2006]. Different silicon nitride materials may have similar fatigue behaviour although they degraded faster in cyclic loading than static loading [Bermudo et al. 1997].

1.3.3. Bearing Elements Life

Bearing fatigue life is obviously important and some models have been presented to calculate/predict the life of steel bearings. Lundberg and Palmgren [1949] performed comprehensive work on the rolling elements dynamic capacity and life by using the Weibull weakest link theory. Fatigue life based on ANSI was also discussed based on Lundberg-Palmgren theory but this may lead to inadequate estimates due to inclusion of unusual loading and operating conditions in ANSI formulas [Harris 1990]. Lundberg-Palmgren is not applicable to silicon nitride based hybrid bearings as ceramic materials fails in tension whereas metallic materials are weaker in shear than tension. Moreover, subsurface cracks or pre-existing defects cannot be handled using this theory [Levesque 2009].

A mathematical model for fatigue life based on an empirical power law which has its origin in Lundberg-Palmgren theory for complete bearings was presented by Ioannides and Harris [1985]. This model was equally valid for bearings and rotating beams. It had a limitation that the initiation stage of fatigue should be much longer than the crack propagation stage. This model was validated only for conventional steel bearings. A new life equation was proposed by Raje and Sadeghi [2008] based on statistical distribution of spalling lives and resultant stress life results. This new life equation is similar in structure to Lundberg-Palmgren equation with a modification term. This equation can only be used for steel bearings. A similar statistical based life theory was also presented by Schmitz [2012] which provides a linkage between rolling contact fatigue and structural fatigue but

again this is only applicable to steel bearings. Stress based life prediction model has also been developed [Yu and Harris 2001] but all these models only cover steel bearings.

Kimura et al. [2002] presented an experimental method for finding rolling contact fatigue life but for steel roller case. High contact stresses and lubricant type affect the rolling bearing element life [Al-Bukhaiti et al. 2011]. Bearing element has longer life under gearbox oil than grease and mineral oil at the same operating contact pressure.

In last two decades, some researchers [Hadfield 1993, Wang 2001, Zhao 2006, Goepfert et al. 2000, Bradshaw 2011] have reported work regarding RCF life of silicon nitride rolling element using experimental techniques. All the existing literature is mainly applicable to steel or silicon nitride having ring or C-cracks and/or radial and lateral cracks.

1.3.4. Surface Defects

Many researchers have outlined the different surface defects which may damage the surface including and causing ultimately failure of bearing. These defect may be ring, lateral and radial cracks or surface missing material or star like crack or some types of inclusions.

Hadfield [1993] highlighted ring, lateral and radial cracks on silicon nitride surfaces and their failure modes using exhaustive experimental study. Wang and Hadfield [2003] had done comprehensive studies on surface defects, RCF and failure modes. They covered different defects including ring, radial, lateral and star defects. Ring cracks had also been classified as long cracks (typically with crack length of 3mm) and short cracks (typically with crack length less than 250 μ m).

A modified four ball machine was used to experiment on silicon nitride with surface line cracks [Wang and Hadfield 2002]. Optical microscopy and scanning electron microscopy were used for the surface analysis. Experiments were performed with gearbox oil as the lubricant and with different line crack lengths and contact pressures. Failure was found and had of two stages; crack propagation from the original line crack and formation of secondary surface cracks and causing fatigue spall by secondary crack propagation conically away from surface and meeting the initial line crack. Gap between crack faces increased due to wear of contacting surfaces and that's reason for the secondary surfaces at the leading edges of the contact.

Ueda [1989] performed comprehensive theoretical study for different surface cracks caused by blunt, sharp and sliding indenters in ceramics. He derived the mathematical relation for stress intensity factor for all three cases. He also mentioned different stresses in rolling contact like compressive and tensile stresses and conical shape propagation in the ceramics with blunt indenter cracks. In case of sharp indenter cracks, plastic deformation occurs under the contact loading plane and crack arises in high tensile area and radial cracks occurs as crack moves in radial direction and lateral crack in case of un-loading and in lateral direction. In sharp indenter case, both elastic and plastic stresses developed and crack growth is governed by residual and elastic stresses. In the sliding contact, at the contact and ahead of it, compressive stress dominates whereas behind the indenter, tensile stress pattern prevail. Stress pattern is majorly dependent upon the coefficient of friction (μ) and cracking and plastic deformation is due to μ . Although this is comprehensive work but only covers contact surfaces without pre-damage/defects.

Major work in the literature regarding surface defects within silicon nitride is related to surface ring or C-cracks [Fujimoto et al. 1992, Zhao 2006, Khan 2006, Levesque and Arakere 2008, 2010a, b]. Radial and lateral crack profiles were created on silicon nitride surfaces using Vickers and Knoop indentation [Lube 2001] without finding rolling contact fatigue life of silicon nitride. Different crack profiles can be generated including half-penny and radial using different indentation load and microstructure of silicon nitride [Miyazaki et al. 2010]. Very shallow surface dents within EHL contacts have been discussed [Ville and Nelias 1999, Morales-Espejel and Gabelli 2011] but majorly for steel surfaces. Very little work is available regarding surface missing material and star like features within silicon nitride.

Artificial defects having transverse and longitudinal furrows, conical and spherical dents were studied experimentally using two-disc machine and mineral oil was used as lubricant. Different indentations shapes were produced using special indenters on the specimen surface. Surface roughness, specimen hardness and temperature were changed to observe their effect on the crack initiation. Crack initiation around four different types of defects is controlled by the stress field induced by the normal and tangential forces resulting from micro-EHL around the defects [Cheng et al. 1994]. Although this work has some similarities with the work being considered in the missing material part but main factors being targeted are different. Secondly, specimens were taken from AISI 52100 steel with longitudinal surface roughness of approximately $0.188\mu\text{m}$.

Surface indentation due to particle contamination can change the pressure and stress field and can cause surface initiated fatigue [Diab et al. 2003, Gabelli et al. 2008]. Local stresses related to lubrication film developed at the dent are significant to the crack initiation mechanism. Flaking type of failure occurs well before getting maximum Hertzian stress to initiate surface crack in SAE 52100 material with some surface micro holes [Kida et al. 2006].

Melander [Melander 1997] did FE analysis for short cracks at inclusions in bearing steel. These inclusions configurations were; a pore, a manganese sulphide inclusion, a through cracked alumina inclusion, an un-cracked alumina inclusion and finally a titanium nitride inclusion. These inclusions were 20 μm in diameter and cracks were allowed to grow from 2 μm to 8 μm . This study was for bearing steel.

1.3.5. Experimental Techniques

Different experimental techniques have been used for simulating the actual rolling contact fatigue phenomenon in laboratory. Each rig has its own advantages and limitations to use. In general, five ball machine provides more traction than four ball machine due to more contact of lower balls with the upper ball. Different other techniques like balls-on-rod, disc-on-rod, contact rings, ball on plate and full scale experiment have also been used. Main advantages of the 4-ball machine over the 5-ball is that the 4-ball machine kinematics are statically determinate whereas the 5-ball machine has a kinematically indeterminate structure. In five ball machine, contact angle produces a higher spin roll ratio and increased dynamic effects has much influence on ceramic materials.

Scott and Blackwell [1973] were the first who reported the work for experimenting hot pressed silicon nitride balls using modified four ball machine. This machine was designed to find lubricant properties and but then it has been used for both lubricant and material strength and failure mechanism of materials [Tourret and Wright 1977]. Literature [Scott and Blackwell 1978, Hadfield 1993, Ahmed 1998, Kang 2001, Wang 2001, Zhao 2006, Khan 2006, Karaszewski 2008, Wang 2010, etc.] provided enough information regarding experiments conducted using modified four ball machine. In modified four ball machine, three lower balls are driven by the upper ball in the collet. Five ball machine was first reported by Parker and Zaretsky from NASA [1975]. Comparative study has been published among the different test rigs including four and five ball machines [Hadfield et al. 1995, Kang and Hadfield 2003] to see the machine effect on the rolling contact fatigue

of rolling element bearing. In five ball machine, contact angle between upper ball and lower balls is 54.7° in contrary to 35.3° in four ball machine.

Kimura et al. [2002] conducted large no. of experiments on four ball rollers to see the effect of traction and micro-slip. They presented [from literature, Halling, J., "Principles of Tribology", The Macmillan, New York, pp. 174-201,1975] the analysis for quantitatively estimation of micro-slip (small relative tangential displacement in a contacting area at an interface) and especially when it happened by traction. The wear experiments were conducted on the four-roller assembly without lubrication where rollers were of carbon steel under normal load of 265-1089N and rotational speed of 800-2000rpm. The contact fatigue life was determined by using Amsler friction machine (Two Roller machine) with lubrication and normal load of 2940kN (Top Roller). Fatigue life was determined by the vibration sensor at the onset of contact fatigue damage and it always happened in lower roller. Plastic flow i.e., forward flow/movement in the surface layer was due to repetition of contact and was measured by displacement of small Vickers indentation. It was observed that wear was heavier for driver whereas shorter life was for follower roller and due to this reason that damage is concentrated in thin subsurface layer with driver and thick in follower.

Kalin and Vizintin [2004a,b] presented unique rolling contact device (ball-on-flat) and having complements over several available devices because of its point contact geometry and broad range of specimens. Variety of samples can be experimented with variable speeds and loads and surface conditions and particularly have importance in ceramics and coated materials, fine surface finish, and sharp tolerances of samples.

Zhao [2006] conducted experiments using modified four ball machine to assess the rolling contact fatigue performance subjected to different crack sizes, various lubricants (Grease, Gearbox oil and Traction fluid), applied loads and at specific orientation. It was concluded that RCF life influenced by load, lubricant and crack size and crack branching was also observed along the crack propagation. Grease and Gearbox oil shown the better performance whereas shorten life in case of traction fluid due to high stress intensities around the cracks. New thing was secondary cracks and crack branching which eventually causing final failure.

Different tribo-testers provide different results due to traction, contact geometry and other parameters. Khan [2006] had used modified four ball machine for refrigerant as lubricant

for ring crack experiments using silicon nitride rolling elements bearing. Configurations within tribo-testers influence the sample's rolling contact life [Mosleh and Bradshaw 2011, Mosleh et al. 2011]. A three point contact machine was used for pure rolling (without sliding) fatigue test to find the rolling contact fatigue of different categories of silicon nitride rolling element bearing [Zhou et al. 2011]. This machine can be used for high rotation speed of ball (23000rpm) and 7GPa contact stress can be achieved using this machine.

Rolling contact fatigue life of low cost sintered and reaction bonded silicon nitride was found using ball-on-rod and modified four ball testers. Increasing trend of rolling contact fatigue life was observed for pre-cracked balls from coarse to fine and conventional surfaces conditions. Both testers provided similar results [Wang et al. 2010]. Ball-on-rod tester is mainly used in USA to find both lubricant properties and the materials RCF performance. Ball-on-rod tester's design was described by Glover [1982].

1.3.6. Failure Modes in Silicon Nitride

In contrary to steel rolling elements [Tallian 1967], silicon nitride balls normally fail due to spalling, and according to some researchers, delamination may also occur as a failure mode. Fleming et al. [1977] presented a mathematical model for subsurface crack propagation in sliding contact for delamination wear. Five processes are involved in the delamination wear including transmission of forces, deformation, crack nucleation, crack propagation and wear sheet separation. LEFM (Linear Elastic Fracture Mechanics) can be used for subsurface crack propagation in delamination wear (for coefficient of friction greater than 0.5), wear increase by contact stresses and proportional to normal load. For a given size of asperity contact, there is a one depth and one effective length for which the stress intensity factor is the maximum. All the work presented was regarding steel and nothing was mentioned about ceramics and silicon nitride. Suh [1977] presented an overview of delamination theory [Fleming et al. 1977] of wear and work update (experimental and analytical) regarding delamination. He used different steels to support his theory and work.

A pitting model was presented by Keer and Bryant [1983] for rolling contact fatigue using angled-surface braking crack with the interaction of Hertzian contact including friction. By increasing the crack's length and calculating stress intensity factor, estimate of fatigue can be found. Crack growth mechanism as the shearing mechanism and occurs when crack is

directly under the contact region; crack curving parallel to surface is due to tensile stresses and final cleavage is due to the fatigue crack propagation to the surface or nearest crack.

Bower [1988] presented a two dimensional model for surface initiated rolling contact fatigue. It was the similar work presented previously by Keer and Bryant [1983] for influence of the fluid pressure on the crack faces and also incorporated the frictional locking effect between the faces of the crack. It has been discussed three different possible way of crack propagation i.e., mode II crack growth due to cyclic shear stresses; fluid forced in the crack by the load and growth by fluid trapped inside the crack. From the experiments, some very interesting results were also found; crack only propagate if fluid lubricant used to the contacting surfaces; crack always propagate in the direction of the motion and for relative sliding between two driving surfaces.

Brittle fracture under the sliding contact was highlighted by Bower et al. [1994] and two limiting cases of friction were considered. Fracture load by the indenter was calculated and was compared with load that causing plastic deformation in the solid. Residual tensile strength after contact load was also calculated. Brittle fracture only happened in high brittle materials like glass and ceramics and brittle fracture damage is severe but wear rate due to fracture is slow. For the perfectly bonded cylinder to the surface, load ratio ($\frac{P}{Q^{frac}}$) play an important role and crack path depends on this ratio (P is normal load and Q^{frac} is critical tangential load). For small load ratio, crack goes to the surface whereas for larger value it goes to the depth and eventually comes to the surface. Furthermore, contact fracture reduces the strength and the critical residual stress is a small fraction of a stress required to fracture the solid in the absence of contact loading.

Hadfield et al. [1993a,b 1994, 1995] carried out an extensive experimental study using a modified 4-ball machine and on crack-free and artificially cracked balls. (These cracks were mainly part-circular Hertzian cone or ring cracks, also referred to as ‘C’ cracks). Prevailing failure mechanism found was delamination in the crack-free state and spalling in the case of pre-cracked balls. Lubrication had a key role in rolling contact performance and life and that good quality lubricants not only increase the life but also lead to better performance. Under oil lubricants, it was found that balls with ring cracks had shorter lives than those with radial and lateral cracks. Failure mode with ring cracks in oil was by spalling, whereas secondary spalling was also observed when kerosene oil was used. A major finding was that failure of silicon nitride balls (with and without cracks) was non-

catastrophic spalling. In the case of radial and lateral cracks, three different failure modes were observed based on type of lubricant;

- 1: Lateral crack spall
- 2: Radial crack propagation and surface delamination
- 3: Radial crack damage and surface bulging.

Experimental studies on the sub-surface cracks on balls with delamination were observed using dye penetrants and scanning acoustic microscope. Two different combinations with silicon nitride/silicon nitride and steel/silicon nitride contacts at different contact pressures, lubricants and shaft speeds were studied. Sub-surface crack growth travelled relatively large distances from the original area of surface damage and can be divided into three stages;

- First stage spalling (incipient ring crack spall) occurs in case of kerosene oil due to its penetration capability and initial crack propagation.
- Second stage spall with more material removal at the incipient phase and the deepest micro-crack initiated from the depth of 105 μm and reached to 145 μm .
- Third and final stage was more severe material removal and final fracture was taking place due to lubricants hydrostatic pressure produced large bending moments within the material. It was also revealed from the surface analysis that progressive ring crack spall identified ring, conical and tertiary phase crack growth and spall depth was related to maximum subsurface shear stress.

Porosity has dominant role which controls wear mode and performance [Hadfield 1998]. Experimental and numerical study was conducted using low and high viscosity lubricants on the crack free and ring-cracked balls. Fatigue failure of lubricated rolling silicon nitride is depend on the contact stress and type of lubricant and is independent of rolling direction. Contact stress makes the ring crack grows towards the inside and the lubricant is the key factor for pitting and spalling [Wang and Hadfield 1999].

Performance is critically dependant on the crack location and spall failure only occurs at specific locations in case of ring defects. The life decreases as β (angle of the chord of the ring crack circle to the central line of the contact track) increases and life decrease as δ (distance of the centre of the ring crack circle to the central line of the contact track) decreases and the worst condition happened when $\beta=90^\circ$ and $\delta=0$ [Wang and Hadfield

2000b]. Radial and lateral cracks were tested using modified four ball machine. Lubricant was found trapped and due to hydrostatic pressure crack propagated and eventually delamination failure occurred [Hadfield et al. 1995].

Fatigue spalling was recorded as the failure mode in case of ring cracks. Secondary cracks were the important part of failure which propagate and finally meet the initial cracks and causing elliptic spall. Secondary surface cracks formed due to high tensile stress which is due to presence of surface cracks and this tensile stress increases as crack depth and crack gap increases. Crack face friction coefficients play an important role in the failure and rolling contact fatigue and secondary crack formation decreases as coefficients increases [Wang and Hadfield 2004].

A recent experimental study by Thoma et al. [2004] was conducted using four-ball apparatus to determine failure mechanism and time to failure for silicon nitride and Zirconia balls. Zirconia balls found has short life and also could not sustain similar contact loads like silicon nitride did. Silicon nitride balls from different manufacturers showed different life depending upon composition of additive materials and porosity level. It's seen that materials with highest porosity level found most undesirable tribological properties whereas surface roughness does not have prominent influence on the performance of balls.

Micro-spalling is due to surface initiated issues like particle dents, corrosion pitting and asperity contacts [Gloeckner et al. 2009]. The maximum contact friction power region is most likely to develop micro-spalling.

1.3.7. Laser machining

Laser micro- and nano-machining has been used for tribological applications such as laser surface texturing. In laser surface texturing [LST], friction is reduced between mating surfaces due to micro- and nano-scale laser surface treatment which reduced the contact area between the surfaces [Prodanov et al. 2013]. Textured surfaces are also attributed towards better sealing [Zhu et al. 2010] and provide lubricant pockets [Vilhena et al. 2009]. Surfaces are normally textured using a pulsed Nd:YAG due to its good beam quality and high ablation efficiency [Meijer 2004]. Surface topography is measured by an established non-contact method like white light interferometry. Although a reasonable literature is available for laser machining for tribological surface texturing but little is available for specifically silicon nitride micro machining for simulating missing material

type of defect with different depth, diameter and shape to find the tolerance and failure modes (chapter 4 and 5).

1.3.8. Residual Stresses

Residual stresses induced during rolling contact have been discussed in literature [Hadfield et al. 1993c, Hadfield and Tobe 1998, Kang et al. 2002 and Khan et al. 2005, 2006, 2007]. These stresses are measured using x-ray diffraction techniques. These stresses are found in compressive in nature and had positive effect on rolling contact fatigue life of silicon nitride. Maximum residual stresses measured were below than 200MPa and are found useful for rolling contact fatigue life for ceramic material as it has increased the rolling contact fatigue of silicon nitride.

1.3.9. Numerical Simulations

Many researchers have used different numerical schemes for diagnosing the contact stresses and deformations, crack propagation and stress intensities. Finite element and boundary element analysis has been widely reported for investigating stress field, stress intensity factors and deformations. Wang and Hadfield [2000b, 2001, 2003, and 2004] and Zhao et al. [2006b] have done extensive Beasy (BEM based commercial software for structural analysis) for investigations of the ring and line cracks Fracture mechanics approach been used for rolling contact problem by applying Hertzian point loading with normal pressure and tangential traction. Ring crack geometry was modeled according to experimental observations and was a conic shape with a crack as a radius of 0.21mm and crack angles were 50° and 40°, maximum contact pressure was 4.0GPa and 5.6GPa, maximum crack depth 0.05mm and ϕ_0 (half angle of ring crack arc) was 45°. Stress intensity factors (K_I , K_{II} and K_{III}) were calculated and RCF failure predicted by comparing these factors to the fracture toughness (K_{IC}) and crack propagation threshold (ΔK_{th}). Although they did extensive work by using different crack depths, crack angles and contact pressure but all their work related to surface ring cracks and there are no clear evidences of highlighting the importance of hydrostatic pressure effects in silicon nitride.

To find the acceptable defect (crack) size and surface behaviour, Wang and Hadfield [2003] modeled the pre-existing line crack defects in silicon nitride by using the 3D BEM. Existence of line cracks increased the surface tensile stress which leads the secondary fracture near the pre-existing flaw. These secondary flaws have the dominant effect on the

final pitting and changes in crack geometry significantly change the surface stress at the leading or trailing edge of the contact area. In RCF of surface ring crack, crack can propagate both inside and outside of the contact path; although outside contact path may be faster than inside the contact path [Kida et al. 2004]. Minimum crack size to grow depends on the contact conditions and mainly on contact pressure [Jun et al. 2011].

Crack front propagation depends on the ring crack location and failure only occur under certain positions ($\beta=90^\circ$ and $\delta=0$, and then $\beta=45^\circ$ and $\delta=0$). Crack propagation under rolling contact only occurs underneath the surface and creation of secondary cracks plays important role in life calculations [Wang and Hadfield 2001]. 2D FEM approximations show that stress intensity factor of mode II (K_{II}) is approximately one tenth of the stress intensity factor of mode I (K_I) and hence it showing that tensile stresses play an important role [Wang and Hadfield 2003].

Lubricant effect was modeled by the different friction coefficients [Zhao et al. 2006b]. Stress intensity factors for mode I and II are assessed to find their effects and concluded that when the crack lies outside the contact circle K_I play an important role and it decreases as crack grow and it becomes zero when crack lies in the contact circle. K_{II} mainly depends on load, crack length and crack face friction and it becomes positive to negative as crack approaches contact circle. Higher RCF life found in case of viscous lubricants like gearbox oil and grease. Again, their remarkable work is only related to ring and line cracks.

Levesque and Arakere [2010a] has made the 3D FEA analysis of non-planar surface flaws (c-cracks or partial cone cracks) geometries to find out the maximum stress intensity factors to determine the maximum permissible flaw size (critical flaw size) in silicon nitride geometry. Computationally intensive model was generated using quadratic (mid-node) elements and hexahedral elements to properly capture the contact stress. The direct iterative solver was used which is most accurate available solver for the displacements calculation in Abaqus. Loading was made using FORTRAN subroutine DLOAD and UTRACLOAD for normal and traction loads. Maximum Hertz pressure used for tolerable flaw size was 2.8GPa. Under elastohydrodynamic lubrication, effective coefficient of friction is taken as 0.05-0.09. Crack modeled was on the basis of experimental observations with aspect ratio of 0.3 and 30° angled from the surface. It was concluded from this study that traction between ball and raceway has very prominent effect on the direction of crack growth and stress intensity factors. Critical flaw size can be found from

the drawing the graph of SIFs vs. crack size and by looking at the effective threshold of K_{th} which can be found from experiments.

SIFs has been extracted for surface analysis in rolling contact fatigue from FEA using most appropriate available approach i.e., crack tip opening displacement (CTOD) [Levesque and Arakere 2010b]. Sub-modeling technique was used to reduce the computational size of the model. Comprehensive and accurate (~0.5% error) empirical equations for K_I , K_{II} and K_{III} developed for hybrid ball bearings subjected to different penny surface flaws. Subsurface analysis was conducted to predict and characterize crack size and shape [Levesque and Arakere 2008]. A 3D model was developed for partial cone crack analysis using FEA software (Abaqus) and incremental crack growth procedure (FRANC 3D/NG). FRANC 3D/NG has strong capability to simulate the crack growth without describing the crack path. Both methods support each other and their results were verified by the experiments. This method can be considered as a substitute to XFEM technique which is now extensively used in Abaqus for crack modeling with updating meshing with the crack growth. This extensive work is related to cone cracks only.

Ball bearing raceway fatigue spall has been analysed using elasto-plastic numerical analysis by Branch et al. [2009]. Analysis presents critical stresses and strains and it was verified by stress field calculated from XRD techniques. A transient elastic and elasto-plastic analysis [Arakere et al. 2010] of spalled raceways has highlighted the impact of ball on the raceways and contact stresses resulting in material degradation propagation of trailing end in circumferential direction. Although ball bearings raceways has much influence on the silicon nitride performance and life in the hybrid bearing applications but effect of trapped lubricant and rolling effect is missing in their extensive research study.

An explicit finite element simulation model has been used to investigate crack initiation and spall formation in machine elements subject to RCF [Slack and Sadeghi 2010, Bomidi et al. 2013]. Their comprehensive work was based on continuum damage mechanics approach to capture both crack initiation and propagation which finally led to spalling but they only targeted 52100 (and JIS SUJ2 – equivalent to 52100) bearing steel material. The initiation and propagation of fatigue cracks (grain debonding) was simulated with mesh partitioning procedure.

Coupled analysis has been presented by some researchers highlighting the role of fluid in the rolling contact fatigue. Fluid-solid solver [Balcombe et al. 2011] was used for this

coupled problem. Linear elastic fracture mechanics (LEFM) was used to model solid body and finite volume (FV) formulation of Reynold equation to model the lubricant film. Coupled approach suggested the reduced propagation rate when a only LEFM is utilized. Crack propagation direction can be predicted using coupled EHD (Elasto Hydrodynamic) and that would be in the direction of load [Bogdanski 2002]. Crack having fluid trapped inside (squeeze oil film) caused intense effect and can cause crack to initiate and propagate. Lubricant can cause different crack propagation rate as dry and wet conditions of the crack interior [Bogdanski et al. 2005]. Speed of the moving part having surface crack is important as suddenly changing load can cause sudden drop in liquid pressure which can cause cavitation [Bogdanski 2005]. A similar work was reported for cracked surfaces (due to previous mechanical and thermal treatments) by Glodez et al. [2008] for the fluid entrapment and crack propagation. All the existing literature is mainly related to pre-crack surfaces and then analysis is conducted to find the effect of lubricant on the existing crack (in term of propagation).

Recently, surface cracks were successfully modeled parametrically without considering any lubrication and found that subsurface crack propagation in silicon nitride is almost parallel to the surface [Kadin et al. 2012]. Surface and subsurface crack propagation within rolling element bearing has been modeled by many researchers using fracture mechanics approach [Bormetti et al. 2002, Mazzu 2012, O'Brien et al. 2011, Ringsberg and Bergkvist 2003, etc.]. Theory of critical distances is also being used for metallic and non-metallic materials without considering any fluid effect for crack sizes of some definite lengths [Taylor 2007]. But very little work is available regarding cavity under the contact and having full of liquid (hydrostatic pressure) and their effect on the material tolerance in case of silicon nitride.

1.4. State-of-the-Art from Literature Survey

From the extensive literature search, it has been revealed that different types of surface defects within silicon nitride ball surfaces in rolling bearings have been investigated and discussed. Researchers have highlighted and extensive experimental and numerical research has been conducted in line and ring cracks (with and without squeeze oil film). Fracture mechanics approach was widely used especially for crack propagation. Rolling element bearings with surface star like feature and missing material type of defects have not been properly investigated to find defect tolerance and failure modes.

Therefore, in this research study, both experimental and numerical approaches are used to investigate the core issues related to material defect tolerance and the failure modes and to investigate the influence of lubrication on the performance and life of rolling element bearing. A detail study is conducted to assess the defect geometry and characterize them on the basis of pit size to total star extent. Preliminary experiments are then conducted to find lubricant influence on the performance of silicon nitride rolling element bearing with surface star features. Based on preliminary study extensive experimental study is conducted on laser machined surface missing material type of defects with different shapes (right cylindrical, conical and oblique cylindrical) and dimensions (diameter: 50-100 μ m and depth: 5-50 μ m) and at different contact pressures. Laser machined surface cavities dimensions and shapes are aligned with surface missing material type of defect during manufacturing process. A well-defined failure mechanism found in missing material type of defects along with star features. As most of the cavities (missing material) were failing close to cavity base, so exhaustive parametric study is conducted for hydrostatic pressure effect to find potential location of crack initiation based on the surface/subsurface stress field.

1.5. Outlines of Thesis

Chapter 1 presents the background of the research, a comprehensive literature survey and review, together with the novelty of the research and measurable objectives. This chapter also outlines the structure of the thesis.

Chapter 2 describes the materials used, experimental techniques and procedures that will be used and/or have been used historically for the rolling contact fatigue studies. Experimental procedure for the modified 4-ball machine and design of experiments for rolling contacts fatigue experiments subjected to different surface defects are also discussed in this chapter.

Chapter 3 gives the results of RCF experiments on silicon nitride balls with natural star defects. It discusses the categorisation of these defects in terms of crack to pit size. Surface analysis using optical microscopy, SEM topography and white light interferometry is also presented. Attempts to create artificial star features are described in this chapter.

Chapter 4 outlines the work regarding laser machining and the production of artificial defects using laser technology. It also gives details the geometries of the various artificial defects on the surfaces of silicon nitride balls.

In chapter 5, experimental results on silicon nitride balls having artificial missing material defects are presented. Different types and sizes of laser machined cavities used for rolling contact experiments are discussed. Results on the two different types of silicon nitride material are also compared to determine the effects of material type on defect tolerance. Surface analysis using optical microscopy, white light interferometry and scanning electron microscopy are also presented. EDS analysis on some of the samples is also given in this chapter.

Chapter 6 describes finite element modeling of artificial missing material cavities using Abaqus. Results are presented as 2D and 3D static and quasi static analysis to examine the effect of rolling. Stress fields are calculated to display stress magnitudes and their locations, to determine possible reasons for crack initiation and hence spalling. The second part of chapter 6 covers hydrostatic pressure effects in lubricated rolling contact. Results are presented to show potential position, location and orientation of crack initiation and propagation.

Chapter 7 presents discussion, conclusions together with recommendations for future research.

References and appendices are presented at the end of this study.

Chapter 2 Experimental Methodology

Research methodologies consisted of two parts; experimental studies and numerical analysis. In this chapter, focus is to target experimental procedure and techniques to conduct this research. Main topics discussed are the selection of experimental materials, different lubricants, main experiment rig, samples categorization, defect finding and positioning on the experiment rig. Other discussions are about the different surface analysis apparatus and tools used to conduct pre- and post-surface analysis are also discussed in this chapter.

2.1. Materials Experimented

The entire ceramic test materials used in the experimental study was silicon nitride: but, steel bearing balls were also used in experiments to simulate hybrid rolling contacts.

2.1.1. Silicon Nitride Balls

As with most ceramic materials, silicon nitride is usually manufactured from the starting point of a very fine, pure powder which after initial forming or shaping is densified by different techniques including sintering, hot pressing and hot isostatic pressing (HIP). (An exception to this is a process known as reaction bonding in which components are formed from silicon metal powder and then sintered in nitrogen to form silicon nitride in-situ). Additives such as aluminium oxide, zirconium oxide and iron oxide are added to the starting powder to promote densification. Hot isostatic pressing is generally used to produce bearing grade silicon nitride as it gives almost zero porosity combined with a fine grain structure, leading to appropriate levels of strength, toughness and hardness for use in bearing applications [Wang et al. 2000]. Zhao [2006] showed that one type of silicon nitride had improved performance over another type even though both materials had been hot isostatically pressed. Such differences in performance relate to differences in composition (additives) and grain morphologies. Therefore, for the current study, two types of silicon nitride material were used in experiments – Type A being a premium bearing grade material and Type B a less highly engineered material. The ball diameter was 12.7mm with average surface roughness Ra of approximately up to 0.01 μ m. Typical physical and mechanical properties of silicon nitride material (in comparison with M50 steel) are given in the Table 2.1 [Jahanmir 1994, Harris 1990]. This comparison is given as

M50 steel rolling elements are being used in aerospace applications and silicon nitride is also being considered as alternative to M50 steel due to its some superior properties.

2.1.2. Steel Balls

The steel balls used as counter surfaces in RCF testing were made from 1% carbon chromium steel (AISI 52100/EN31). These were also 12.7mm diameter and surface roughness 0.02 μ m Ra, respectively. The hardness of these steel balls is on average HV800-840. The modulus of elasticity and Poisson ratio are 210GPa and 0.3 respectively. Steel and silicon nitride ball samples are provided by SKF.

Table 2.1: Physical Properties comparison of Silicon Nitride and M-50 Steel

Physical Properties		Silicon Nitride		M-50 Steel
		Class A	Class B	
<i>Density (kg/m³)</i>		3200	3200	7900
<i>Modulus of Elasticity</i>	<i>psi</i>	45*10 ⁶	45*10 ⁶	30*10 ⁶
	<i>GPa</i>	310	310	210
<i>Coefficient of Thermal Expansion per °C</i>		3.2*10 ⁻⁶	N/A	11.9*10 ⁻⁶
<i>Hardness</i>	<i>Knoop K₁₀₀</i>	2200	N/A	N/A
	<i>Rockwell C</i>	80		60
<i>Poisson Ratio</i>		0.28	0.27	0.3
<i>Fracture Toughness (MPam^{1/2})</i>		6.0	6.0	>16.0

2.2. Lubricants Used

As lubricant type and nature both have significant effect on performance of silicon nitride balls [Stolaraski and Tobe 1997], therefore different types of lubricants were used during this experimental study. Lubricants were selected on the basis of their common use and applications : traction fluid, thin mineral oil, grease and gearbox oil. Lubricant properties are shown in the Table 2.2.

2.3. Specimen preparation/pre-experiment study

Due to the manufacturing process and especially during final lapping and polishing processes, silicon nitride balls are susceptible to various surface defects. These include cracks, star features, porosity and missing material as well as linear features - scratches and

contact marks. Some defects or features are very small in size, often below size of 100 μ m, and are consequently very difficult to detect by visual inspection even at high magnifications. Fluorescent penetrant inspection (FPI) is commonly used to find small defects.

2.3.1. Fluorescent Penetrant Inspection

Sample have to be cleaned thoroughly using an ultra-sonic bath with a solvent such as acetone so that all grease, debris and other dust particles are removed from the surface. After cleaning, samples are soaked in a high sensitivity fluorescent dye (Britemor 668) for a period of time (10-15minutes depending on the type and nature of the defects) so that fluorescent dye can penetrate into defects. After soaking and draining, samples are immersed in remover solution (Diluted Diethylene Glycol Monobutyl Ether/hydrophilic) to remove excess penetrant from the sample/ball surface. After washing and drying in hot air the sample is then ready for examination under the optical/light ultra violet illumination. Balls are usually examined in a darkened room at low (x5 to x10) magnification. Defects or features of interest are then circled using a fine permanent marker for later examination at higher magnifications. This method is commercially used for non-destructive testing.

Surface inspection can also be carried out at stages during experiments for example to monitor growth, any secondary cracking or new features.

Table 2.2: Properties of different lubricants.

Lubricant	Density (kg/m³)	Viscosity	Pour Point	Flash Point
<i>Traction Fluid</i>	880-920 (at 25°C)	28-38 cSt (28-38 mm ² /sec) (at 40°C)	-42°C	150°C
<i>Thin Mineral Oil</i>	876 (at 20°C)	8.81 cSt (8.81 mm ² /sec) (at 40°C)	-47°C	101°C
<i>Gearbox Oil</i>	858 (at 15°C)	101 cSt (at 40 °C) 15.4 cSt (at 100 °C)	-57°C	224°C
<i>Grease</i>	960 (at 20°C)	70 cSt (at 40°C) 9.4 cSt (at 100°C)	N/A	NA

2.3.2. Surface Inspection

After FPI, sample is put under the light microscope with ultraviolet light source to detect the defect and encircle it. After then sample is put/inserted into the collet using defect positioning mechanism to have defect in contact track. Surface inspection also being made during to the experiment so that any new feature appears on the surface can be monitored.

2.4. Rolling Contact Fatigue Experimenting

Different types of testers are used for conducting RCF experiments . These include disk-on-disk, ball-on-rod, ball or roller-on-flat plate, V-groove machines as well as 4-ball and 5-ball testers. No single RCF experimental device can fully reproduce or simulate the complex conditions encountered in full scale hybrid bearings. However, 4-ball (and 5-ball) machines do give a reasonable approximation of bearing conditions and are relatively easy to operate using readily obtainable components (test and support balls) that do not require machining or other pre-treatments.

2.4.1. Main Experiment Rig/Modified Four Ball Machine

The Plint TE92HS microprocessor controlled rotary Tribometer (Fig. 2.1) is widely used for low and high load rolling contact experiments at different speeds and temperatures and can also be operated under controlled environments. The machine used in this study was configured as a modified 4-ball machine according to Institute of Petroleum (UK) IP 300 Rolling Experimental Procedures. It consists of a steel fabricated main body with experiment chamber and thermocouple arrangement.

The upper ball is held in the collet which is rotated by the motor whereas the lower balls are located in a fixed cup and are driven by the upper or test ball. The cup is filled with oil and can be refilled during the experiment through the cover plate. Thermocouple arrangement is made to maintain or control temperature during experiments. The required pressure is applied by the pressure head. The upper ball is subjected to 2.25 stress cycles per spindle revolution as calculated using following formula [Appendix A1, Tourette et al. 1977]. Stress factor is further used to calculate number of stress cycles. Hertz contact theory [Johnson 1985] is used to calculate contact pressure and contact radius. Contact load calculations and Stress factor are detailed in Appendix A (A1 and A2).



(a)

(b)

Figure 2.1: Modified four ball machine (a) machine and control unit (b) 4-ball experimenter

2.4.2. Defect Positioning Procedure

Defect positioning in 4-ball machine is very important in rolling contact experiments on surface defects. The defect positioning mechanism [Wang 2001] is shown in Fig. 2.2.

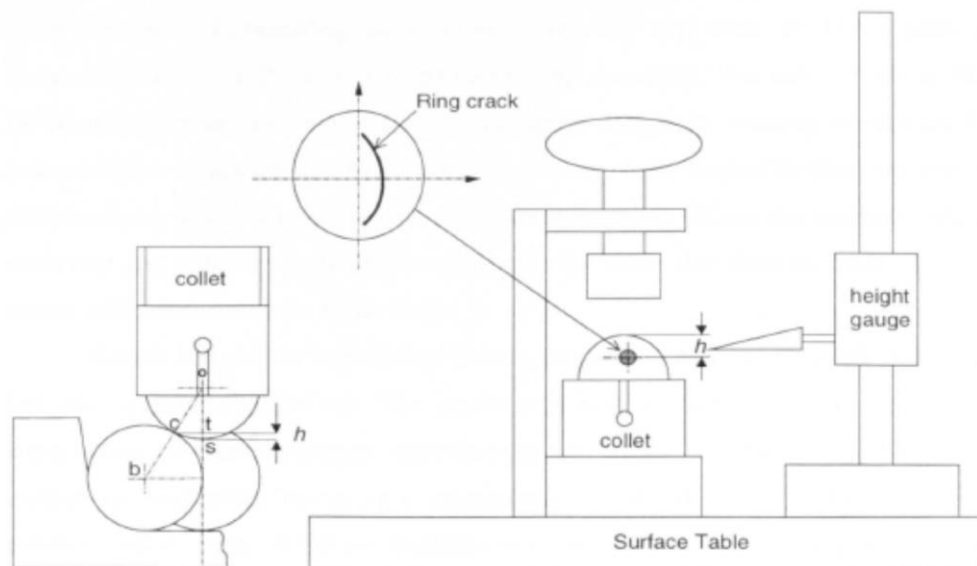


Figure 2.2: Schematic drawing of defect positioning in modified four ball machine [Reproduced from Wang 2001]

The defect positioning procedure is as follows :

- After observing the defect/feature, encircle the defect with 1-2mm circle diameter under the light microscope with ultra violet light source
- Measure total height of the ball after loosely inserting the ball into the collet
- Adjust the scale so that its knob be at the position = total height - h
- Where $h = \text{radius} - (\text{radius} * \cos\phi)$ (2.1)
where radius = 6.35mm and contact angle = $\phi = 35.3^\circ$ and hence $h = 1.17\text{mm}$ (see Fig 2.3)
- Adjust the defect at the height of 1.17mm from the top surface of the ball by scale
- Press the ball into the collet

2.4.3. RCF Experiment Procedure using modified 4-ball machine

After defect positioning, collet is inserted into drive spindle of the machine. The cup and lower support balls are cleaned using acetone in an ultrasonic bath. The cup is filled with the lubricating oil and the three balls. The safety cover is fitted on the machine and by initializing the COMPEND program, the machine is started. COMPEND is Plint program to operate and program experiments on the modified 4-ball machine. Machine sensitivity is increased so that it will automatically stop when a ball failure is signalled by increased vibrations. The machine normally can be run overnight without any supervision provided that a minimum amount of lubrication is maintained during the experiment. The lubricant level can be maintained during experiment through a hole in the cover plate. The collet and test ball is periodically taken off to examine the test ball using an optical microscope and afterwards can be re-inserted into the drive spindle and the test continued. After completing the required number of stress cycles/number of hours the machine is stopped. The balls are taken off from the collet and cup, cleaned in the ultrasonic bath using acetone and post experiment surface analysis is conducted on the test ball. The cup is also examined after the experiment to look for surface damage and replaced if necessary. [Appendix B – Modified four ball machine calibration].

2.5. Surface Analysis

Pre- and post-test inspection and surface analysis is very important in tribology. Advanced surface analysis techniques are used including white light interferometry and scanning electron microscopy (SEM) as well as conventional optical microscopy.

Although FPI technique was used for cross-sectioned samples (chapter 5) to investigate subsurface cracks in silicon nitride in this current study but some other techniques have also been reported to image subsurface flaws. These techniques are cross-polarization confocal microscopy [Liu et al. 2011], scanning acoustic microscopy [Lawrence et al. 1990] and resonant ultrasound spectroscopy [Petit et al. 2005]. (Some other vibration based techniques have also been used for fault detections for low speed rolling element bearing [Mechefske and Mathew 1992, Tandon and Choudhury 1999])

2.5.1. Optical Microscopy

An Olympus BX60 microscope is used for the preliminary surface analysis. Samples/balls are examined before the experiment, during the experiment and also after the experiment. This microscope is capable of up to 1,000 x magnification with different objective lenses of x5, x10, x20, and x50 and x100 magnification. An Olympus digital camera is also fitted with the microscope to record and capture pictures. Images are analysed by the operating software, Olympus Pro Analysis. Software is also providing the opportunity of stitching images, which gives a magnified overall picture of the surface area. Polarizing filters are used for enhancing the image quality and clarity with samples containing peaks and valleys. The Olympus microscope is shown in Figure 2.3.

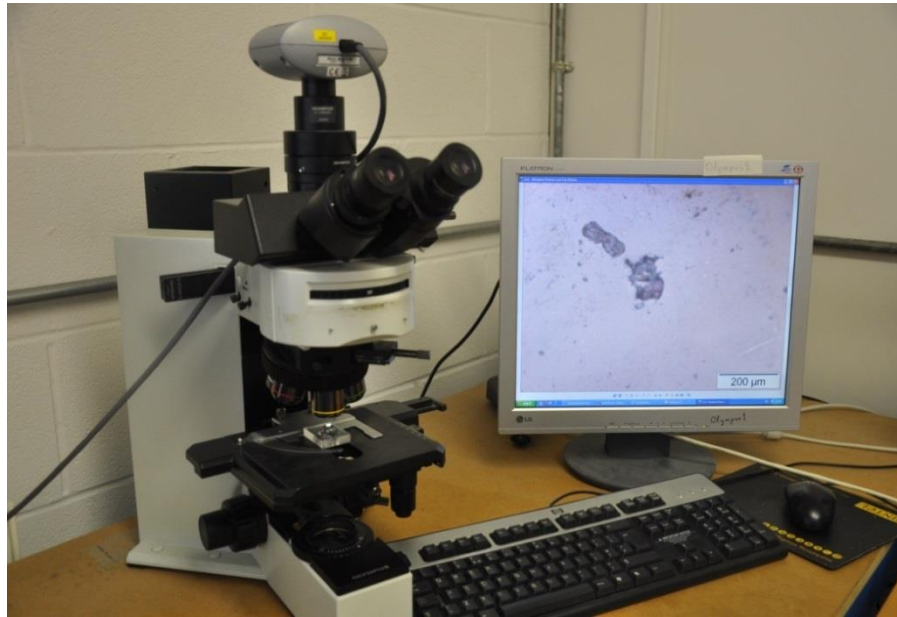


Figure 2.3: Olympus BX 60 Light Microscope (showing star feature-category 5)

2.5.2. White Light Interferometry

White light Interferometer (Zygo Interferometer – New View 5000) is used for surface analysis and mapping. The surface finish of the original surface can be measured and compared with the surface morphology after the experiment. The three-dimensional surface mapping profilometer can accurately measure the surface roughness, the size and periphery of the defect, the step heights and the volume loss although there can be some doubt or inaccuracy with features having sharp (vertical) boundaries.

The sample is placed under the main platform and light is focussed and adjusted so that fringes are clearly visible. Volume loss, 3D surface profiling and stitching are the powerful features of this instrument. Figure 2.4 shows white light interferometer used for surface analysis in this research study.



Figure 2.4: White Light Interferometer (Zygo Interferometer)

2.5.3. Scanning Electron Microscopy

Electron microscopy is widely used for surface analysis. Electron microscopy can be categorized into two main classes; Scanning electron microscopy (SEM) and transmission electron microscopy (TEM). In this research, only SEM was used for detailed surface analysis (TEM is normally used for higher magnifications than SEM).

SEMs are used for very high magnification and high resolution images and surface analysis and energy dispersive spectroscopy (EDS) for elemental analysis. SEMs are used for magnification normally up to 40,000x and also for some cases are used for magnification up to 1,000,000x. Sample should be electrically conductive in nature and non-conducting samples need to be coated to avoid electrical charging. Cleaned samples are put in the vacuum chamber with appropriate working distance. Parameters such as voltage, current and magnification are controlled through operating console. Higher voltages give better resolution but may lead to more charging problem with non-conductive samples. Generally, biological samples are examined at low voltages and non-biological samples are examined at higher voltages. Figure 2.5 shows the SEM used for this research work.



Figure 2.5: Zeiss Supra 35 VP SEM (Courtesy: ETC Brunel University)

2.5.3.1.1 Coating on non-conducting material samples before SEM

Coating is normally done before using scanning electron microscopy on non-conducting material samples. Gold and carbon coating are commonly employed for this purpose. Sputter coater was used for gold coating whereas Agar Carbon coater is used for carbon coating (Figure 2.6).



(a)



(b)

Figure 2.6: (a) Sputter Coater for Gold Coating (b) Agar Turbo Carbon Coater for Carbon Coating

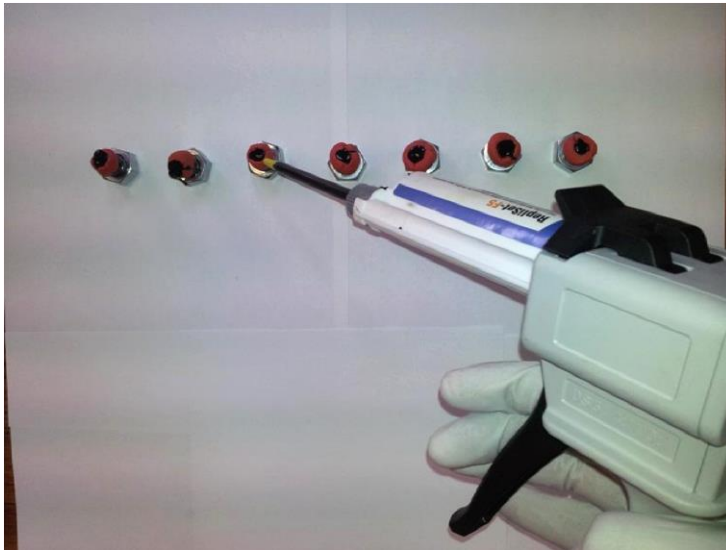
2.6. Use of Replicas

Replicas are used for reproducing engineering surfaces for examination and measurement particularly in situations where it is difficult or impossible to take actual samples or in-situ measurements. They can be taken from any solid surface - metals, ceramics, plastics and glasses. Replicas have applications ranging from metrology, forensic investigation, power generation, aerospace, chemical plants offshore industries and others. Replicas have different types and sub-types based on the applications and conditions. Commonly F-Type and T-Type replicas are used based on the nature of the application: F-Type for horizontal and sloping surfaces and T-Type for vertical and overhead surfaces. More details are given in Appendix C.

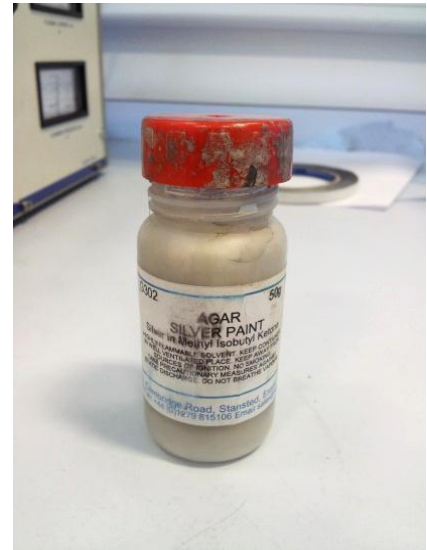
2.6.1. Replica Procedure

In this study, replicas were taken from samples with missing material. Since some examples of hole contained irregular surfaces with re-entrant angles a flexible replica compound (Repliset F5) was used. The sample surface was ultrasonically cleaned in acetone and then were dried using a hot air drier to remove all acetone. Plasticine material was used to make a wall around the cavity of missing material. The two component replica compound was applied using a dispenser gun with a special mixing nozzle. The compound was applied carefully to the position of interest on the sample surface. Samples were not moved during the curing time (around 5minutes) so that replica compound could settle and fill inside the cavity completely. After curing the replica was carefully removed from the surface and examined using microscopy and interferometry. Replicas could also be observed using scanning electron microscopy after carbon or gold coating.

Figure 2.7 (a) shows dispenser gun with mixing nozzle and needle arrangement used for replica application on the sample surface and Figure 2.7(b) shows the silver paint that was used to make the replica conductive for SEM applications after coating. Silver paint is normally used to make non-conductive surfaces electrically and thermally conductive. Further details for Agar silver paint are given in Appendix D.



(a)



(b)

Figure 2.7: (a) Applying replicating material to sample surface using replicating system
(b) Silver conductive paint for coating

2.7. Summary

In this chapter, brief description of experimental techniques/equipments to conduct experimental part of this research study is discussed. Materials properties of tested samples (silicon nitride – both class A and B) and steel balls (AISI 52100 and M50 steel) are provided at the start of this chapter. Lubricants properties and sample preparations are also described along with surface analysis techniques i.e., light microscopy, interferometry and electron microscopy. At the end, materials coating (to have conductive sample for electron microscopy study) and replica study details are also discussed. Based on the experimental technique discussed in this chapter, rolling contact fatigue experiments are then conducted on surface star like features (chapter 3) and missing material type of defects (chapter 5).

Chapter 3 Experiments on stars features

Surface defects on silicon nitride surface during manufacturing may be of any shape and nature. These may be of C-crack or half penny crack, star features, missing material and contact marks (Appendix E, F). This chapter presents the classification of natural star features found on silicon nitride balls used in hybrid ball bearing. It describes RCF testing of natural star features and the effect of different lubricants on the performance of hybrid rolling elements is also discussed. Pre- and post-test surface examination and analysis using optical microscope, white light interferometer and scanning electron microscope are also presented in this chapter. Surface star features are further investigated to observe the effect of pit size to total star extent at high contact pressures. Attempts to generate artificial star on silicon nitride surface are also discussed in this chapter.

3.1. Natural Star Categorization

Silicon nitride balls from a batch known to contain star type features were cleaned and inspected according to the FPI procedure (Section 2.3.1-2). A number of star features were found and then given a more detailed examination. Star defects were classified into five different categories depending on the extent of any missing material. (Tip-to-tip lengths did not show sufficient variation to be used for classification).

Category 1: No missing material (or very small area below 10 μ m) – Figure 3.1

Category 2: Minor missing material (10 μ m to 30 μ m) – Figure 3.2

Category 3: Medium missing material (30 μ m to 60 μ m) – Figure 3.3

Category 4: Major missing material above than 60 μ m – Figure 3.4

Category 5: Star feature with nearly all material missing – Figure 3.5

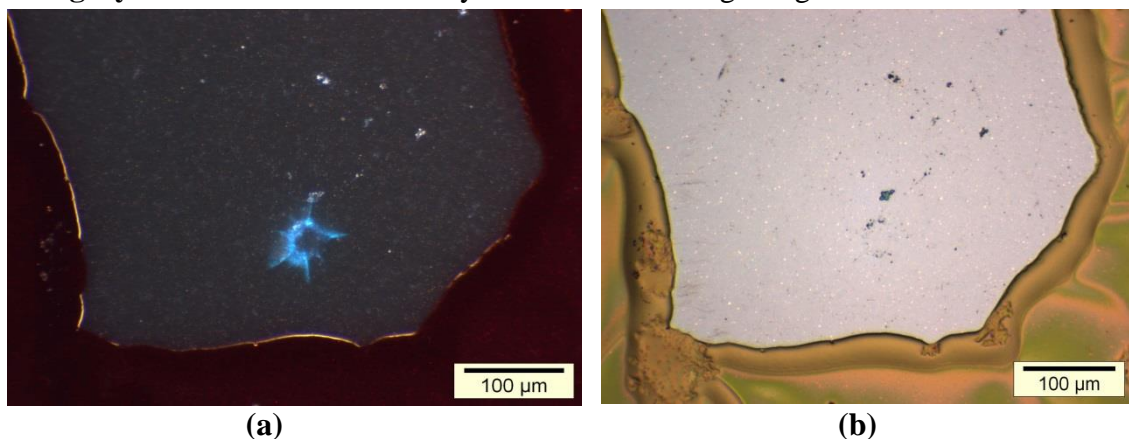
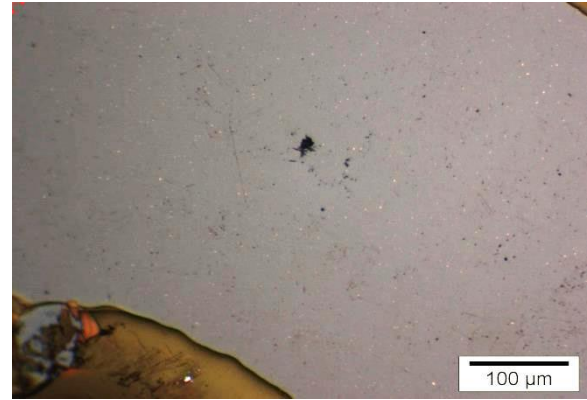


Figure 3.1: Star feature category 1 (a) UV illumination (b) white light illumination



(a)



(b)

Figure 3.2: Star feature category 2 (a) UV illumination (b) white light illumination

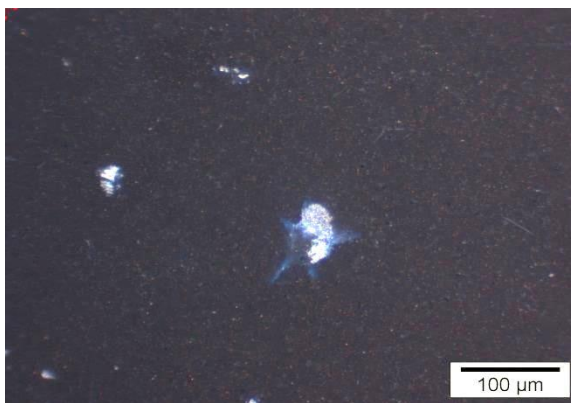


(a)

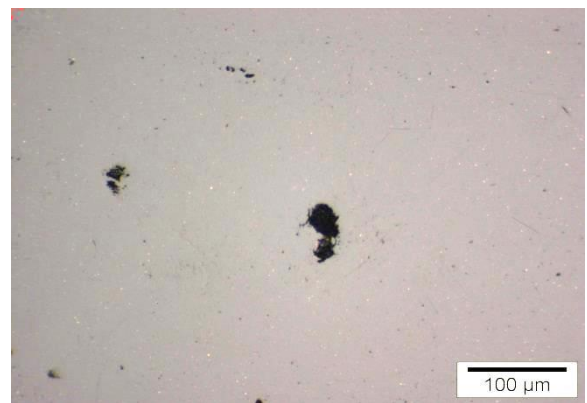


(b)

Figure 3.3: Star feature category 3 (a) UV illumination (b) white light illumination

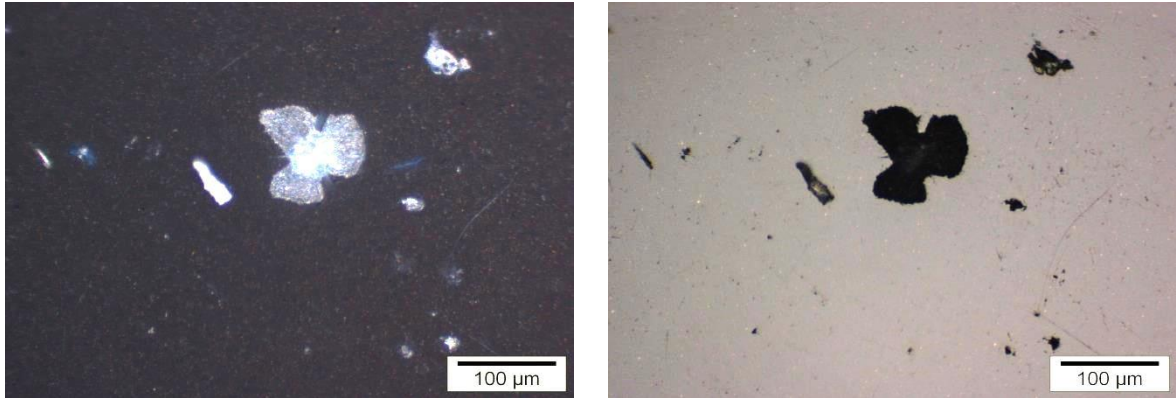


(a)



(b)

Figure 3.4: Star feature category 4 (a) UV illumination (b) white light illumination



(a)

(b)

Figure 3.5: Star feature category 5 (a) UV illumination (b) white light illumination

3.2. RCF experiments on star features

Initially category 1 and 5 stars were selected for the rolling contact experiments. All tests on category 1 stars were conducted with four different lubricants and at a contact pressure of 3.8GPa. Based on these results, experiments on category 5 stars were carried out using only thin mineral oil as the lubricant and generally at the higher contact pressure of 4.8GPa. Finally some experiments were also conducted by taking star features of equal extent but variable pit size to observe the effect of pit size on the rolling contact fatigue performance of silicon nitride balls.

All experiments on natural stars were conducted under the following operating conditions;

- Contact pressure: 3.8 – 4.8GPa*
- Temperature: $75\pm 5^{\circ}\text{C}$ **
- Speed: 7500 rpm***

*This contact pressure range is well above service range of bearing. However, under certain circumstances like in gust, a bearing may need to stand that much pressure. Secondly, in order to find tolerance for future applications of hybrid bearings, it was necessary to test at slightly higher pressure. Other objective was to accelerate fatigue process as these bearings already have been tested at very high pressure (5-10GPa).

**This temperature was selected as most of bearing has operating temperature from 60°C to 90°C and due to limitations of time and resources, it was not possible to run at all conditions, so an optimum temperature was selected for rolling contact fatigue experiments.

***Bearings are run at range of speed. Higher load bearing normally run at low speed whereas low load bearing run at higher speed. In the literature a range of speed has been reported from 3000-1000rpm. In order to have an appropriate balance between time and dynamic effects, this speed range was selected.

3.2.1. Experiments on category 1 Stars

Category 1 type of star features experiments are further divided based on lubricant used. All the experiments using category 1 stars are conducted at the contact pressure of 3.8GPa, shaft rotational speed of 7500rpm and bulk oil temperature of 75°C. These preliminary experiments are conducted for low fatigue cycles of 30million stress cycles. Some experiments are stopped before pre-defined time (number of revolutions) due to new features appearance (Tribolayer, Material loss, Local loss, Surface delaminations etc.–described in nomenclature) on the specimen surface (in the contact track). These new features were considered as criteria to stop the experiment for further investigation.

3.2.1.1 Experiments with Traction Fluid

Two experiments (Table 3.1) were conducted using traction fluid in which some material loss, surface delamination a tribolayer were observed. However, in either test, no spalling failure was observed. Two additional experiments (Table 3.2) were also conducted to support results of main experiments.

Table 3.1: Main experiments conducted on star feature category 1 using Traction Fluid

Experiment ID.	Ball ID	Star feature length (µm)	Stress Cycles (10⁶)	Outcome
<i>CITF1</i>	NS1	77	30	Stopped due to <i>Material loss</i> and <i>Surface delamination</i>
<i>CITF2</i>	NS2	84	10	Stopped due to <i>Local loss</i> and <i>Tribolayer</i>

Table 3.2: Additional exp. conducted on star feature category 1 using Traction Fluid

Experiment ID	Ball ID	Stress Cycles (10⁶)	Outcome
<i>CITF3</i>	NS3	30	Stopped due to <i>Local loss, Surface delamination</i> and <i>Tribolayer</i>
<i>CITF4</i>	NS4	22	Stopped due to <i>Tribolayer</i> and some <i>Surface delamination</i>

Figs 3.6-3.7 are showing the pre-test and post-test images of the silicon nitride ball surfaces for traction fluid experiments. Surfaces were carefully cleaned using acetone in ultrasonic bath before and after experiments to conduct surface analysis. A special holder was used to hold ball surfaces clean during surface analysis. Surface analysis was conducted every 3 million stress cycles because of the sensitive nature of the defect. In the first experiment (Fig. 3.6), material loss was found as material came out during rolling contact.

This experiment on a star that initially had no associated pit or hole and was stopped after 30 million stress cycles. SEM images show that the material loss was shallow and some erosive wear could be seen on one side of contact. In the second experiment (Fig. 3.7) using traction fluid, a lubricant-solid particle deposition (tribolayer) was observed on the contact track. Crack surfaces were also widened during the experiment. This experiment was stopped before pre-set number of revolutions/stress cycles just to observe the new changes on the surface. Damage probably started from crack broadening and then growth was observed. Further over-rolling caused local loss (experiment C1TF2) and finally material loss as found in the first experiment (C1TF1).

Additional experiments on traction fluid were also conducted to observe this deposition/tribolayer mechanism. Test (C1TF3) was stopped after 30 million stress cycles. Fig. 3.8 shows the ball surface after testing. Optical microscope images of the contact track are shown in Fig. 3.8 (a). The ball was then heated in a furnace to 500°C with a dwell time of 1 hour to burn off debris and then again surface analysis was performed using light microscopy (Fig. 3.8a-b) and 2D and 3D interferometry images are shown in Fig. 3.8c-d.

In the second experiment (C1TF4), the test was stopped after 22 million stress cycles as a similar mechanism was observed on the surface. Post-test surface analysis (Figure 3.9) shows surface deposition and wear mechanism on the contact track. These additional experiments supported the outcome of main experiments.

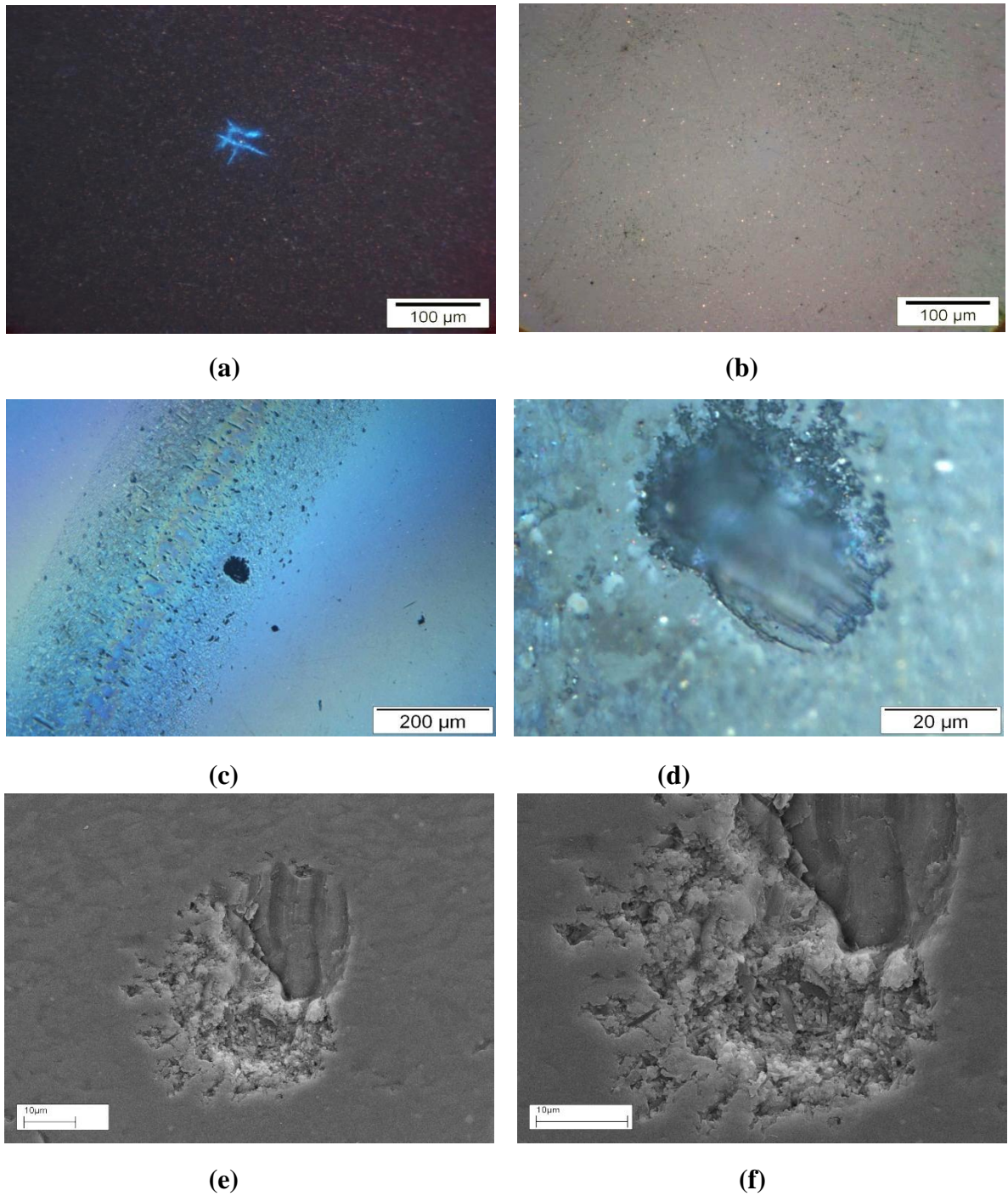
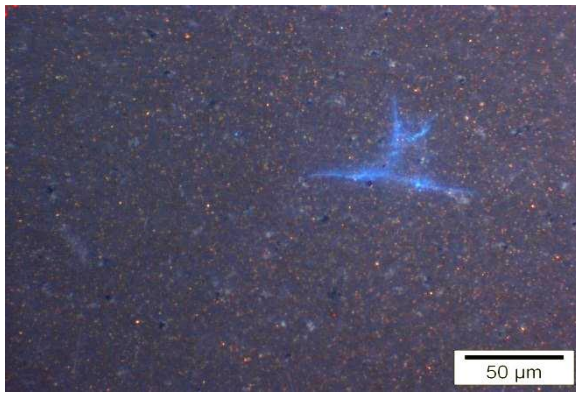
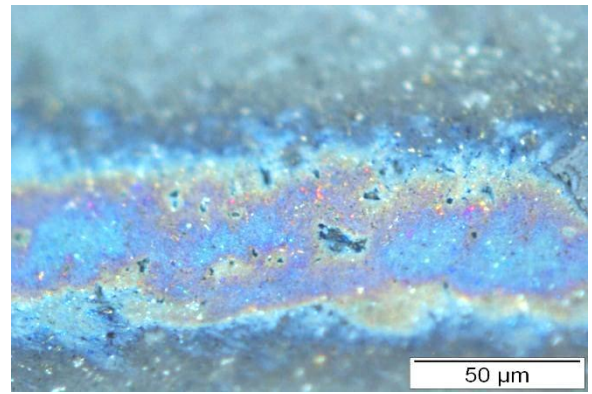


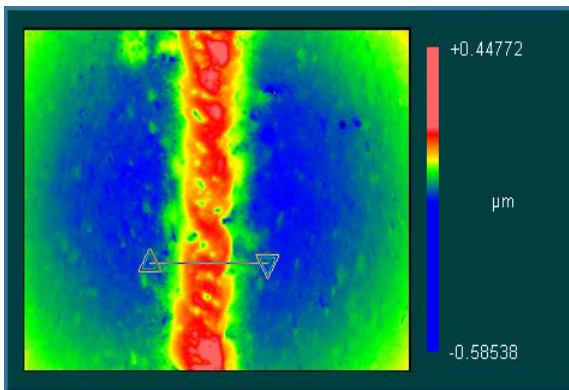
Figure 3.6: Experiment C1TF1 (a) Pre-experiment analysis using white light illumination (b) pre-experiment analysis using UV illumination (c) and (d) post-experiment (30million stress cycles) OM images (white light) (e) and (f) post-experiment SEM images



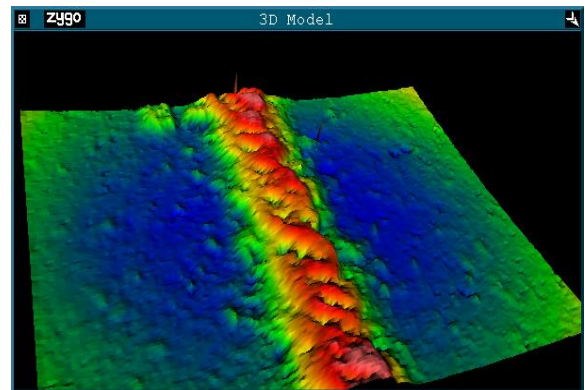
(a)



(b)



(c)



(d)

Figure 3.7: Experiment C1TF2 (a) pre-experiment OM image (b) post-experiment OM image (c) and (d) post experiment WLI images for surface deposition

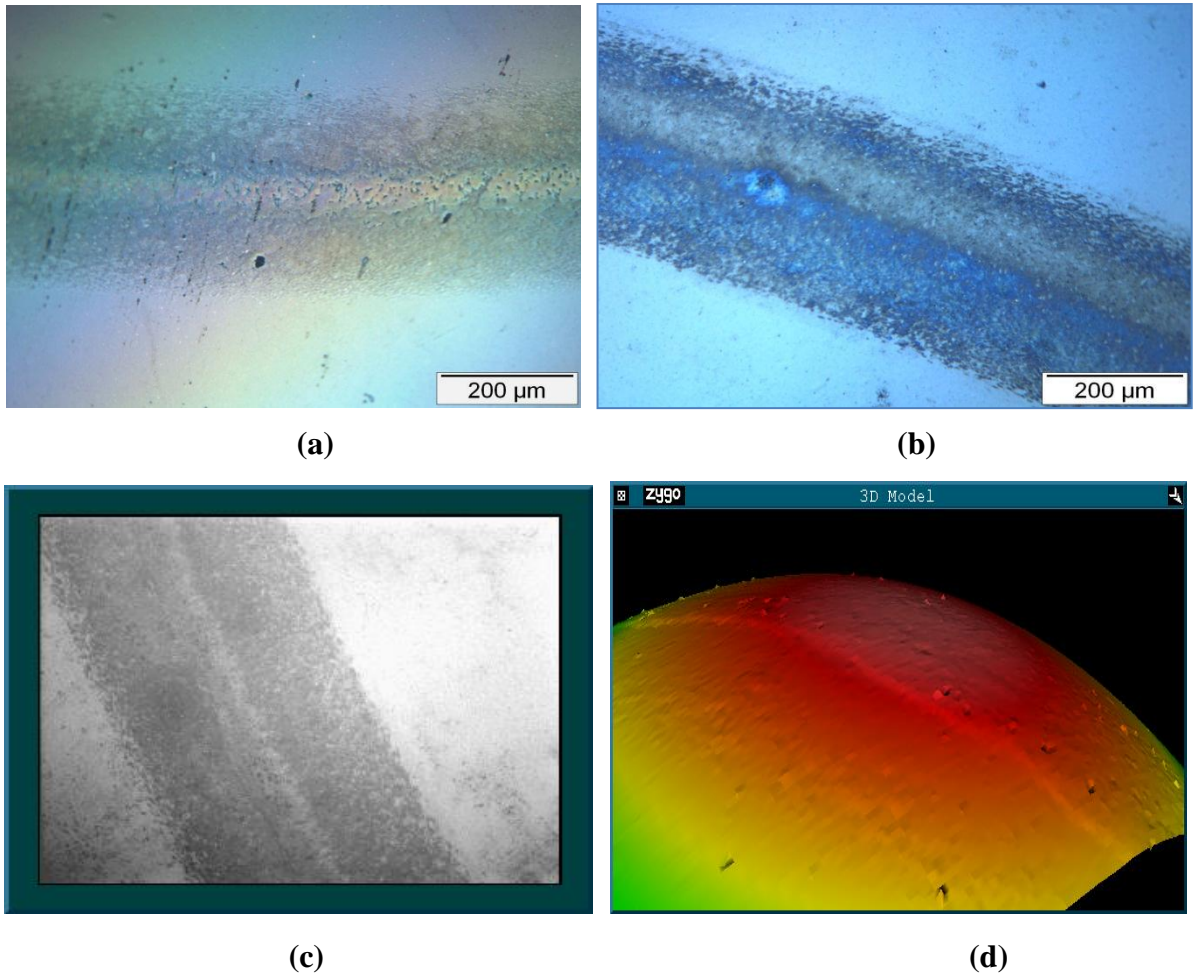


Figure 3.8: Post-experiment (C1TF3) analysis of silicon nitride surface using microscopy (a) post 30million stress cycles (b) post-heat treatment at 500°C and dwell time of 1hour (c) and (d) post-heated at 500°C and dwell time of 1hour (interferometry 2D and 3D images)

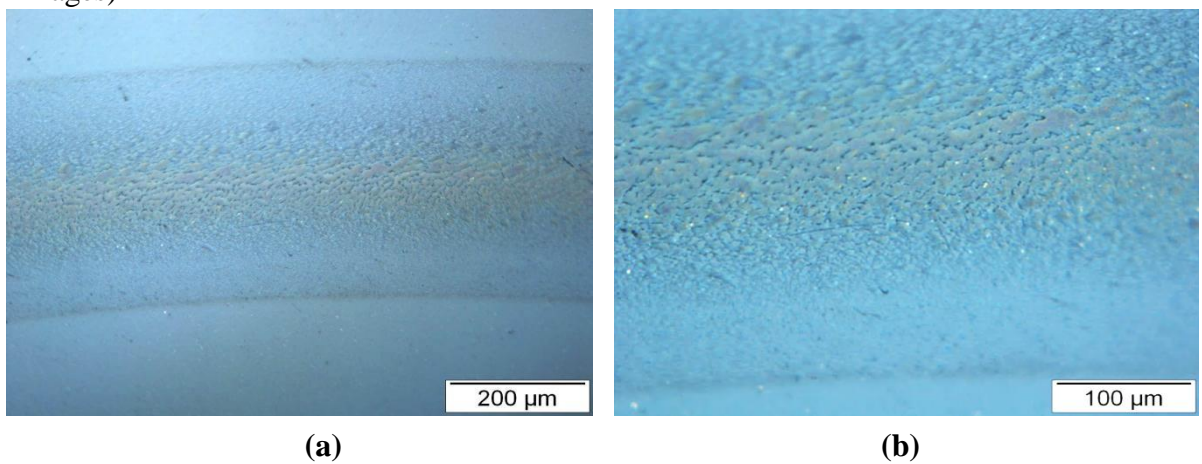


Figure 3.9: Post-experiment (C1TF4) surface analysis of silicon nitride surface using microscopy (a) at 100x magnification (b) at 200x magnification

3.2.1.2 Experiments with Thin Mineral Oil

Two main experiments (Table 3.3) are conducted using thin mineral oil and followed by two additional experiments (Table 3.4) to verify results of main experiments.

Table 3.3: Main experiments conducted on star feature category 1 using TMO

Experiment ID	Ball ID	Star feature length	Stress Cycles (10^6)	Outcome
<i>CITM1</i>	NS5	87 μ m	8	Stopped due to <i>Material loss</i> and due to <i>Crack growth</i>
<i>CITM2</i>	NS6	91 μ m	8	Stopped due to <i>Uplift</i>

Table 3.4: Additional experiments conducted on star feature category 1 using TMO

Exp. ID	Ball ID	Stress Cycles (10^6)	Outcome
<i>CITM3</i>	NS7	18	Stopped due to <i>Local loss</i> and due to <i>Surface delamination</i>
<i>CITM4</i>	NS8	6	Stopped due to <i>Crack broadening</i> and <i>Surface delamination</i>

As with traction fluid, experiments with thin mineral oil involved stopping the test at intervals and examination of the features. Figure 3.10 shows the pre- and post-surface examination of C1TM1. In this case, the experiment was stopped after 8 million stress cycles due to changes observed on the surface.

In this experiment, material loss within domain of defect was observed along with some crack growth on one side of the defect. Material loss and surface wear observed in mineral oil was more than observed in traction fluid experiments. This may be due to low viscosity of mineral oil (8.81cSt) than traction fluid (28-38cSt) and hence thin film thickness. Film thickness calculation is based on combination of fluid mechanics and material science (Appendix G). SEM post experiment surface analysis is shown in Figure 3.11.

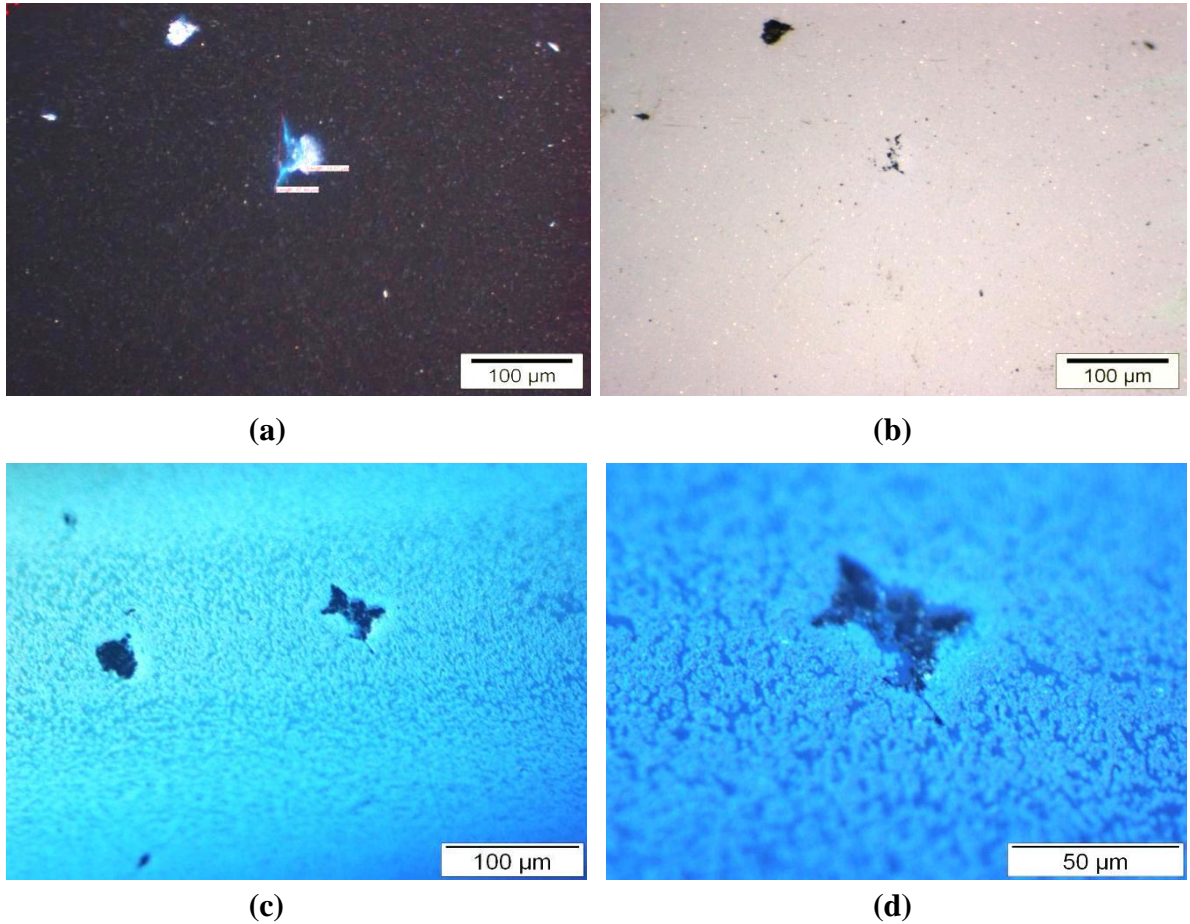


Figure 3.10: Experiment C1TM1 (a) pre-experiment UV illumination (b) pre-experiment white light illumination (c) and (d) post-experiment OM image

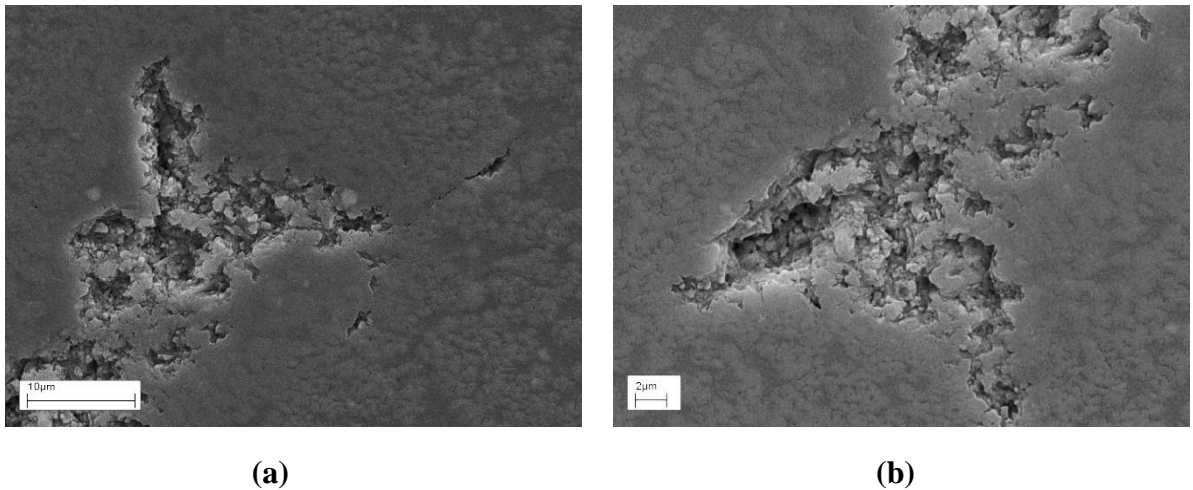


Figure 3.11: Experiment C1TM1 (a) and (b) post-experiment SEM images

In the second experiment (C1TM2), surface wear and uplift was found (Fig. 3.12) after 8 million stress cycles. This uplift mechanism may be due to lubricant penetration of the thin lubricant into the star cracks and then pushing up the top surface by hydrostatic pressure.

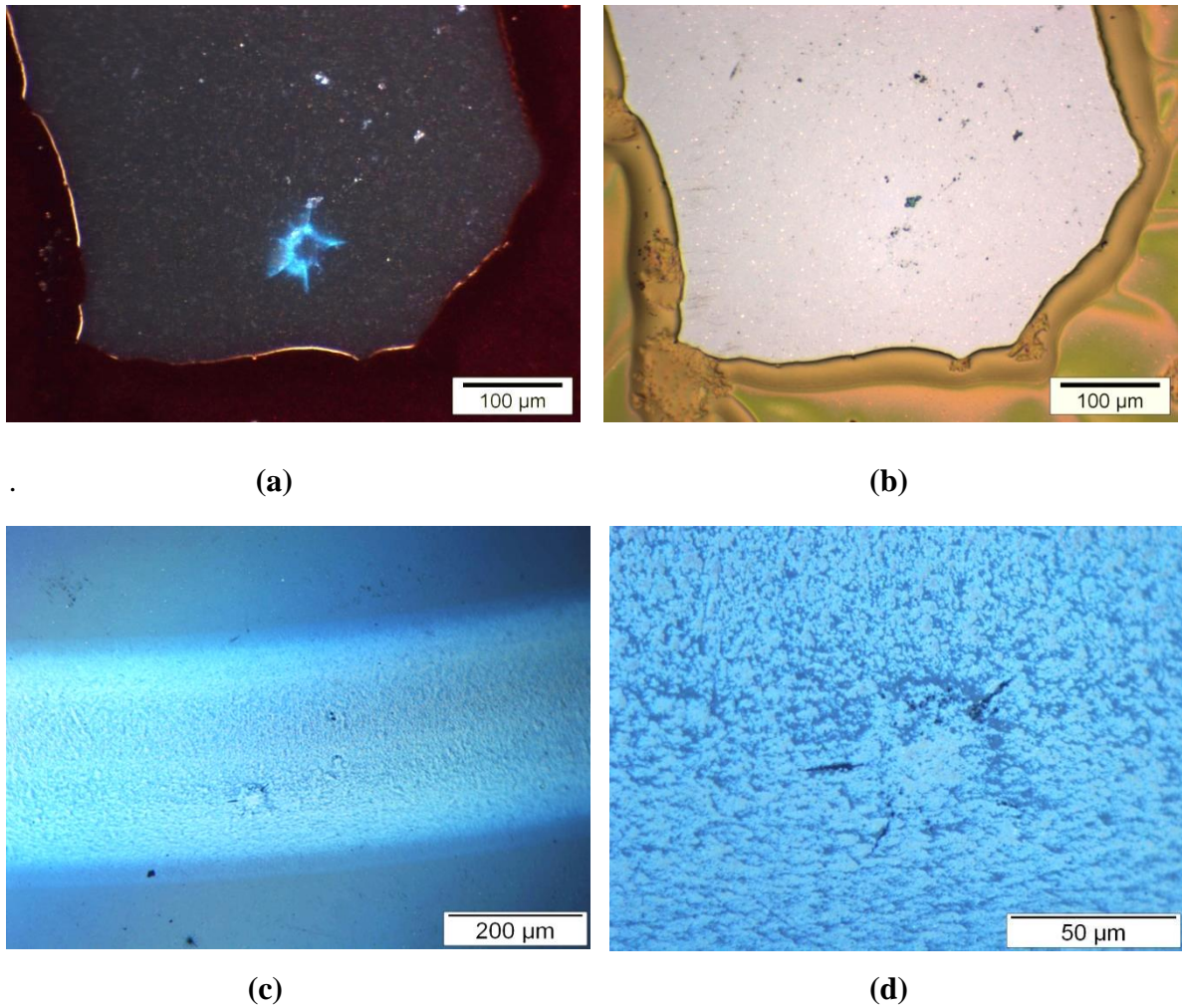


Figure 3.12: Experiment C1TM2 (a) pre-experiment UV illumination (b) pre-experiment white light illumination (c) post-experiment OM image (d) post-experiment OM image at high magnification

This uplift is shown in the magnified view using interferometry in Figure 3.13. Additional experiments using mineral oil also shown some surface wear and surface crack opening/widening. These features are defined in the nomenclature section of the thesis. Again trend is similar in thin mineral oil experiments (C1TM3 and C1TM4) as observed for traction fluid experiments i.e., damage was started from crack broadening and then crack growth and final local and material losses were observed if test is run further. C1TM4 experiment was stopped earlier (after 6million stress cycles) and only crack broadening was observed whereas in the first experiment, local loss was observed after 18million stress cycles due to further over-rolling.

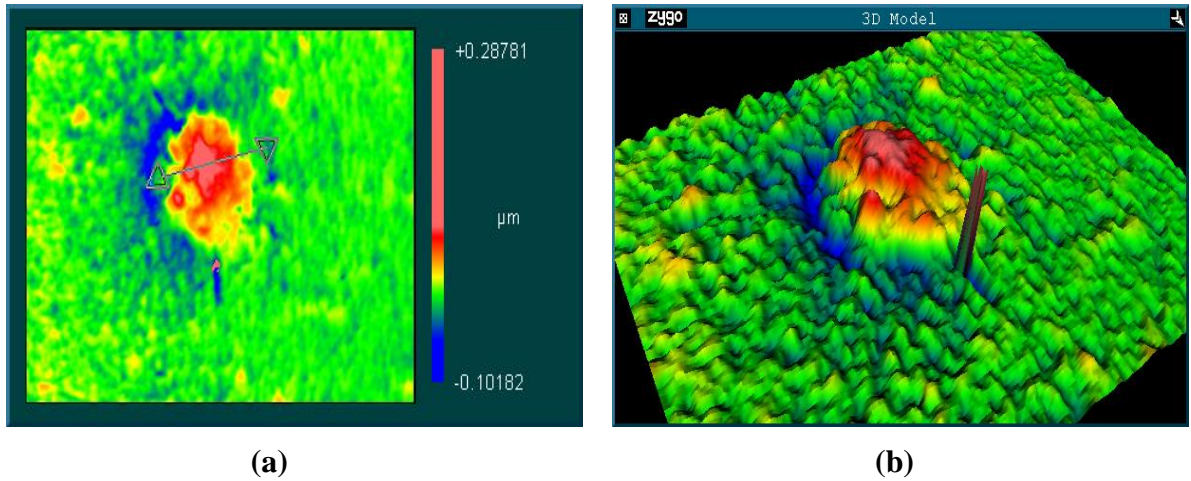


Figure 3.13: Experiment C1TM2 (a) 2D and (b) 3D image interferometry

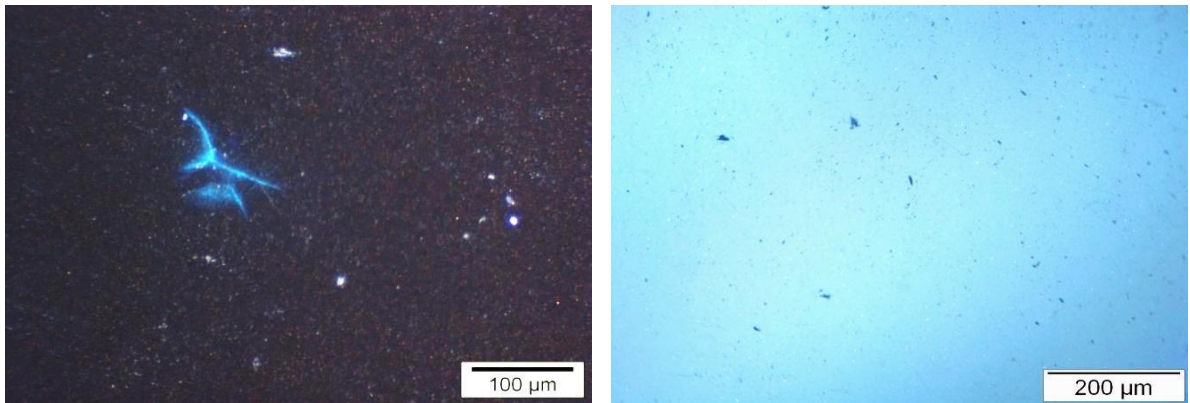
3.2.1.3 Experiments with Gearbox Oil

As these are preliminary experiments to assess lubricant performance using star features of category 1, so only two experiments were conducted for each lubricant case. Experiments conducted using gearbox oil are given in Table 3.5. Two category 1 stars with different tip-to-tip crack lengths were tested.

Table 3.5: Experiments conducted on natural star feature category 1 using Gearbox oil

Exp. ID	Ball ID	Star feature length (μm)	Stress Cycles (10^6)	Outcome
<i>C1GR1</i>	NS9	130	30	<i>Completed</i>
<i>C1GR2</i>	NS10	82	30	<i>Completed</i>

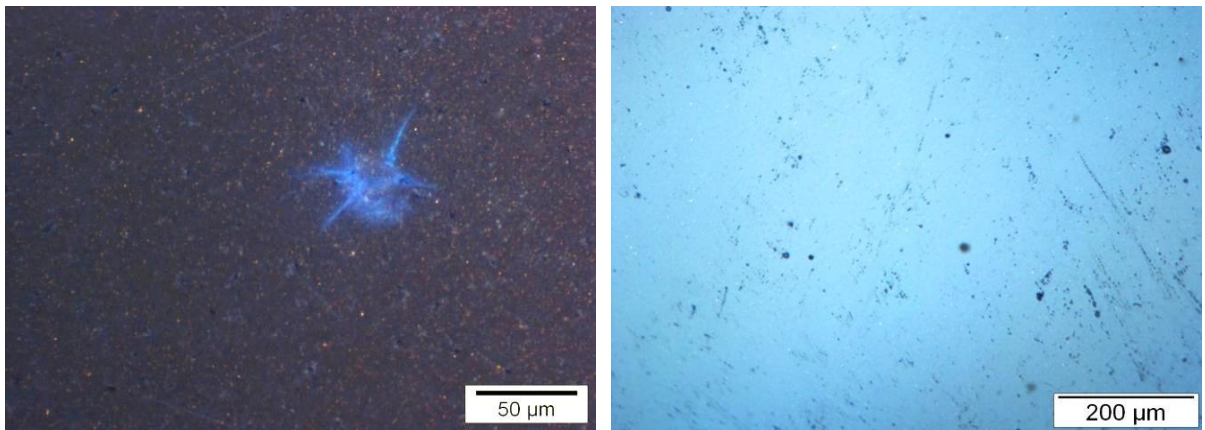
In case of gearbox oil as lubricant, both experiments are conducted for pre-set number of stress cycles (30million). In contrary to traction fluid and thin mineral oil experiments, no new features were observed on the ball surfaces. The defects could not be observed on the surface, see Figs. 3.14 and 3.15 which show the pre- and post-test surface analysis of gear box oil experiments. Using light microscopy, it is hard even to detect the star cracks after testing, indicating that the cracks had been filled. No wear was observed on the surface in both experiments using gearbox oil as lubricant. These results showing the better performance of gearbox oil compare to thin mineral oil and traction fluid.



(a)

(b)

Figure 3.14: Experiment C1GR1 (a) pre-test UV illumination (b) post-test white light



(a)

(b)

Figure 3.15 Experiment C1GR2 (a) pre-test UV illumination (b) post-test white light

3.2.1.4 Experiments with Grease

Similarly to other lubricants, two preliminary experiments are conducted using grease as lubricant. Experimental details are shown in the Table 3.6.

Table 3.6: Details of experiments on Category 1 stars using Grease

Exp. ID	Ball ID	Star feature length (μm)	Stress Cycles (10^6)	Outcome
<i>C1Grsl</i>	NS11	96	10	Stopped due to <i>Crack growth and Broadening</i>
<i>C1GrS2</i>	NS12	101	4	Stopped due to <i>Crack broadening</i>

The outcome of the experiments was similar to that of gearbox oil in that there was no pull-out of material, but crack broadening meant that the stars could be seen after testing. This relatively poor performance of grease compare to gearbox oil may be due to rapid viscosity loosening of grease at higher temperature than gearbox oil (Table 2.2). Although crack broadening was happened after 4-5million stress cycles but further over-rolling also caused crack to grow (experiment C1Grs1).

Details of the experiments are given in Table 3.6 and the appearance of the stars before and after testing are shown in Figs. 3.16-3.17.

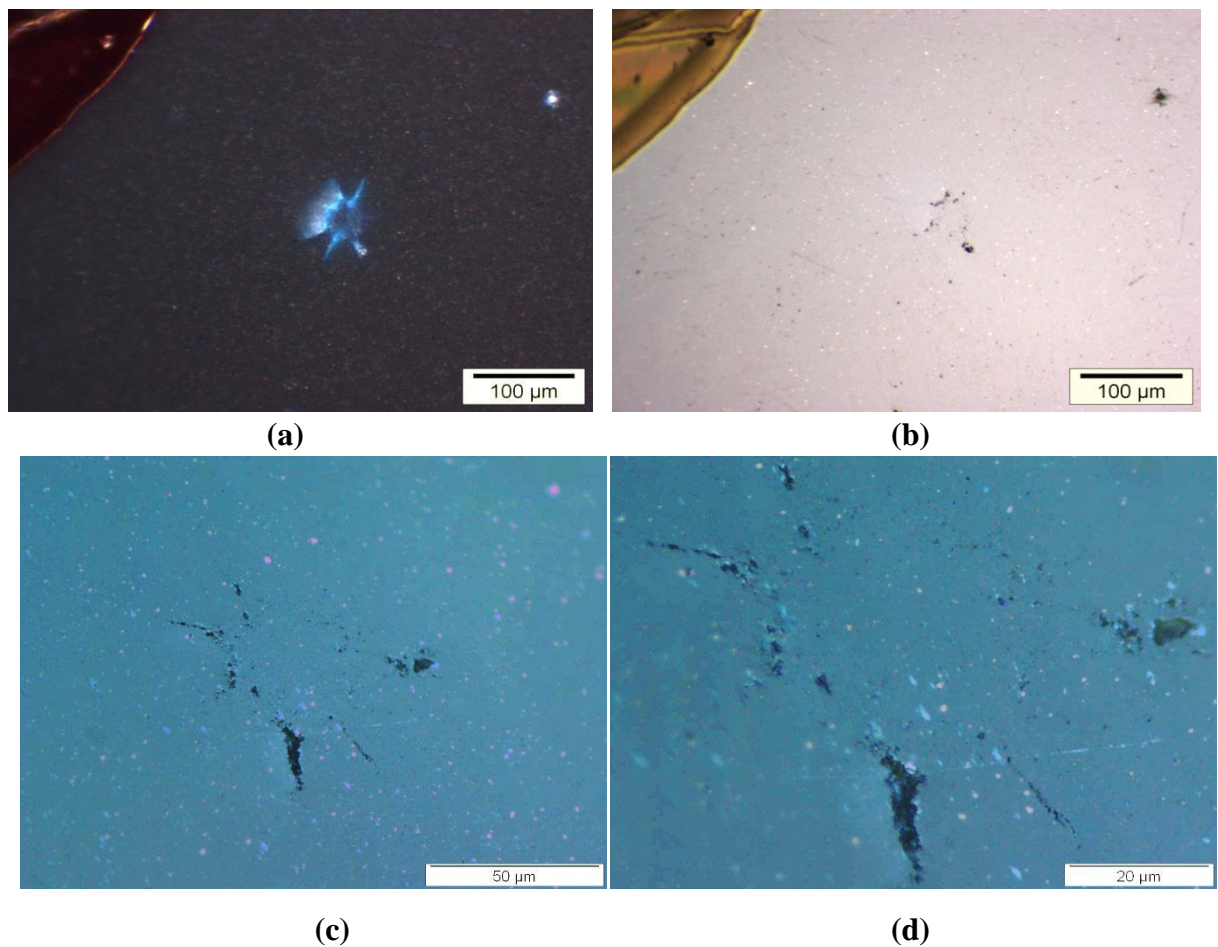


Figure 3.16: Experiment C1Grs1 (a) pre-experiment UV illumination (b) pre-experiment white light illumination (c) and (d) post-experiment OM images

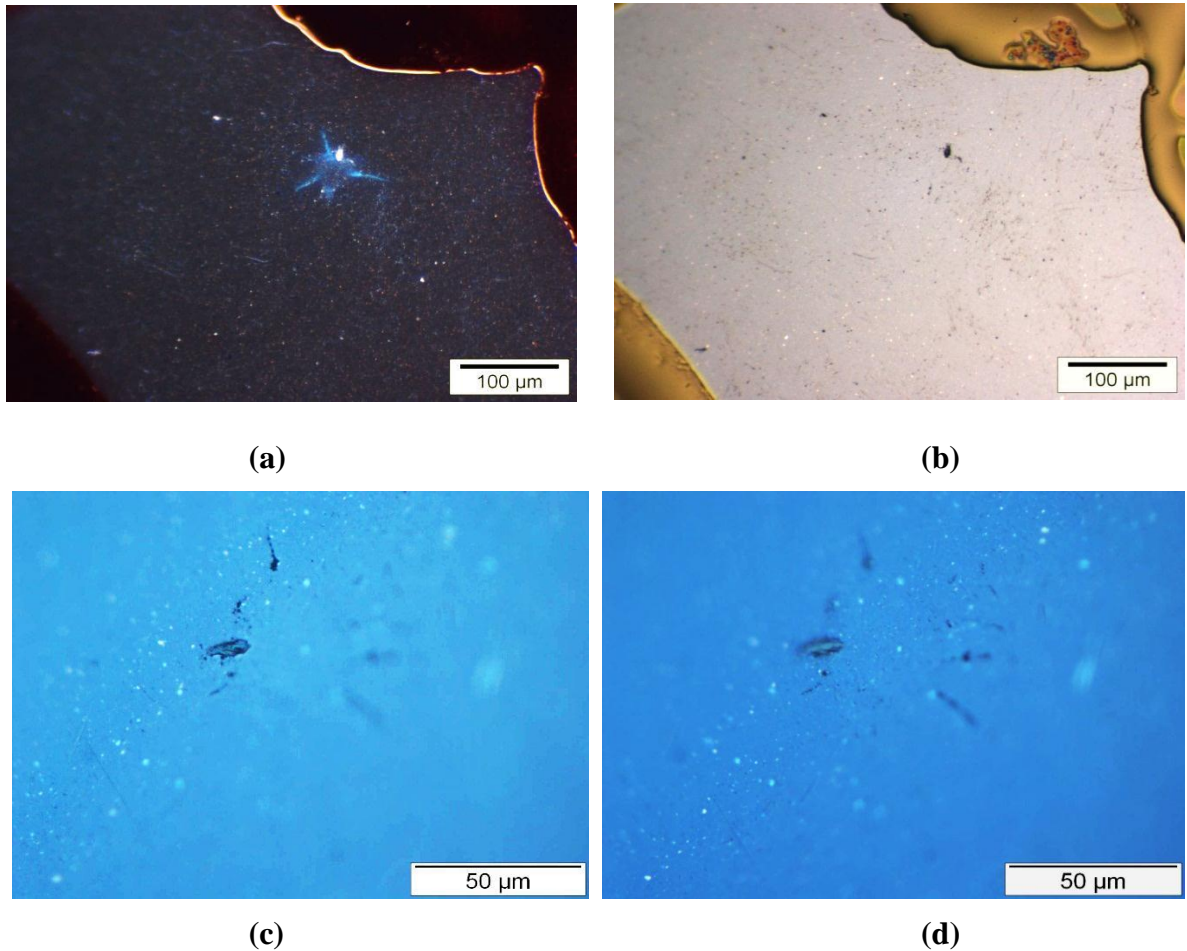


Figure 3.17: Experiment C1Grs2 (a) pre-experiment UV illumination (b) pre-experiment white light illumination (c) and (d) post-experiment OM images

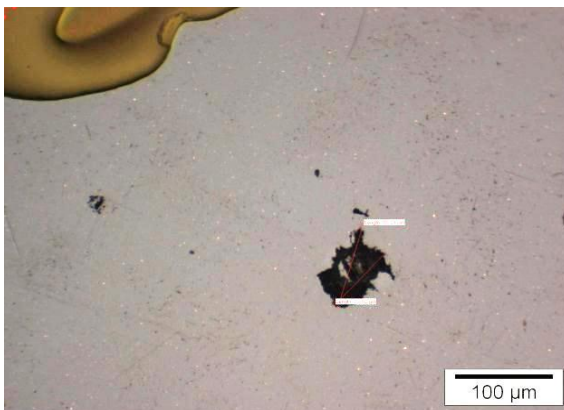
3.2.2. Experiments on category 5 Stars

After the category 1 experiments, stars having pit sizes almost the size of the total star feature (Category 5) were tested. The same temperature and speed was used but the lubricant for all tests was thin mineral oil. This was selected as it had shown poor performance in the category 1 experiments in the sense that features were observed after a shorter running time. Experiments conducted on this category are tabulated in Table 3.7. First experiment (C5TM1) was conducted at the original contact pressure of 3.8 GPa used for Category 1 stars to observe the effect of lubricant and material behaviour under longer running times.

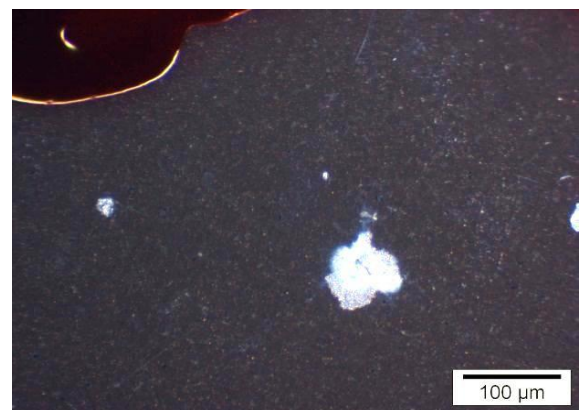
Fig. 3.18 shows the defect before experiment and Fig. 3.19 after 100 million cycles. There was some wear on the leading edge and the maximum depth of the defect also increased from 4.5 μ m to 6 μ m as measured by interferometry.

Table 3.7: Details of experiments on Category 5 stars

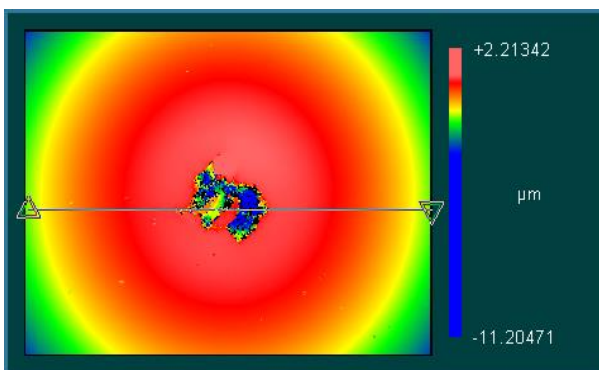
Exp. ID	Ball ID	Contact Pressure (GPa)	Defect dimension (μm)	Stress Cycles (10^6)	Outcome
<i>C5TM1</i>	NS13	3.8	Star: 86, Pit: Almost star size	100	<i>Completed</i>
<i>C5TM2</i>	NS14	4.8a	Star: 119, Pit: Almost star size	20	<i>Stopped</i>
<i>C5TM3</i>	NS15	4.8	Star: 81, Pit: Almost star size	60	<i>Stopped</i>
<i>C5TM4</i>	NS16	4.8	Star: 70, Pit: Almost star size	100	<i>Completed</i>
<i>C5TM5</i>	NS17	4.8	Star: 50, Pit: Almost star size	100	<i>Completed</i>



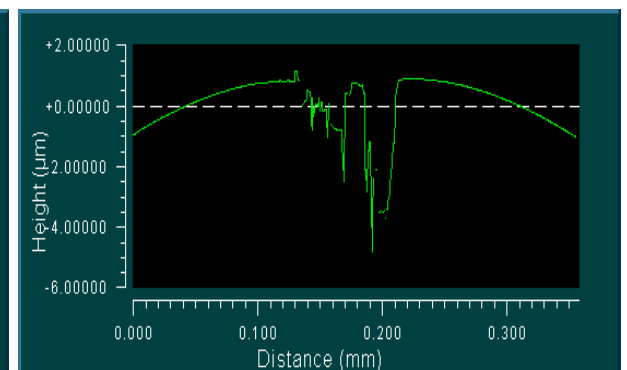
(a)



(b)



(c)



(d)

Figure 3.18: Experiment C5TM1 pre-test (a) white light illumination (b) UV illumination (c) and (d) surface mapping by interferometry

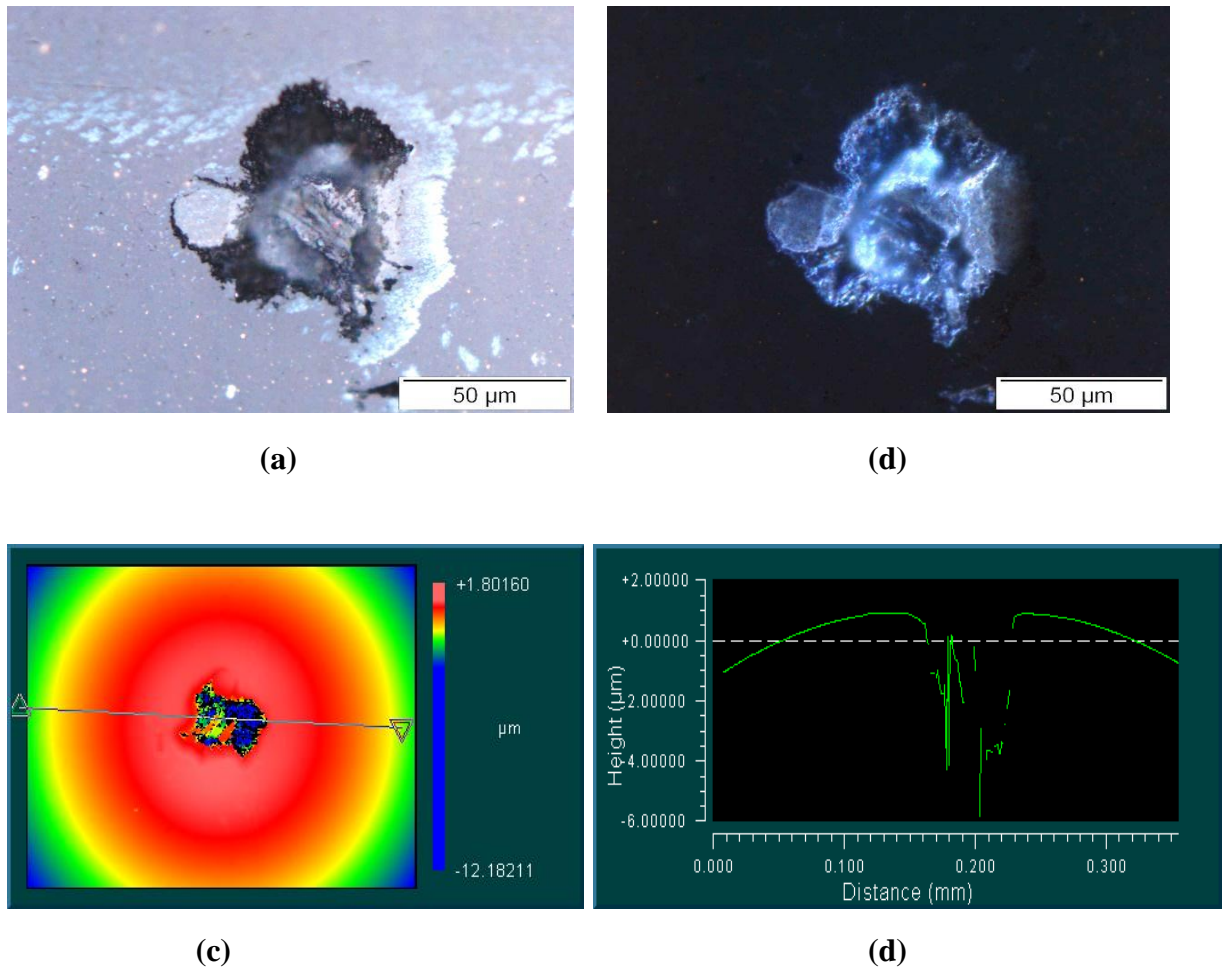


Figure 3.19: Experiment C5TM1 post-test- 100 million cycles (a) white light illumination (b) UV illumination (c) and (d) surface mapping by interferometry

The maximum depth of the feature increased slightly but its extent at the surface was unchanged (apart from the shallow wear areas). Since this first test resulted in little damage and no failure, a higher contact pressure of 4.8 GPa was used in subsequent experiments. In the second experiment (C5TM2), ball rotation or movement inside the collet was observed after 20 million cycles due to the thin lubricant and high friction on the surface. Surface analysis also revealed some small crack growth from the side of the original defect along with surface track wear. Figures 3.20 and 3.21 are showing pre- and post-experiment surface analysis of the sample surface used in the experiment C5TM2.

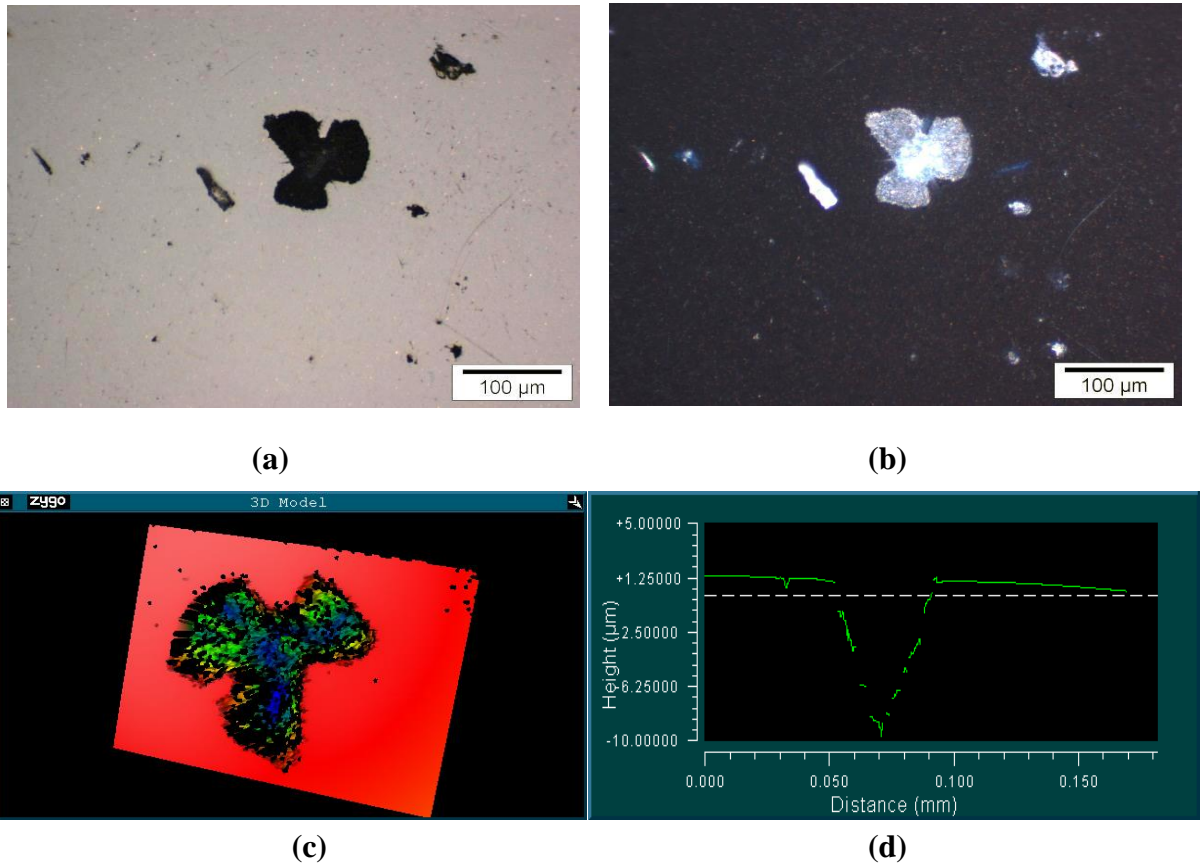


Figure 3.20: Experiment C5TM2 pre-test (a) white light illumination (b) UV illumination (c) and (d) surface mapping by interferometry

Even though the collet was tightened more in the third test, ball rotation again occurred after 60 million cycles when it was found that the defect had moved to a position off the contact track. Post experiment surface analysis of the experiment C5TM3 is shown in the Figure 3.22. With further tightening of the collet, two more experiments were undertaken (C5TM4 and C5TM5). Both experiments successfully completed 100 million cycles. The star defect in experiment C5TM4 had missing material in two parts (Figure 3.23). Post experiment surface analysis for experiment C5TM4 is shown in the Figures 3.24. Although star feature is also consisting of two parts in experiment C5TM5 but major part was under the consideration for this experiment. Similar results were obtained in this final experiment where again the test was run to 100 million cycles without any spalling or significant crack growth. Figures 3.25 and 3.26 are showing pre- and post-experiment surface analysis.

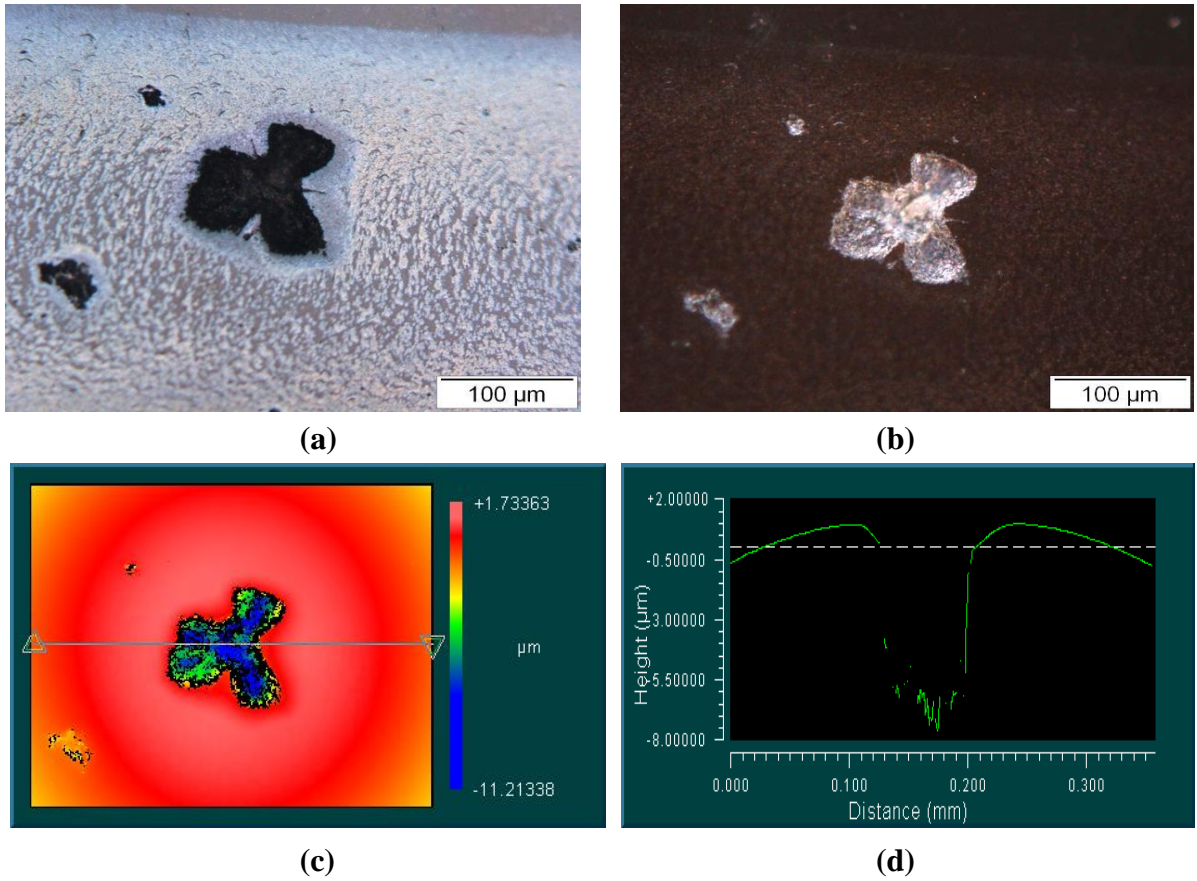


Figure 3.21: Experiment C5TM2 post-test-20 million stress cycles (a) white light illumination (b) UV illumination (c) and (d) surface mapping by interferometry

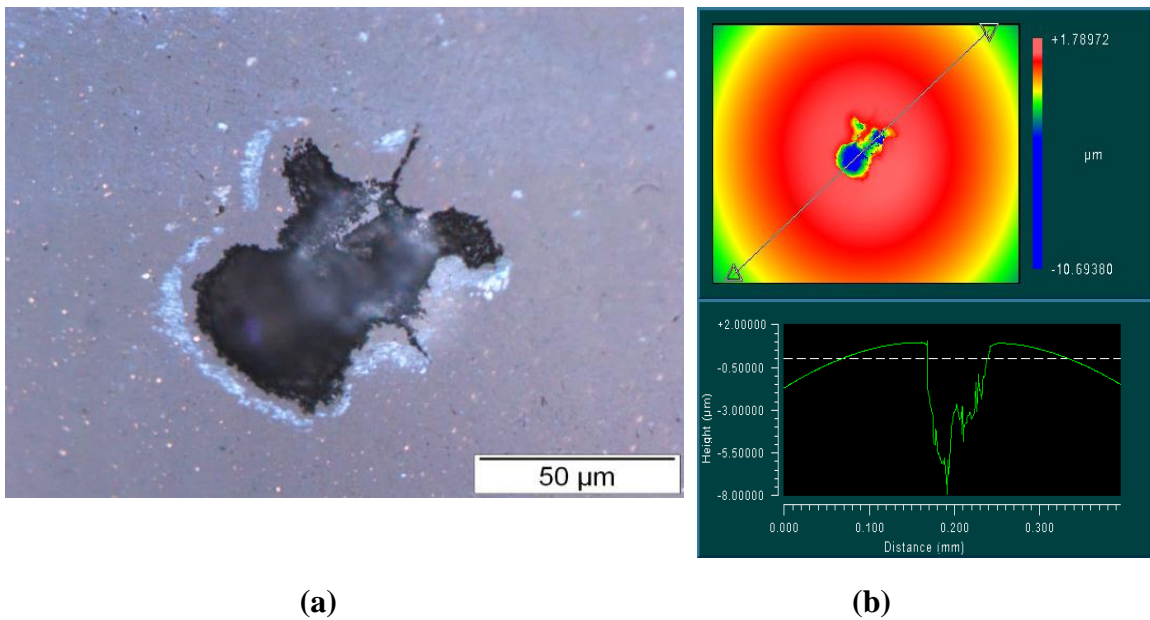


Figure 3.22: Experiment C5TM3 post-test-60 million stress cycles (a) white light illumination (b) surface mapping by interferometry

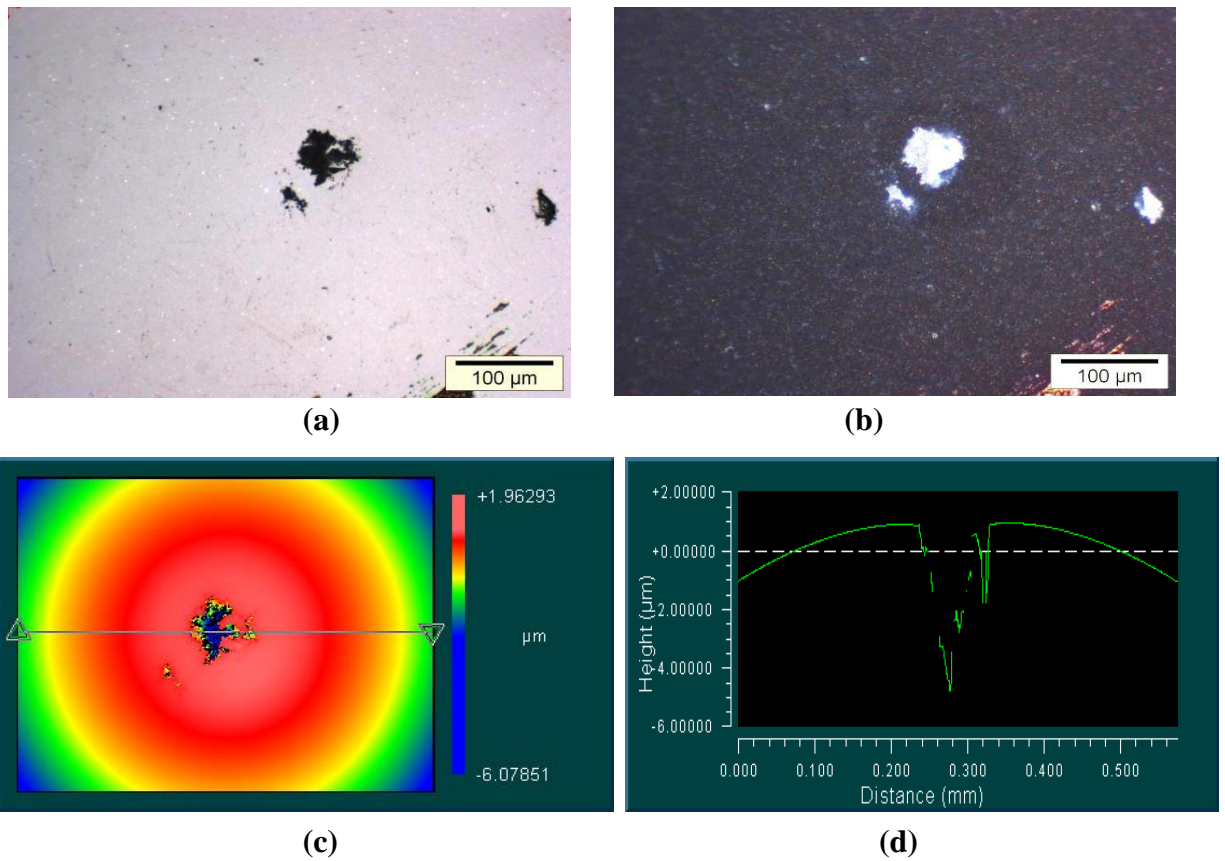


Figure 3.23 Experiment C5TM4 pre-experiment (a) white light illumination (b) UV illumination (c) and (d) surface mapping by interferometry

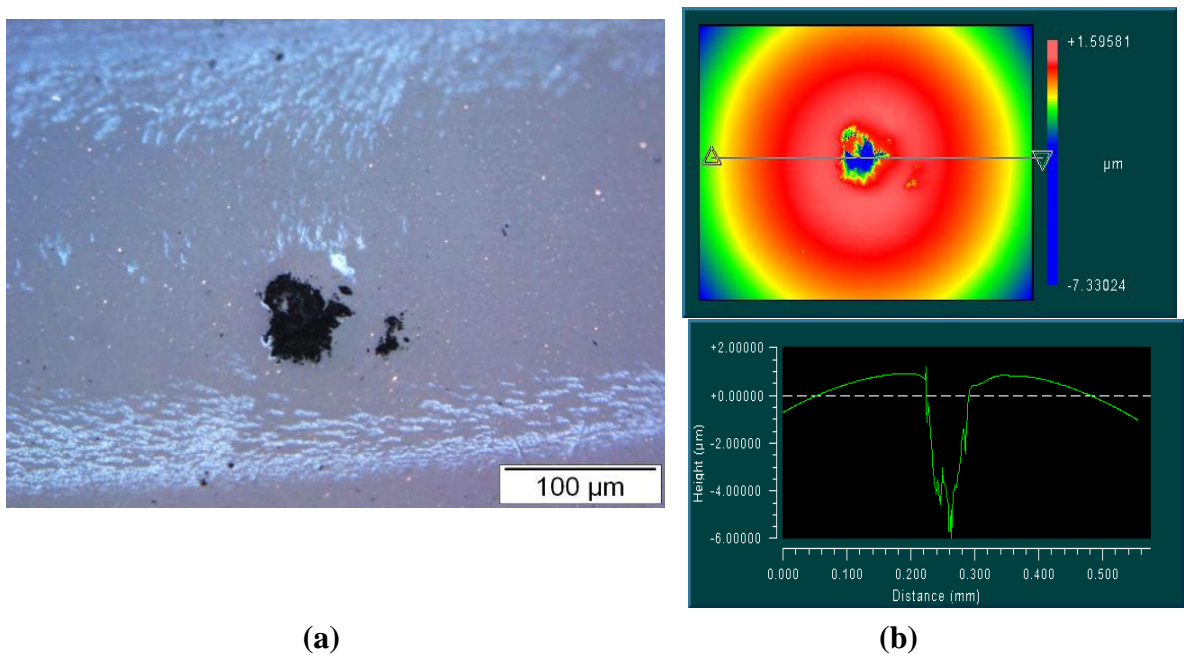


Figure 3.24 Experiment C5TM4 post-test-100 million stress cycles (a) white light illumination (b) Surface mapping by interferometry

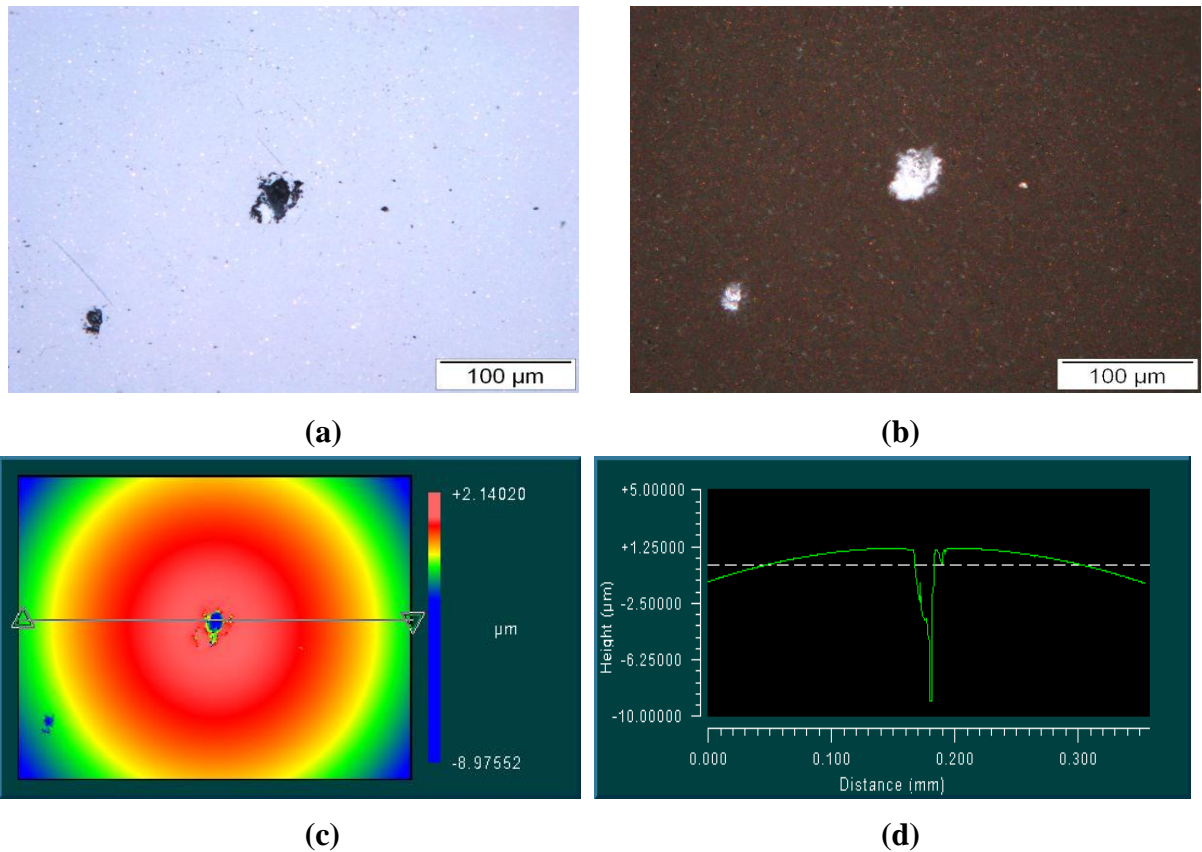


Figure 3.25 Experiment C5TM5 pre-experiment (a) white light illumination (b) UV illumination (c) and (d) surface mapping by interferometry

3.2.3. Experiments on Pit Size

Three further experiments were conducted to determine the effect of pit size on the rolling contact fatigue of silicon nitride. Samples were taken from three categories (1, 3 and 5) with nominally the same overall star defect but increasing pit sizes (10, 50 and almost total star size respectively) as shown in Table 3.8.

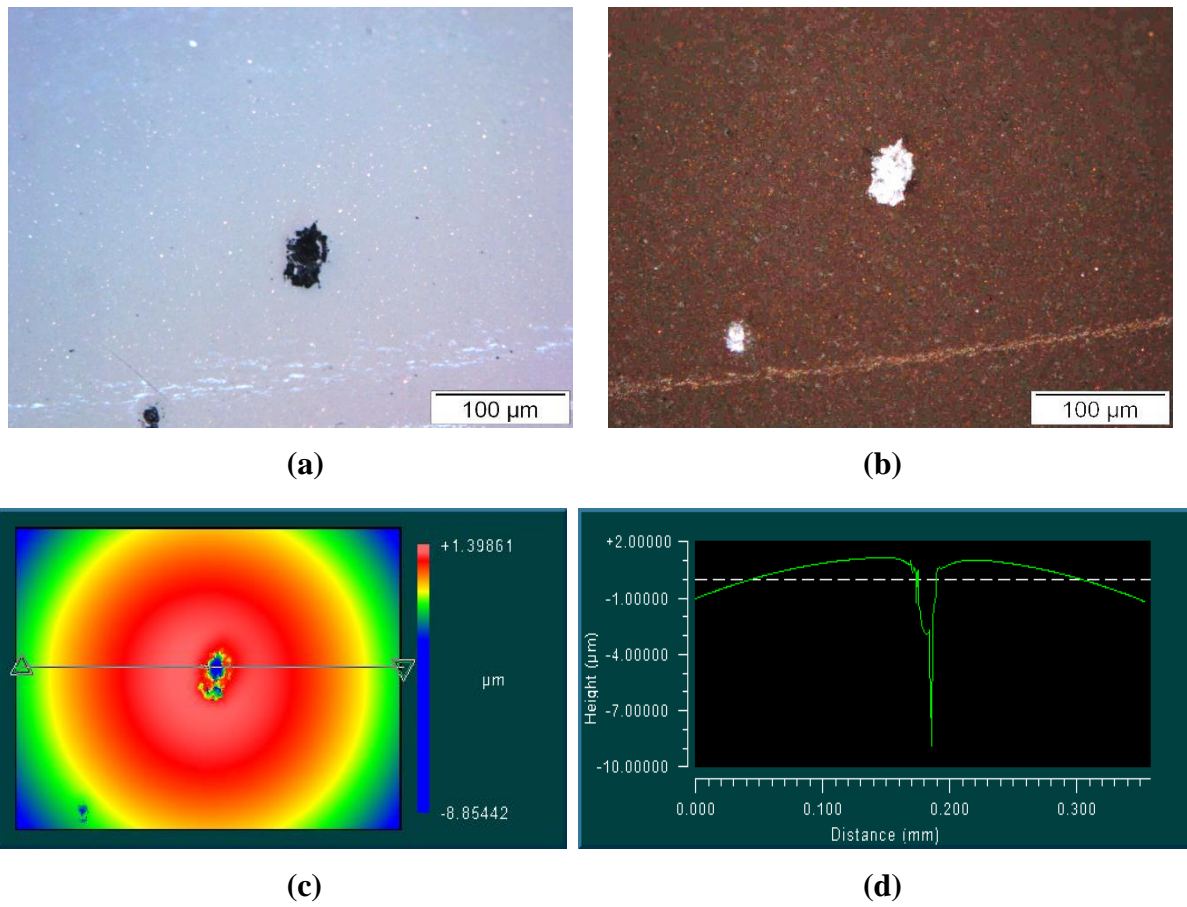


Figure 3.26: Experiment C5TM5 post-test-100 million stress cycles (a) surface analysis using white light illumination (b) Surface mapping by interferometry

Table 3.8: Details of experiments on pit size

Exp. ID	Ball ID	Contact Pressure (GPa)	Defect size (Star, pit) μm	Stress Cycles (10^6)	Outcome
<i>C1TM5</i>	NS18	4.8	Star: 95, Pit: 10	100	Suspended*
<i>C3TM1</i>	NS19	4.8	Star: 96, Pit: 50	100	Suspended*
<i>C5TM6</i>	NS20	4.8	Star: 97, Pit: Almost star size	100	Suspended*

*: Completed predefined number of revolutions but new features also appeared

All three experiments were run up to 100 million cycles without any evidence of a spalling failure. In the first experiment (C1TM5) with a star without missing material (or very small area), there was some indication of crack broadening. Fig. 3.27 shows the feature before testing where some of the cracks were not clearly visibly in white light illumination but after testing they were more apparent (Fig.3.28).

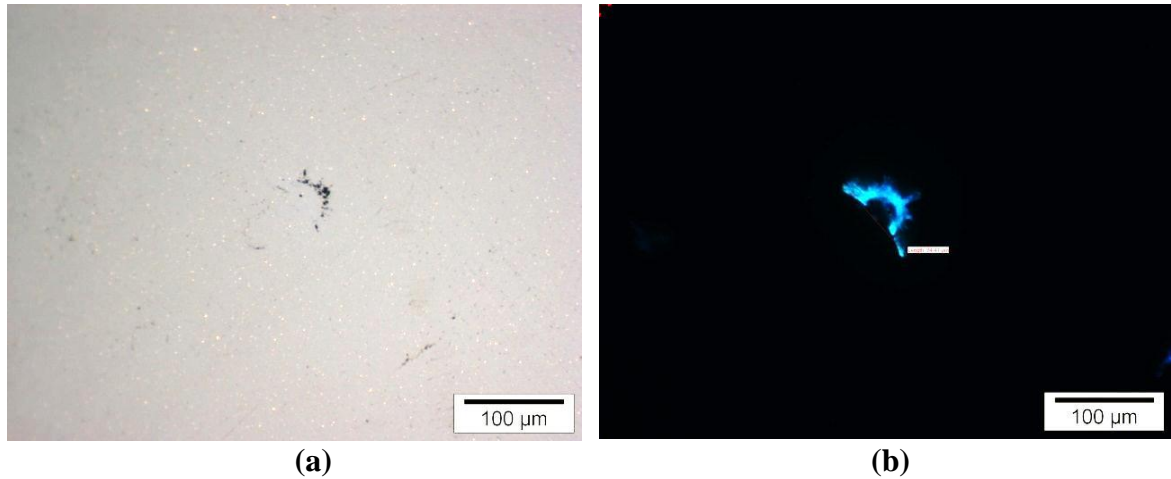


Figure 3.27: Pre-experiment C1TM5 (a) light illumination (b) UV illumination

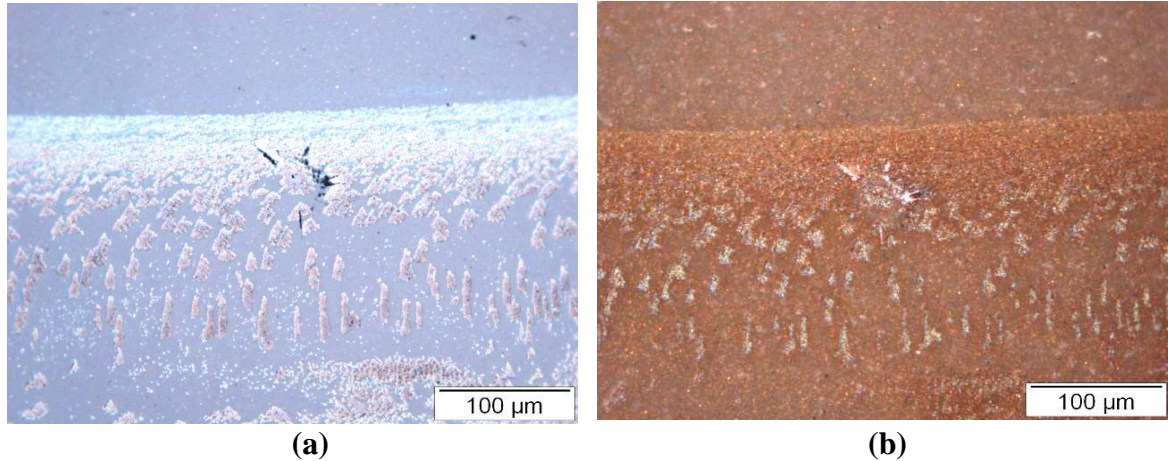


Figure 3.28: Post-experiment C1TM5 (Ball 18, Cat. = 1) (a) light illumination (b) UV illumination

The second experiment (C3TM1) was conducted on a category 3 star containing a 50μm pit with some well-developed cracks (Fig. 3.29). The experiment was halted at regular intervals for surface examination.

After testing, it was observed that some material came out from the defect and the missing material part was extended due to over-rolling (Fig. 3.30). Apart from this extension, surface wear was also observed which was more severe than in the first experiment. Profilometry after testing (Fig. 3.31) showed that the crack had deepened from $6\mu\text{m}$ to $11\mu\text{m}$.

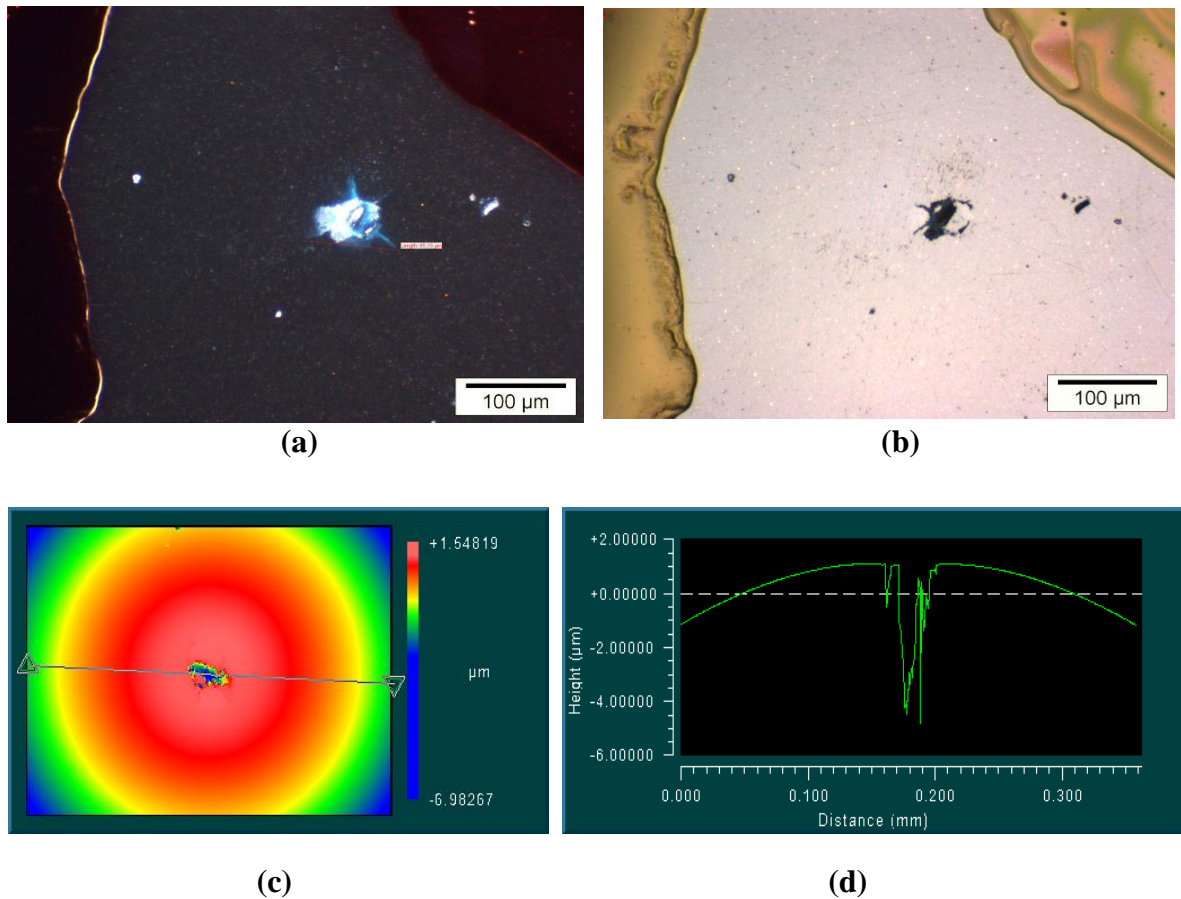


Figure 3.29: Experiment C3TM1 pre-experiment (a) white light illumination (b) UV illumination (c) and (d) surface mapping by interferometry

In the third experiment (C5TM6), a Category 5 star feature was tested. This had no observable radial cracks but a strong lateral crack associated with the major missing material/pit part. This can be seen under UV light in Fig. 3.31.

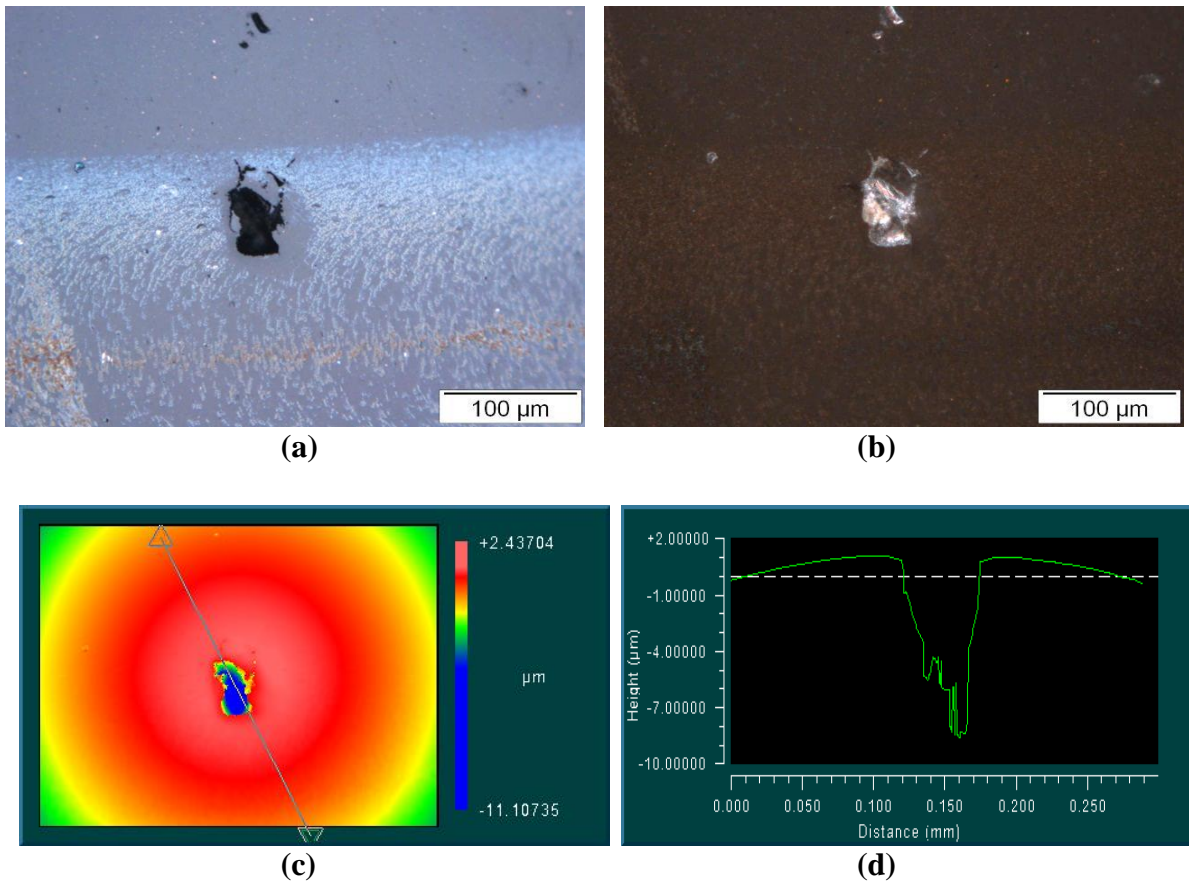


Figure 3.30: Experiment C3TM1 post-experiment (a) white light illumination (b) UV illumination (c) and (d) surface mapping by interferometry

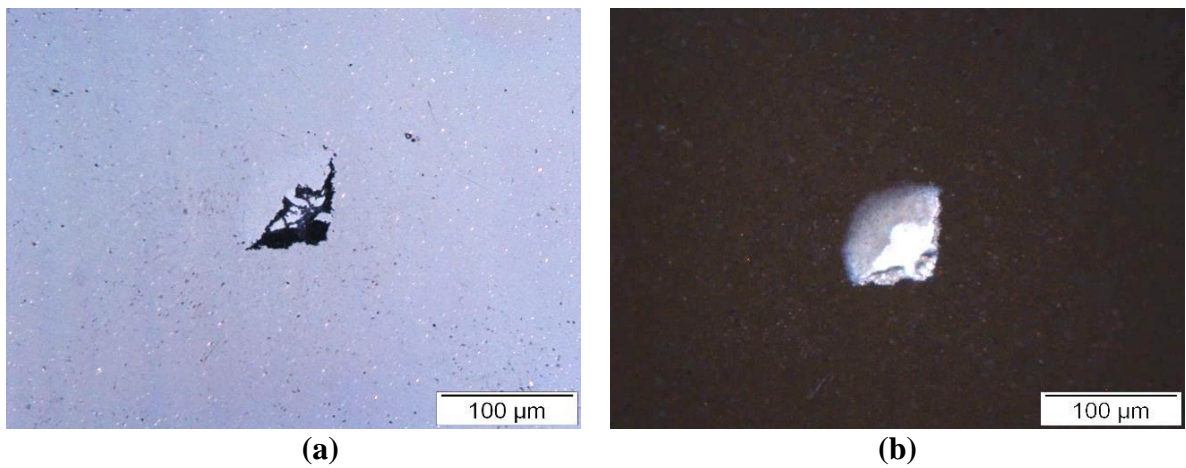


Figure 3.31: Experiment C5TM6 pre-experiment (a) white light illumination (b) UV illumination

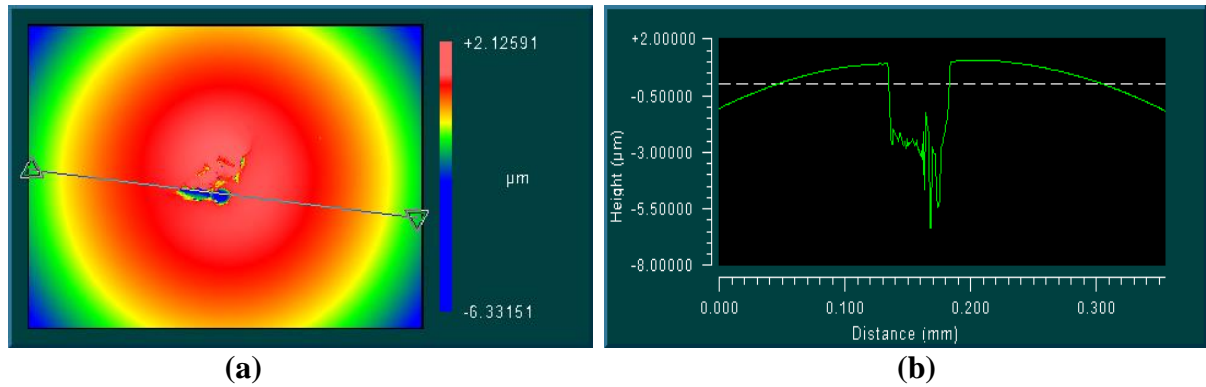


Figure 3.32: Experiment C5TM6 pre-experiment (a) and (b) surface mapping by interferometry

After 68 million stress cycles it was found that material had broken out from the whole lateral crack zone leaving behind cavity of depth $15\mu\text{m}$ (Fig 3.33-3.34). The experiment was continued further to complete 100 million stress cycles but there was no obvious change of surface morphology at the end of the test. There was no sign of any further crack initiation or propagation outside the extent of the defect.

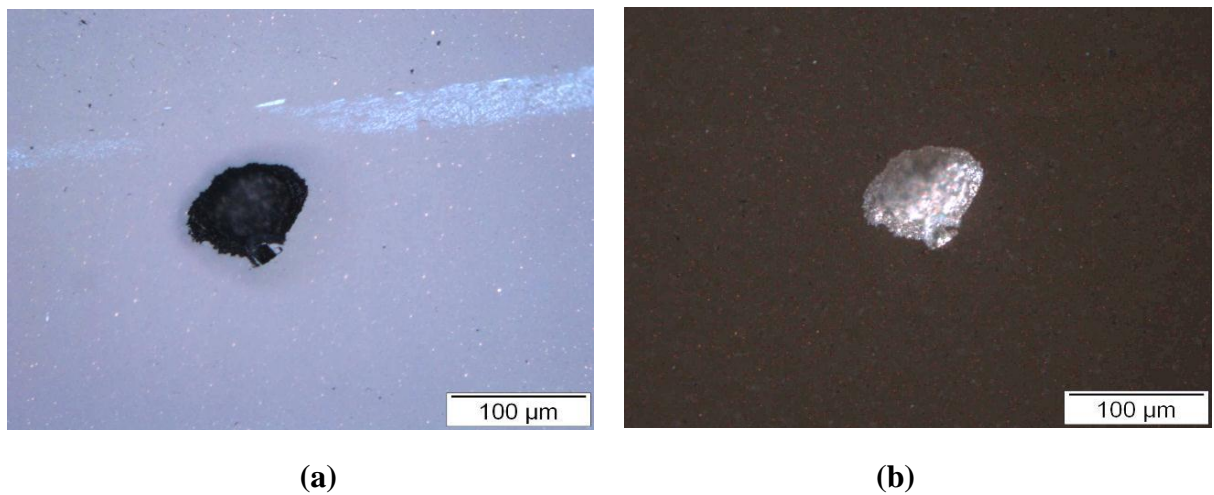


Figure 3.33: Experiment C5TM6 post-test-100 million stress cycles (a) white light illumination (b) UV illumination

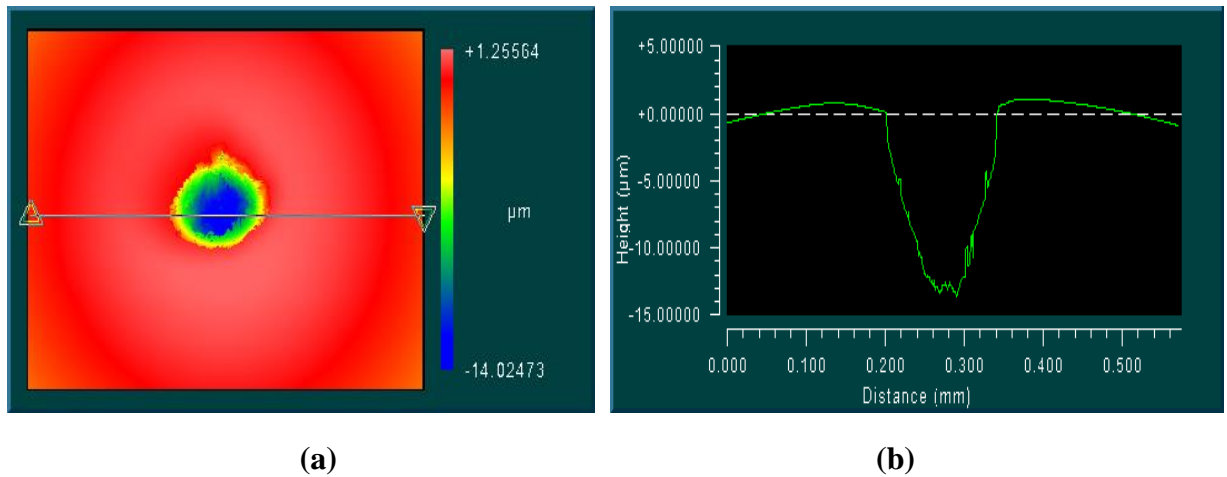


Figure 3.34: Experiment C5TM6 post-test-100 million stress cycles (a) and (b) surface mapping by interferometry

3.3. Star features – Discussion/Conclusions

In the first series of experiments on Category 1 stars, the main aim was to show the influence of lubricant in rolling contact with these features. Experiments were stopped when new features or significant changes (crack growth/crack front widening/material loss within defect extent etc.) were observed. The high viscosity gearbox oil used as a lubricant showed better performance than the other lubricants which tend to rapidly lose their viscosity with temperature. Therefore, experiments conducted at 75°C would lead to greater penetration of the lubricant into defects which could adversely affect RCF performance. Another reason to have poor performance of mineral oil and traction fluid may be due to stress intensities in the cracks and better performance of gearbox oil due to crack face friction [increasing crack face friction reduces the mode II stress intensity factor – Zhao 2006]. Figure 3.35 summarises results on testing of Category 1 stars (major experiments) with different lubricants and the main reason for suspension. (These results produced similar trend (in terms of lubricant performance) as was reported for steel bearing under micro-indentation [Al-Bakhaite et al. 2011]). Although delamination has been reported as failure mode in silicon nitride but in case of surface star feature, minor delamination is considered tolerable for rolling element bearing.

These results indicate that star features are more sensitive to thin mineral oil, traction fluid and grease as lubricants [ring or C-cracks also produced similar results for silicon nitride – Zhao 2006]. Therefore, all further experiments on star features and missing material were

carried out with thin mineral oil having lowest viscosity out of the lubricants used. Low viscosity mineral was less effective than traction fluid (relatively more viscous) and this trend is different for steel bearing case tested with same viscosity lubricants [Nakajima and Mawatari 2005]. Lubricant has influence on the rolling contact performance of rolling element bearing; viscous lubricant provide better performance than low viscous lubricant [a similar trend was reported for steel bearing – Rico et al. 2003]

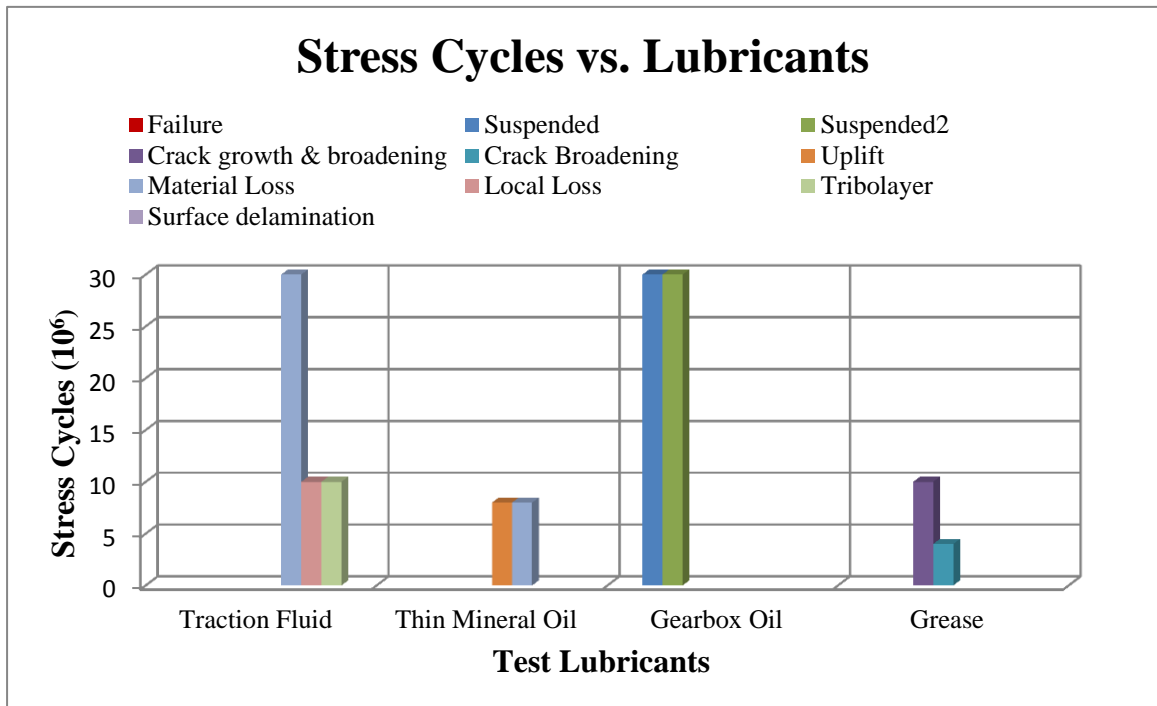


Figure 3.35: Comparison of different lubricants for star features category 1 experiments

No spalling failures or significant growth of defects occurred when the nominal contact pressure was 3.8 GPa. This level is above most contact pressures seen in service with hybrid bearings. However, further tests on stars were carried out at a higher contact pressure of 4.8 GPa. Experiments on Category 5 stars with significant missing material did not lead to spalling failure. The largest of this type of defect tested had a maximum depth of 11 μ m and defect cross corner size of 122 μ m. In all experiments, surface wear was observed on the contact track; however, it was more severe in case of larger defect sizes at 4.8GPa. In some cases, crack widening was also observed. Along with contact pressure and defect size, defect location and orientation on the contact track is also important [Awan et al. 2013a]. Centrally located defects on the contact track have more pronounced effects than defects positioned at the edges of track due to a reduction in the nominal contact pressure. This phenomenon is discussed in detail in Chapter 5.

Star features have variable patterns and geometries which makes it difficult to generalise. However, the results of this study indicate that they do not constitute a significant risk of failure in hybrid bearings. Missing material associated with some stars is typically the result of material flaking out from a sub-surface lateral crack. This can occur during ball finishing or subsequently under rolling contact fatigue. Category 1 or 2 stars containing little or no missing material may suffer from flaking if lateral cracks are present. But in this case the effect is to convert them to Category 4 or 5.

The main conclusions are that star defects on silicon nitride balls are not very harmful to performance under rolling contact in hybrid bearings. At that worst, stars can be considered to be missing material defects 50 – 100 μm in extent with depths of 5 - 10 μm . They therefore constitute the lower limit of size to be considered in the following chapters on missing material.

3.4. Artificial star Creation

3.4.1. Artificial star feature using course diamond paste

In order to create artificial star defect using rough diamond paste, first silicon nitride surfaces were cleaned using ultrasonic bath. Rough diamond paste of 45 μm was applied on the required surface of silicon nitride and other silicon nitride ball was used to hit the sample ball. This diamond paste size was selected to have star size of lower limit (around 50 μm). Finally, ball surface again cleaned and conducted surface analysis. Polishing operation is conducted on the ball surface to remove material and get relatively rough star feature on the surface. Figs 3.36-3.37 are showing such defects on the silicon nitride after polishing the surface. Defects/cracks obtained were not in regular shape and also not reproducible. Therefore, this method did not adopt and tried other techniques as mentioned in the next section.

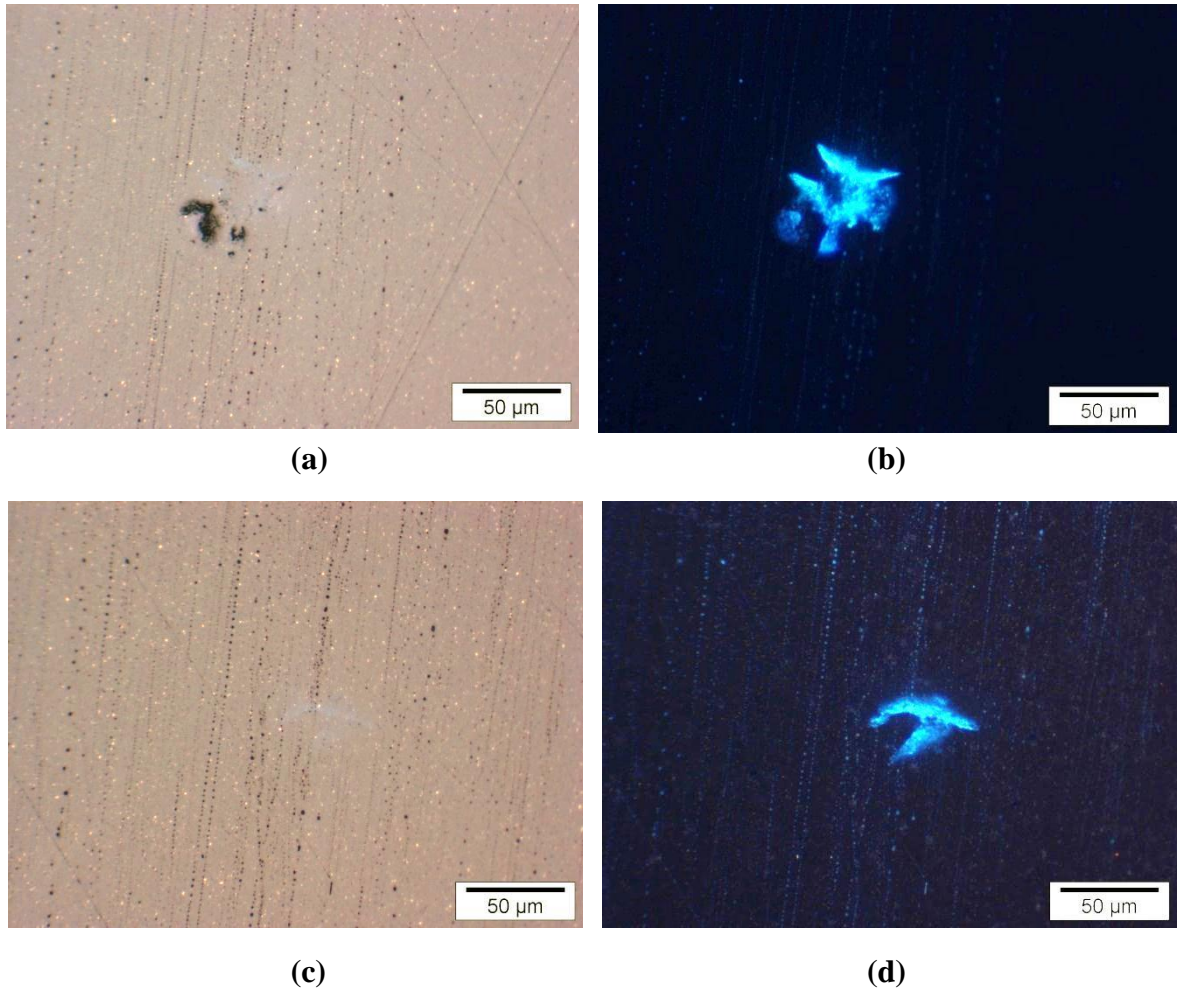


Figure 3.36: Artificial star making using diamond paste (a) and (c) light illumination for sample 1 and 2 (b) and (d) UV illumination for sample 1 and 2 (Work done at ERC)

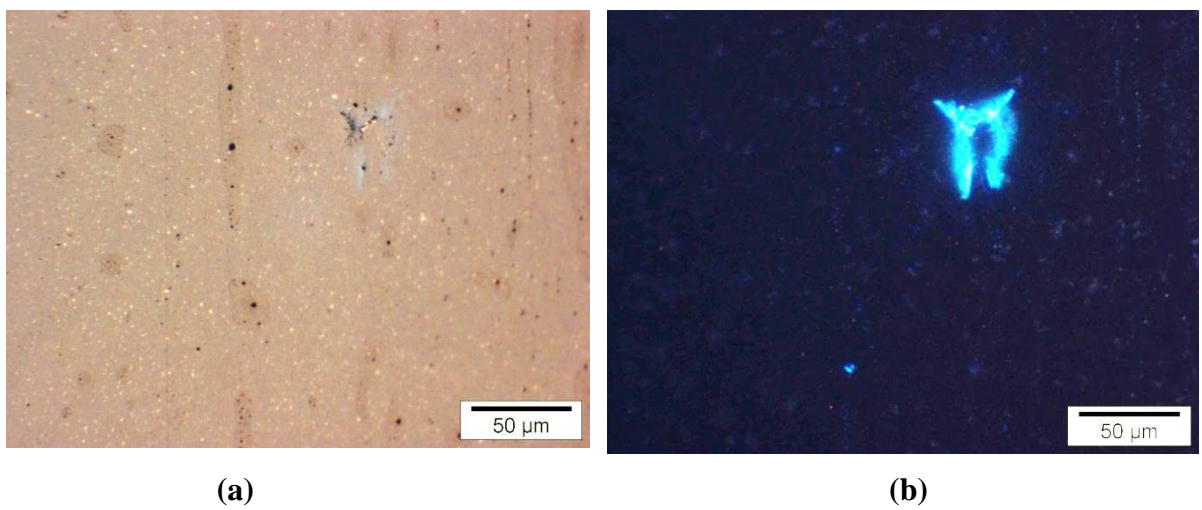


Figure 3.37: Artificial star making using diamond paste (a) light illumination for sample 3 (b) UV illumination for sample 3 (Work done at ERC)

3.4.2. Artificial star using Vickers indenter

In order to get regular and reproducible star defects, rough Vickers indenter was used to make indentation on the surface. Different approaches were opted according to requirements;

1. Cut off the Vickers tip to make it blunt for further use
2. Drill central cavity into silicon nitride material using laser micro-machining and then make indent in centre of cavity
3. Find old and blunt Vickers to make indentation

In order to cut off the Vickers tip, calculations [Appendix H] are made using different force values to find cross corner indent distance on the silicon nitride surface. So, in order to get star size (indent) of 100-140 μm , 15 μm tip had to be removed. For further processing, different suppliers were contacted to blunt (cut off) the tip of the Vickers Indenter. Due to very hard nature of diamond material and very precise cutting (and exact flat surface at the tip), this was unsuccessful.

In the second case, cavities were created on the silicon nitride surfaces and sharp diamond indenter was employed to produce a star. In order to avoid any central pressed cavity by Vickers indentation, a laser machined ball was used. Vickers indentation was done on the ball surface approximately in centre of the cavity. The Vickers diamond just pressed the material at the cavity corners and did not produce any cracks with this methodology.

Finally, a well-used Vickers indenter was employed to give a rough indentation (not very sharp) to simulate artificial star scenario. Indentation was made by applying different loads on flat silicon nitride surfaces in order to confirm the feasibility of this methodology. Finally lapping and polishing process was conducted on the indented surface and around 8 μm material removed from the surface. Reasonable surface star like indent was obtained from this methodology as shown in the Fig 3.38-3.41. Further procedural details are given in Appendix H.

3.5. Summary

In the first part of this chapter, star features are categorised based on pit size to total star extent to have better understanding of effect of crack size (star) and pit size (missing material) on the rolling contact fatigue of silicon nitride. Experiments conducted on category 1 (almost star without pit/missing material) are discussed using four different types of lubricants. Based on preliminary experiments on category I, further experiments

were conducted on category 5 (almost missing material/pit area) using thin mineral oil and are presented in the second part of the chapter. This lubricant was selected as it had poor performance than other lubricants. Effect of pit size on the rolling contact fatigue of silicon nitride is discussed in third part by taking same size star with variable pit areas. Different methods to create artificial star features are outlined in the last section of this chapter. As star features in general were converting into missing material type of defects after few millions cycles, therefore, next two chapters are dedicated to missing materials creations and testing.

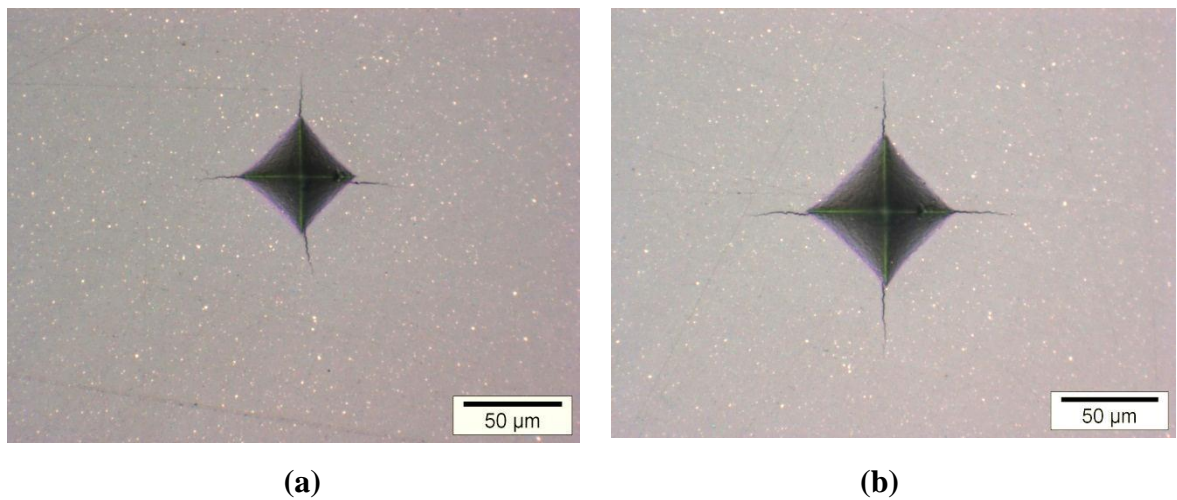


Figure 3.38: Light microscopy for Vickers indentation (a) for 3kg_f (b) for 5kg_f (Work done at ERC)

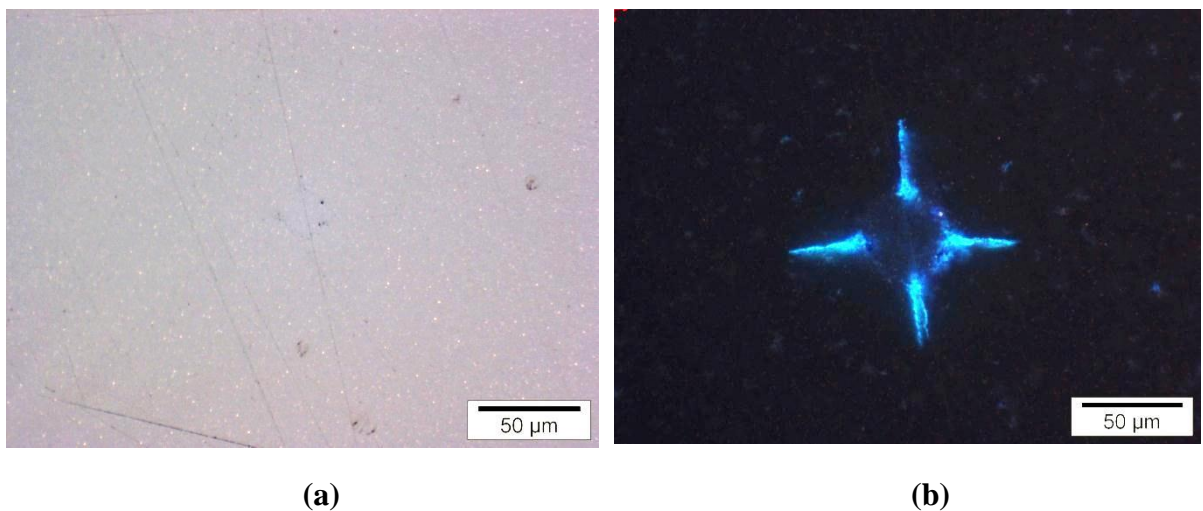


Figure 3.39: Artificial star - post polishing 3kg_f (a) indentation by light illumination (b) indentation by UV illumination (Work done at ERC)

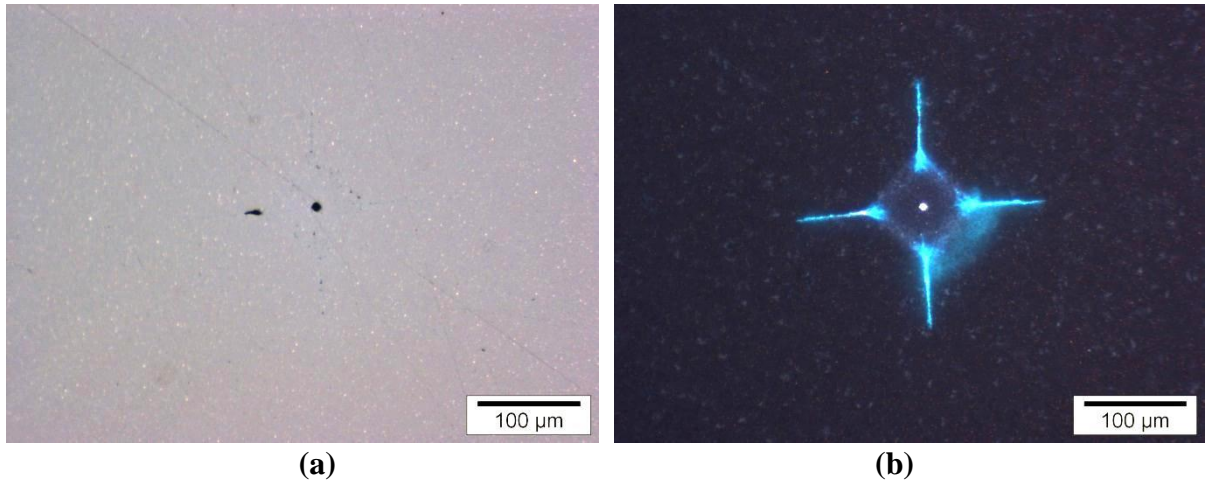


Figure 3.40: Artificial star - post polishing 5kg_f (a) indentation by light illumination (b) indentation by UV illumination (Work done at ERC)

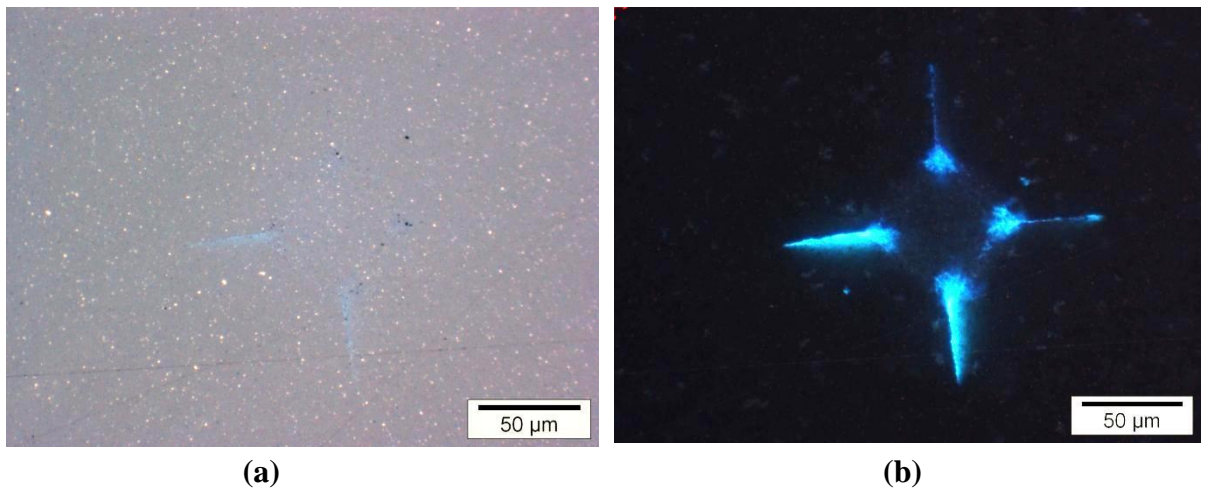


Figure 3.41: Artificial star-post polishing 10kg_f (a) indentation by light illumination (b) indentation by UV illumination (Work done at ERC)

Chapter 4 Laser Machining and Controlled Defects

Missing material on the surface of silicon nitride balls can take various forms – small and large pores, pits/holes, gouges and voids resulting from pull-out of inclusions during ball finishing. For both experimental and modeling purposes it was necessary to machine reproducible artificial areas of missing material. Since such artificial defects would have to be 50 to 100 μ m in extent (diameter) and 5 to 50 μ m in depth to be representative of actual missing material, very precise and reproducible machining would be necessary. In the first part of this chapter, non-conventional machining methods including ultrasonic machining, electron beam and laser machining are reviewed. Then the proposed geometries and dimensions of artificial controlled defects are outlined and the machining methods to produce artificial missing material defects on the surface of silicon nitride balls are described.

4.1. Non-Conventional Machining

Different types of non-conventional techniques are used for very precise and controlled machining at the micro and nano scale level. The principles of mechanical, chemical and electrical machining methods are outlined in Appendix I. Three of the techniques were considered to be promising for producing artificial defects in silicon nitride - laser machining, electron beam machining and ultrasonic machining. Literature, both scientific and commercial, was reviewed to determine which approach would be best for machining controlled defects in a very hard, non-conductive material to the required precision without causing any considerable collateral damage.

4.1.1. Ultrasonic Machining (USM)

Ultrasonic machining is a material removal process in which material is removed by repetitive impact of abrasive particles carried in a liquid medium on to the work surface by a shaped tool, vibrating at ultrasonic frequencies. The process can be used for almost all types of material including diamond, tungsten, tungsten carbide and other conducting and non-conductive materials. USM can be applied to a range of machining processes such as drilling, grinding, profiling, threading, coining, wiring and wire drawing and even welding. Also it can be used for drilling screw threads in curved holes. It gives good surface finish and accuracy. Moreover, no heat generation during machining avoids thermal effects on

the material surface as well as maintaining accuracy. However, ultrasonic machining has some disadvantages in production - high tool wear, low material removal rate and is an expensive process.

The components of an ultrasonic machining unit are:

1. Ultrasonic transducer
2. Concentrator
3. Tool
4. Abrasive slurry
5. Abrasive feed mechanism
6. Tool feed mechanism

Typical machining parameters are:

Amplitude of vibration: 15-50 μ m

Frequency of vibration: 19-25 kHz

Feed Force: related to tool dimension

Abrasive size: 15 μ m-150 μ m

Abrasive material: Al₂O₃, SiC, B₄C, diamond, boron silicon carbide

Since it is a mechanical process, USM is particularly applicable to hard, high melting point, non-conductive material such as ceramics.

4.1.2. Electron Beam Machining (EBM)

Machining using an electron beam is an electro-thermal process in which material is removed by a high velocity stream of electrons impinging on the work piece where the kinetic energy of the beam is converted to heat which makes the material melt and vaporize locally. An EBM unit has similar components to an electron microscope – a tungsten cathode heated to produce electrons, which after passing through an annular anode are focussed by (electro) magnetics and then steered or rastered on the work piece surface by deflection coils. The electron beam can be pulsed by means of a biased grid beneath the cathode giving pulse durations of 50 μ s to 15ms. Pulsing avoids loss of power or deflection of the beam by vapour.

EBM is applied to a wide range of materials and the spot size (10 – 100 μ m) gives a high degree of precision as well as a good surface finish. There is little or no chemical and

thermal distortion and physical and ‘metallurgical’ damage is limited to the immediate vicinity of the machined area. A principle drawback is that the process has to be operated under high vacuum to avoid attenuation of the beam by air molecules.

4.1.3. Laser Machining or Laser Beam Machining (LBM)

Since their invention in 1960, lasers have been used for a wide range of applications including the cutting, drilling machining and welding of many different types of material [Rizvi and Apte 2002, Meijer 2004]. LASER stands for Light Amplification by Stimulated Emission of Radiation. Lasers produce intense beams of coherent light in the form of photons. In principle, light produced by a laser should be completely polarised and coherent (both temporally and spatially), but in practice there is some spread in frequency/wavelength.

A laser consists of three main components:

- An energy (or pump) source– typically a pulsed xenon or krypton arc light (known as a flash tube or flash lamp) or a diode laser
- Gain (or lasing) medium in which photons are emitted and amplified
- An optical resonator to concentrate photons in standing waves in a longitudinal direction (usually mirrors – one completely reflective and one partially reflective)

Lasers can be classified according to the type of laser medium (and sometimes according to laser power) which determines wavelength and power characteristics – gas (including excimer), dye, solid state, metal vapour, chemical, semiconductor (including diode).

Most laser machining is carried out on relatively soft, low melting point or weakly bonded materials for example some non-ferrous metals, semiconductor and other electronic materials, polymers and rubbers. Laser beams are focussed and directed by optical lenses and material is removed by ablation; that is molecules are disassociated and vaporised without melting. For high melting point or highly bonded materials such as steels, superalloys, hard metals and ceramics, only gas and solid state lasers will produce sufficient power for ablation of the material. Typical industrial lasers used in industry are shown in Figure 4.1.

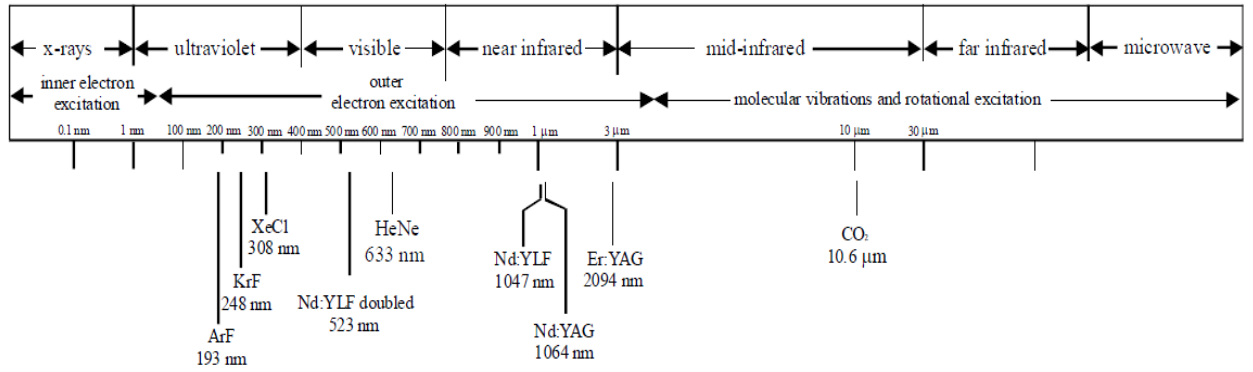


Figure 4.1: Typical Industrial Lasers used for different purposes [Karlicek 2011]

- Gas Lasers
 - Excimer Lasers (wavelength: 193-351nm)
 - CO₂ Lasers (wavelength: 10.6μm)
- Solid state lasers
 - Nd doped crystals and glasses
 - Yttrium aluminium garnet Nd-YAG (1.064μm)
 - Yttrium lithium fluoride Nd-YLF (1.047μm)
 - Yttrium orthovanadate Nd-YVO₄ (1.064μm)

Of the gas types, CO₂ lasers have the highest power but the long wavelength makes them less suitable for micro machining while Excimer lasers have low wavelengths but insufficient power for ablating ceramics.

Neodymium doped solid state lasers can produce high power densities and are more flexible. Wavelengths can be shortened by using optical devices which can double, triple or quadruple the frequency of the beam (also referred to as 2nd, 3rd or 4th harmonic generation). Furthermore it is possible to generate short, high energy pulses by Q-switching and mode-locking. Pulse times of the order of nanoseconds are typical.

4.2. Laser Machining of Missing Material Defects

In the present study, laser micromachining was used for the production of controlled missing material surface defects. It was thought that ultrasonic machining would be less likely to produce reproducible holes of the required shapes and dimensions. Although fine

wire could be used for tooling, the depths of holes would be considerably less than the normal tool-work piece distance of 0.1mm. Also there is a tendency for tapering of cavity walls with this process. Electron beam machining has promise but the spot size is usually of the same magnitude as the required hole diameters. Due to melting, it is common for a re-solidified layer to form on the shoulder of a hole. Laser machining is more flexible in operation since it does not require a vacuum and there are many optical and beam steering devices available for machining very small features. In particular an optical trepanning unit [Karnakis 2005] can be used for holes. With this, the beam is first focussed at the centre of the hole and then spirals outwards until the correct diameter has been machined. This technique gives sharp and vertical edges.

4.2.1. Laser Machining of Holes

Machining of missing material in the form of holes was carried out by Laser Micromachining Limited (LML), St Asaph, Wales. A (laser) diode pumped Nd-YVO₄ solid state laser (DPSS) was used with 3rd harmonic generation to give a shorter wavelength. The inside view of the workstation is shown in Figure 4.2.

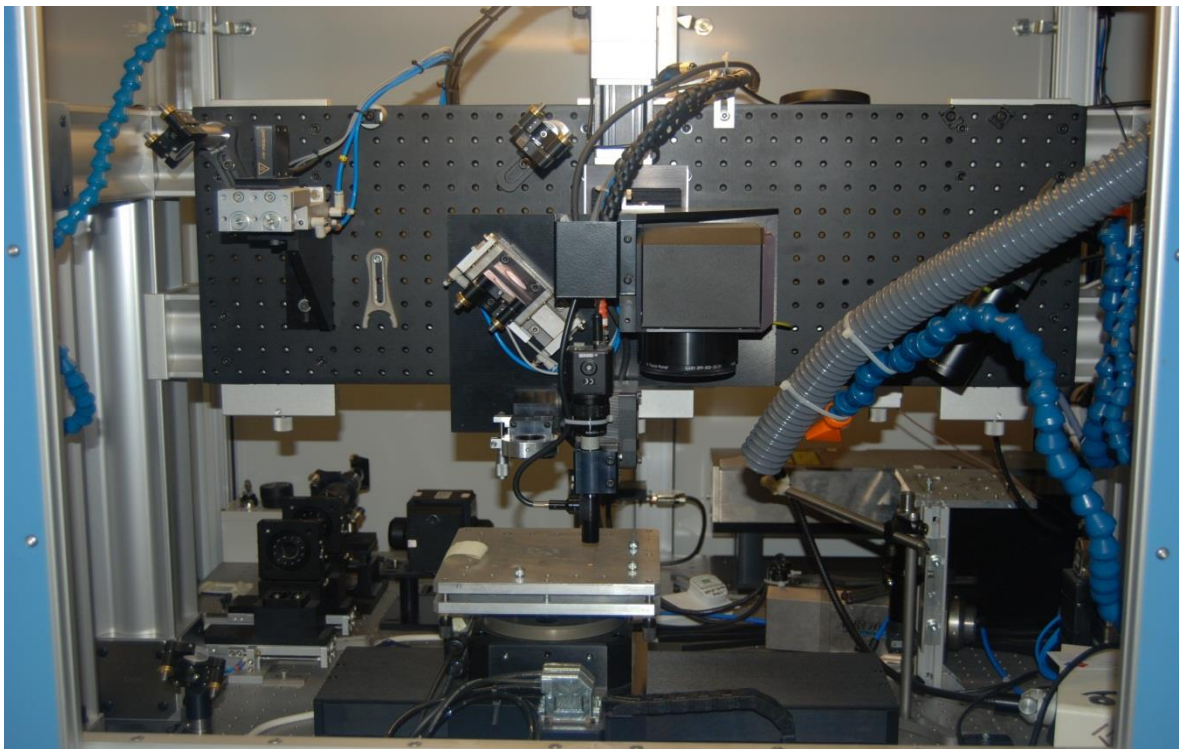


Figure 4.2: Laser Workstation (courtesy: Laser micromachining Limited, UK)

This unit was operated with the following parameters:

- Wavelength : 355nm
- Maximum power: $P = 10W$
- Pulse repetition rate = $R = 30k-100kHz$
- Single pulse ablation depth = $d = 100-200nm$
- Laser focal spot diameter: $\omega = 20\mu m$

The laser beam was focussed and converged by mirrors and other optical devices and holes were produced by optical trepanning. Machining was controlled by computer and the quoted accuracy was $1\mu m$. Care was taken to ensure a smooth base to the cavity and that the walls were vertical.

Three shapes were considered for laser machining with different dimensions of diameter and depth (some natural missing material shapes and depth are shown in Appendix F). Depths observed in natural missing material defects (Category 3 stars, Chapter 3.1) were in the range from $4-11\mu m$. The proposed shapes for the holes to be machined are shown in Figure 4.3. Two holes (diametrically opposite) were machined into each silicon nitride test sample with both holes having the same nominal dimensions and shape.

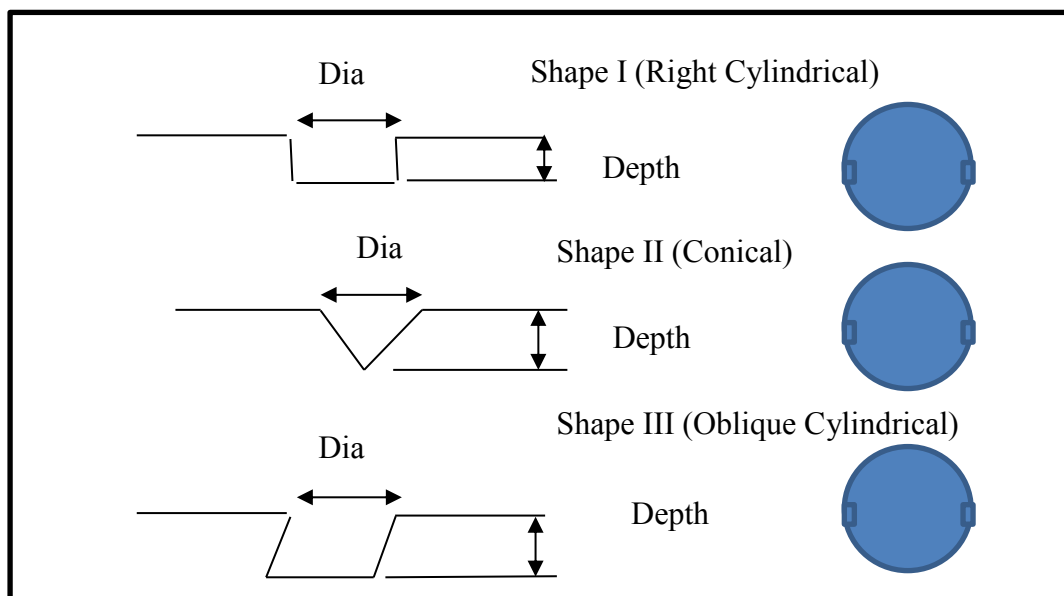


Figure 4.3: Proposed shapes for laser machining

Details of the shape and dimensions of holes machined into test balls made from Material A are given in Appendix J.

At a later stage, balls made from Material B were also machined but only with Shape I holes. The machining process was slightly modified to improve the bottom corners of the cavities. Details of dimensions of holes machined into Material B balls are given in Appendix J.

Shape of typical missing material is shown in the Figure 4.4.

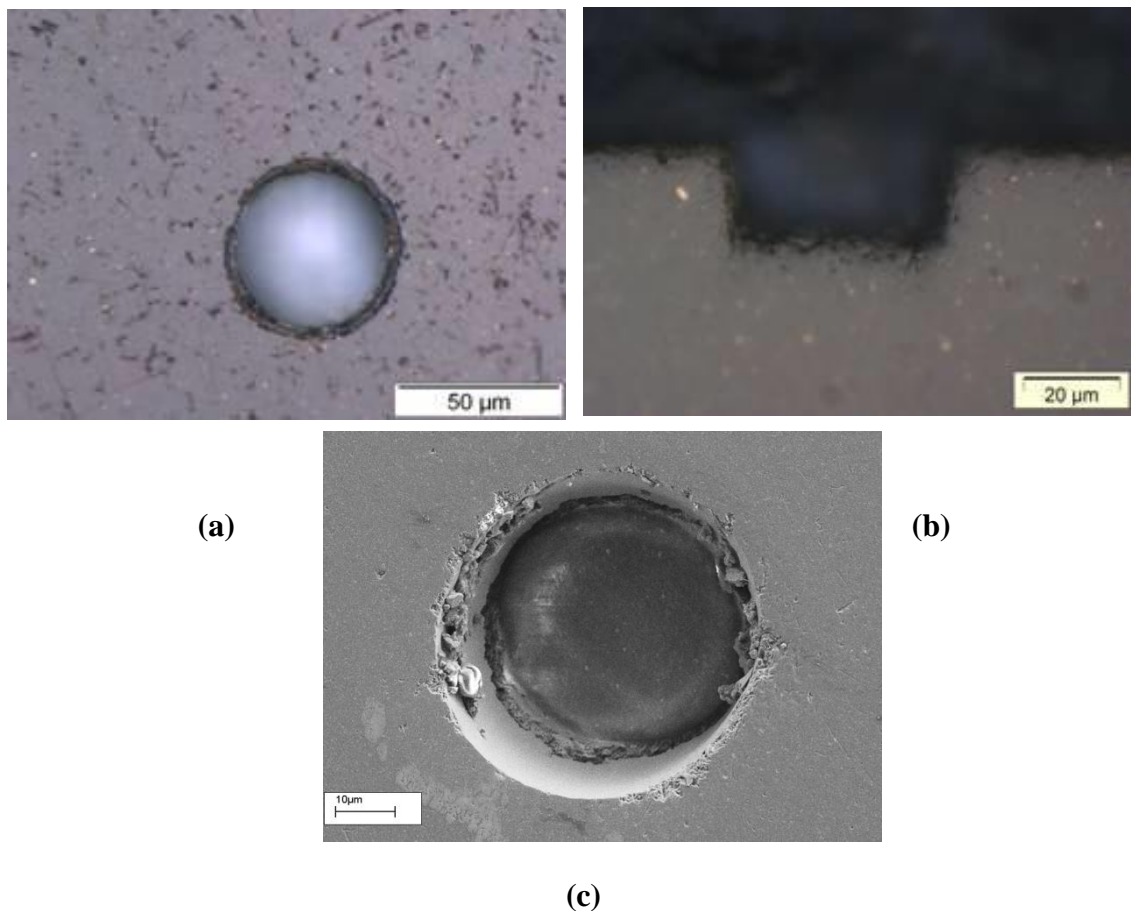


Figure 4.4: Typical laser machined hole (a) Optical microscopy – top view (b) optical microscopy – cross-sectional view (c) Scanning electron microscopy

4.2.2. Laser Machining of Slots

Some balls (Material A) had slots machined on the surface to simulate linear types of missing material (i.e. gouges). This meant that in RCF testing there would be no hydrostatic effects due to entrapped fluids. Machining of slots or trenches was done by

Clark-MXR, Dexter, Michigan, USA. This company has developed, and specialises in, ultrafast laser technology based on Ti-sapphire (titanium-sapphire) solid state lasers and Yb-doped (Ytterbium doped) fibre lasers. ('Ultrafast' in this context refers to the duration of pulses and not the repetition rate). Ti-sapphire lasers have wavelengths in the red and near-infrared range (600 – 1100nm) and can be self modelocked to give extremely short pulses in the femtosecond range. Yb-fibre lasers have a longer wavelength of 1550 nm, usually frequencies doubled to 775nm and are also modelocked. Using a technique known as chirped pulse amplification, the delivered power density is very high. (Chirped pulses are spread out in time by gratings or prisms and then rise in intensity to a maximum to avoid damage to optical components). Short high energy pulses are very effective in ablating materials and are claimed to give sharper edges [Dausinger et al. 2003].

Some parameters of the Clark-MXR CPA 2101 IMPULSE Workstation used for the machining or trenching of slots are as follows (full details are in Appendix K) :

- Wavelength : 775nm
- Pulse duration : 100 – 200fs
- Repetition rate : 1 kHz
- Pulse energy : 0.8mJ

The workstation had a fully controllable system in 3-axes which allowed positioning to a nominal accuracy of 1 μm . Slots or trenches approximately 2mm in length and 4 to 10 μm in depth were machined on a number of silicon nitride balls. The profile/shape classification was the same as for the holes (Fig.4.4) – a rectangular slot or right cylindrical (shape I), a V-groove or conical (shape II) and an angled slot or oblique cylindrical (shape III). Two diametrically opposed slots were machined on each ball. Dimensions of the slots are given in Appendix J.

4.3. Summary

In this chapter, a brief comparison is provided for different micromachining techniques to produce artificial missing material type of defects within silicon nitride surface. Based on relatively less collateral damage (and quoted accuracy) of laser micromachining, this technique was considered for micromachining. Parameters to machine silicon material to produce artificial cavities and missing material shapes are also highlighted in this chapter. Full details of cavities (holes and slots) for both material A and B are given in Appendix J.

Chapter 5 Experiments on Missing Material

Natural star surface features having major surface pits and flaking were an important feature within silicon nitride balls (chapter 3). Natural star features were converted into missing material features after few million stress cycles. Techniques to produce artificial missing material defects were discussed in chapter 4. Extensive experiments were conducted on artificial surface defects and are discussed in this chapter. Two different classes of material were used to investigate RCF in rolling contact subject to surface missing material. Three different shapes were selected (as discussed in chapter 04) for missing material machining (material A). Majority of experiments are conducted on shape I (right cylindrical) but few experiments are also conducted on shape II (conical) and shape III (oblique cylindrical), which are discussed in this chapter. A full guide to the various rolling contact experiments is shown in a chart format in Appendix L.

The main experimental variables were :

- *Hole (or slot) profile – Shapes I, II and III*
- *Diameter (or width) – 50, 75 and 100 μ m*
- *Depth – 10, 20, 30 μ m (and few 5 and 50 μ m)*
- *Materials – Class A and Class B*
- *Contact pressure – 3.8, 4.2, 4.5 and 4.8 GPa*

Thin mineral oil was used as lubricant for all the experiments in artificial missing material experiments as it was found relatively less effective in case of star feature experiments. All experiments were conducted at a spindle rotational speed of 7500rpm and bulk oil temperature of 75°C. This temperature of 75°C was considered for this experimental research programme as normal operating conditions for ball bearings are 60°C to 71°C for electric motor, average maximum temperature is 82°C for fan, 38°C to 82°C for pumps, 71°C to 82°C for gear drives¹.

Pre- and post-experiments surface analysis of the samples/silicon nitride balls using OM, WLI and SEM has also been discussed. Replicas were also taken to confirm profiles and base geometry.

¹<http://www.maintenanceresources.com/referencelibrary/bearings/common.htm>

5.1. Experiments on Shape I (Holes) – Material A

Majority of experiments conducted on missing material cavities are using shape I (right cylindrical) cavities and material A. In shape I experiments, precisely laser drilled hole/cavity was under observation; however, few experiments are also conducted on slot/notch to observe hydrostatic pressure effect. These experiments are further sub divided into small hole, medium hole and large hole experiments.

5.1.1. Small Hole Experiments (50 μ m diameter)

Rolling contact experiments are done on small hole cavities at low contact pressure (3.8GPa), high contact pressure (4.8GPa) and intermediate contact pressure (4.5GPa). Low and high contact pressures experiments are listed in Table 5.1. Small hole experiments conducted at intermediate pressure (4.5GPa) are listed in Table 5.2. Some experiments are also conducted using sharp corners cavities and are detailed in Table 5.3.

The first experiment on a hole 50 μ m diameter and 10 μ m deep was run in steps of 30 million stress cycles at increasing loads/contact pressures of 3.8, 4.2 4.5 and 4.8 GPa. The experiment was suspended after 120 million cycles with no spalling failure (successfully completed). During this experiment the steel balls were replaced after each step of 30 million cycles and the lubricant was replenished. Pre- and post-experiment surface analysis was conducted after carefully cleaning the surfaces in ultrasonic bath arrangement (as discussed in chapter 2). Figure 5.1 shows images of the original hole and after 120 million cycles. There was some edge wear and erosive wear observed on the leading edge, but there was no evidence of more serious damage or change. FPI was also conducted post experiment to check any sign of crack initiation from cavity base but there was no sign of crack at the base. EDS analysis is also performed on the leading side (erosive part) of the defect to find chemical composition. Details are given in section 5.8 (EDS).

The remaining experiments in the first series with small holes are listed in Table 5.1. Since the first experiment had not failed, the contact pressure was raised to 4.8GPa for experiments 02 and 03 which also were shallow depth (10 μ m) to confirm (support the results of first experiment) the defect tolerance at this high load.

Experiment 02 was suspended (successfully completed) after 30 million cycles to check for cracks, erosive wear and tribolayers under the higher contact stress. Due to sensitivity of the defect nature, surface analysis was performed at regular interval of 3million stress cycles. However, little change was observed in the post-test inspection (Fig. 5.2).

Table 5.1: Experiments conducted on small diameter hole (Shape I/right cylindrical) at low and high contact pressures

Exp. ID	Ball ID	Contact Pressure (GPa)	Hole Dimensions (μm)	Stress Cycles (10^6)	Outcome
<i>Exp. 01</i>	B03H01	3.8GPa up to 30 4.2GPa 31-60 4.5GPa 61-90 4.8GPa 91-120	Dia: 50 Depth: 10	Total: 120	<i>Completed</i>
<i>Exp. 02</i>	B03H02	4.8	Dia: 50 Depth: 10	30	<i>Completed</i>
<i>Exp. 03</i>	B31H01	4.8	Dia: 50 Depth: 10	100	<i>Completed</i>
<i>Exp. 04</i>	B26H01	4.8	Dia: 50 Depth: 20	5	<i>Spalling</i>
<i>Exp. 05</i>	B27H01	4.8	Dia: 50 Depth: 20	46*	<i>Stopped</i>
<i>Exp. 06</i>	B28H01	4.8	Dia: 50 Depth: 20	50**	<i>Stopped</i>
<i>Exp. 07</i>	B29H01	4.8	Dia: 50 Depth: 20	3	<i>Spalling</i>
<i>Exp. 08</i>	B29H02	4.8	Dia: 50 Depth: 20	7	<i>Spalling</i>
<i>Exp. 09</i>	B30H02	3.8	Dia: 50 Depth: 20	100	<i>Completed</i>
<i>Exp. 10</i>	B21H01	3.8	Dia: 50 Depth: 30	100	<i>Completed</i>
<i>Exp. 11</i>	B22H01	3.8	Dia: 50 Depth: 30	100	<i>Completed</i>
<i>Exp. 12</i>	B23H01	4.8	Dia: 50 Depth: 30	6**	<i>Stopped</i>
<i>Exp. 13</i>	B23H02	4.8	Dia: 50 Depth: 30	6.5	<i>Spalling</i>
<i>Exp. 14</i>	B21H02	4.8	Dia: 50 Depth: 30	100	<i>Completed</i>
<i>Exp. 15</i>	B22H02	4.8	Dia: 50 Depth: 30	7	<i>Spalling</i>

*: Experiment stopped due to surface rotation in the collet

** : Experiment stopped due to crack net/incipient spall on the ball

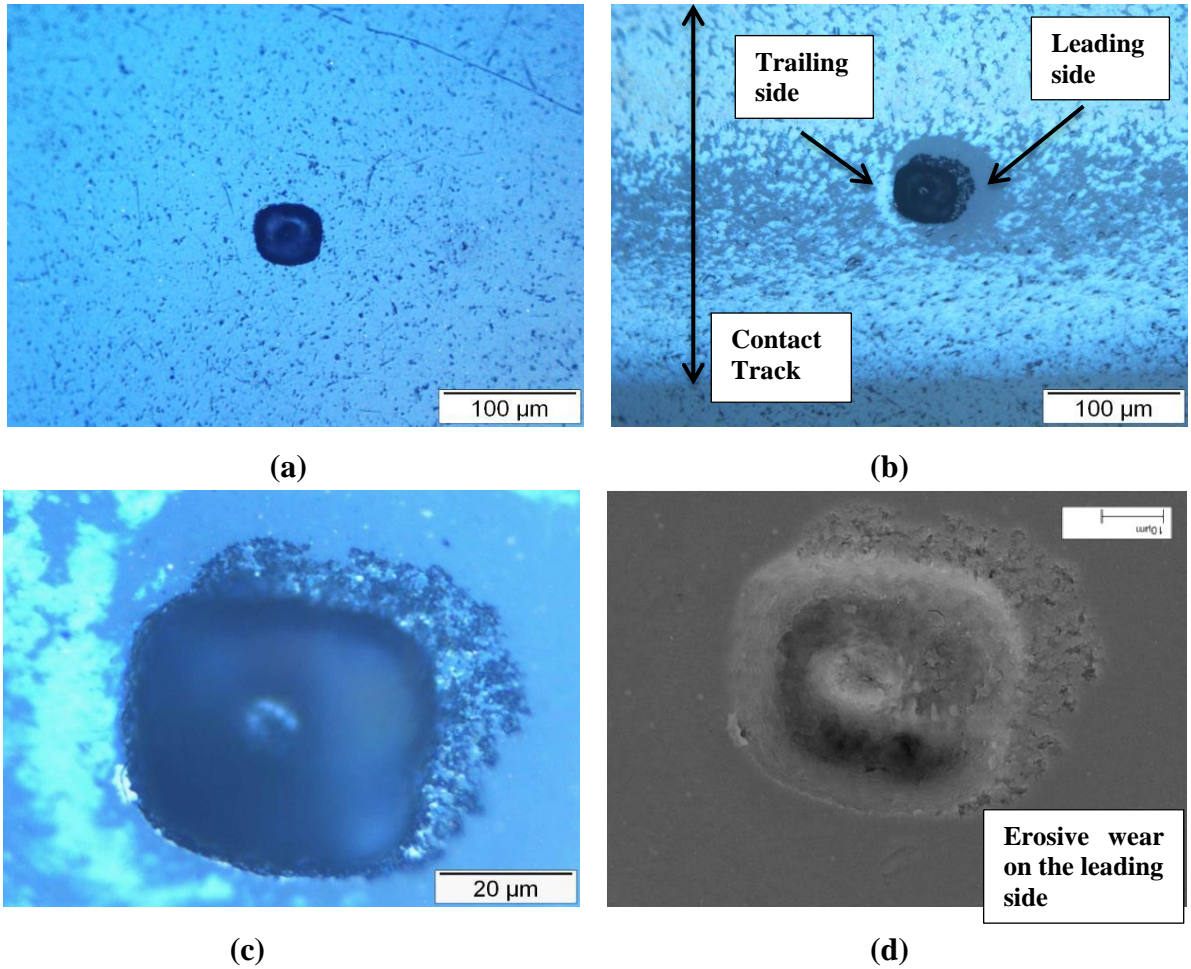


Figure 5.1: Experiment 01 (a) pre-experiment (b) post experiment (120M) (c) post-experiment- higher magnification OM image (d) post experiment SEM image

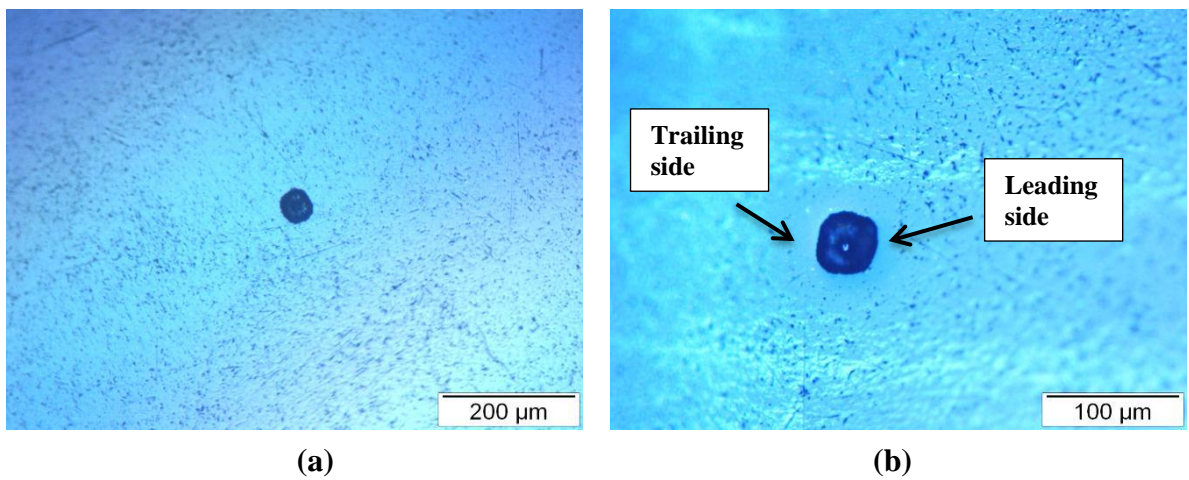


Figure 5.2: Experiment 02 (a) pre-experiment (b) post-experiment (30M) OM image

Experiment 03 was therefore allowed to run to completion (100 million cycles). Figure 5.3 shows the hole before testing. It can be seen that the base of the hole was not flat, having a notch in one location. Although in the Figure, vertical scale is μm and horizontal measurement are taken in mm, therefore, it seems that there is long notch on one side of the hole. Hole profile shown in the Figure (5.3) is showing at certain position where line is drawn, it might have different profile at other locations. (This type of profile was observed with other holes and is discussed in more detail in next section). Post surface analysis using light microscopy is shown in the Figure 5.4 which does not showing any sign of damage, cracks or significant wear.

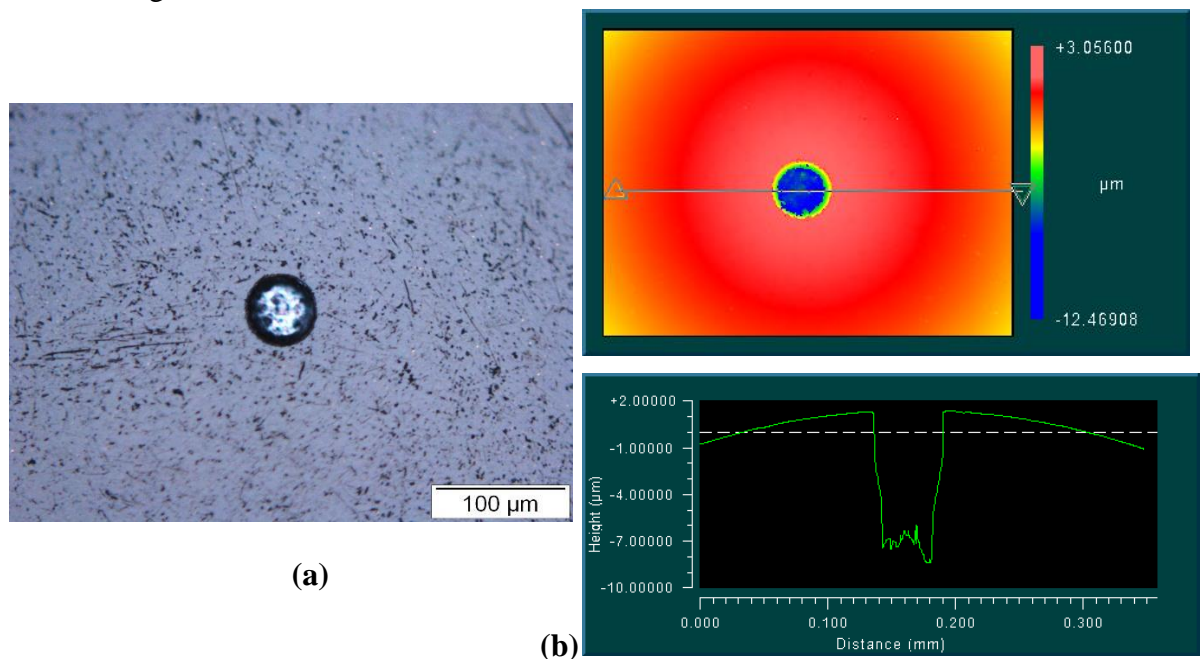


Figure 5.3: Pre-experiment (03) surface analysis using (a) microscopy (b) interferometry

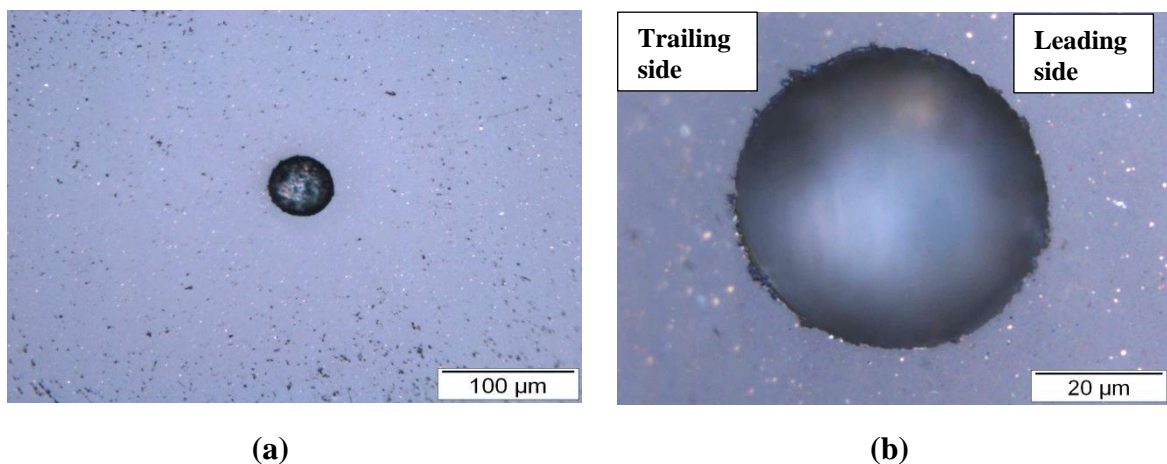


Figure 5.4: Post-experiment (03, 100million stress cycles) surface analysis using microscopy (a) low magnification (b) higher magnification

It can be concluded that holes less than 50 μm in diameter and 10 μm deep can tolerate RCF at contact pressures up to 4.8GPa without suffering significant damage for stress cycles up to 100millions.

In the second phase of small hole experiments (exp. 04 to 09), tests were conducted on the more deeper cavities of 20 μm to compare effect of depth on the rolling contact fatigue of silicon nitride. Experiment 04 was stopped just after 5million stress cycles due to failure/spalling. Pre- and post-experiment surface analysis is shown in the Figure 5.5-5.6.

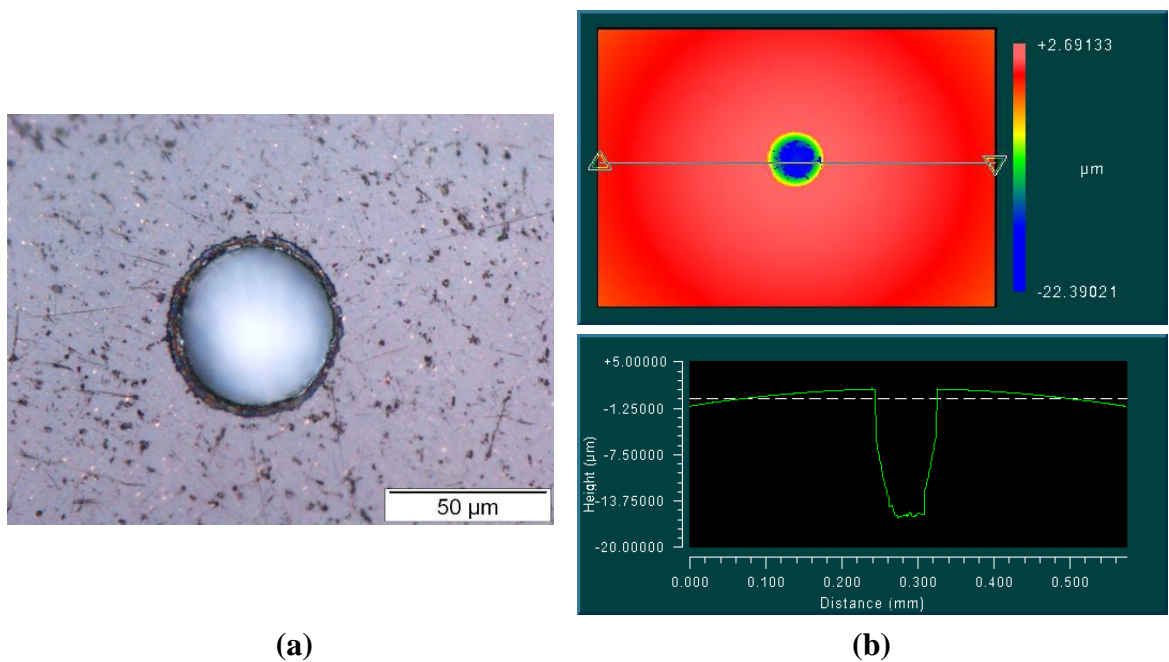


Figure 5.5: Pre-experiment (04) surface analysis using (a) microscopy (b) interferometry

Post-experiment surface analysis shows crack might had started from the hole base and travelled to leading and trailing side. Maximum depth found was 45 μm on the trailing side and spall length was 840 μm . Although base profile of this sample's cavity was relatively smoother than previous experiments but due to deeper cavity, it triggered failure process. Four more experiments were also conducted at this high contact pressure of 4.8GPa on these small hole of 50 μm diameter with depth of 20 μm . Most of the experiments resulted into spalling but few experiments are also suspended due to sample rotation within collet and to capture crack networks (incipient spalls). Details of these experiments are given below.

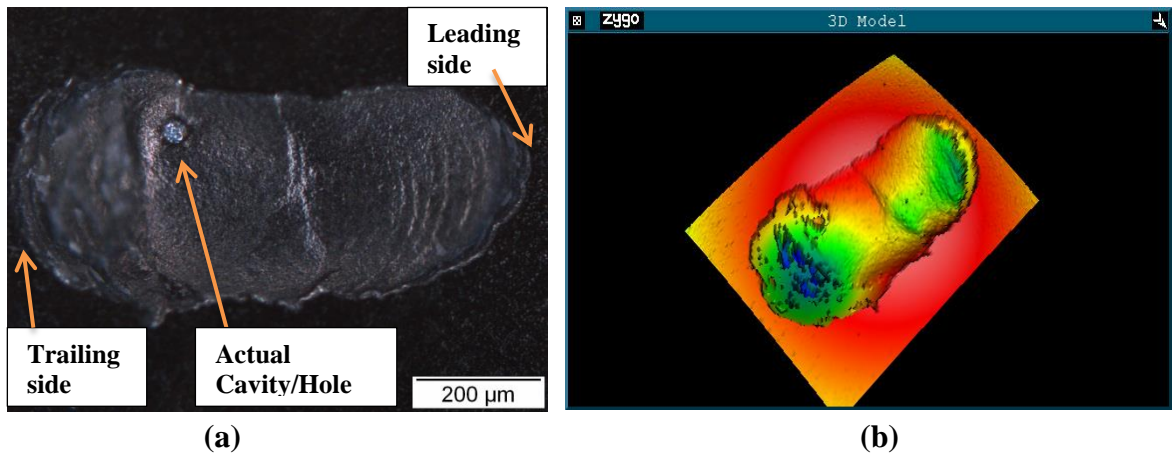


Figure 5.6: Post-experiment (04) analysis using (a) microscopy-dark field (b) 3D-surface mapping using interferometry

Experiment 05 was stopped after 46million stress cycles when rotation in the collet observed. Pre-experiment and pre-rotation samples are shown in the Figure 5.7.

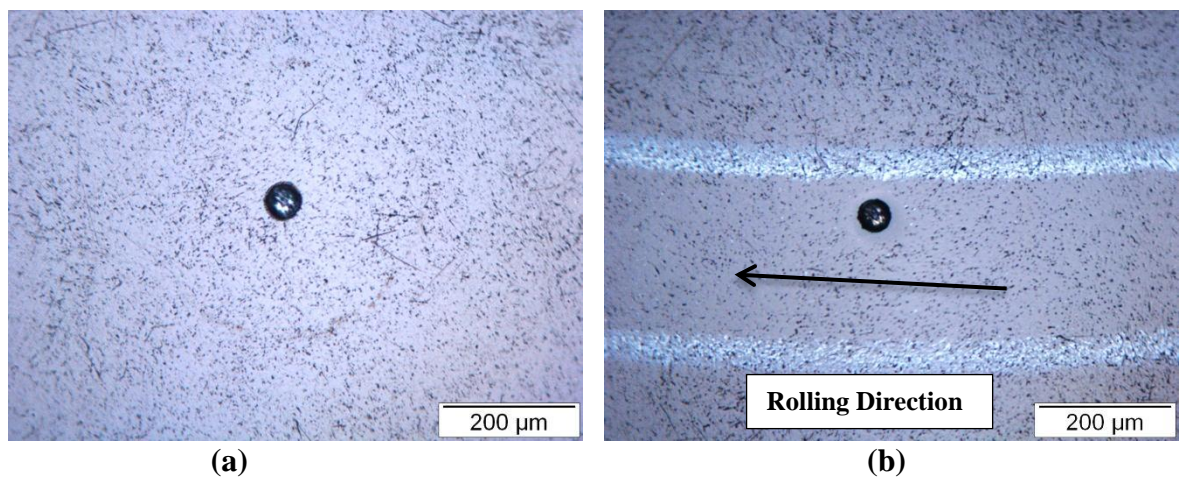


Figure 5.7: Surface analysis using microscopy (experiment 05) (a) pre-experiment (b) post-experiment

Experiment 06, conducted at high contact pressure of 4.8GPa, again suspended post 50 million stress cycles due to incipient spalls/crack networks on the surface. The secondary cracks on the leading edge of the hole clearly constitute an incipient spall.

Pre- and post-experiment surface analysis is shown Figure 5.8. Cross sectioning analysis of this test sample is discussed in failure mechanism section (5.9.3).

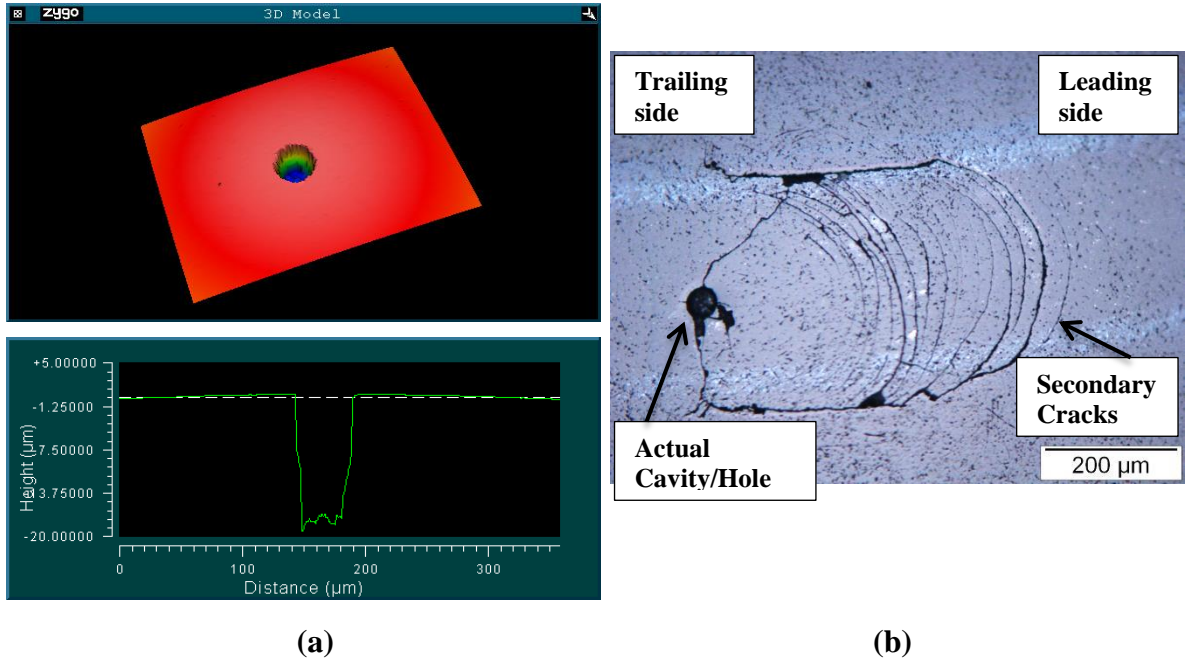


Figure 5.8: Surface analysis (experiment 06) (a) pre-experiment analysis using light interferometry (b) post-experiment analysis using light microscopy

Two more experiments (exp. 07 and 08) are also resulted in failure/spalling after 3 and 7 million stress cycles respectively. Figure 5.9 is showing post spalling surface analysis of experiment 07, where remnants of secondary cracks are visible on the leading edge side.

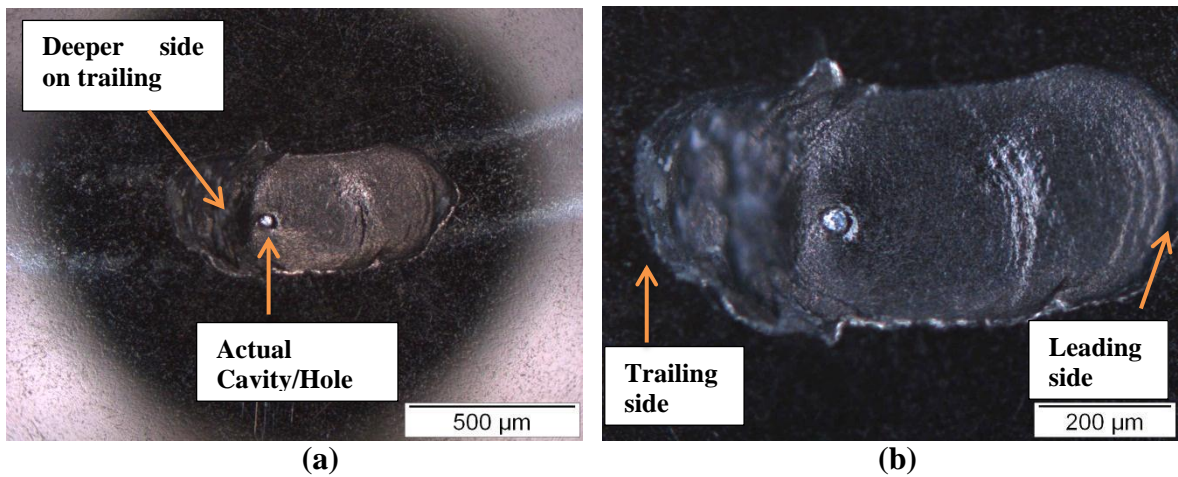


Figure 5.9: Surface analysis (experiment 07) (a) post-experiment analysis using light microscopy-dark field (b) post-experiment analysis using light microscopy-dark field

Figure 5.10 is showing pre- and post-surface mapping by white light interferometry (experiment 8). The original hole is represented by a flat area in the centre (right) giving a reference depth of 20 μm .

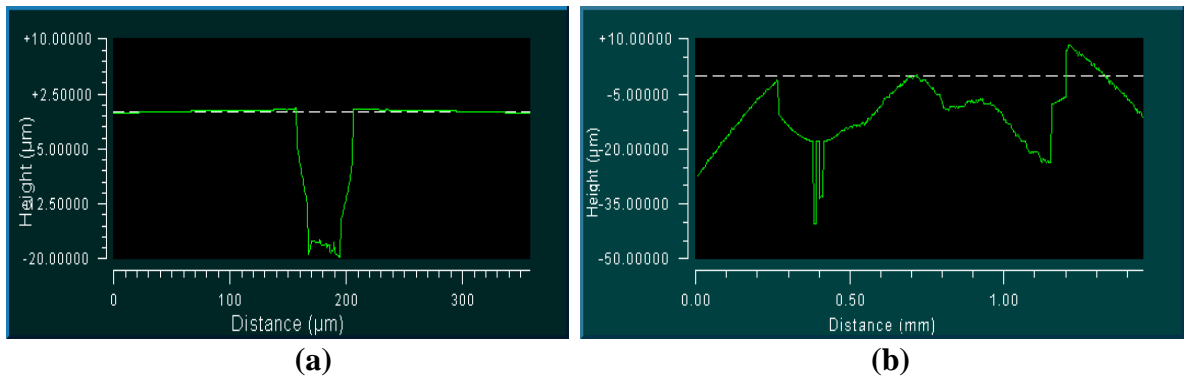


Figure 5.10: Surface mapping (experiment 08) using interferometry (a) pre-experiment (b) post-experiment

Similar trend was observed in both experiments 07 and 08, i.e., deeper spalling side was on trailing edge and relatively shallow side was on leading edge of rolling direction. This trend is supporting the failure mechanism as seen in the experiment 04 and 06 with same pressure and similar defect size. Maximum spall depths found in both cases were around 55 μm and 45 μm respectively. Total spall length was around 880 μm and 885 μm in experiment 07 and 08 respectively.

Since small diameter holes with depth 20 μm had either failed by spalling or showed an incipient spall at a nominal contact pressure of 4.8GPa, the load was reduced to give 3.8GPa in experiment 09. This test was suspended after 100 million cycles without any observable features. Pre- and post-experiment surface analysis of sample surface is shown in the Figure 5.11. So, small diameter cavities can be tolerable for low nominal contact pressure of 3.8GPa without any major damage/failure.

Finally, holes of nominal depth 30 μm were tested in experiments 10 to 15. The first two experiments, 10 and 11, were conducted on balls with deeper holes (30 μm) at low contact pressure of 3.8GPa. Again, both experiments ran for 100 million cycles without any spalling. Only some minor edge wear was observed.

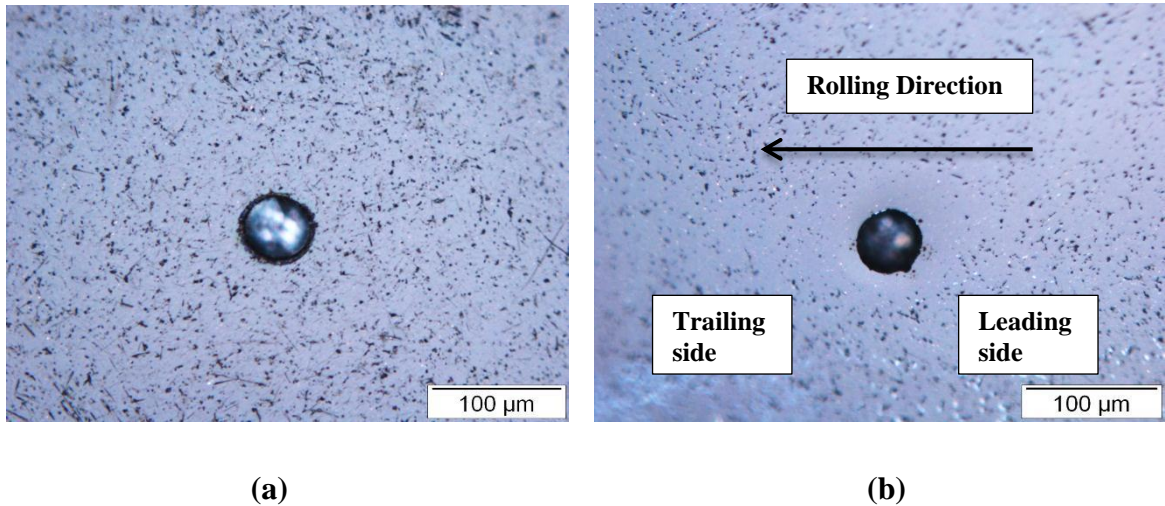


Figure 5.11: Surface analysis using microscopy (experiment 09) (a) pre-experiment (b) post-experiment

Pre surface analysis is shown in the figure 5.12, showing hole base profile (experiment 10).

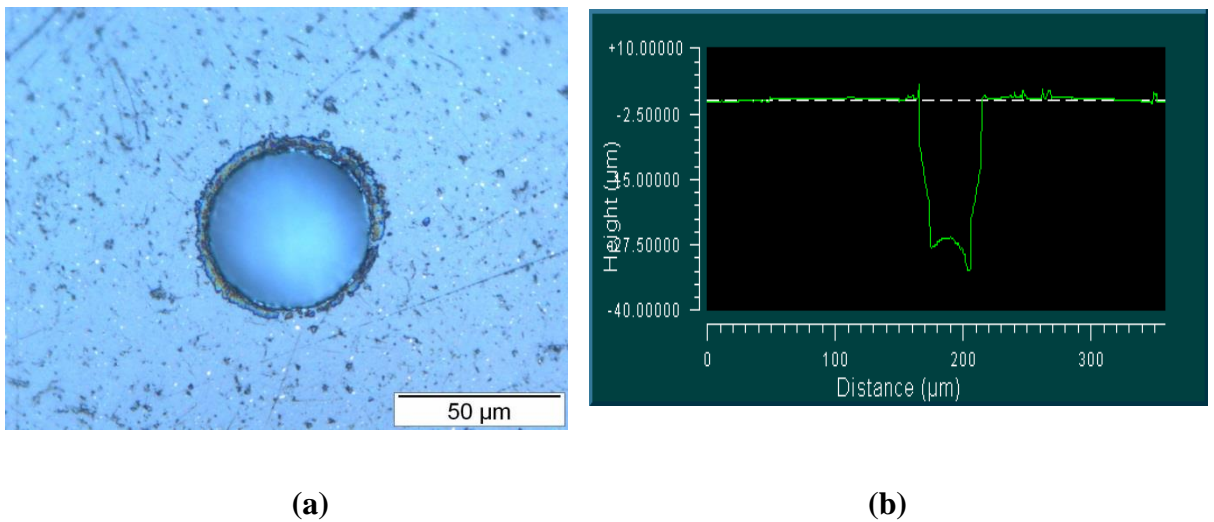


Figure 5.12: Pre-experiment surface analysis/mapping (experiment 10) (a) using light microscopy (b) using interferometry

Although surface mapping was done by light interferometry in pre-experiment stage, showing sharp edge/notch on one side of the cavity but still this test was completed up to 100million stress cycles without any failure. Surface analysis was conducted during the experiment after every 20million stress cycles to observe any crack/incipient spall. Post-experiment surface analysis (Figure 5.13) is showing surface wear on the contact track. There was no sign of any crack from the surface or from the hole base.

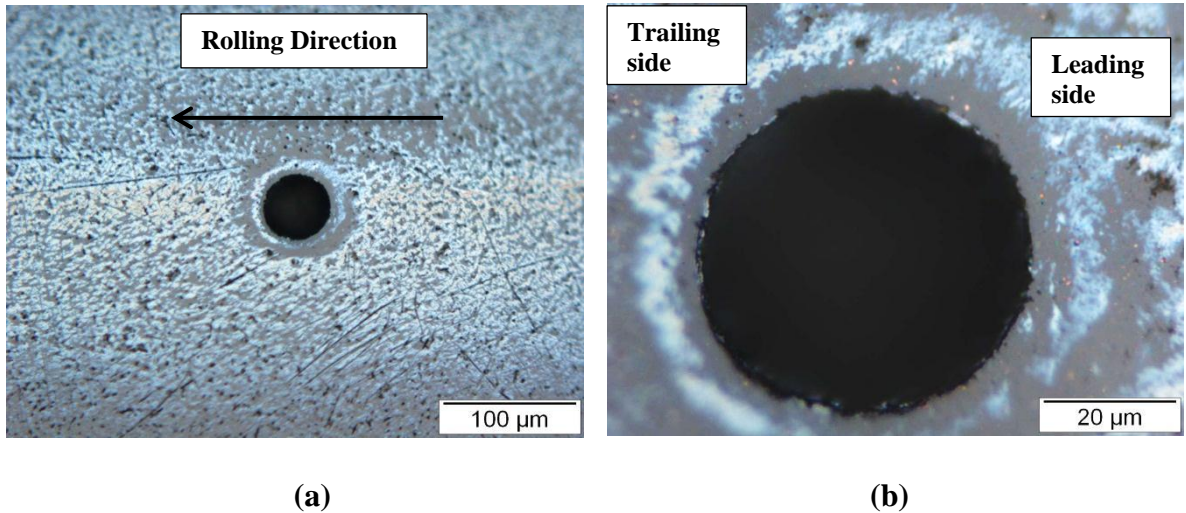


Figure 5.13: Post-experiment surface analysis (experiment 10) using microscopy (a) low magnification (b) higher magnification

Pre-experiment surface analysis is shown in the Figure 5.14 for experiment 11.

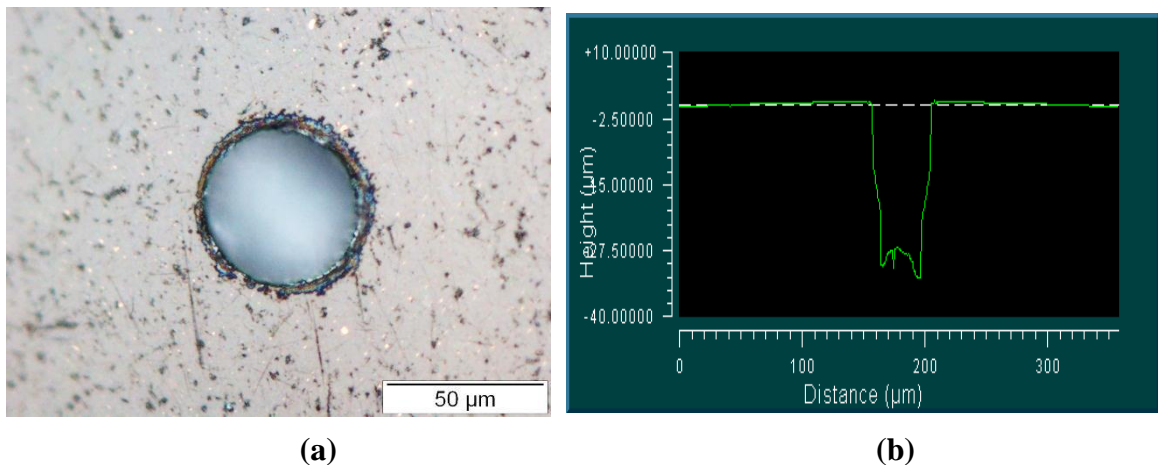


Figure 5.14: Pre-experiment surface analysis/mapping (experiment 11) (a) light microscopy (b) interferometry

Pre-experiment surface analysis is showing hole base is of similar profile with previous experiment sample, having sharpness on one side of the base. More wear on the contact track especially around cavity edges/edge wear was found (Figure 5.15) like in experiment 01. Hole was centrally located on the track as in the case of last experiment (experiment 10). Lubricant's marks are also visible in the post surface analysis (Figure 5.15). Materials debris were also found in the cavity but there was no sign of any failure or incipient spall.

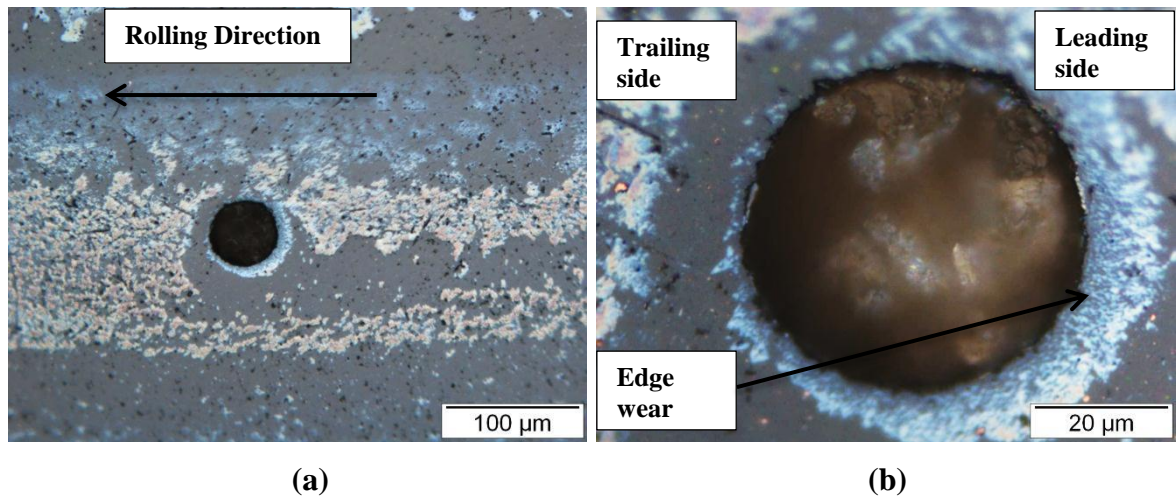


Figure 5.15: Post-experiment surface analysis (experiment 11) using microscopy (a) low magnification light illumination (b) high magnification-light illumination

After confirming the tolerance at low contact pressure, four further experiments on 30 μ m deep small diameter holes were then run at the higher contact pressure of 4.8GPa. Three of these led to spalling or incipient spalling after low numbers of stress cycles. Pre- and post-experiment surface analysis is shown in the Figure 5.16 and 5.17 (experiment 12). Experiment was stopped post 6million stress cycles due to crack network/incipient spall on track. Secondary cracks can be seen on the leading edge of the cavity. Cross sectioning analysis is presented in the failure mechanism section (at the end of this chapter).

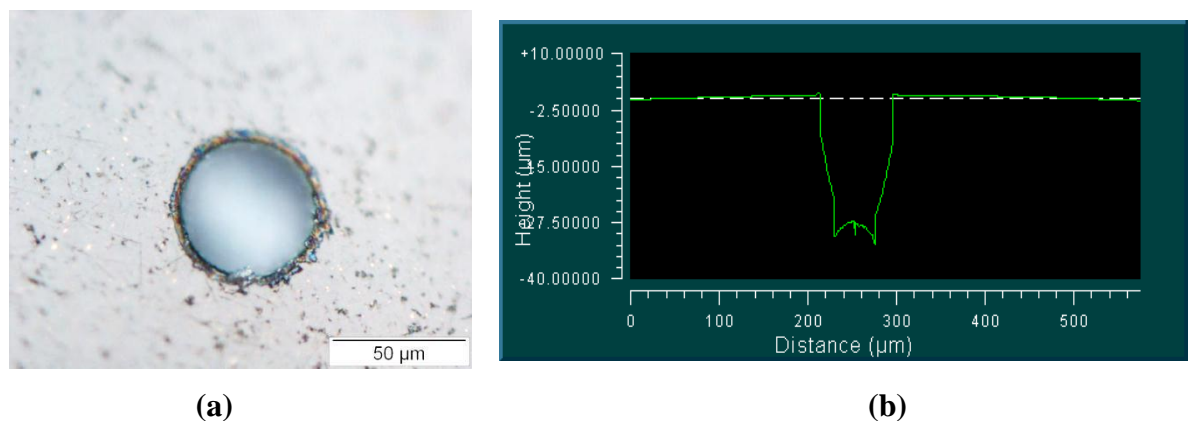


Figure 5.16: Pre-experiment surface analysis/mapping (experiment 12) (a) using light microscopy (b) using interferometry

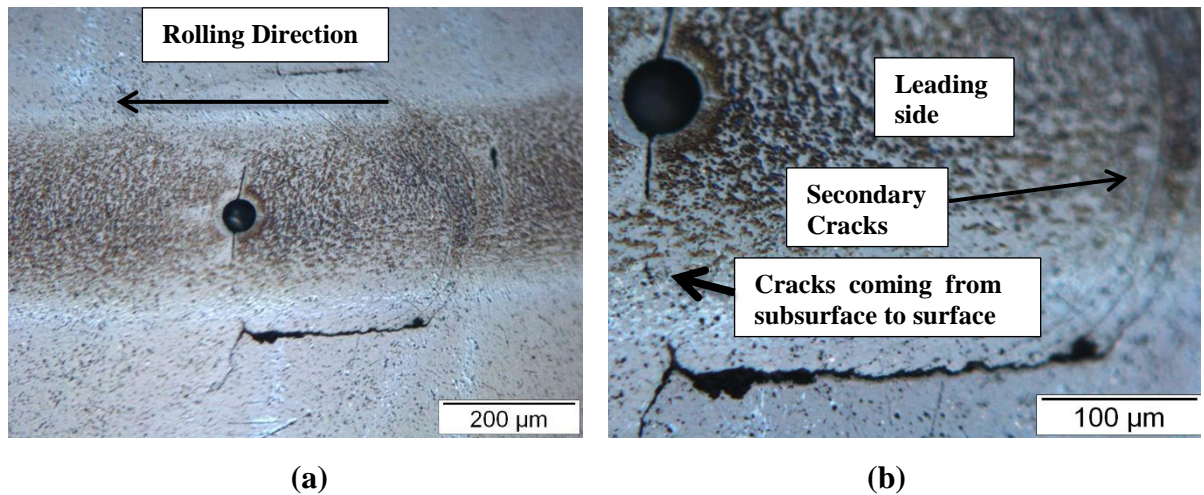


Figure 5.17: Post-experiment surface analysis (experiment 12) using microscopy (a) low magnification light illumination (b) high magnification-light illumination

Spalling was observed in the second experiment (experiment 13) of this series (Figure 5.18). After 6.5million stress cycles, a full scaled spall/failure triggered the machine stopped. Spall total length was 860μm and maximum depth was 70μm on the trailing side.

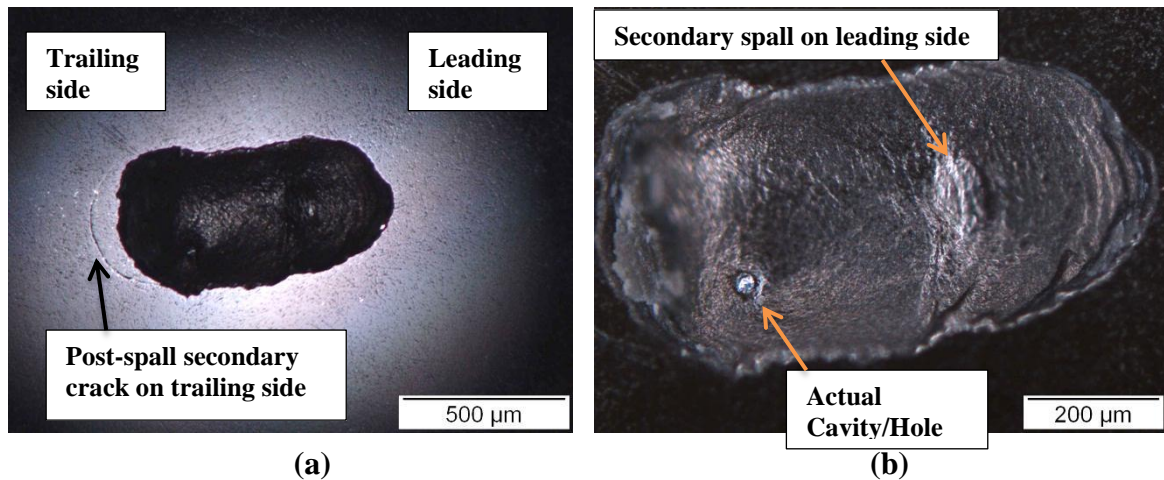


Figure 5.18: Post-experiment surface analysis (experiment 13) using light microscopy-dark field (a) lower magnification (b) higher magnification

On the leading side of rolling direction, it can be seen that there is another small spall that might happened after initial spall. On the trailing side, a secondary crack can be seen and few more over-rolling cycles may cause to take it off. Multi-spalling concept is discussed in detail in the section 5.1.3.

Although experiments 12 and 13 confirmed the failure in case of smaller diameter cavities with depth of 30 μm at the contact pressure of 4.8GPa, however, two further experiments were also conducted to fully understand failure mechanism and also to see any possibility of tolerance if the defect is not centrally located rather than placed somewhere close to contact track edges. Experiment 14 confirmed the defect tolerance till 100million stress cycles under same operating conditions except defect location on the track. Cavity was placed close to the track and also had better surface base profile. Figure 5.19 is showing pre- and post-experiment surface analysis of silicon nitride surfaces in experiment 14.

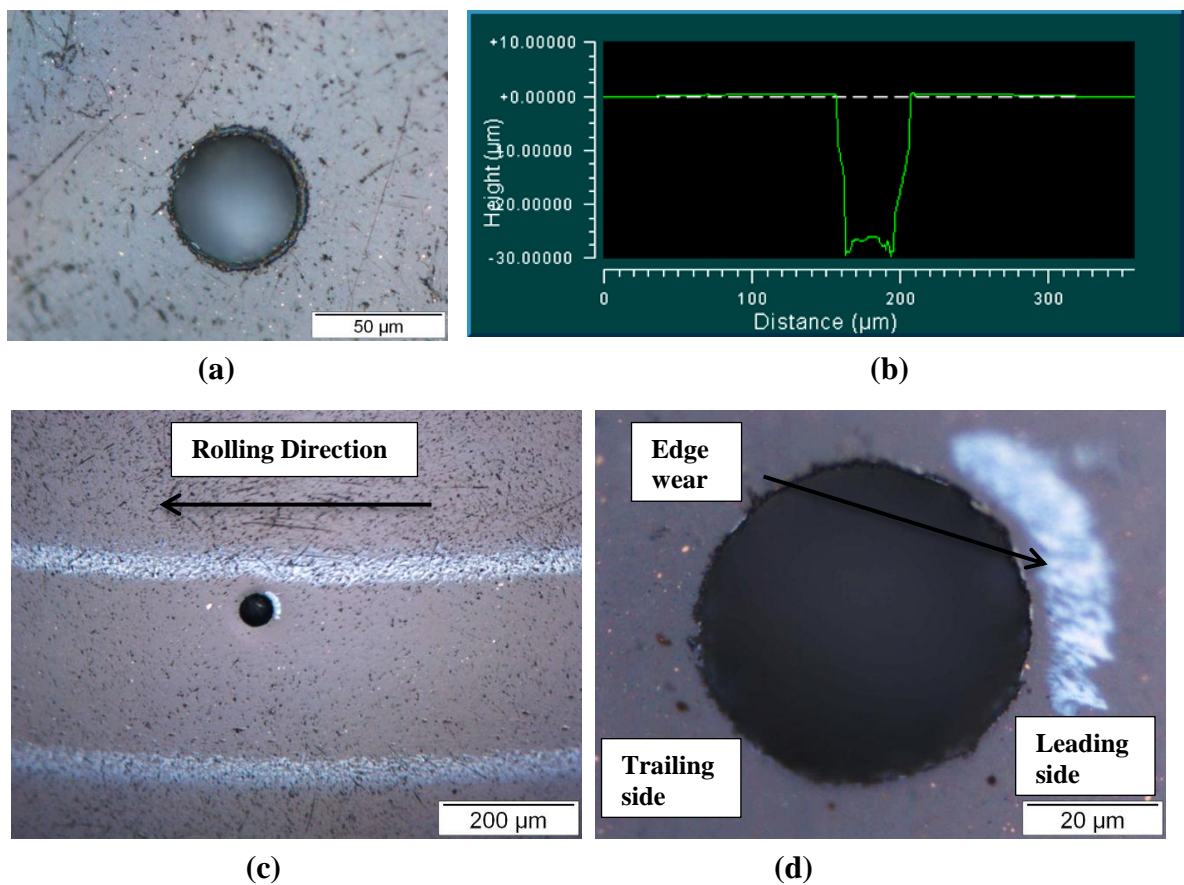


Figure 5.19: Surface analysis/mapping (experiment 14) (a) and (b) pre-experiment using microscopy and interferometry respectively (c) and (d) post-experiment analysis by microscopy

Defect located close to contact's track edges has less chance to fail due to less effective pressure (experiment 14); further study has been discussed in the section contact pressure effects. Experiment 15 resulted into spalling post 7million stress cycles. Pre- and post-experiment analysis is shown in the Figure 5.20.

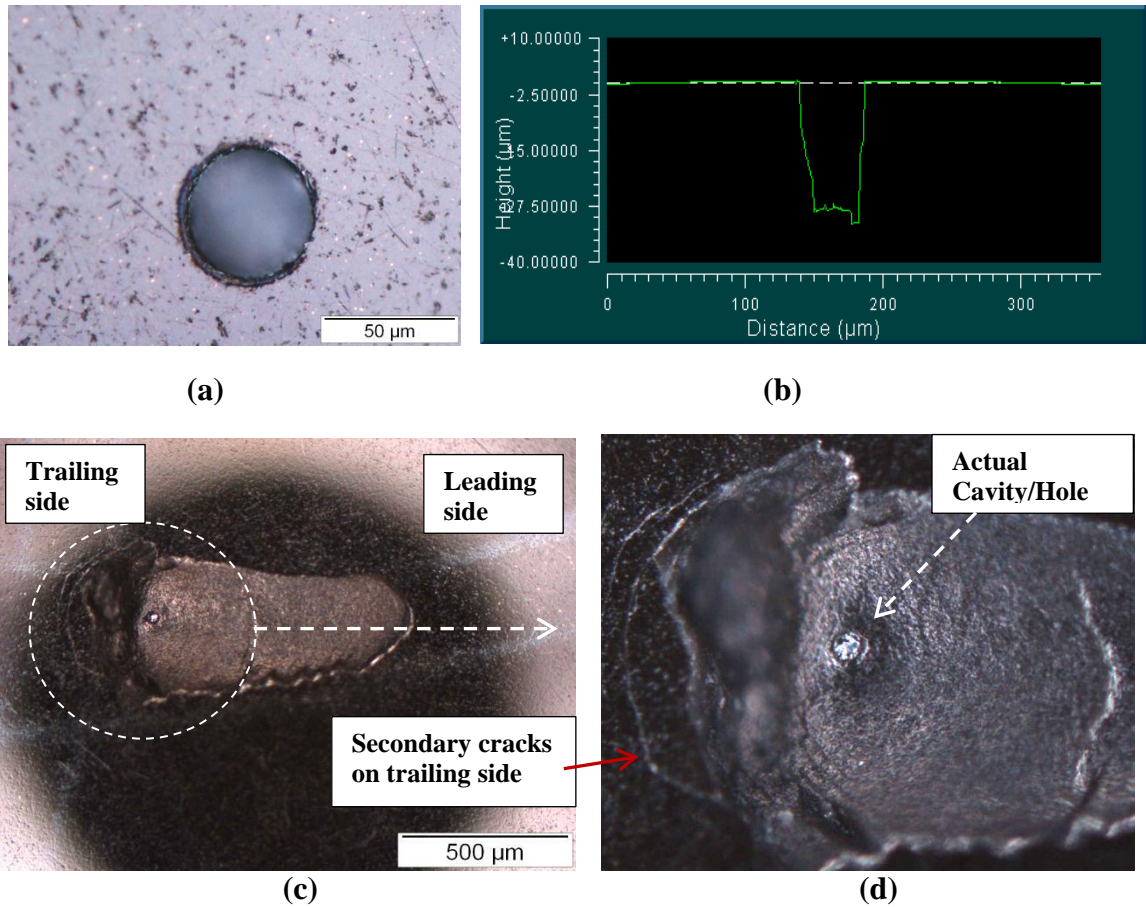


Figure 5.20: Surface analysis/mapping (experiment 15) (a) and (b) pre-experiment using microscopy and interferometry respectively (c) and (d) post-experiment analysis by microscopy

Spall's total length was $1070\mu\text{m}$ (including secondary cracks area on the trailing side) and maximum depth was around $40\mu\text{m}$. Secondary cracks on the trailing side are onset of further spalling or completion of current spall. Defect was centrally located in this case and crack travelled $750\mu\text{m}$ in the leading side and finally came to the surface. Failure mechanism is similar to previous experiments and is detailed in the section failure modes in missing material.

It has been now clearly established that smaller diameter hole with depth of $30\mu\text{m}$ would be tolerable for up to 100million stress cycles at low contact pressure whereas for high contact pressure, spalling would happen.

Further five experiments were conducted at intermediate pressures i.e., 4.5GPa with cavity of depth of 20 and $30\mu\text{m}$. These experiments are listed in table 5.2.

Table 5.2: Experiments conducted on small diameter hole (Shape I/right cylindrical) at Intermediate Pressure (4.5GPa)

Exp. ID	Ball ID	Contact Pressure (GPa)	Hole Dimensions (μm)	Stress Cycles (10^6)	Outcome
Exp. 16	B26H02	4.5	Dia: 50, Depth: 20	100	Completed
Exp. 17	B30H02	4.5	Dia: 50, Depth: 20	70	Spalled
Exp. 18	B24H01	4.5	Dia: 50, Depth: 30	100	Completed
Exp. 19	B24H02	4.5	Dia: 50, Depth: 30	100	Completed
Exp. 20	B25H01	4.5	Dia: 50, Depth: 30	100	Completed

This phase of experiments started from depth of $20\mu\text{m}$ cavities as shallow cavities were tolerable till 100million stress cycles for contact pressure up to 4.8GPa. This pressure was chosen as if rolling element material does not fail at this pressure then it would be less chances to fail at 4.2GPa. Experiment 16 suspended post 100million stress cycles, pre- and post-experiment surface analysis is presented in Figure 5.21-5.22.

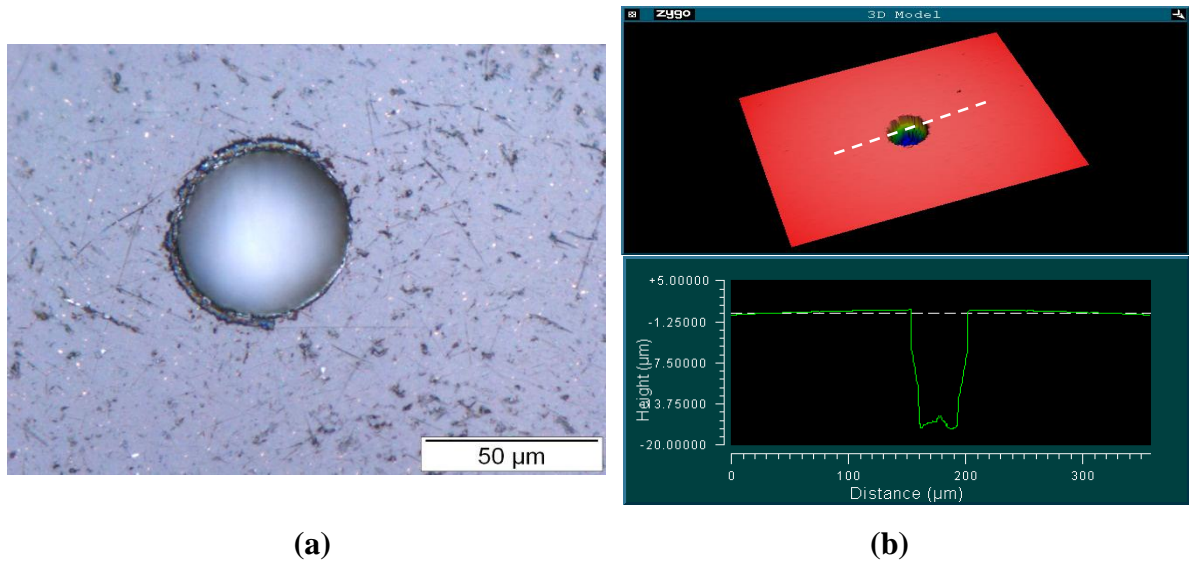


Figure 5.21: Pre-exp. (16) surface analysis/mapping using (a) microscopy (b) interferometry

Four out of the five experiments ran to completion at 100 million cycles without any significant damage or cracking in the hole region. Again, it was observed that some of the

holes were located off the centre line of the contact track possibly due to slight movement of the ball in the collet due to the high applied load and relatively low viscosity lubricant. The single failure (experiment 17) occurred after 70 million cycles. The spall showed regions of the shallow surface wear at both ends of the spall (Figure 5.23). This may have been due to a slight delay in the vibration sensor shutting down the machine.

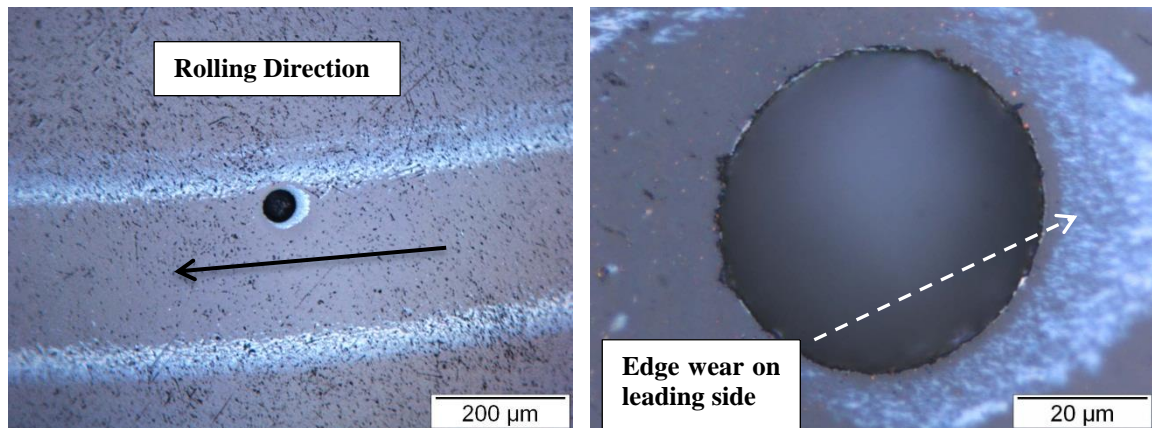


Figure 5.22: Post experiment (16) Surface analysis using microscopy

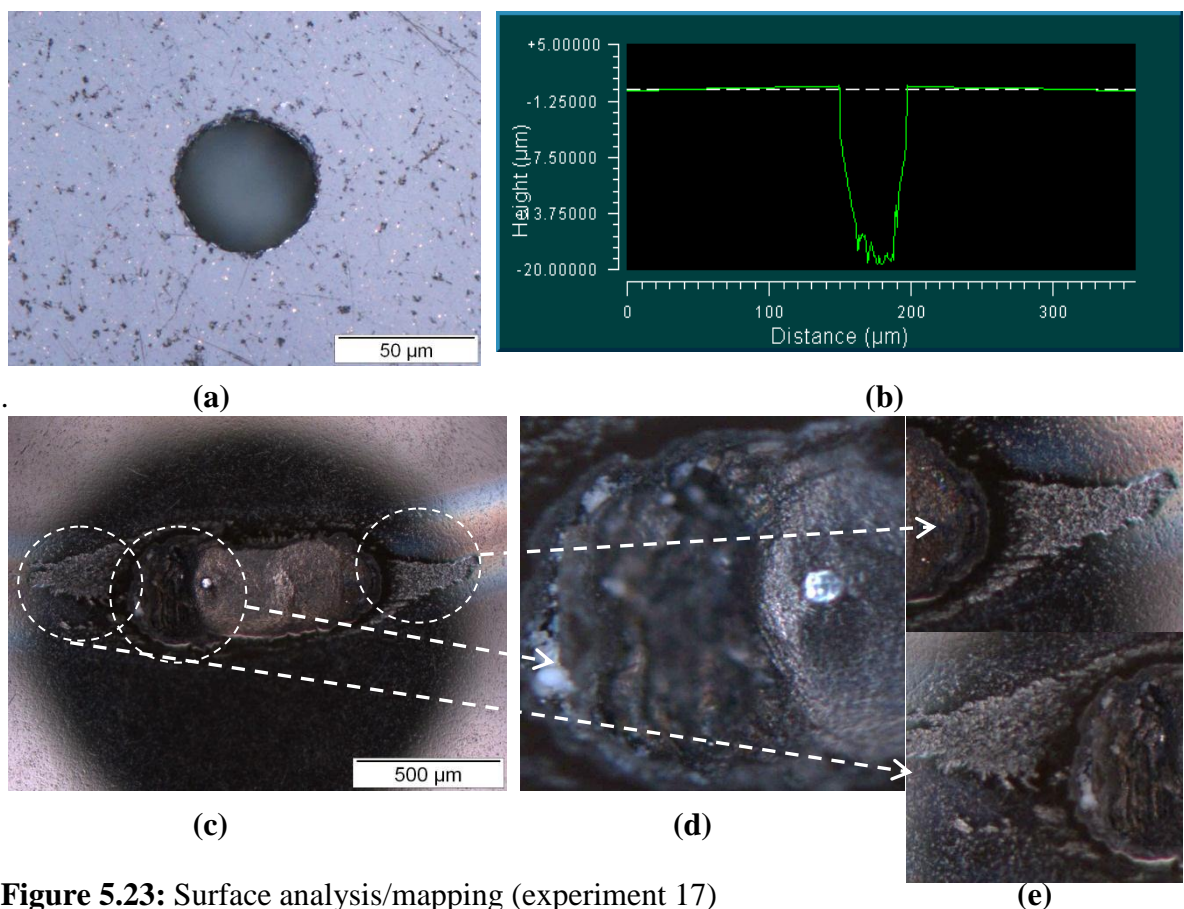


Figure 5.23: Surface analysis/mapping (experiment 17)

(a) and (b) pre-experiment using microscopy and interferometry respectively (c) post-experiment spalling (d) trailing side (e) delamination on leading and trailing side

Figures 5.24-26 showing the post experiment surface analysis for three further experiments (experiment 18-20), conducted using intermediate pressure of 4.5GPa, and on cavities of depth of 30 μ m. As it can be seen that these cavities were located off-centre or too close to contact edges and effective pressure around the cavities was less than the centre of the contact. This concept is discussed further in the section contact pressure effects.

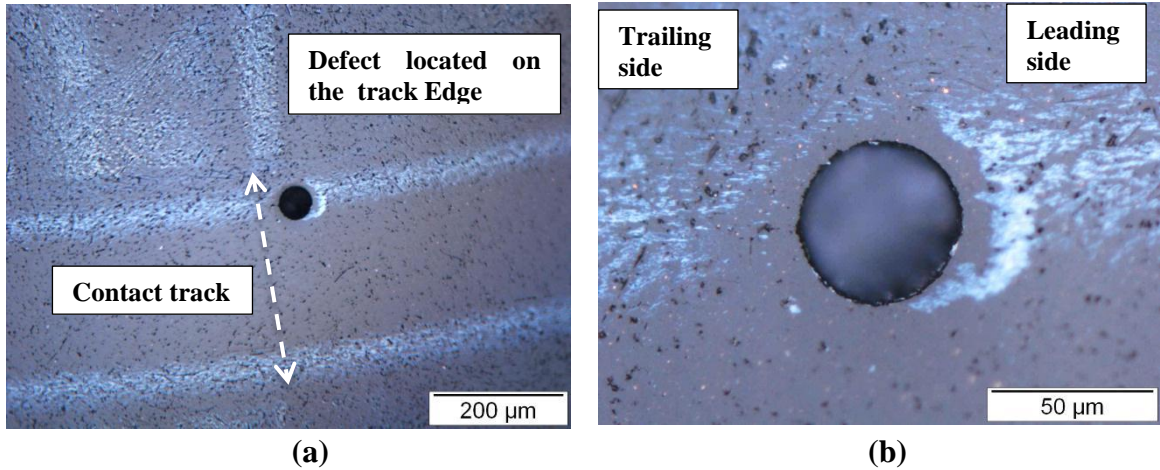


Figure 5.24: Surface analysis (experiment 18) using microscopy (a) low magnification (b) higher magnification

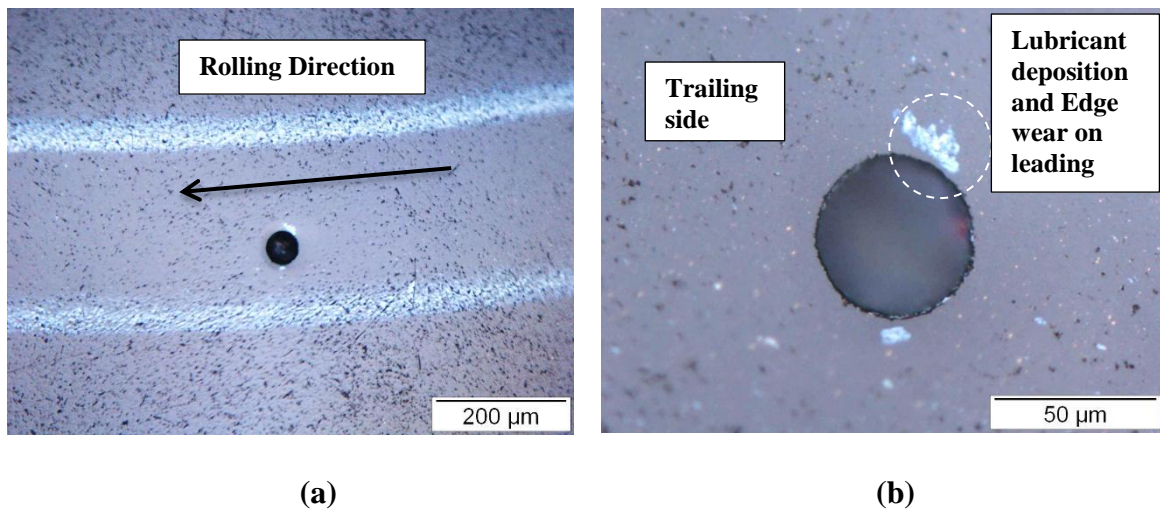


Figure 5.25: Surface analysis (experiment 19) using microscopy (a) low magnification (b) higher magnification

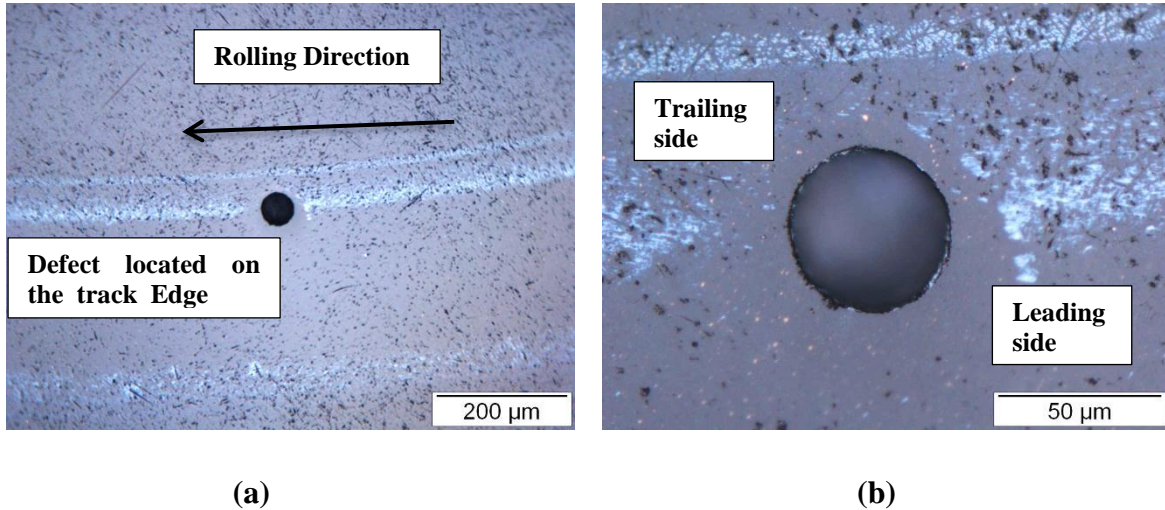


Figure 5.26: Surface analysis (experiment 20) using microscopy (a) low magnification (b) higher magnification

In order to study the hole base effects, two further experiments (exp. 21-22, listed in Table 5.3) were conducted by considering the 20 μ m depth cavities and running at high and low contact pressures. Both cavities had sharp edges/corners/notches and caused early failure (3million stress cycles). Pre- and post-surface analysis is showing (Figures 5.27-5.28) base profile in the pre-experiment and post 3million stress cycles spall. Spall obtained in experiment 21 (4.8GPa) is having little different pattern and depth than experiment 22 (3.8GPa) and more deeper than experiment 22. Similarly, trailing side was larger than the leading side in experiment 21 and it seems that it happened due to secondary spall on the trailing side and larger area on trailing side also gives some indication.

Table 5.3: Experiments conducted on small diameter hole (Shape I/right cylindrical) at low and high contact pressures with sharp base corners

Exp. ID	Ball ID	Contact Pressure (GPa)	Hole Dimensions (μ m)	Stress Cycles (10^6)	Outcome
Exp. 21	B15H01	4.8	Dia: 50, Depth: 20	3	Spalled
Exp. 22	B15H02	3.8	Dia: 50, Depth: 20	3	Spalled

Spall length was around 1mm and 700 μ m (without including secondary crack on trailing side) to 790 μ m (including secondary cracks area) in experiment 21 and 22 respectively.

Similarly maximum spall depth was around 100 μm for high load and 64 μm for low contact pressure of 3.8GPa

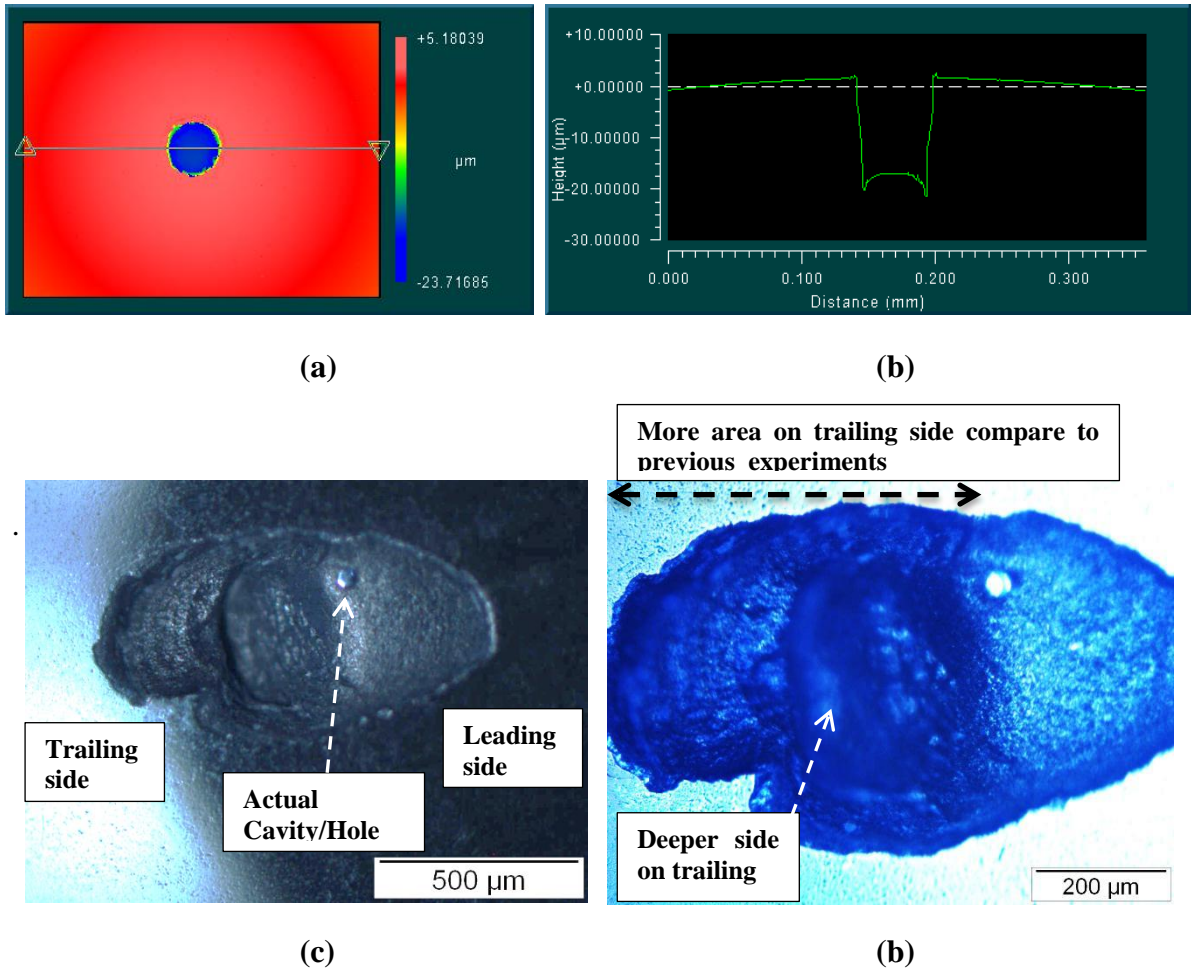


Figure 5.27: Experiment (21) surface analysis (a) and (b) pre-experiment using interferometry (c) and (d) post-experiment microscopy

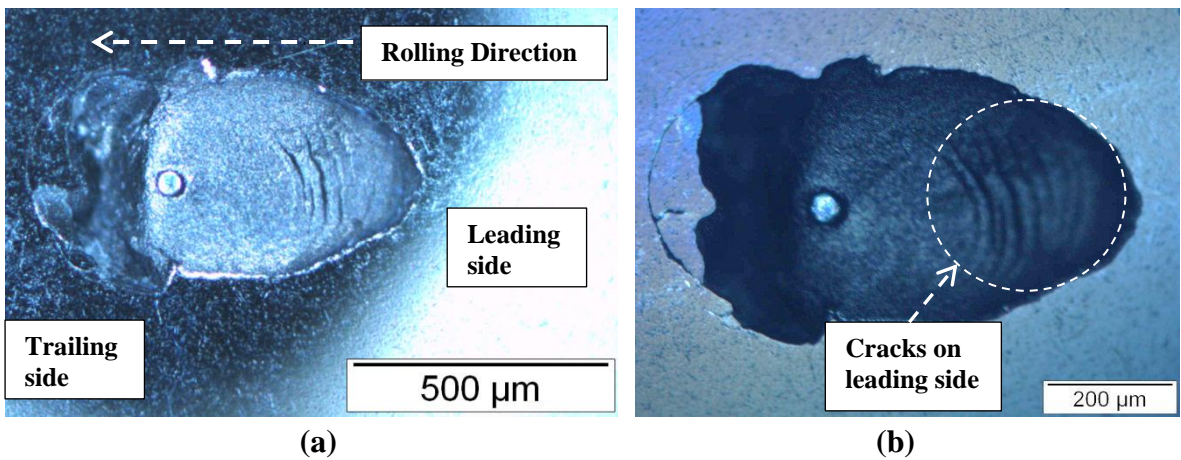


Figure 5.28: Post-experiment surface analysis (experiment 22) using microscopy (a) dark field illumination (b) light illumination (bright field)

So, after conducting large number of experiments on smaller diameter of 50 μ m for different pressure range (3.8GPa-4.8GPa), different depth range (10 μ m-30 μ m) and for different hole base profile, next phase of experiments started for medium hole (diameter = 75 μ m).

5.1.2. Medium Hole Experiments (75 μ m diameter)

In this phase of experimental programme, 8 tests were conducted on the ball samples having medium sized holes and are listed in Table 5.4. Depths of holes ranged from 5 μ m to 30 μ m and contact pressures were either 3.8 or 4.8GPa.

Table 5.4: Details of experiments on medium size holes (Shape I/right cylindrical)

Exp. ID	Ball ID	Contact Pressure (GPa)	Hole Dimensions (μm)	Stress Cycles (10^6)	Outcome
<i>Exp. 23</i>	B56H01	3.8	Dia: 75, Depth: 10	100	<i>Completed</i>
<i>Exp. 24</i>	B56H02	3.8	Dia: 75, Depth: 10	4	<i>Spalled</i>
<i>Exp. 25</i>	B57H01	3.8	Dia: 75, Depth: 10	100	<i>Completed</i>
<i>Exp. 26</i>	B57H02	3.8	Dia: 75, Depth: 10	20	<i>Spalled</i>
<i>Exp. 27</i>	B75H01	4.8	Dia: 75, Depth: 5	100	<i>Completed</i>
<i>Exp. 28</i>	B75H02	4.8	Dia: 75, Depth: 5	100	<i>Completed</i>
<i>Exp. 29</i>	B02H01	3.8	Dia: 75, Depth: 30	30	<i>Completed</i>
<i>Exp. 30</i>	B02H02	4.8	Dia: 75, Depth: 30	6	<i>Spalled</i>

First experiment (experiment 23) was conducted on the depth of 10 μ m and at contact pressure of 3.8GPa. This pressure was applied as small hole samples with depth of 10 μ m were not failing at this pressure and to check the effect of cavity diameter/extent on the defect tolerance. Surface analysis was conducted at post-experiment stage, is shown in the Figure 5.29, showing some edge wear on the leading side but no major damage was found.

Second test (experiment 24) was also run on the same operating conditions to verify the results but in this case, spalling observed post 4million stress cycles. Pre-experiment analysis (Fig 5.30) revealed that one side of the cavity is sharper than the other side so

more chances to start the crack, propagate and finally causing full scale spalling. Defect location on the track was close to the edge but it seemed that sharp edge was located towards the track centre and pressure difference on two opposite sides of the defect might have triggered this failure (Figure 5.31).

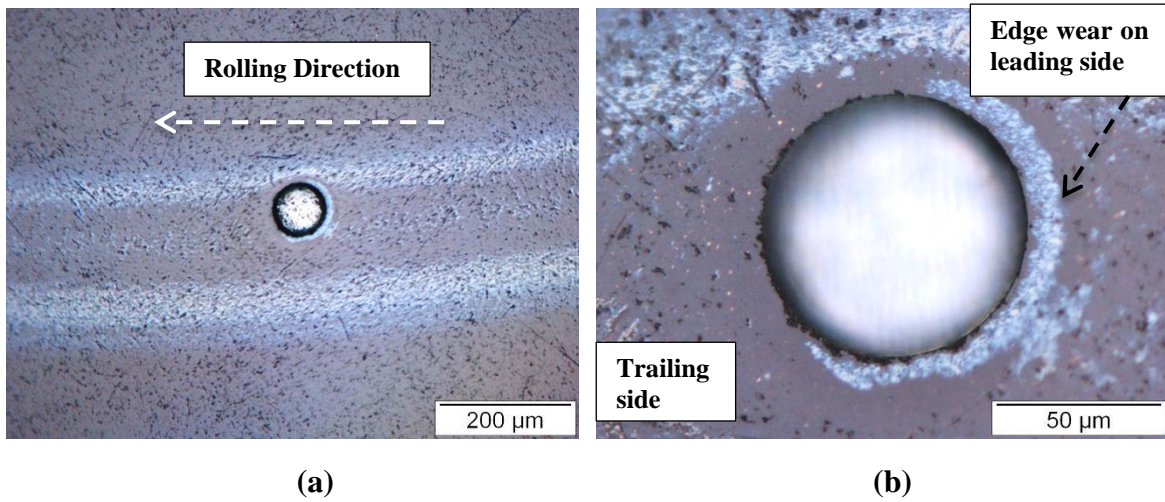


Figure 5.29: Post experiment surface analysis (experiment 23) using light microscopy (a) low magnification (b) higher magnifications

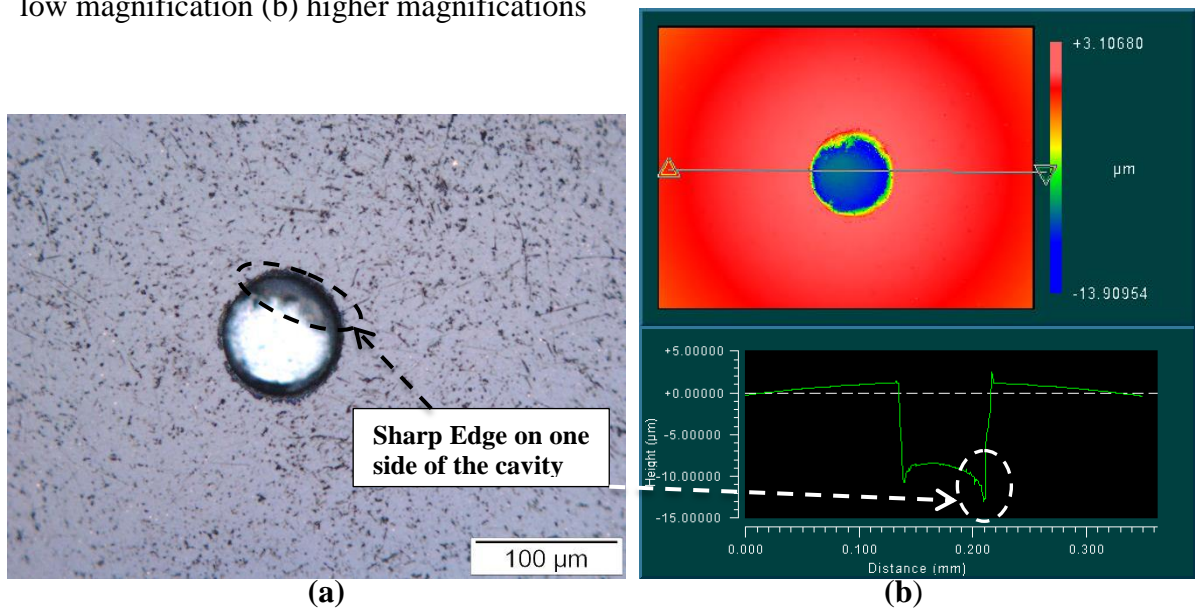


Figure 5.30: Pre-experiment surface analysis/mapping (experiment 24) using (a) microscopy (b) interferometry

Failure pattern (Figure 5.31) is similar to previous failure modes but this time machine was stopped before it getting full scale spall on the trailing side and hence maximum spall depth is much shallower than previous results. Secondary cracks causing deeper cavity on

the trailing side can be seen in post-test analysis. Maximum depth was around $40\mu\text{m}$ and total spall length was $628\mu\text{m}$.

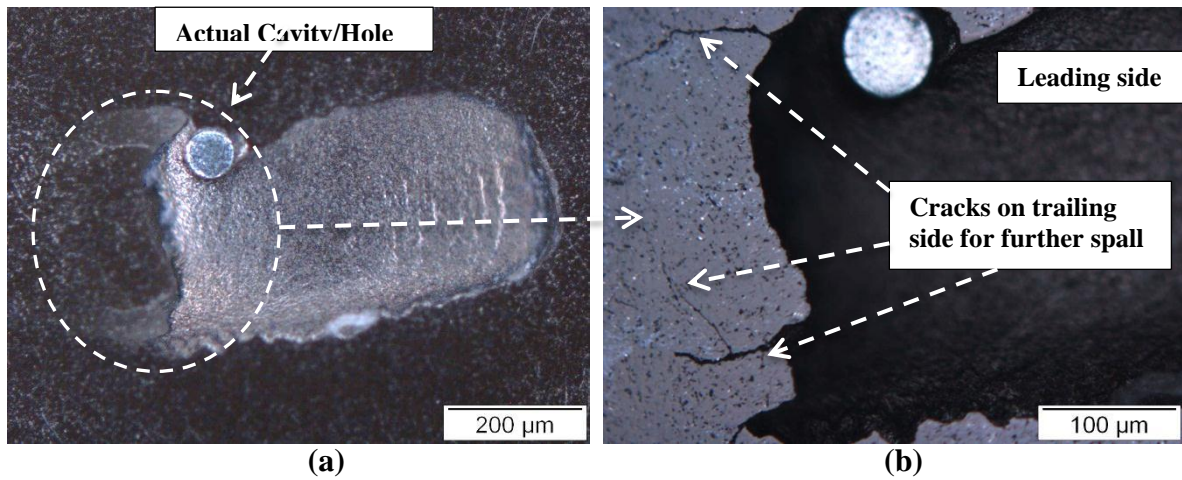


Figure 5.31: Post-experiment surface analysis (experiment 24) using OM (a) at low magnification (b) at high magnification

Two more experiments (experiment 25 and 26) were also conducted at these operating conditions to verify the results and fully understand failure mechanism. In the experiment 25, it repeated the result of experiment 23 and could not get any failure in post 100million stress cycles, whereas, in experiment 26, a spalling observed post 20million stress cycles.

Figures 5.32-33 are showing pre- and post-experiment surface analysis of experiments 25-26 respectively.

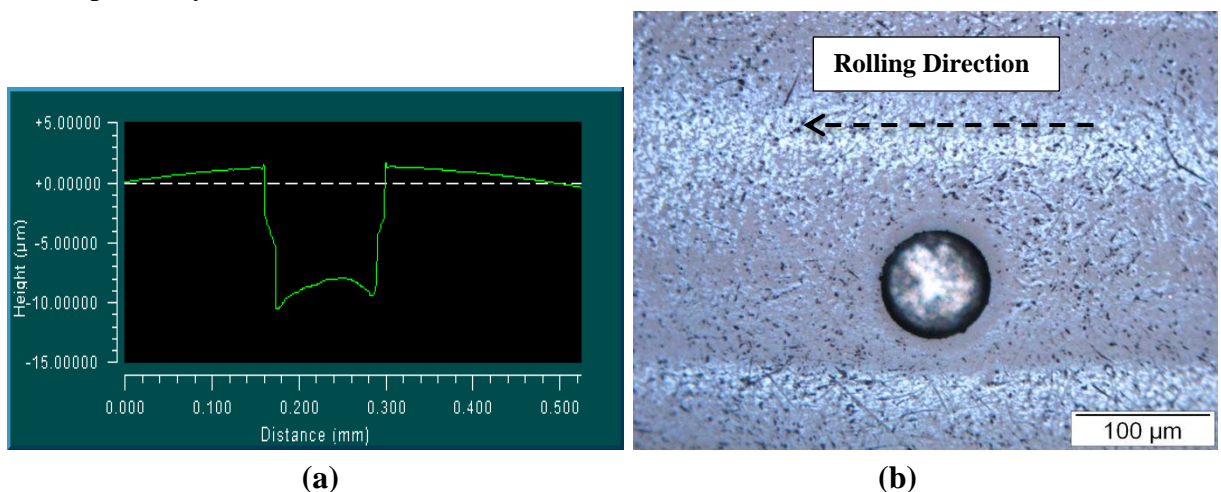


Figure 5.32: Surface analysis/mapping (experiment 25) (a) Pre-experiment surface mapping of hole profile using interferometry (b) Post-experiment analysis using microscopy

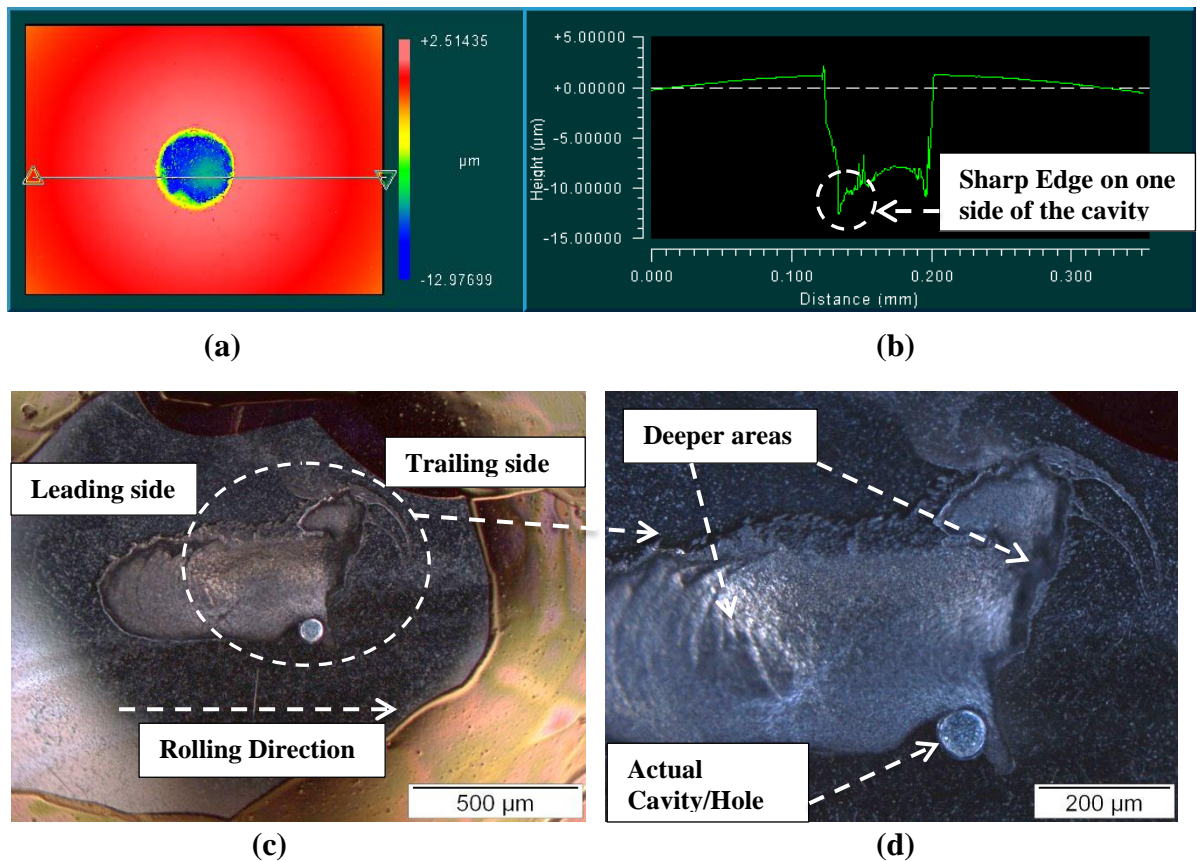


Figure 5.33: Surface analysis/mapping (experiment 26) (a) and (b) pre-experiment using interferometry (c) and (d) post-experiment analysis by microscopy (dark field illumination)

Hence these holes were failing at 3.8GPa as there are sharp corners and edges. Two further experiments were conducted with further shallower depth (5μm) but at higher pressure of 4.8GPa.

First experiment (experiment 27) on the cavity with medium diameter of 75μm and shallower depth of 5μm was suspended post 100million stress cycles. Pre- and post-experiment surface analysis was conducted using light microscopy and white light interferometry (Fig 5.34). Experiment 28 was repetition of experiment 27 to verify the results at same operating conditions. Although in both experiments, surface profile of the cavity base was somehow different yet they produced similar results and could not find any sign of failure until 100million stress cycles. Moreover, their location on the contact track was also different from each other but tolerance resulted from both experiments. Pre- and post-experiment surface analysis of sample used in experiment 28 is shown in Figure 5.35.

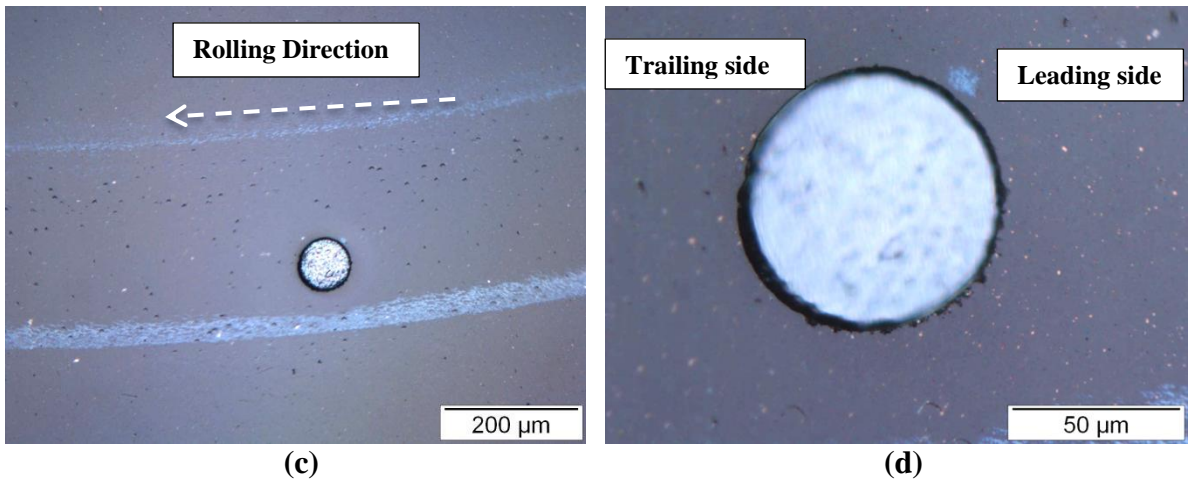
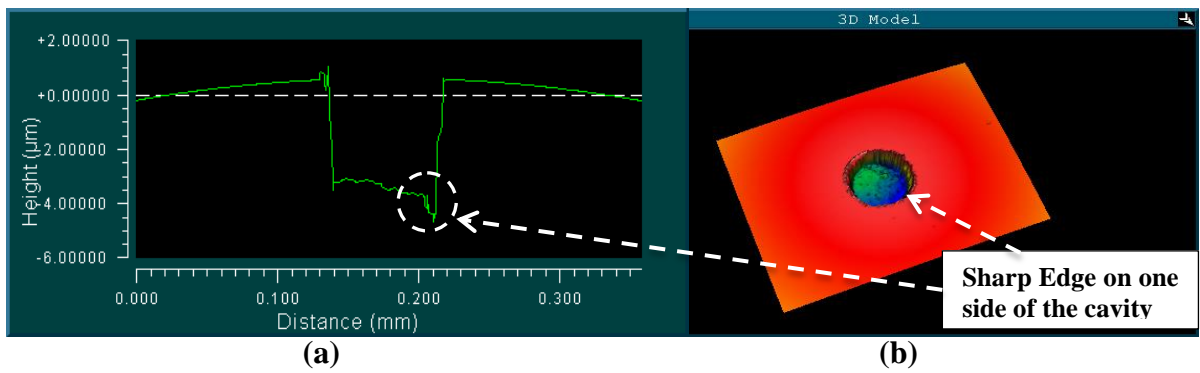


Figure 5.34: Surface analysis/mapping (experiment 27) (a) and (b) pre-experiment using interferometry (c) and (d) post-experiment analysis by microscopy

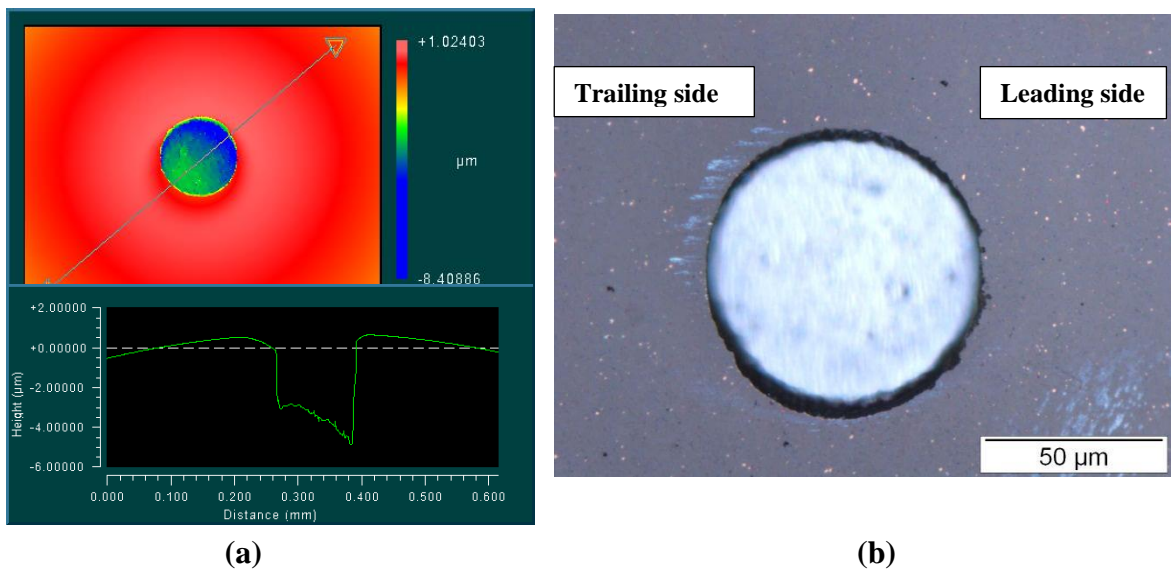


Figure 5.35: Surface analysis/mapping (experiment 28) (a) pre-experiment using interferometry (b) post-experiment analysis by microscopy

Two more experiments (exp. 29 and 30) were also conducted on medium diameter cavities with more deeper hole of 30μm depth. These cavities were exclusively machined without

any sharp edges/corners at the base but are more likely to shape II. Previous experiments have revealed that most of the failure happened in earlier cases (low fatigue cycles), therefore, first experiment was conducted for just 30million stress cycles at contact pressure of 3.8GPa. Experiment 29 was suspended post 30million stress cycles without getting any failure or sign of failure (Figure 5.36). Experiment 30 was then conducted at 4.8GPa to find tolerance at this pressure. spalling was observed after 6million stress cycles. Pre and post-experiment surface analysis is shown in the Figure 5.37.

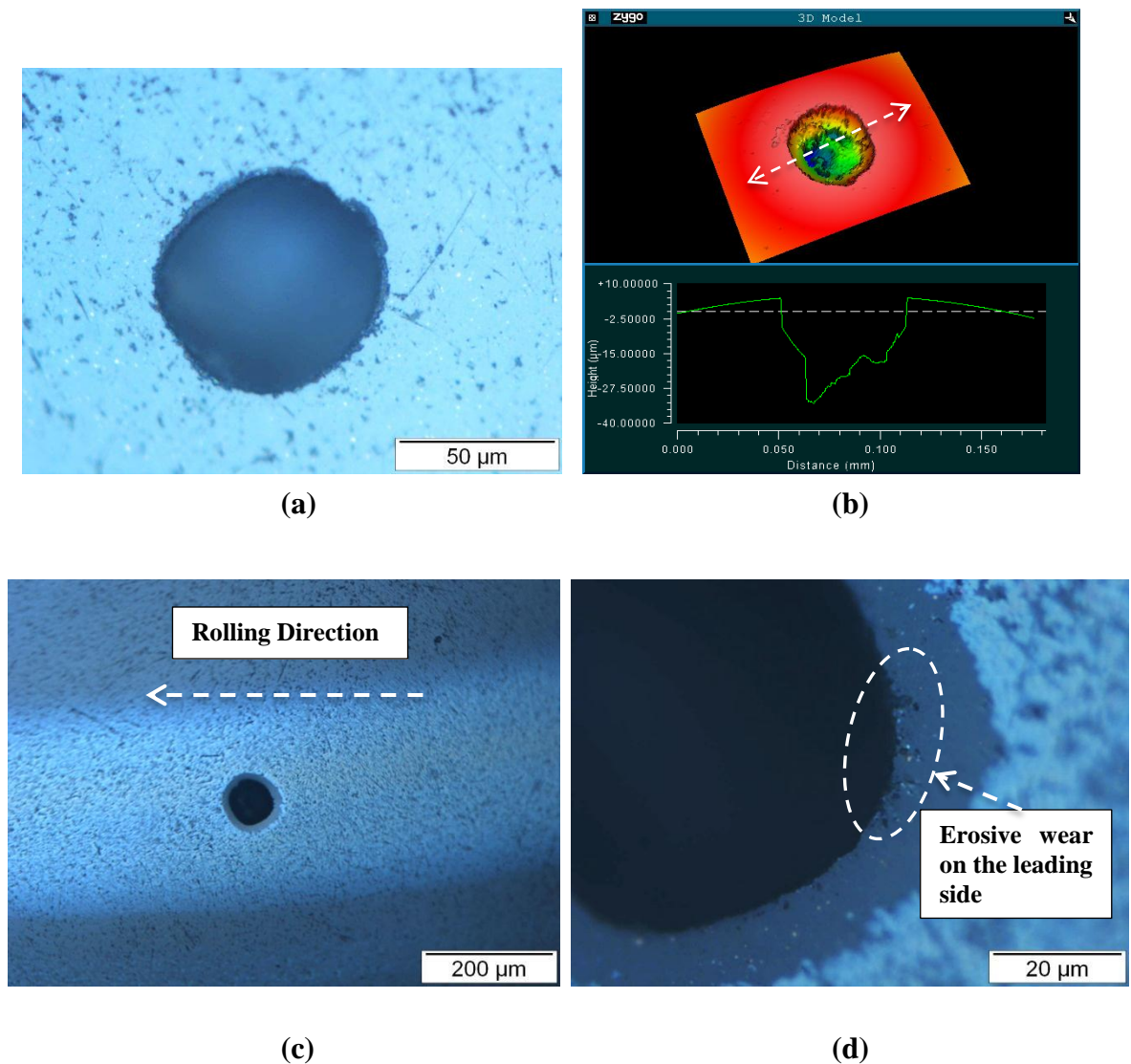


Figure 5.36: Surface analysis/mapping (experiment 29) (a) and (b) pre-experiment using microscopy and interferometry respectively (c) and (d) post-experiment analysis by light microscopy

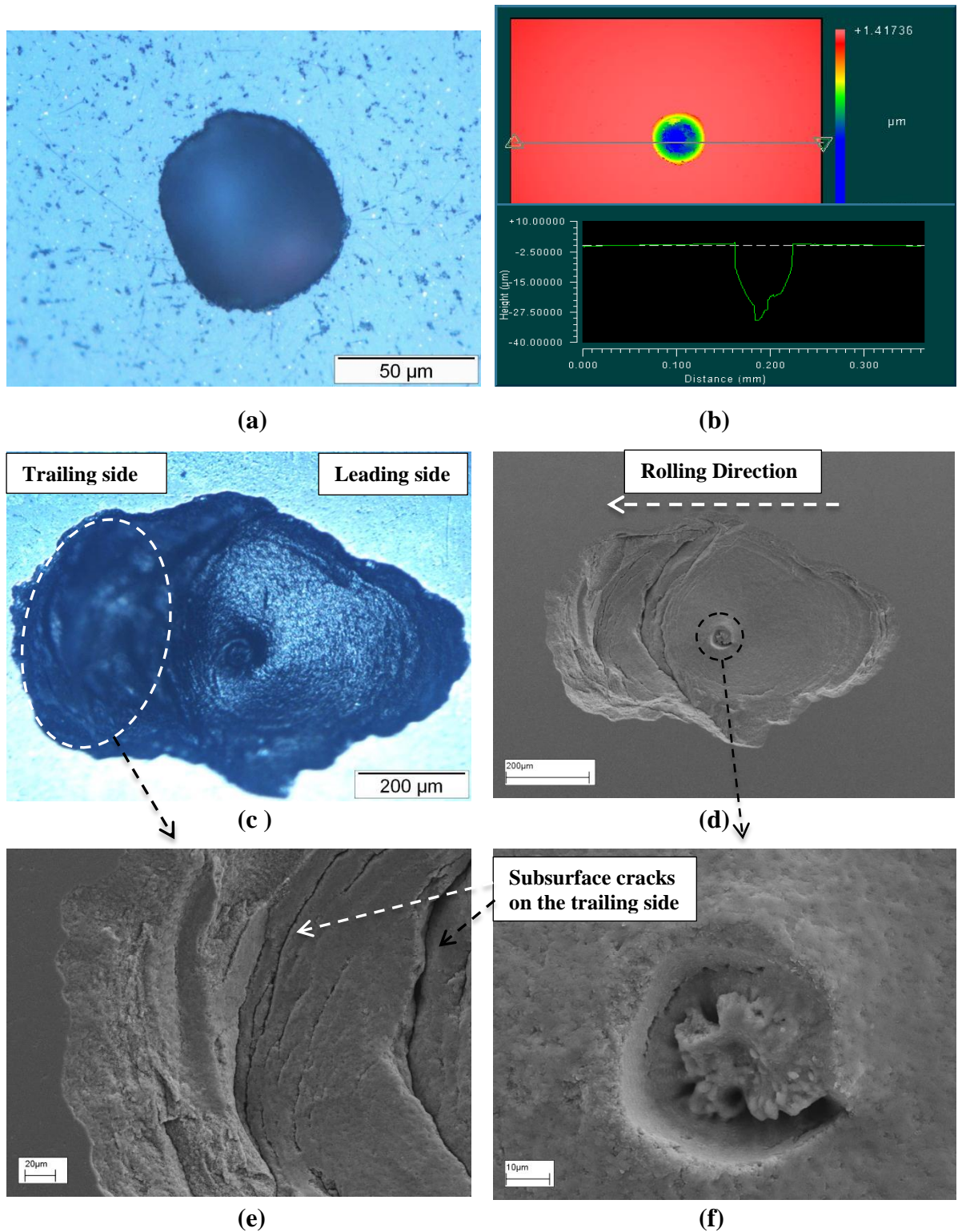


Figure 5.37: Surface analysis/mapping (experiment 30) (a) and (b) pre-experiment using microscopy and interferometry respectively (c) and (d) post-experiment analysis showing spall by microscopy and SEM respectively (e) and (f) SEM images showing cracks on trailing side and base of original cavity

Figure 5.37c-d showing original cavity base and possible crack initiation position towards all directions and especially leading and trailing sides. It also showing the larger subsurface cracks on the trailing side caused deeper cavity on the one side of the spall. Failure mechanism is discussed at the end of this chapter.

After conducting eight experiments on the medium diameter cavities with shape I (right cylindrical) profile, following tolerance level can be concluded that medium diameter cavities are tolerable for shallow depths of 5 μ m and 10 μ m up to 100million stress cycles for contact pressure of 3.8GPa provided that cavity has flat base profile especially in 10 μ m depth case. However, increase in pressure can reduce their tolerance and spalling may observe at high pressure of 4.8GPa for 10 μ m depth cavities. More shallower cavities of 5 μ m are tolerable for all pressure range (3.8-4.8GPa). Deeper cavities can tolerable at 3.8GPa for few million stress but may fail beyond 30million stress cycles. Higher pressure has severe effects on the performance for deeper cavities and results in spalling.

5.1.3. Large Hole Experiments (100 μ m diameter)

This series of experiments are listed in Table 5.5. Cavities having diameter of 100 μ m with depth of 5 and 10 μ m are tested at 3.8, 4.5 and 4.8GPa using thin mineral oil and bulk oil temperature of 75°C.

Table 5.5: Experiments conducted on large diameter hole (Shape I/right cylindrical)

Exp. ID	Ball ID	Contact Pressure (GPa)	Hole Dimensions (μm)	Stress Cycles (10^6)	Outcome
<i>Exp. 31</i>	B41H01	4.8	Dia: 100, Depth: 10	0.1	<i>Spalled</i>
<i>Exp. 32</i>	B42H01	4.8	Dia: 100, Depth: 10	0.3	<i>Spalled</i>
<i>Exp. 33</i>	B41H02	3.8	Dia: 100, Depth: 10	15	<i>Spalled</i>
<i>Exp. 34</i>	B42H02	3.8	Dia: 100, Depth: 10	60	<i>Spalled</i>
<i>Exp. 35</i>	B78H01	4.8	Dia: 100, Depth: 5	100	<i>Completed</i>
<i>Exp. 36</i>	B78H02	4.8	Dia: 100, Depth: 5	5.6	<i>Spalled</i>
<i>Exp. 37</i>	B79H01	4.5	Dia: 100, Depth: 5	100	<i>Completed</i>

Large hole diameter experiments started by taking cavity of depth $10\mu\text{m}$ at contact pressure of 4.8GPa to observe failure mechanism. First experiment (exp. 31) resulted into spalling post 0.1million stress cycles and caused machine to stop. In order to confirm the results, second experiment (exp. 32) is also conducted at same operating conditions and spalling was found post 0.3million stress cycles. Pre- and post-experiment surface analysis is shown in the Figures 5.38-5.39.

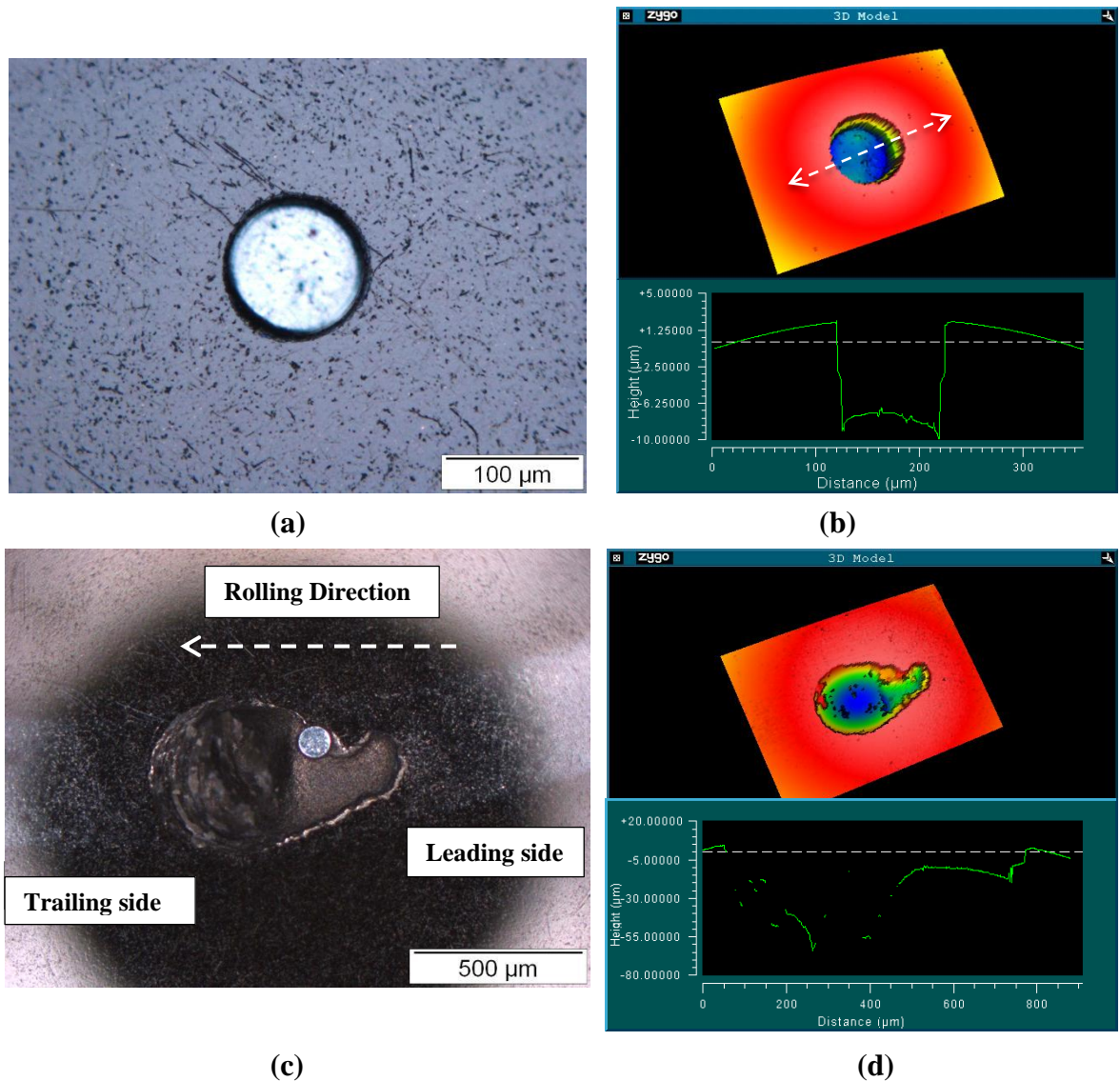


Figure 5.38: Surface analysis/mapping (experiment 31) (a) and (c) pre and post-experiment analysis using microscopy, (b) and (d) pre and post-experiment surface mapping using interferometry

Similar failure trend was observed as found in previous experiments. Spall found had total length of $700\mu\text{m}$ and maximum depth was more than $60\mu\text{m}$ (Figure 5.38). Possibly crack was initiated from the hole base and travelled in all directions and finally reached to the

surface. Trailing side of the spall was larger than leading side. Second experiment (exp. 32) also produced similar results but having two spalls and it is an example of multi-spall phenomenon possibly happened due to over-rolling after first spalling. Total length and maximum depth were over 1300 μm (1.3mm) and more than 50 μm respectively. Delamination was also found on both leading and trailing side of the spall.

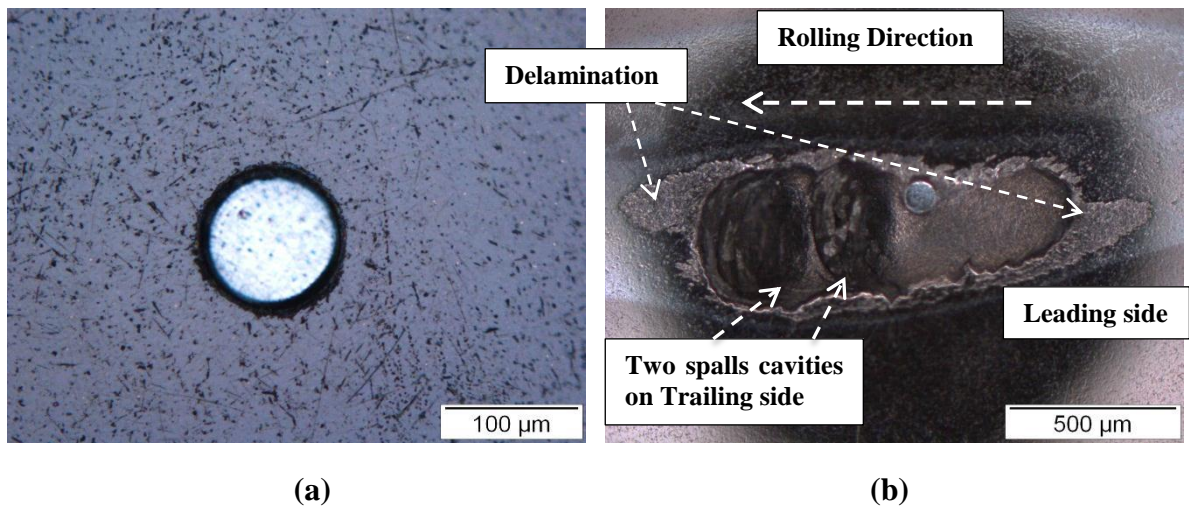


Figure 5.39: Surface analysis (experiment 32) using microscopy (a) pre-experiment (b) post-experiment

Pressure was reduced to 3.8GPa for further experiments after getting failure for two experiments for large diameter cavities and at 4.8GPa. Experiment 33 was conducted for same diameter and depth cavity but at contact pressure of 3.8GPa. This experiment also resulted into failure post 15million stress cycles. Fourth experiment (exp. 34) in this series was a repetition of previous experiment (exp. 33) to confirm the results. Again, spalling was observed post 60 million stress cycles.

Multi-spalling (Figure 5.40) was observed in the experiment 33 due to possible larger size of the cavity and continuous over-rolling after primary spall. Secondary spalls not only found on the trailing side but also on the leading side. Total spall length was around 2.2mm and maximum depth found was on the trailing side of the spall. Delamination was also observed in post experiment surface analysis. In the second experiment (exp. 34), although cavity hole base was reasonably flat and only a single spall was observed post 60million stress cycles (Figure 5.41). Cavity was located close to the edge of the track and similar failure mechanism observed. Spall of 800 μm long with depth over 50 μm at the trailing side was found.

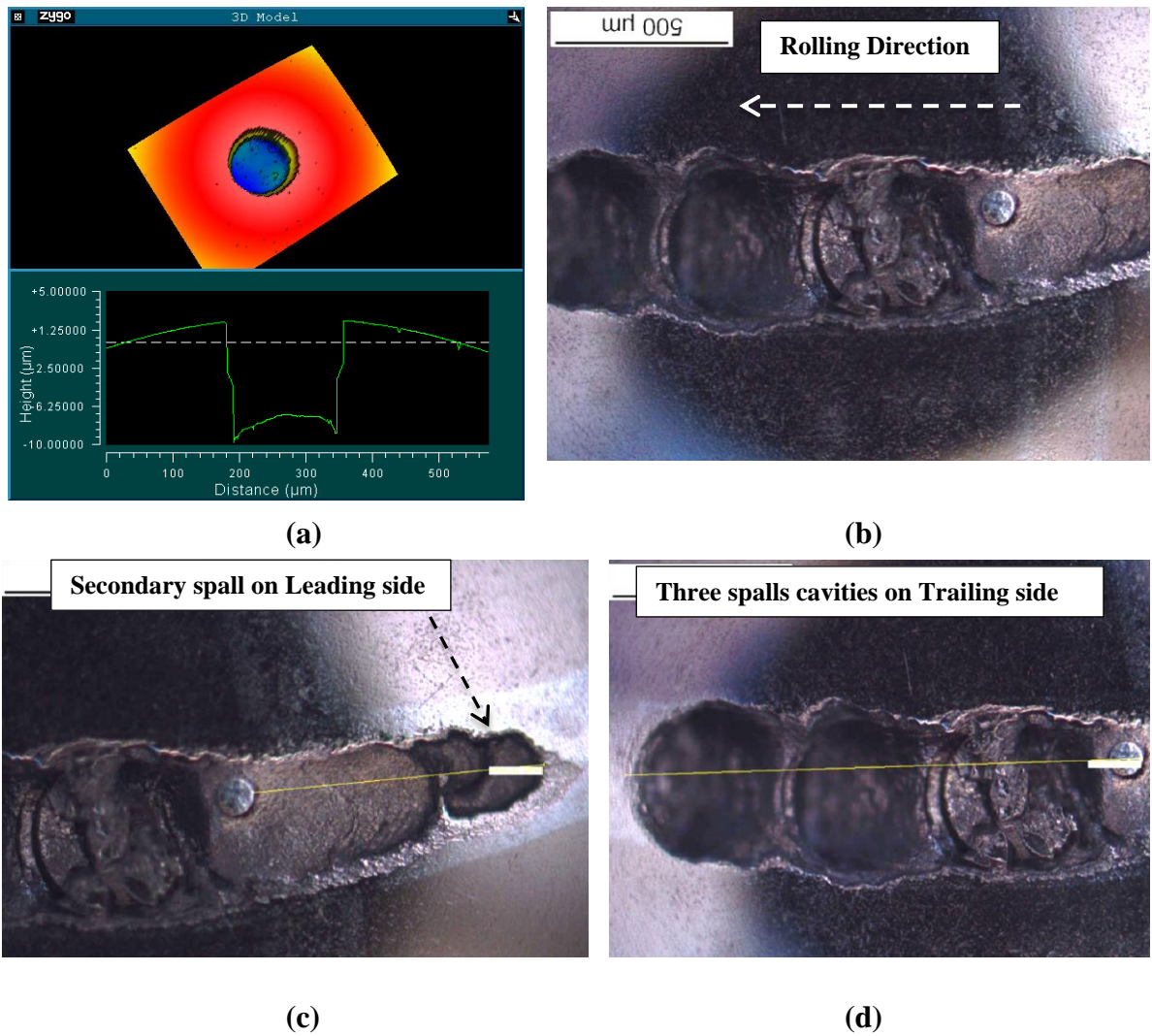
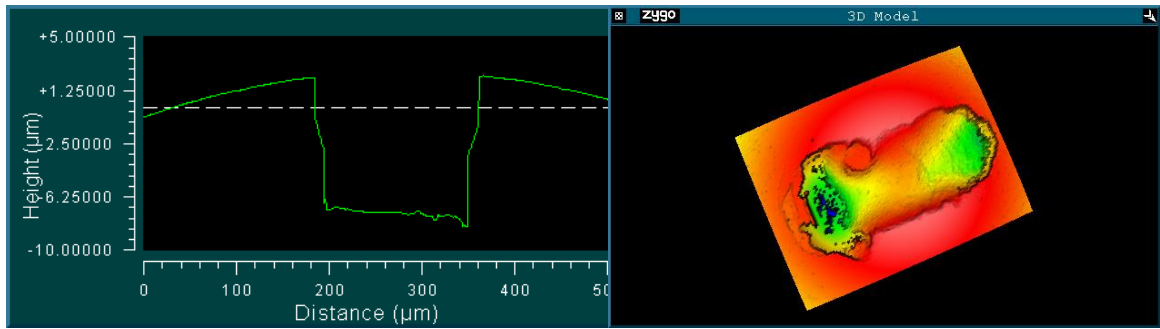


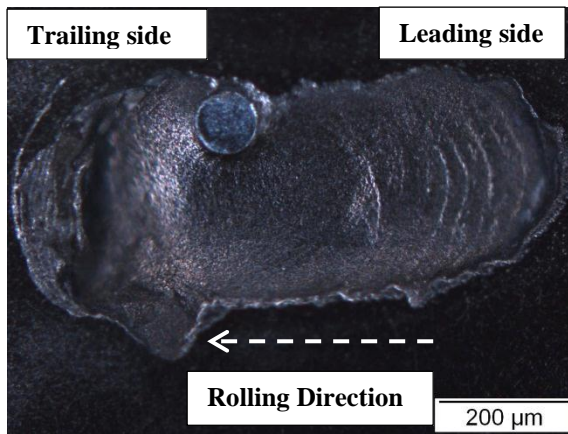
Figure 5.40: Surface analysis/mapping (experiment 33) (a) pre-experiment surface mapping using interferometry (b) post-experiment surface analysis using microscopy (c) and (d) post-experiment analysis using microscopy on leading and trailing side respectively

After conducting experiments at 3.8 and 4.8GPa contact pressure for depth of 10μm, further two tests were conducted on more shallow depth of 5μm at 4.8GPa. Test 35 was suspended post 100million stress cycles and second (experiment 36) caused failure in post 5.6million stress cycles. Figures 5.42-43 are showing surface analysis for experiment 35 and 36 respectively.

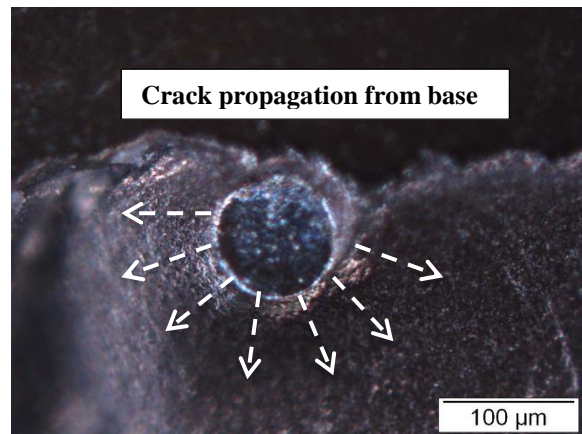


(a)

(b)

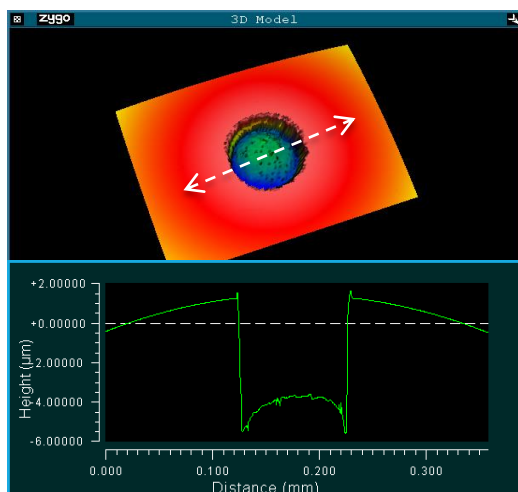


(c)

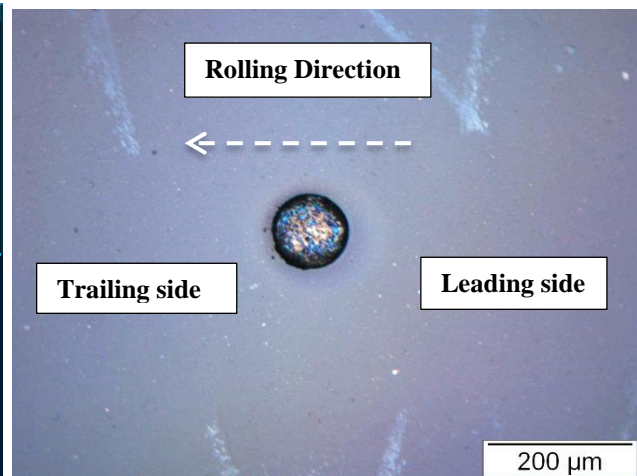


(d)

Figure 5.41: Surface analysis/mapping (experiment 34) (a) pre-experiment surface mapping using interferometry (b) post-experiment 3D surface profile (c) and (d) post-experiment surface analysis using microscopy

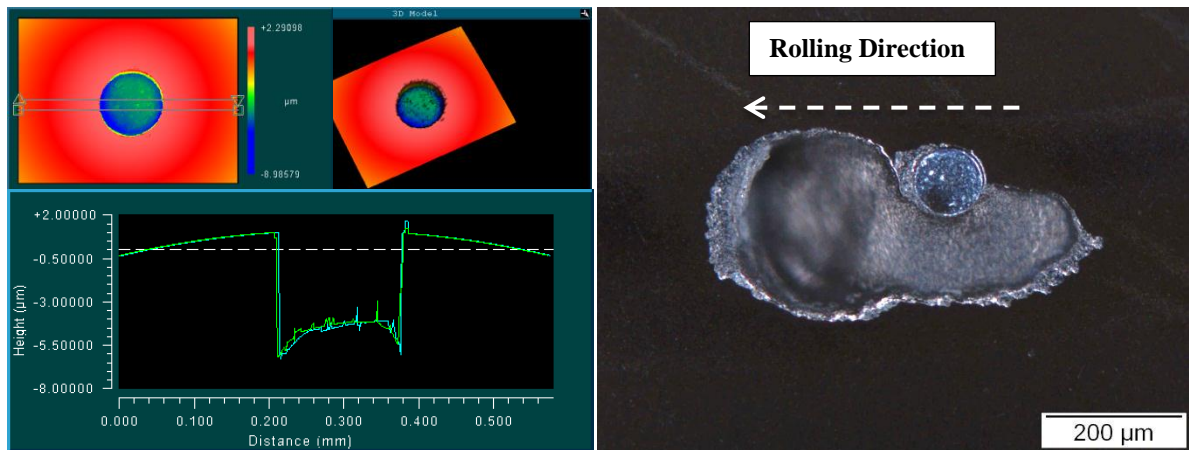


(a)



(b)

Figure 5.42: Surface analysis/mapping (experiment 35) (a) pre-experiment surface mapping using interferometry (b) post-experiment surface analysis using microscopy

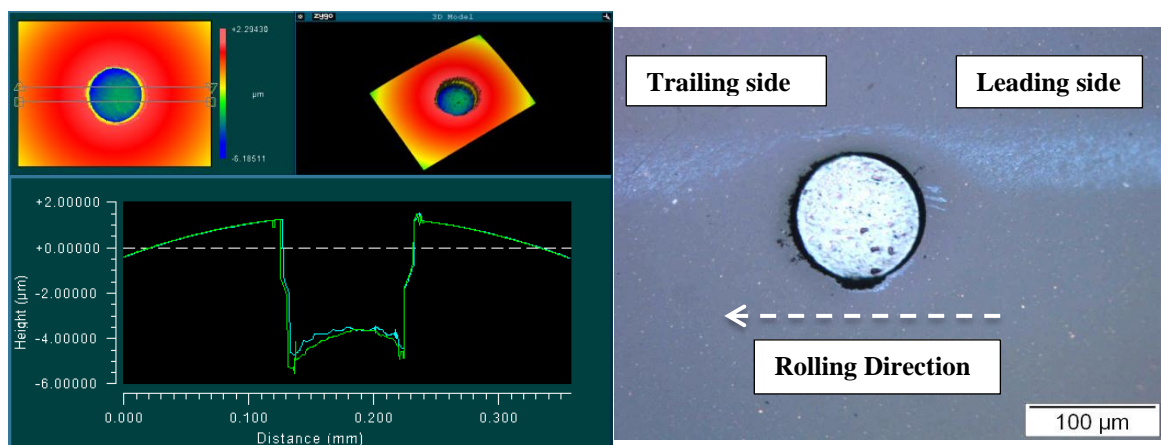


(a)

(b)

Figure 5.43: Surface analysis/mapping (experiment 36) (a) pre-experiment surface mapping using interferometry (b) post-experiment surface analysis using microscopy

Similar spall profile was found as observed for deeper hole of 10 μm (Figure 5.43). Some delamination/edge wear also found on the edges of the spall. Spall had total length of 585 μm and maximum depth of 80 μm on the trailing side. These experiments concluded that material could not tolerance at 4.8 GPa with surface defect of 100 μm diameter and 5 μm depth. One more experiment was also conducted at reduced pressure of 4.5 GPa using cavity of 100 μm and depth of 5 μm. No failure was observed at intermediate pressure (Figure 5.44).



(a)

(b)

Figure 5.44: Surface analysis/mapping (experiment 37) (a) pre-experiment surface mapping using interferometry (b) post-experiment surface analysis using microscopy

So, in this phase of experiments, cavities of 10µm were failing at range of contact pressure (3.8-4.8GPa) whereas more shallow cavities can also fail based on the cavity profile and location on the contact track at the 4.8GPa. However, no failure was observed in one experiment conducted at intermediate pressure of 4.5GPa for hole depth of 5µm.

5.2. Experiments on Shape I (Holes) – Material B

All the experiments conducted for artificial missing material defect (Shape I/right cylindrical) on class B material are on small hole diameter. These experiments were conducted using cavities with 10, 20 and 30µm depths and pressure was ranging 3.8-4.8GPa. These experiments are listed in the Table 5.6.

Table 5.6: Experiment conducted on Shape I (Class B Material)

Exp. ID	Ball ID	Contact Pressure (GPa)	Defect dimension (µm)	Stress Cycles (10⁶)	Outcome
<i>Exp. B1</i>	BB01H01	4.8	Dia: 50, Depth: 10	2	<i>Spalling</i>
<i>Exp. B2</i>	BB01H02	4.8	Dia: 50, Depth: 10	100	<i>Completed</i>
<i>Exp. B3</i>	BB02H01	4.5	Dia: 50, Depth: 10	100	<i>Completed</i>
<i>Exp. B4</i>	BB02H02	4.5	Dia: 50, Depth: 10	100	<i>Completed</i>
<i>Exp. B5</i>	BB04H01	4.5	Dia: 50, Depth: 20	3	<i>Spalling</i>
<i>Exp. B6</i>	BB05H01	4.2	Dia: 50, Depth: 20	7.8	<i>Spalling</i>
<i>Exp. B7</i>	BB06H01	3.8	Dia: 50, Depth: 20	6	<i>Spalling</i>
<i>Exp. B8</i>	BB07H01	3.8	Dia: 50, Depth: 30	1 ^{**}	<i>Stopped</i>

^{**}: Experiment stopped due to crack network on the ball surface

After conducting a range of experiments on material A using different sizes and pressures, further experiments were conducted using ball samples from material B. Test conditions were same as adopted in Material ‘A’ experiments i.e., rotational speed of 7500rpm, bulk oil temperature of 75°C, using thin mineral oil as lubricant and range of contact pressures. First experiment (experiment B1) was conducted for small diameter with shallow diameter

of $10\mu\text{m}$ and at contact pressure of 4.8GPa . This experiments was resulted into spalling post 2 million stress cycles. Surface analysis was conducted at pre- and post-experiment stage for failure modes and investigation to cause failure (Figure 5.45-5.46). Sharp edges were observed on one side of the cavity and possibly caused to failure.

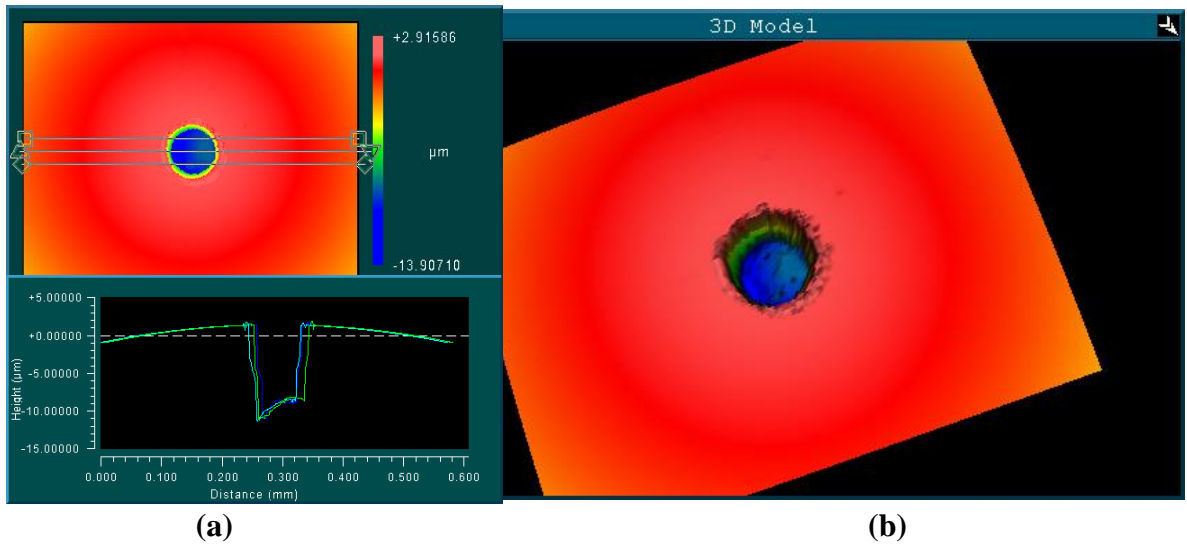


Figure 5.45: Surface analysis/mapping (experiment B1) (a) pre-experiment surface mapping using interferometry (b) 3D cavity profile

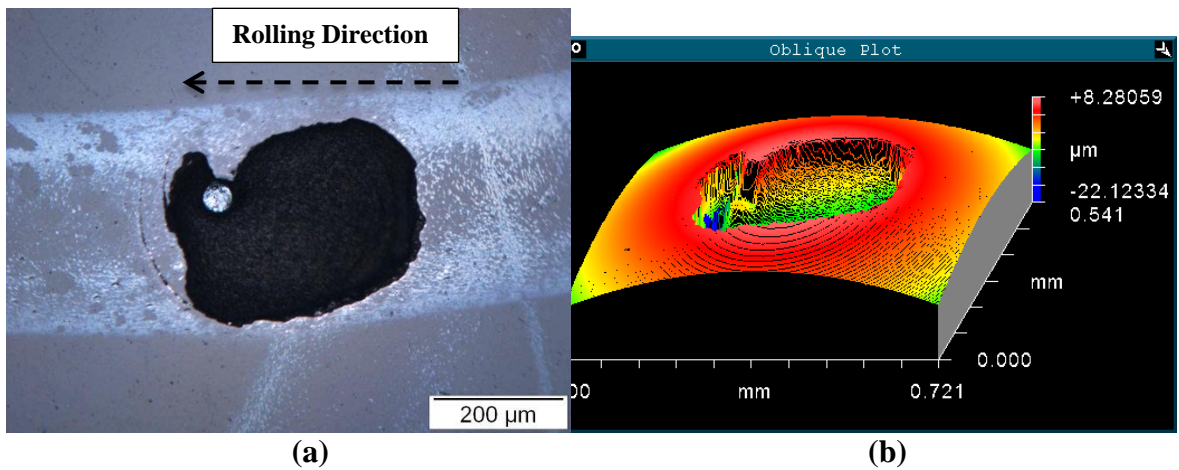


Figure 5.46: Surface analysis/mapping (experiment B1) (a) and (b) Spall profile using microscopy and interferometry

Second experiment (exp. B2) was also conducted using same size of the defect and contact pressure. Experiment was suspended post 100million stress cycles without getting any failure and new features. But it is obvious that defect was located close to contact edge

(Figure 5.47). Some edge wear also found at inner side of the defect edges. It is interesting that material ‘A’ sample was tolerable with same defect size and operating conditions.

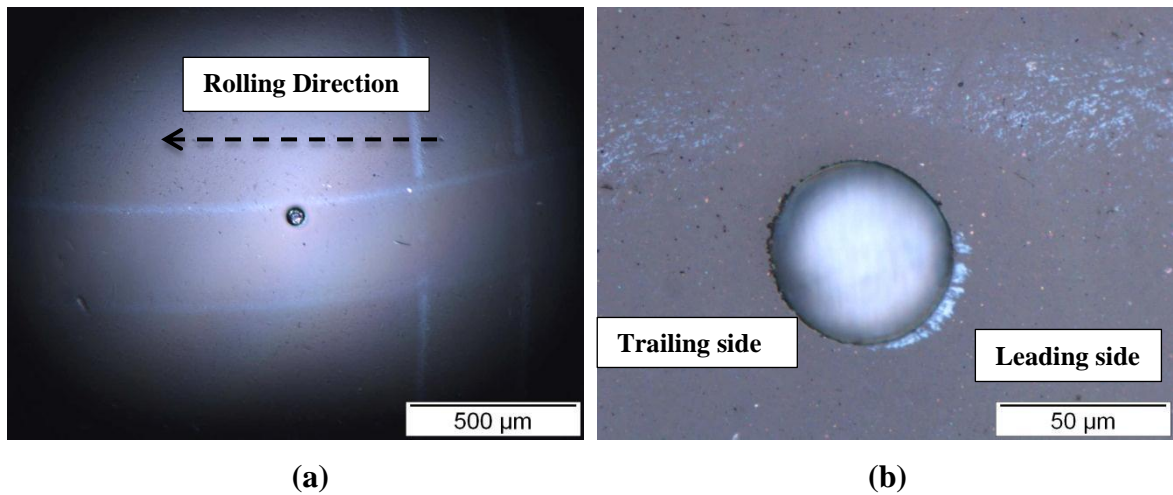


Figure 5.47: Surface analysis (experiment B2) (a) and (b) post 100million stress cycles using microscopy

Pressure was reduced to 4.5GPa for further testing and finding the tolerance of the material at these conditions. Two experiments (exp. B3 and exp. B4) were conducted and in both cases, tolerance was confirmed till 100million stress cycles.

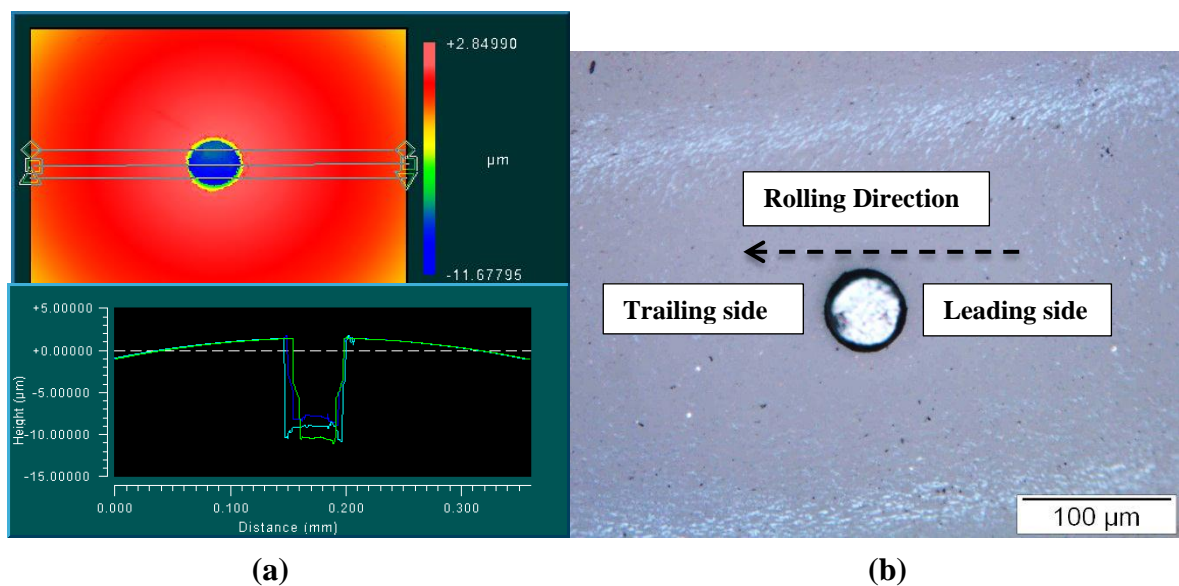


Figure 5.48: Surface analysis/mapping (experiment B3) (a) pre-experiment surface mapping using interferometry (b) post-experiment surface analysis using microscopy

Figure 5.48 explains cavity profile before experiment and post 100million stress cycles. Although cavity was centrally located yet it produced tolerance until a predefined number

of machine revolutions. Pre-experiment analysis also revealed a relatively flat cavity base profile. In the second experiment (exp. B4), cavity was located close to track edge but had more sharp corners (Figure 5.49) to previous experiment case yet it also produced tolerance for up to 100 million stress cycles.

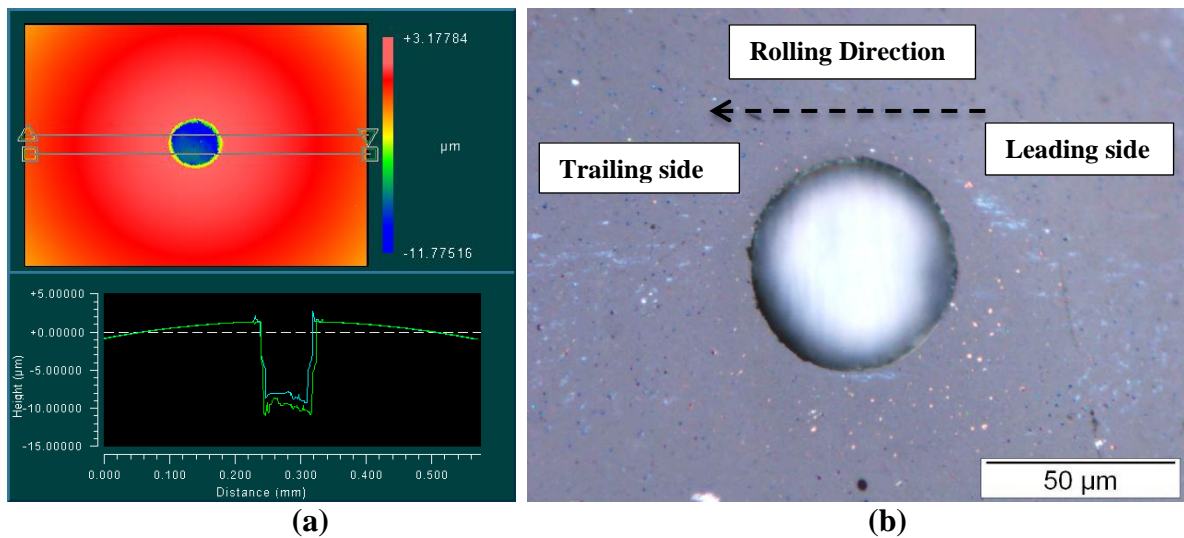


Figure 5.49: Surface analysis/mapping (experiment B4) (a) pre-experiment surface mapping using interferometry (b) post-experiment surface analysis using microscopy

After finding the tolerance of material (B) at 4.8GPa and 4.5GPa for small hole diameter and depth 10 μ m, further experiments were conducted for the depth of 20 μ m. First experiment in this series (Exp. B5) was conducted at contact pressure of 4.5GPa as it was obvious that material will not tolerate pressure of 4.8GPa with cavity of depth of 20 μ m. This experiment was resulted into full scale spalling post 3million stress cycles. Similar profile was found in post-experiment surface analysis as observed before. Spall was found having total length of around 600 μ m and maximum depth of over 90 μ m. Pre- and post-experiment surface analysis of the sample is shown in the Figure 5.50.

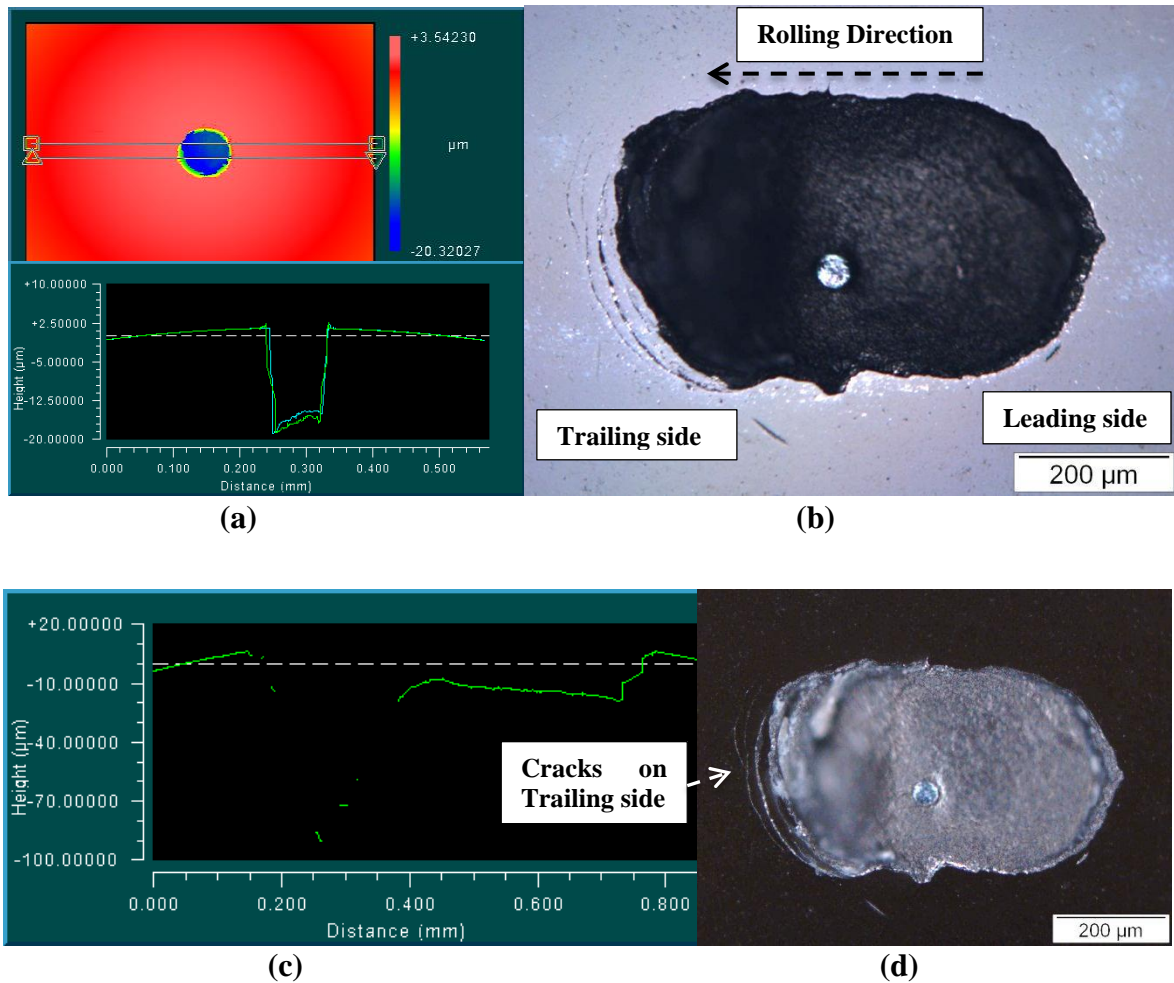


Figure 5.50: Surface analysis/mapping (experiment B5) (a) pre-experiment surface mapping using interferometry (b) post-experiment surface analysis using microscopy (c) spall profilometry (d) spall microscopy - darkfield

Further experiments on class B material with small diameter and depth of $20\mu\text{m}$ were conducted using reduced contact pressure of 4.2GPa . First experiment (exp. B6) of this series provided spalling post 7.8 million stress cycles. Pre-experiment surface mapping showing (Figure 5.51) the hole base profile with same sharp corners. Cavity was not centrally located but still it produced spalling. Spalling profile was $800\mu\text{m}$ long and having maximum depth over $30\mu\text{m}$ on the leading side as secondary cracks were found on the trailing side and further over-rolling may cause to remove the secondary cracks area out.

Experiment B7 was conducted using same size of defect i.e., small diameter of $50\mu\text{m}$ and depth of $20\mu\text{m}$ but at further reduced contact pressure of 3.8GPa . Spalling caused the machine to stop post 6million stress cycles. Surface analysis (5.52-5.53) was conducted pre- and post-experiment using microscopy and interferometry. After conducting number

of experiments on cavities with small hole diameter of $50\mu\text{m}$ and depth of $20\mu\text{m}$, it can be concluded that material B with this type of defect cannot tolerate at these pre-defined pressure conditions (3.8GPa-4.8GPa).

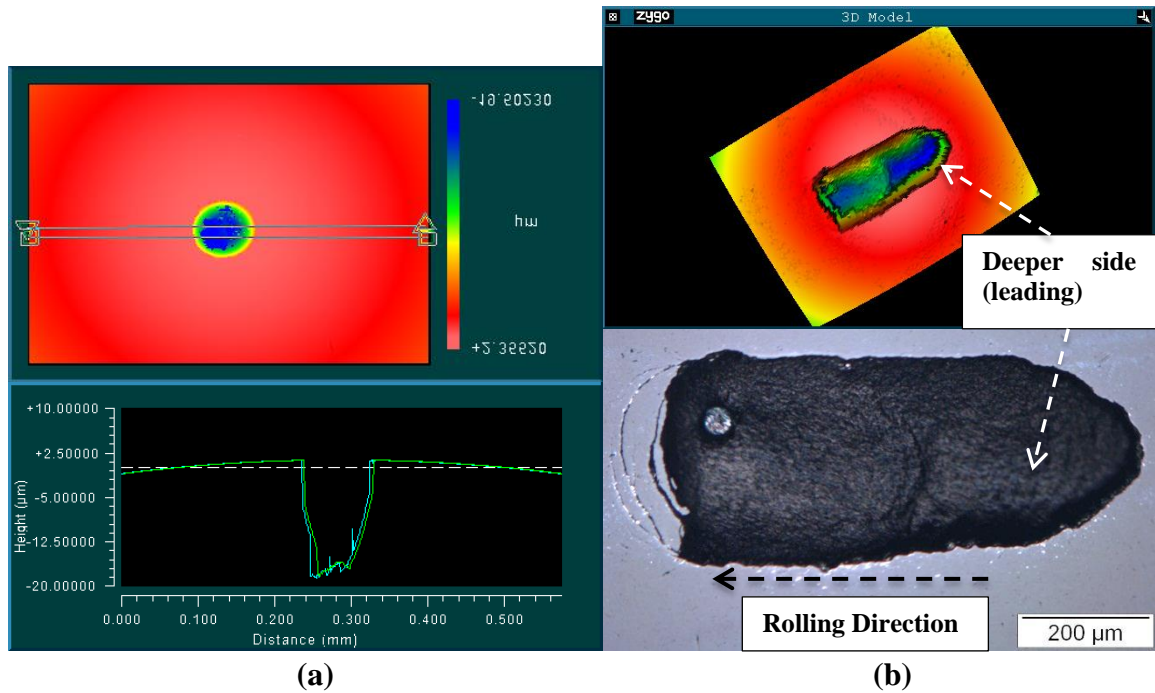


Figure 5.51: Surface analysis/mapping (experiment B6) (a) pre-experiment surface mapping using interferometry (b) post-experiment spall profile using interferometry and microscopy

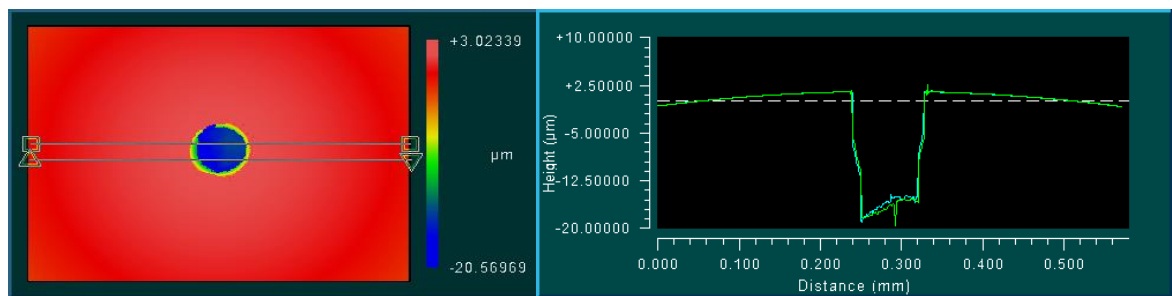


Figure 5.52: Pre-experiment surface mapping (exp. B7) using interferometry

After conducting number of experiments on depth of $20\mu\text{m}$, further experiments were conducted on the depth of $30\mu\text{m}$. Although it was obvious that this material with more deeper cavities will not tolerate at these conditions, however, just for confirmation, one experiment was conducted using small diameter cavity with depth of $30\mu\text{m}$ at low contact pressure of 3.8GPa. This experiment (exp. B8) was suspended post 1million stress cycles

due to crack network on the surface and for cross sectioning to find failure modes (subsurface observations). Pre and post surface analysis is shown in the Figure 5.54.

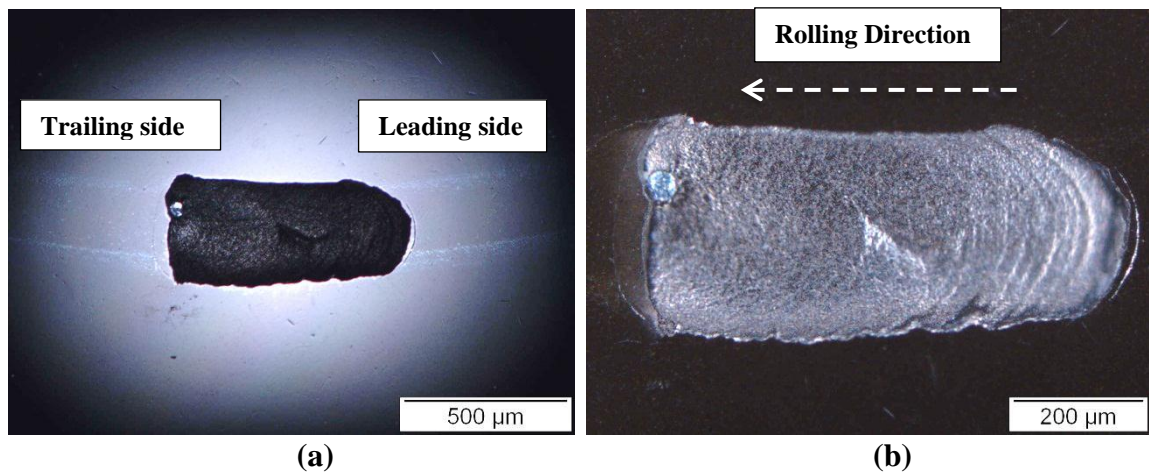


Figure 5.53: Spalled Surface analysis (experiment B7) using microscopy (a) light illumination (b) dark field illumination at high magnification

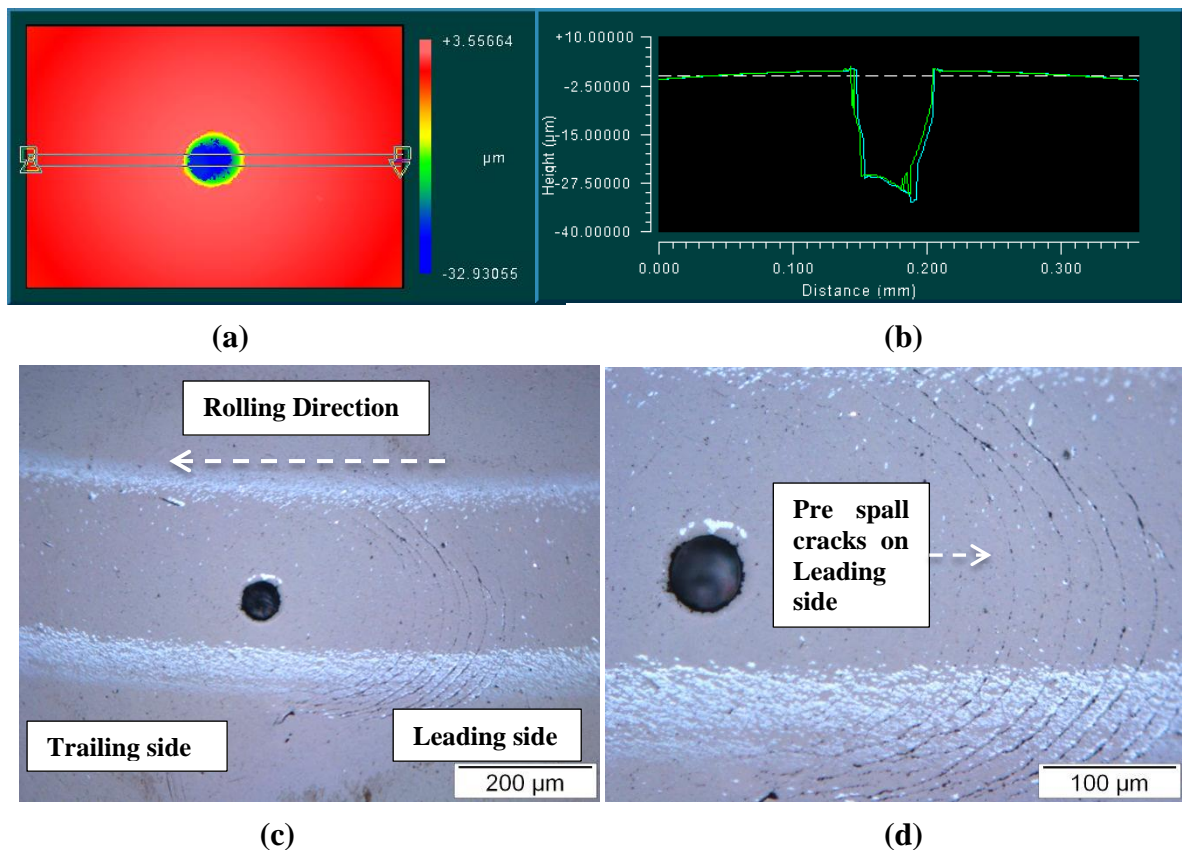


Figure 5.54: Surface analysis/mapping (exp. B8) (a) & (b) pre-experiment surface mapping using interferometry (c) and (d) post-experiment surface analysis using microscopy

5.3. Experiments on Shape I (Slot) – Material A

Experiments on Shape I (right cylindrical) holes showed that when failure by spalling occurred the original hole was visible in the spalled region. This indicated that the failure had been initiated by cracking at the bottom of the hole and subsequent crack growth towards the surface. Therefore a long slot of 100 μ m width and a depth of 10 μ m was tested at a high contact pressure (Table 5.7) with the slot positioned perpendicular to the running track. Experiment is conducted at speed of 7500rpm, typical bearing temperature of 75°C and using thin mineral oil as lubricant.

Table 5.7: Experiment conducted on Long Slot (Shape I/cylindrical)

Exp. ID	Ball ID	Contact Pressure (GPa)	Hole Dimensions (μ m)	Stress Cycles (10^6)	Outcome
Exp. 38	S04101	4.8	Dia/Width: 100, Depth: 10	30	Completed

Although the test was run for just 30million stress cycles but it can be extrapolated that there would be less chances of failure in case of slot. A further feature of this experiment was that fluid entrapment effects would be minimised or absent with a slot. On the basis of this concept, extensive finite element analysis was conducted on the cavities having fluid inside to see hydrostatic pressure effect on the tolerance assessment of the material (chapter 6). Pre- and post-experiment surface analysis is shown 5.55-56.

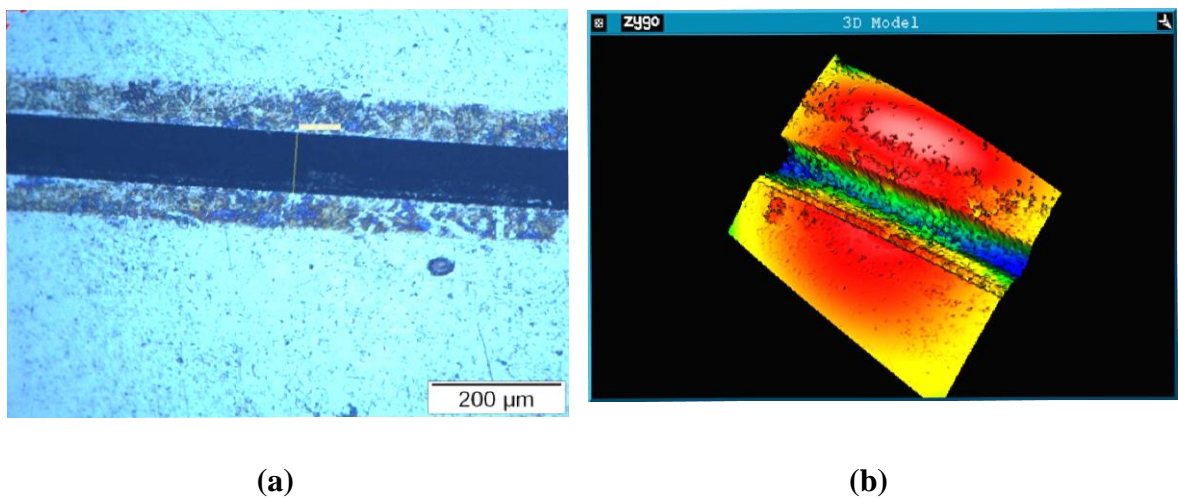


Figure 5.55: Pre-experiment (38) analysis using (a) microscopy (b) interferometry

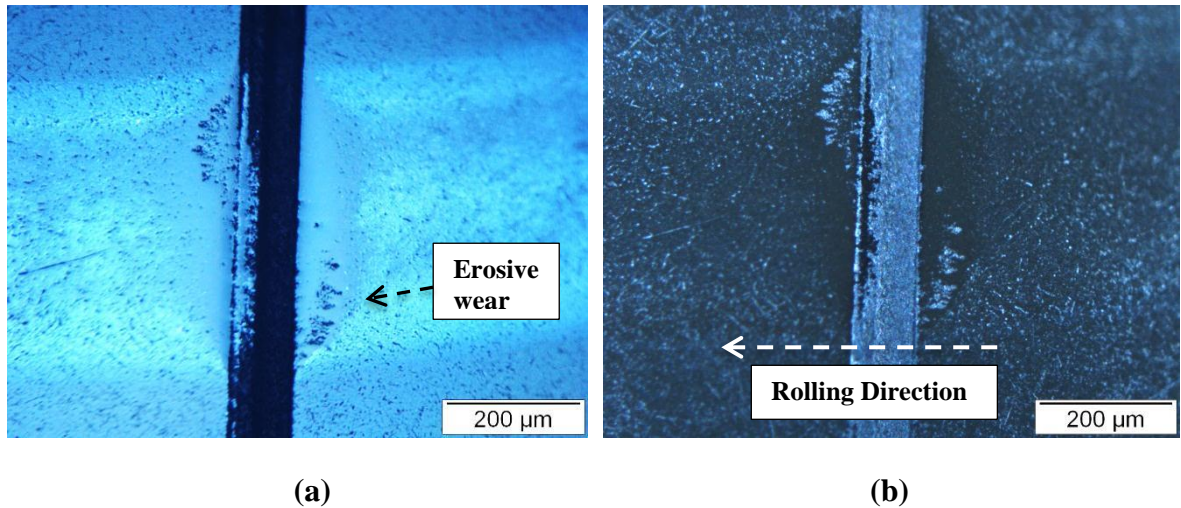


Figure 5.56: Post-experiment (38) analysis using microscopy (a) light illumination (b) dark field illumination

There was some discolouration at the edges of the slot presumably due to some vapour condensation during laser machining (Figure 5.55). After testing there was no evidence of cracks and only some slight erosive wear was found (Figure 5.56).

The erosive wear regions were at opposite sides of the slot from the centreline of the contact track confirming the concept of stick-slip on the inner and outer side of the contact track [Tourret and Wright 1977].

5.4. Experiments on Shape II – Material A

Two experiments are conducted on the shape II (conical) at high contact pressure of 4.8GPa for 30 million stress cycles to check any failure mechanism. Experiments details are given in Table 5.8. All experiments are conducted at speed of 7500rpm, typical bearing temperature of 75°C and using thin mineral oil as lubricant.

Table 5.8: Experiment conducted on Shape II (Conical) – Material A

Exp. ID	Ball ID	Contact Pressure	Hole Dimensions (μm)	Stress Cycles (10 ⁶)	Outcome
Exp. 39	B07H01	4.8GPa	Dia: 50, Depth: 10	30	Completed
Exp. 40	B06H01	4.8GPa	Dia: 75, Depth: 30	30	Completed

Although hole/cavity profile of last two experiments from medium diameter (Figure 5.36-5.37) were close to shape II cavities, yet more better shape cavities were tested to assess their performance and failure modes (if any) at high contact pressure. First experiment (exp. 39) was conducted for cavity of approximate diameter $50\mu\text{m}$ and depth of $10\mu\text{m}$. This experiment was suspended after pre-defined number of machine spindle revolutions (30million). Surfaces analysis is shown in Figure 5.57, highlighting cavity profile and location on the contact track.

Second experiment (experiment 40) was also conducted at the same operating condition but medium hole diameter ($75\mu\text{m}$) and more deeper cavity ($30\mu\text{m}$). This experiment was also suspended post 30million without any failure (Figure 5.58).

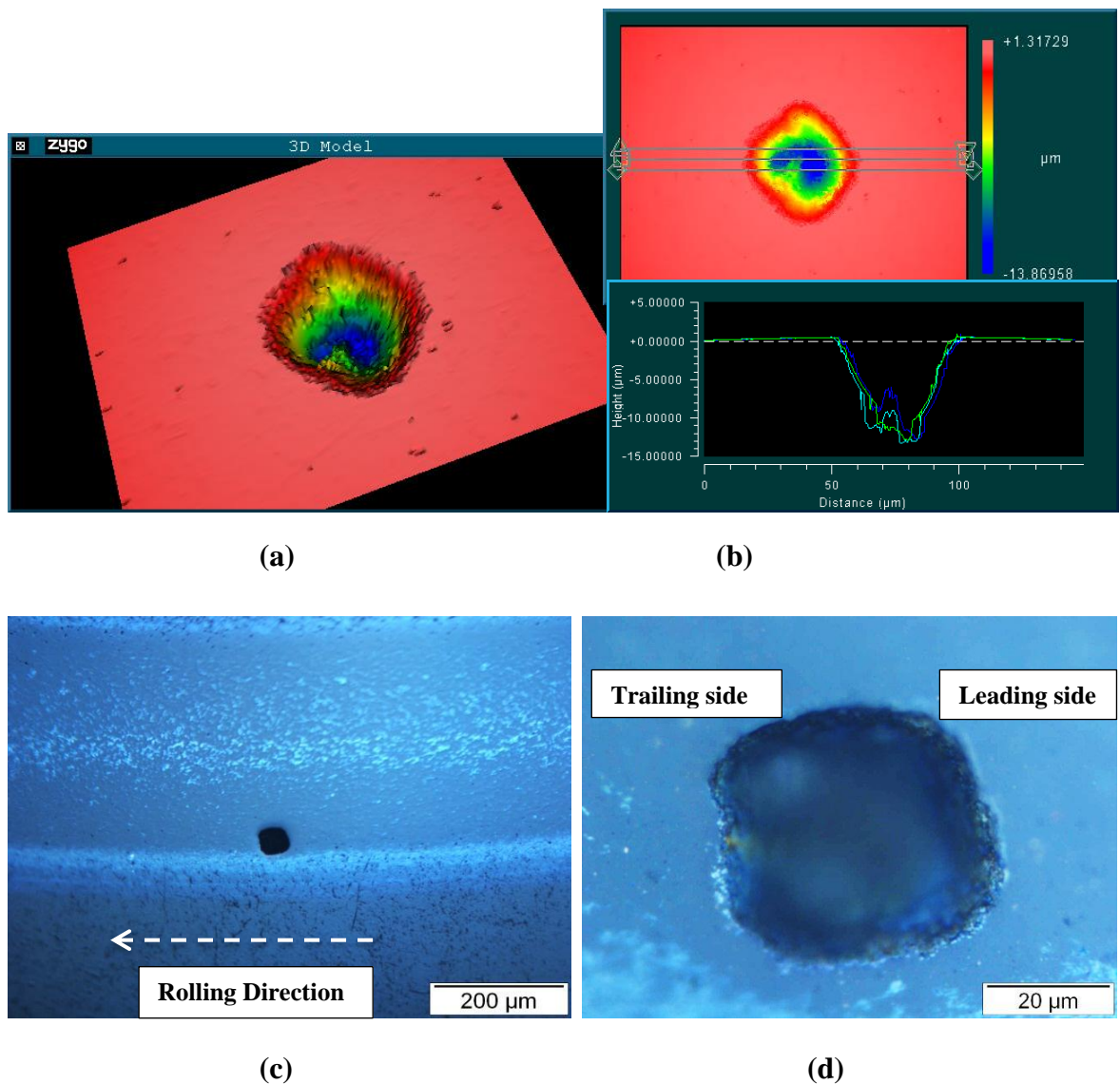


Figure 5.57: Surface analysis/mapping (experiment 39) (a) and (b) pre-experiment surface mapping using interferometry (c) and (d) post-experiment surface analysis using microscopy

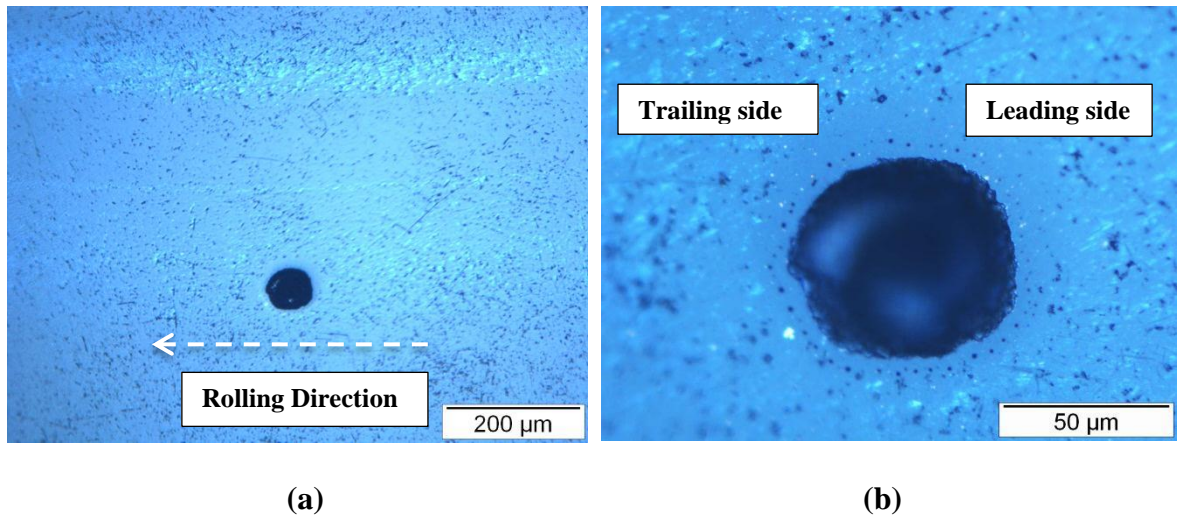


Figure 5.58: Post-experiment (40) surface analysis using microscopy (a) low magnification - showing location on the contact track (b) higher magnification

Although both experiments were suspended without failure and showing more tolerance than category I but it is also important to note that these cavities were located close to contact track edge. Further study is conducted to assess shape performance and contact track effect (contact pressure) is discussed in the next sections of this chapter.

5.5. Shape performance experiments (Shape I, II and III) – Material A

Shape performance experiments were also conducted to assess material rolling contact performance having different missing material shapes. Two experiments were conducted for each category. Experiment details are given below in Table 5.9.

These experiments were conducted by taking large hole diameter (100 μ m) and deeper depth (50 μ m) cavities. Experiments were started from shape I (right cylindrical) and in the first experiment (exp. 41), test was run at low contact pressure of 3.8GPa for 30million stress cycles and surface analysis was conducted after every 3million stress cycles and finally test was suspended post 30millin stress cycles. In the second phase of experiment, contact load was increased to 4.8GPa and spalling caused the machine stopped post 5million stress cycles. Surface analysis (Figure 5.59-5.60) shows that at high pressure, failure occurs. Wear is found on the contact track before getting spalling. Surface delamination/edge wear effect is also found on the edges of the hole on the trailing side. A spalled found post 35million stress cycle was of total length 1mm and maximum depth over 100 μ m at the trailing edge.

Table 5.9: Shape Performance Experiments (Shape I, II and III)

Exp. ID	Ball ID	Shape	Contact Pressure (GPa)	Hole Dimensions (μm)	Stress Cycles (10^6)	Outcome
Exp. 41	S1B1H1	I	3.8 4.8	Dia: 100 Depth: 50	30 6 (Total: 36)	Completed Spalled
Exp. 42	S1B1H2	I	4.8	Dia: 100 Depth: 50	0.15	Spalled
Exp. 43	S2B1H1	II	3.8 4.2 4.5 4.8	Dia: 100 Depth: 50	30 30 30 30 (Total:120)	Completed
Exp. 44	S2B1H2	II	4.8	Dia: 100 Depth: 50	100	Completed
Exp. 45	S3B1H1	III	3.8	Dia: 100 Depth: 50	0.1	Spalled
Exp. 46	S3B1H2	III	3.8	Dia: 100 Depth: 50	0.2-0.45	Spalled

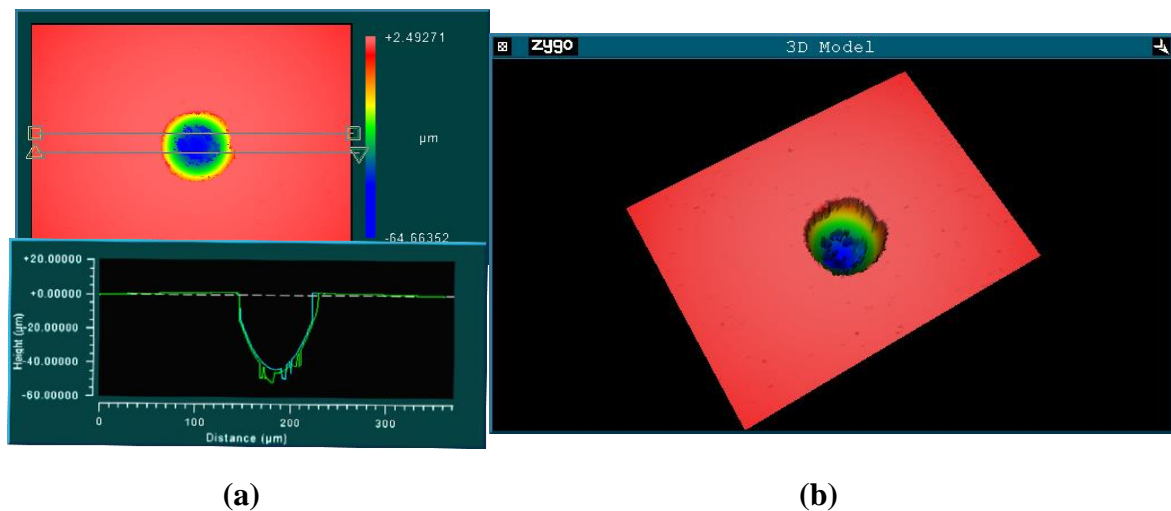


Figure 5.59: Surface mapping using interferometry (Experiment 41) (a) Surface profile (b) 3D image of cavity

Second experiment (42) was also conducted but at the same operating conditions and spalling observed post 0.15million stress cycles. A similar spall profile was found as in the experiment 38, further detail of failure mechanism is explained in the failure mechanism section. Pre- and post-experiment surface analysis is shown in the Figure 5.61. Spall found had total length of 980 μm and maximum depth of 134 μm .

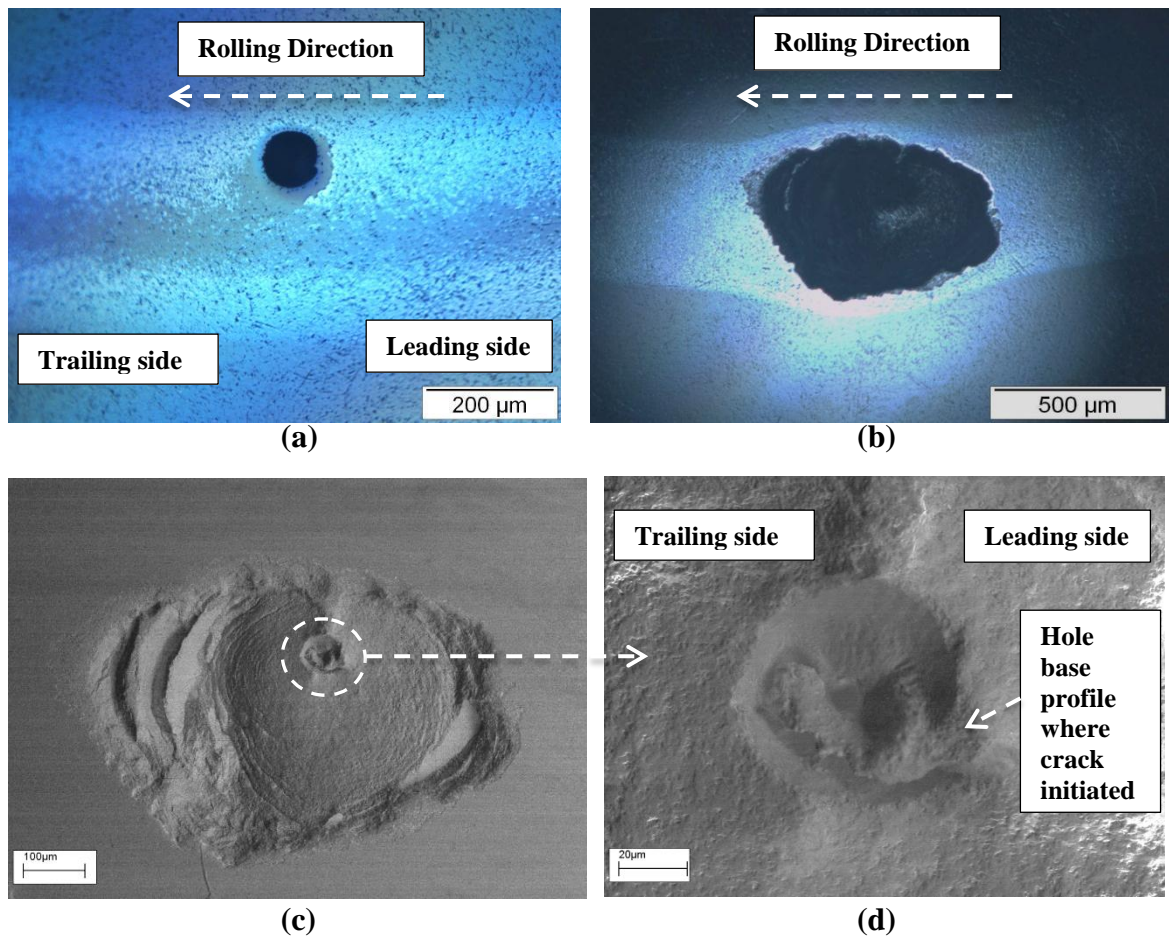


Figure 5.60: Post Experiment (41) surface analysis (a) and (b) post 30 and 35million using light microscopy (c) and (d) post 35million using SEM, showing spall and hole base

In the next phase, two experiments ran on shape II (conical) cavities. Again, experiments were started by taking cavity of diameter $100\mu\text{m}$, depth of $50\mu\text{m}$ and initially ran at 3.8GPa for 30million stress cycles and then surface analysis was conducted. Contact pressure raised to 4.2GPa for another 30million stress cycles and then to 4.5GPa for another 30 million and finally to 4.8GPa and ran for another 30million stress cycles to complete 120million stress cycles cumulative test. Surface analysis was conducted at regular interval. Finally this experiment was suspended (completed successfully) post 120million stress cycles. There was no sign of failure in post experiment inspection but defect was located close to the track edge (Figure 5.62). (depth is not exactly shown due to low magnification lens usage of interferometry)

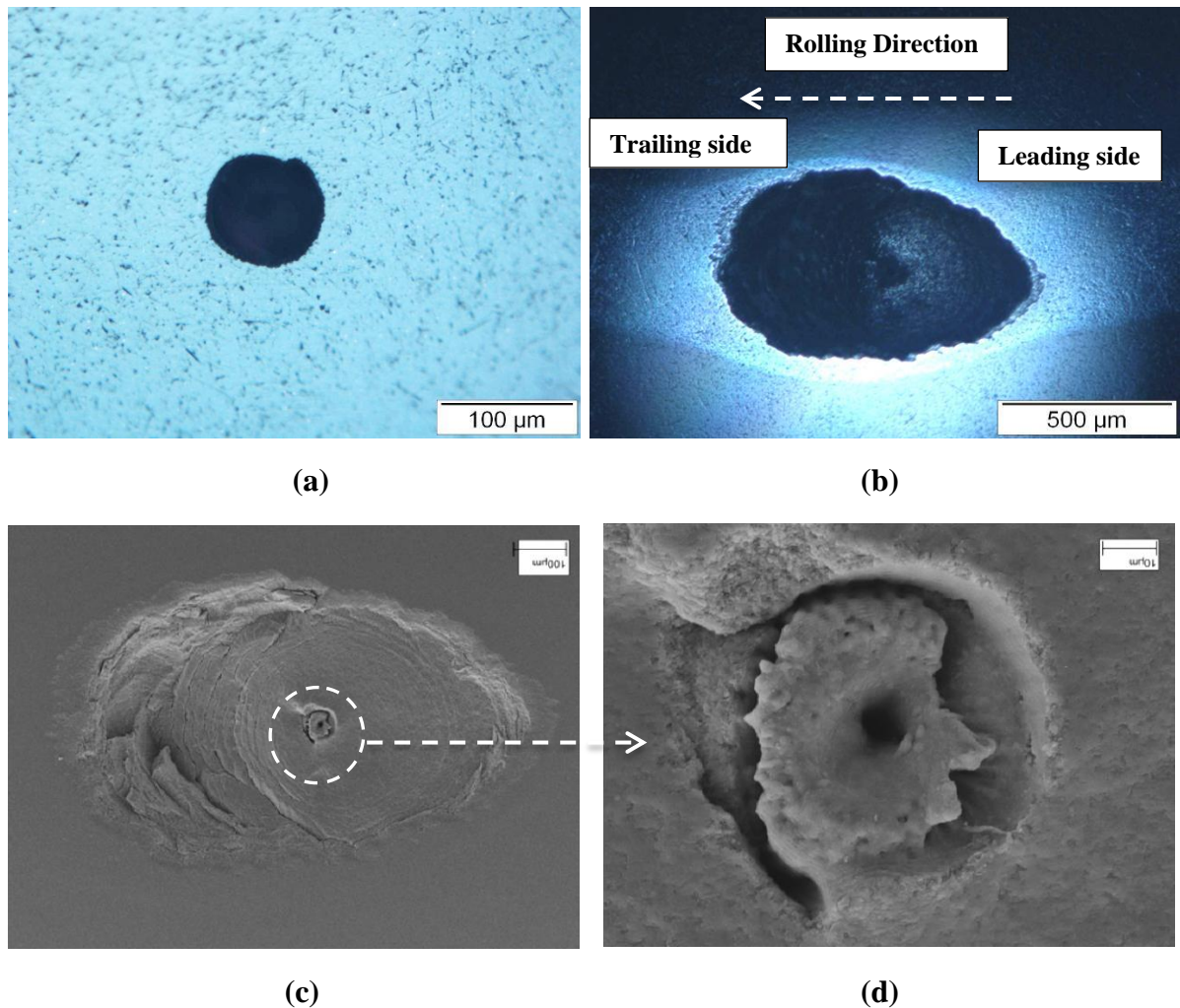
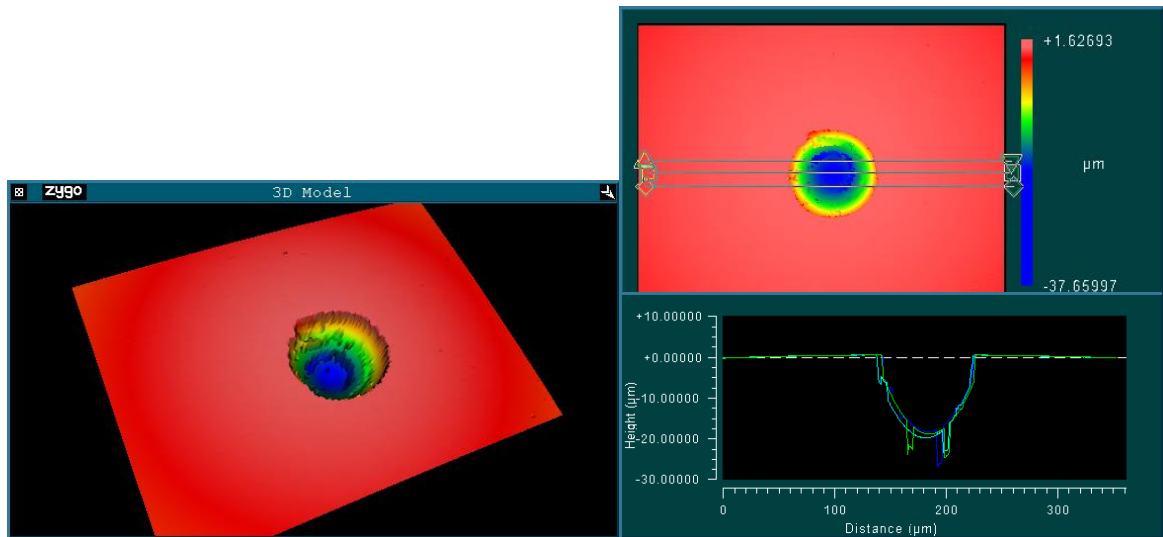


Figure 5.61: Surface analysis (Experiment 42) (a) pre-experiment (b) post 0.15M (c) Spall image - SEM (d) Spall centre (original hole base) - SEM image

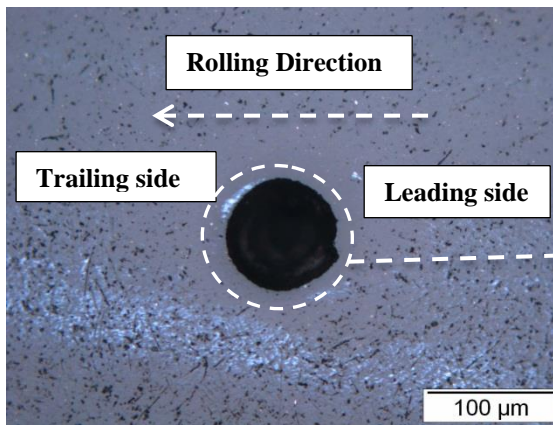
Similarly, second experiment (experiment 44) on shape II (conical) was also conducted but directly on high contact pressure for 100million stress cycles. Hole profile and post experiment surface image is shown in the Figure 5.63. In both experiments, there was no sign of failure or any new features including cracks, severe wear on the contact track or on the edges. These experiments along with two experiments of shape II (exp. 39 and 40) confirmed the tolerance of materials subject to shape II type defects on the surface.

Finally, two experiments were conducted on the shape III (oblique cylindrical) by taking cavity of around 100 μ m diameter and depth of 50 μ m. First experiment (experiment 45) was conducted at low contact pressure of 3.8GPa, resulted into spalling immediately running the test (post 0.1million stress cycles). Spall images are shown in the Figure 5.64.

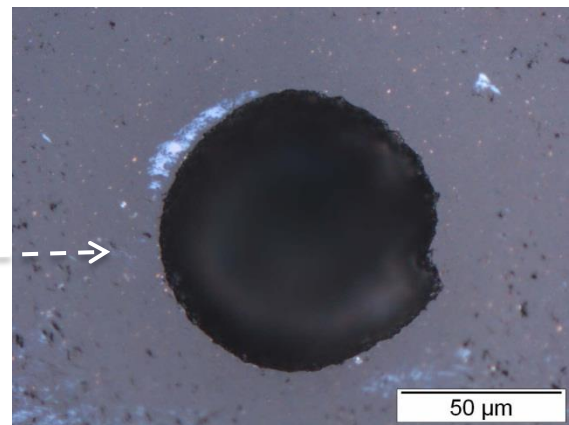


(a)

(b)



(c)



(d)

Figure 5.62: Surface analysis/mapping (experiment 43) (a) and (b) pre-experiment surface mapping using interferometry (c) and (d) post-experiment surface analysis using microscopy



(a)

(b)

Figure 5.63: Surface analysis/mapping (experiment 44) (a) pre-experiment surface mapping - interferometry (b) post-experiment surface analysis – microscopy

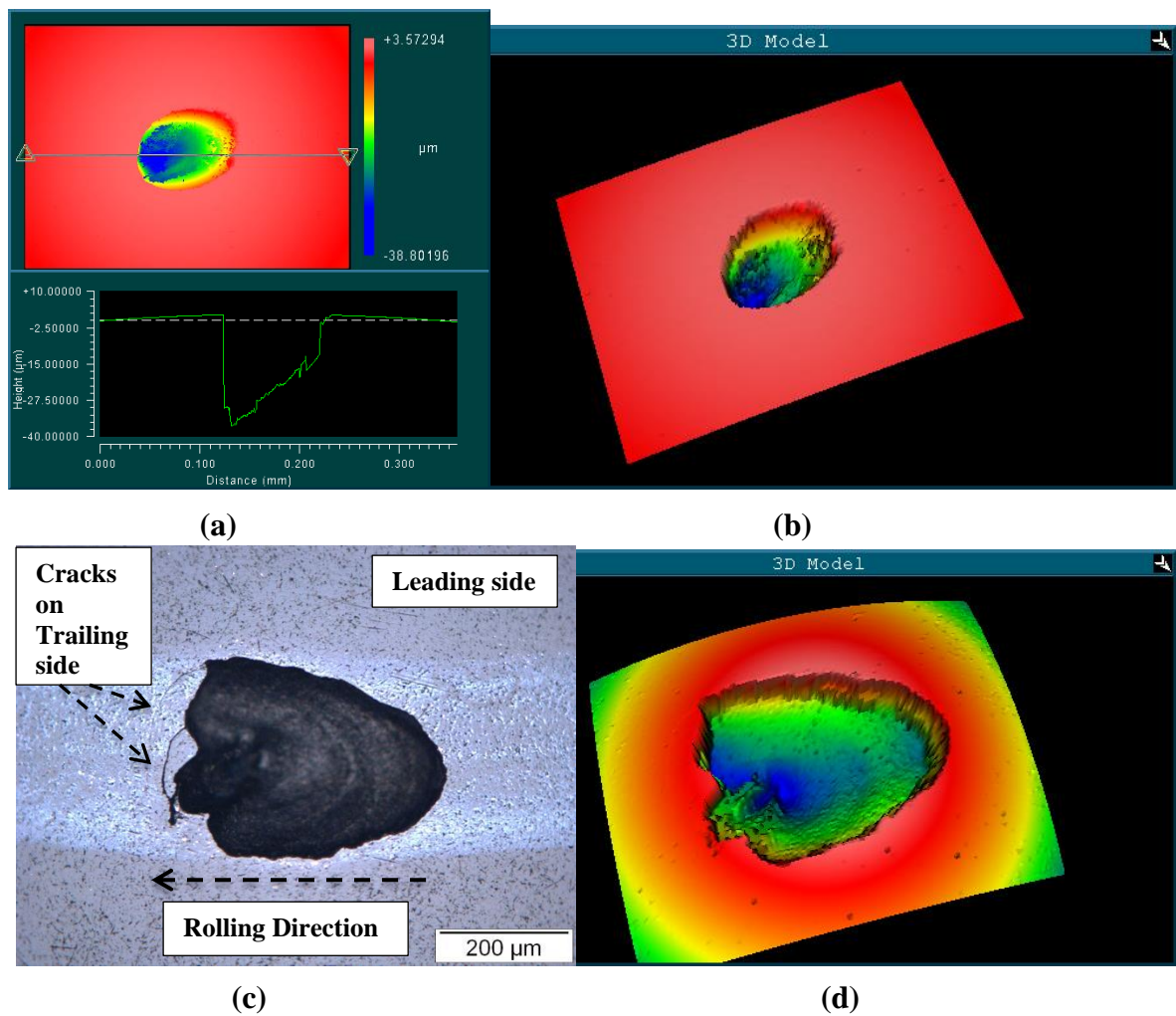


Figure 5.64: Surface analysis/mapping (experiment 45) (a) and (b) pre-experiment surface mapping using interferometry (c) & (d) post-experiment (0.1M) spall profile (OM and WLI)

Second experiment (experiment 46) was also conducted at same operating conditions to verify the results of first experiment. Cracks were observed on the surface post 0.2million stress cycles, however, test was further run until cracks network observed (insipient spall) on the surface. Experiment was suspended post 0.45million stress cycles to cross section the sample for subsurface observations. Pre- and post-experiment surface analysis is shown in the Figure 5.65.

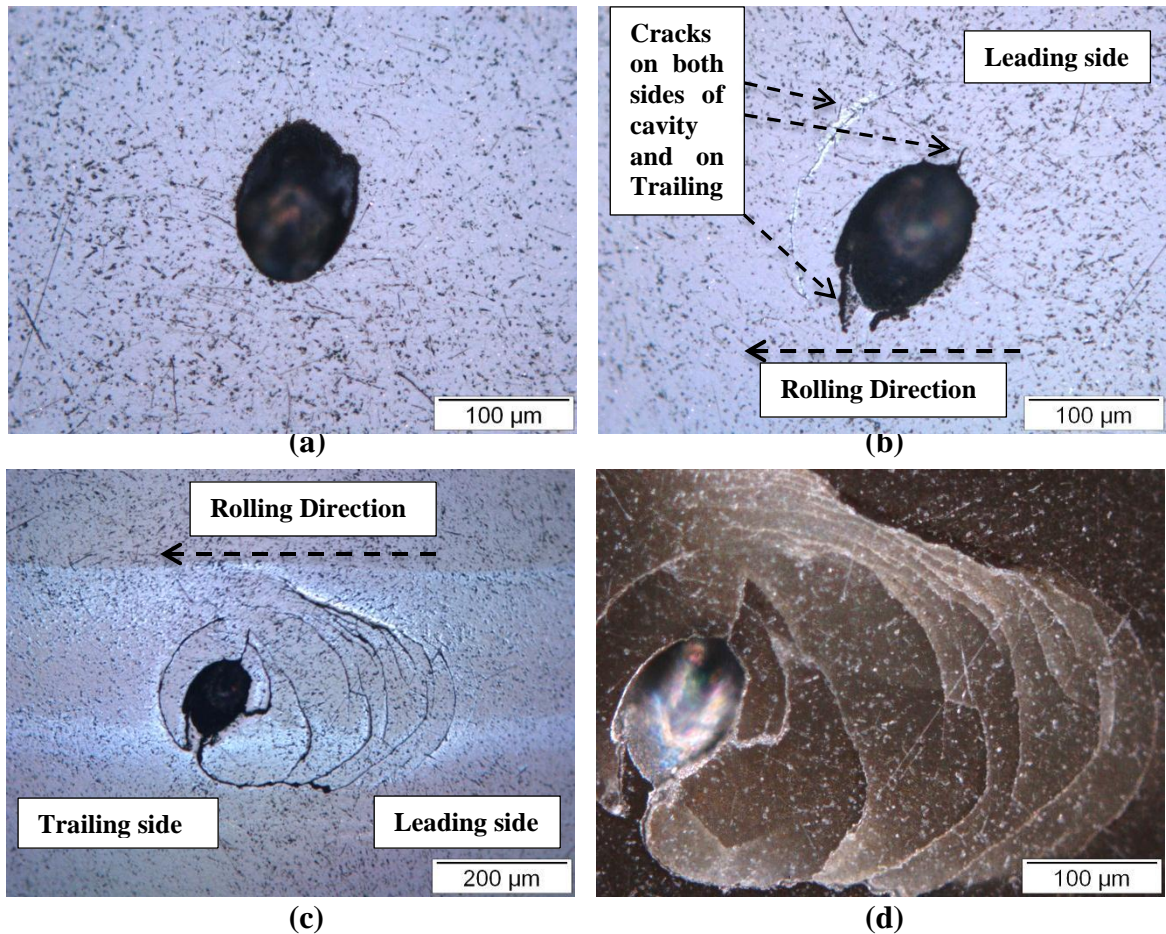


Figure 5.65: Surface analysis (experiment 46) using microscopy (a) Pre experiment (b) post 0.2million (c) and (d) post-experiment (0.45million stress cycles)

Post experiment surface analysis showing the crack from the cavity front and back sides and also from the trailing sides of the rolling direction. Over-rolling caused more cracks to propagate on the surface and making the crack brunch (insipient spall). This failure phenomenon is further discussed in the next section.

After conducting six exps. on the material performance subject to defects of different shapes, it has been observed that shape III (oblique cylindrical) is more prone to failure than shape I (right cylindrical) and shape I is more prone to failure than shape II (conical).

5.6. Contact pressure effect (contact vs. position)

Although general conclusions could be drawn about the effect of hole geometry in rolling contact tests, there were some anomalous results when balls with the same geometry gave different results when tested under the same conditions. One factor that could explain some of these results is the actual profile at the base of the cavity which showed some variation

(section 5.7). However, it was also observed that in some cases the position of the hole was not exactly at the centre of the contact track and sometimes nearly at the edge of the contact track. Apart from the experimental difficulty in exact positioning of a feature, high contact pressures and the frequent stops for inspection during tests meant that the ball could move slightly either in the collet or during re-insertion of the collet.

According to Hertzian theory in spherical contacts, the maximum pressure lies in the middle of the contact and decreases towards the edges. Contact pressure variation can be written as

$$P_r = P_0 \left[1 - \left(\frac{r}{a} \right)^2 \right]^{\frac{1}{2}} \dots\dots\dots(5.1)$$

Where

P_r = Contact pressure at distance ‘r’ from contact centre

P_0 = Maximum contact pressure at contact centre

a = Contact radius

r = Distance from contact centre

Graphs for contact pressure variations (based on equation 5.1) for 4.8GPa and 3.8GPa are shown along with FEA studies in the Appendix M.

It is important to mention that Hertz contact theory assumes that contacting parts surfaces are frictionless and smooth. In case of cavity in the contact, pressure distribution would be somehow different and would be high at cavity edges and zero pressure inside the cavity.

Using the observed difference between the defect (hole) centre and the centre of the contact track, calculated contact pressures were derived for the various experiments. Details of the experiments on Shape I(right cylindrical) and II (conical) holes have been revised to take into account the calculated contact pressures have presented in Appendix N.

Effect of contact pressure (corrected) and depth on the material performance and tolerance is shown in the Figure 5.66-5.69. Although these figures answers failure reasons for some cases however cavity base profile is also an important parameter to affect material tolerance (discussed in the next section). Further discussion is given in the discussion and conclusion section. Figs. 5.66 - 5.68 are showing experimental results for small, medium and large Shape I (right cylindrical) holes for material A only whereas in Figure 5.69 is showing the results for both material A and B for small hole diameter experiments.

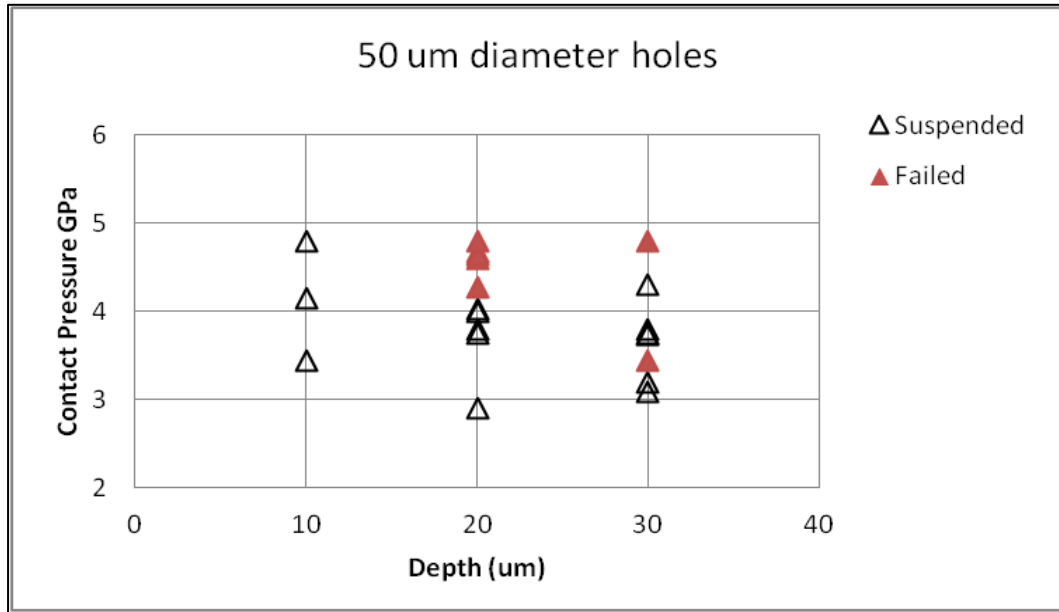


Figure 5.66 Corrected contact pressure vs. hole depth for small diameter holes (50 μ m)

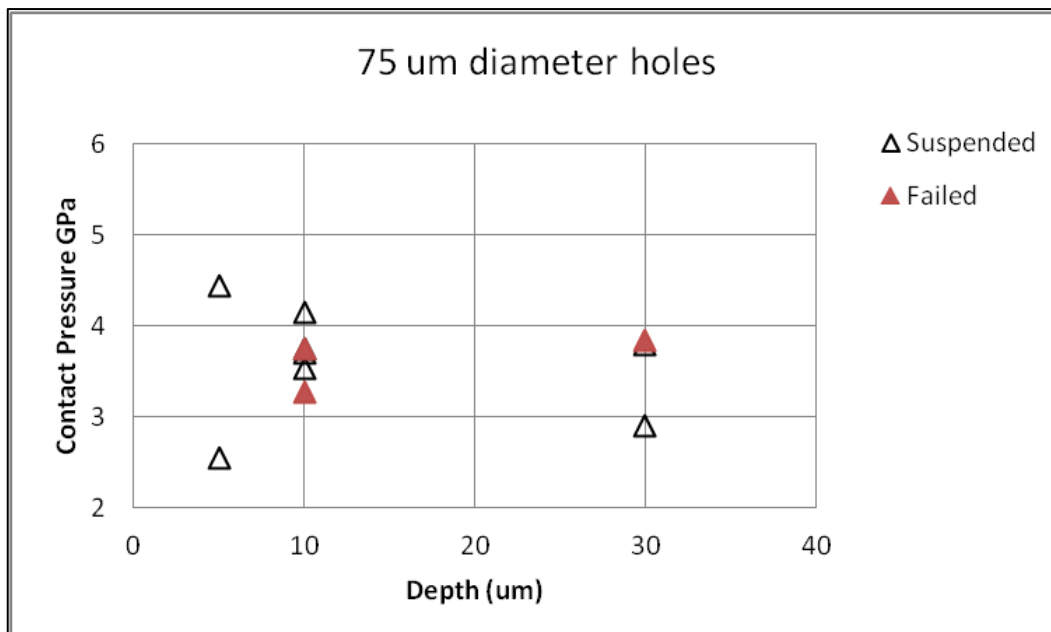


Figure 5.67 Corrected contact pressure vs. hole depth for medium diameter holes (75 μ m)

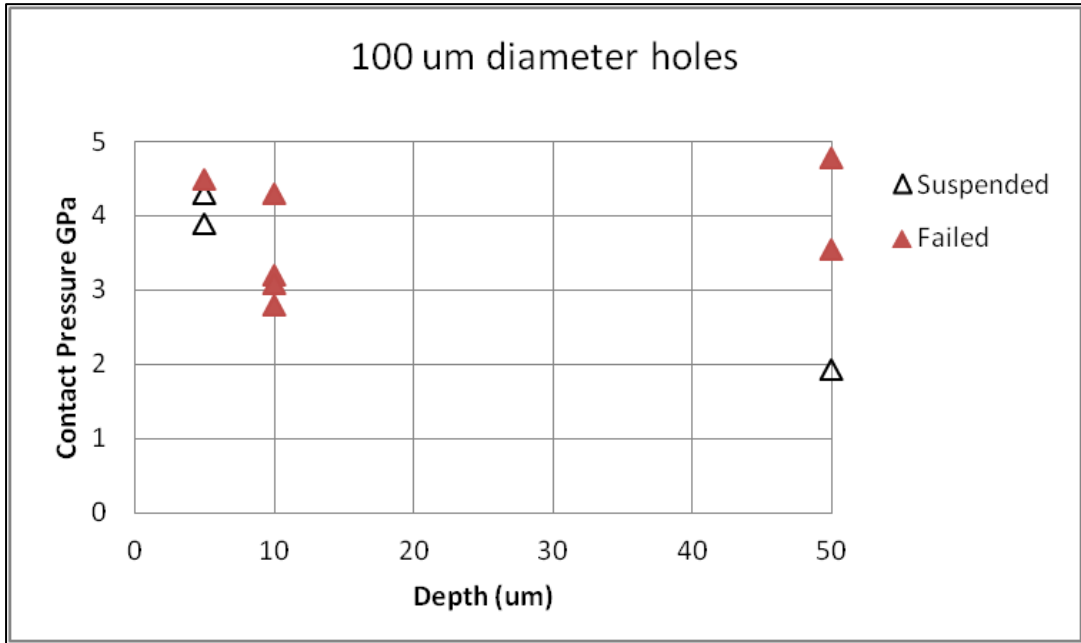


Figure 5.68 Corrected contact pressure vs. hole depth for large diameter holes (100 μ m)

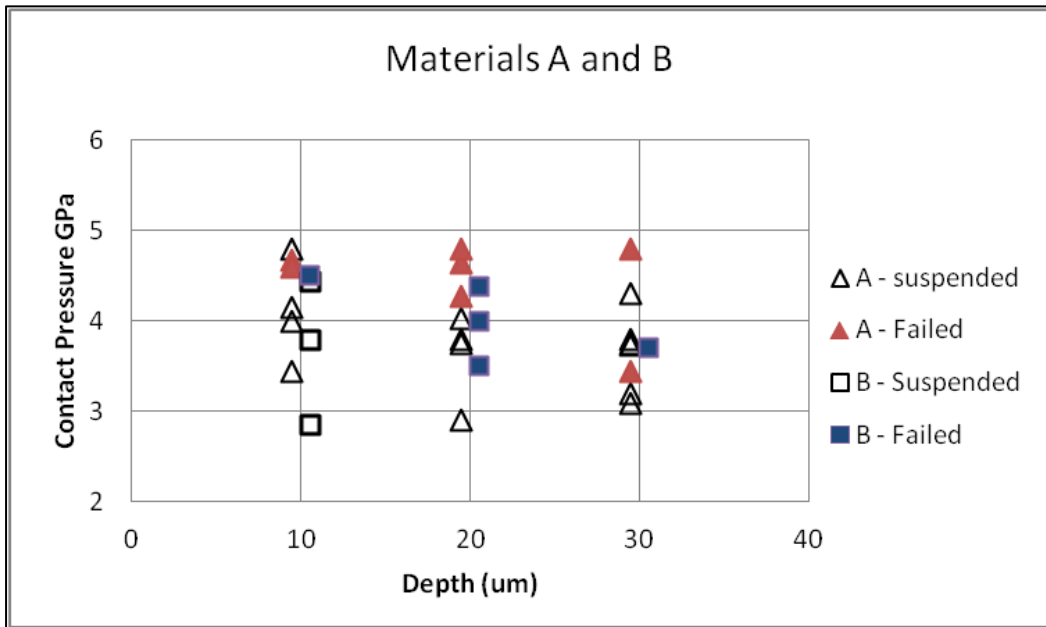


Figure 5.69 Corrected contact pressure vs. hole depth for shape I (right cylindrical) - small holes – Material A and B

5.7. Cavity base effect (Replica Study)

Experiments with same size cavities and operating conditions provided different results and one reason could be effective contact pressure (section 5.6) and another reason could be the cavity base profile. In practice, the laser machined holes showed some deviation from the designed profiles. Although interferometry provided some cavity profiles, some deep, sharp cornered and angled cavities cannot be scanned from interferometry. Replicas used to show better base profile for those cavities. Figure 5.70-5.71 show the cavity profile of typical shape I (right cylindrical), II (conical) and III (oblique cylindrical) shapes. Replica use has been discussed in chapter 2. Replica study explained some of experimental results of unfailed and failed samples due to cavity base profiles.

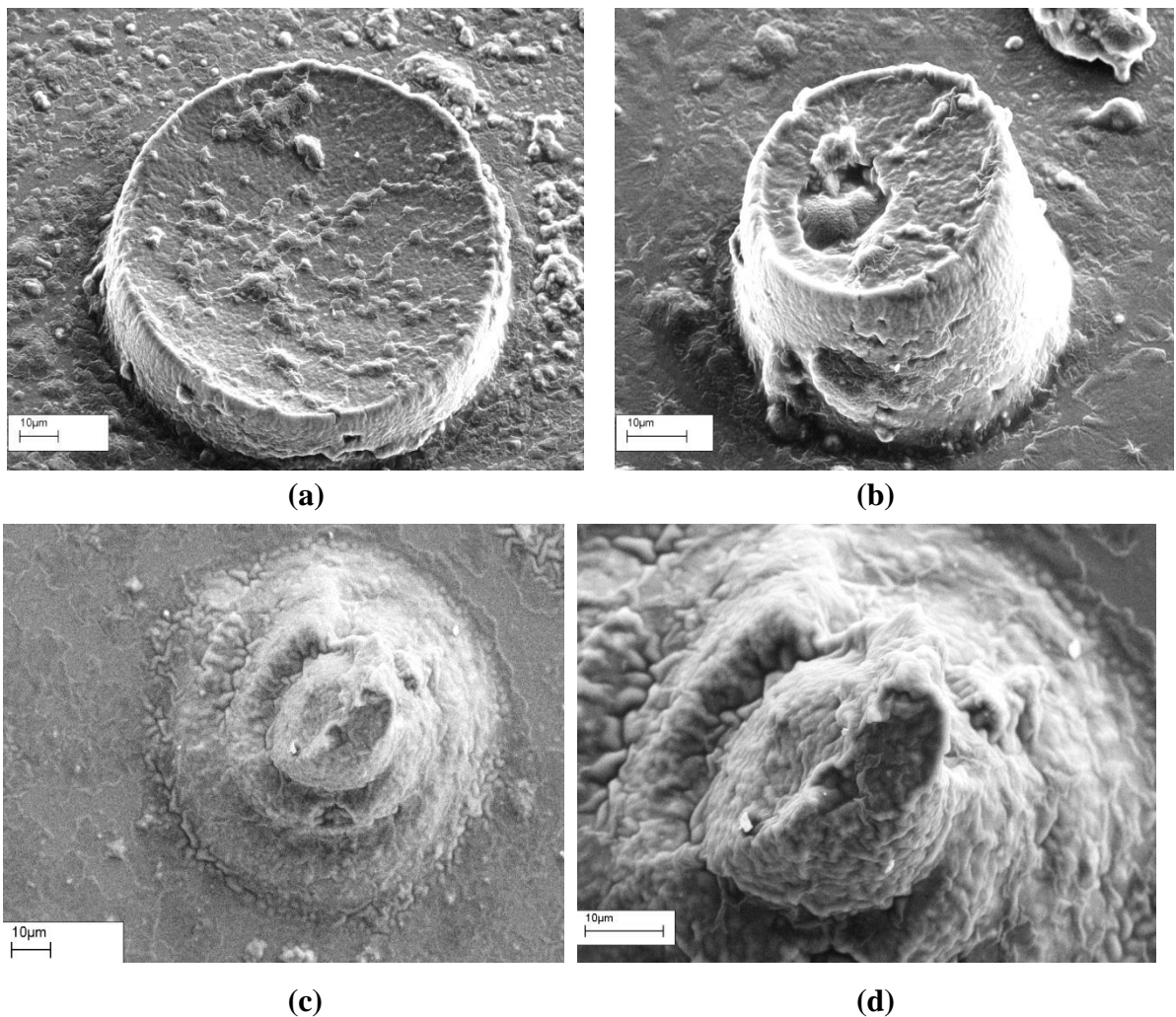


Figure 5.70: Replica cavity profile using SEM (a) and (b) Shape I (c) and (d) Shape II

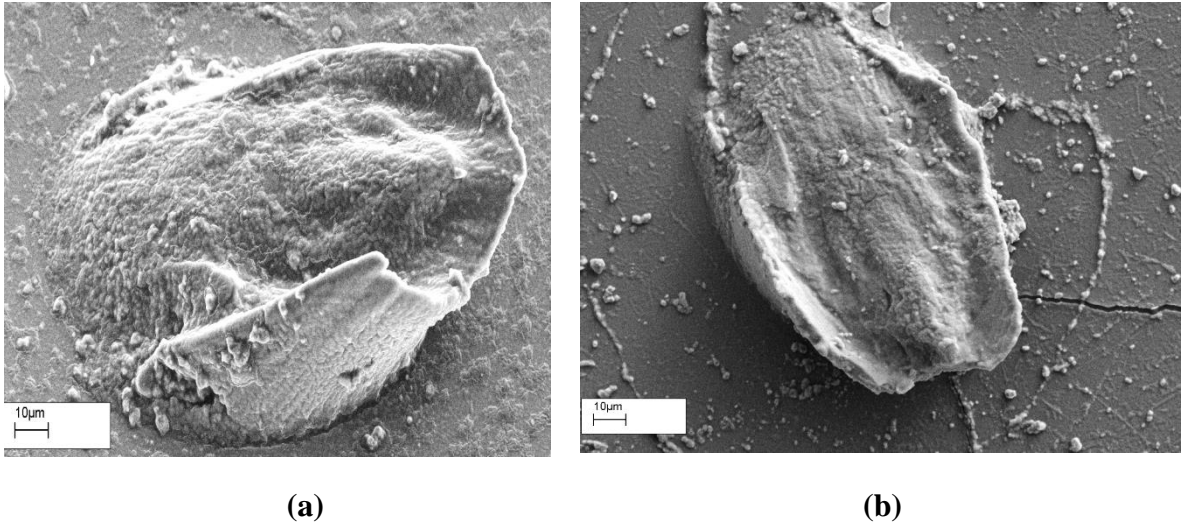


Figure 5.71: Replica cavity profile using SEM (a) and (b) Shape III

5.8. EDS Analysis

Some samples are also inspected through EDS analysis to see the post-experiment surface analysis for any changes in composition on the surfaces. Appendix O gives the EDS analysis of silicon nitride in missing material experiment 1 (on the eroded surface area).

5.9. Failure Mechanism

Failure mechanisms were investigated by both surface examinations of spalls produced under rolling contact and by cross-sectioning. Surface examination of spalls from laser machined holes showed certain similarities. In all cases the bottom of the cavity/hole could still be distinguished in the spall indicating that the failure initiation was cracks forming at or near the bottom corners of the holes. Furthermore, in almost all cases, the spall was deeper on the trailing side than the leading side. (Some experiments resulted in multiple spalls possibly due to continued over-rolling before the machine shut down).

Some experiments did not result in spalls but were classified as ‘failed’ due to crack networks around the hole (incipient spalls). Again, these crack patterns showed similarities with cracks being prevalent on the leading side.

5.9.1. Unfailed Balls

Several balls with 50µm diameter Shape I holes were cross-sectioned without being tested under rolling contact and others after testing to suspension at 100 million cycles (successfully completed predefined number of cycles). No cracks were observed with

untested balls nor with unfailed balls with hole depths of 10 and 20 μm . Some unfailed balls with 30 μm deep holes did show small cracks towards the base of the cavity. As can be seen in Figures 5.72 and 5.73, these cracks were typically only about 5 μm long and it is possible that they were either the result of laser machining or were formed during specimen preparation. Some suspended samples (tested at high pressure and completed number of predefined cycles) with no cracks can be seen in the Figures 5.74-5.75.

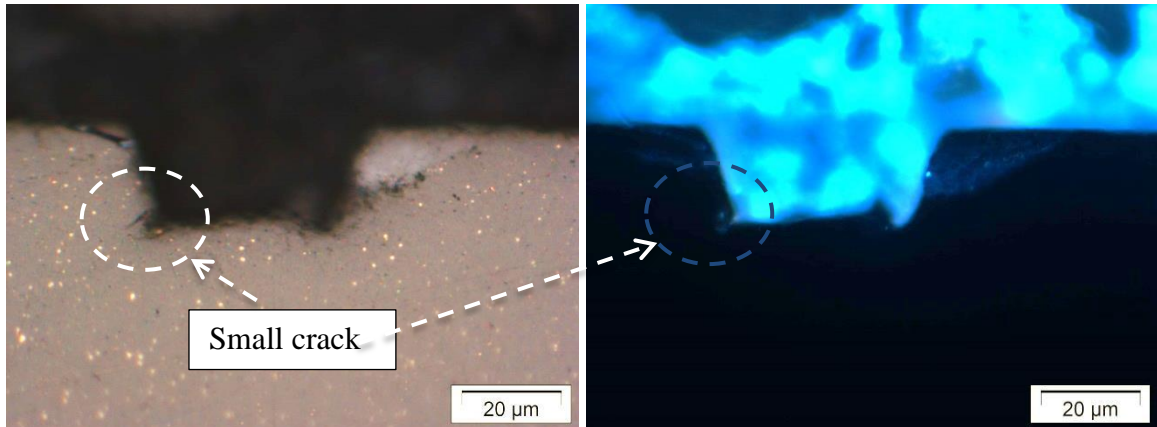


Figure 5.72: Small cracks near cavity base – Experiment 16 (successfully completed)

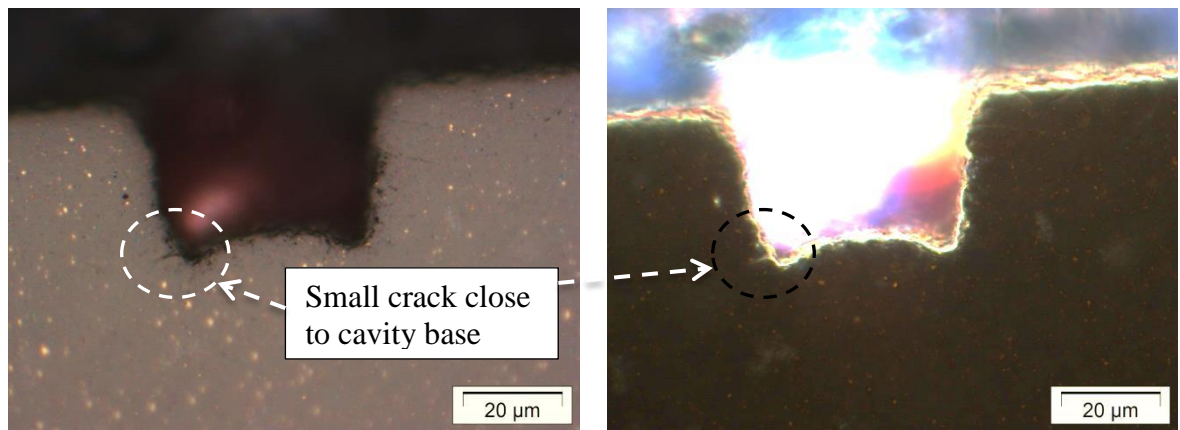


Figure 5.73: Small cracks near cavity base – Experiment 20 (successfully completed)

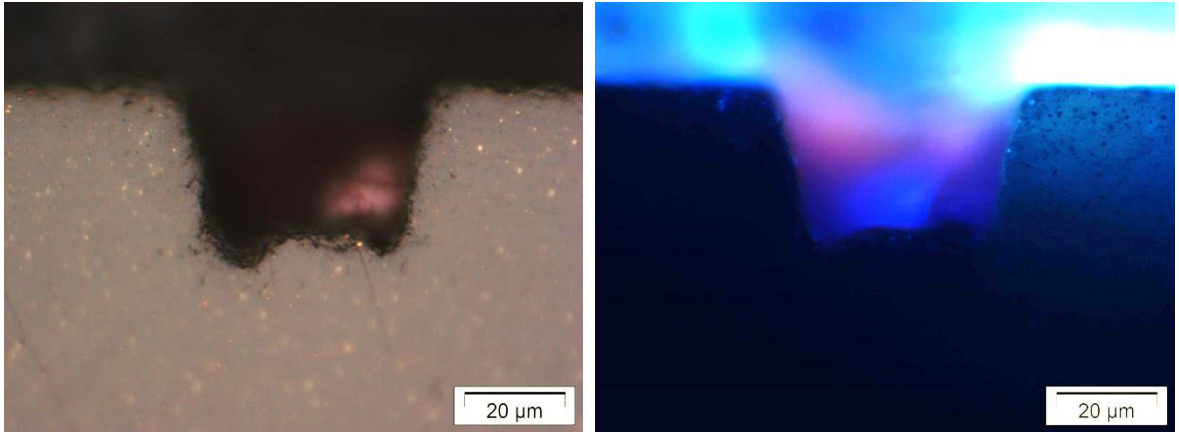


Figure 5.74: No cracks observed – Experiment 18 (successfully completed)

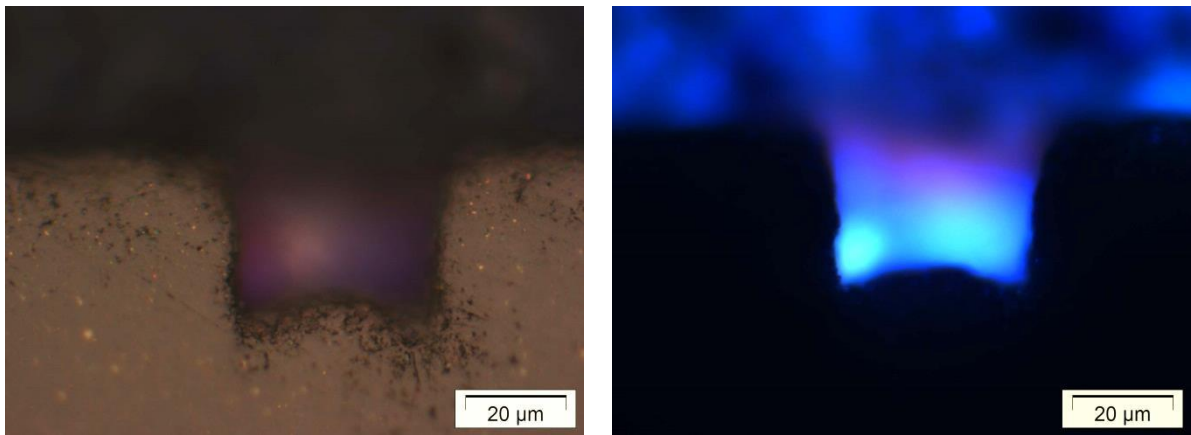


Figure 5.75: No cracks observed – Experiment 19 (successfully completed)

5.9.2. Spalled Balls

Surface examination of a spall is shown in Fig. 5.76. This has a relatively flat (at the depth of 30-40 μm) region on the leading side (right) and a deeper area (more than 70 μm) on the trailing side. Examination under ultraviolet illumination shows little or no fluorescence on the leading side but strong fluorescence on the trailing side indicating deep cracks.

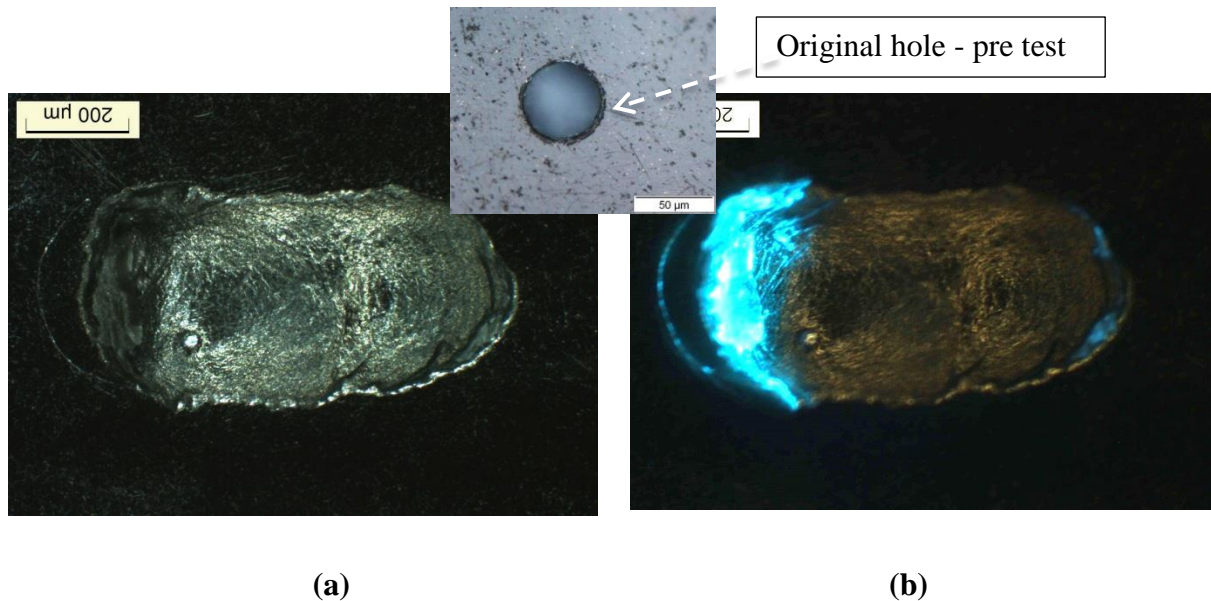


Figure 5.76: Experiment 13 spall profile (original hole : 50 μm diameter and 30 μm depth) (a) dark field illumination (b) UV illumination (original hole also can be seen in the Figure)

A typical failure for a shape I hole is shown in Fig. 5.77. The spalled area on the leading side (right) is relatively flat and smooth but at the trailing side the spall is deeper and uneven. This is apparent both with optical microscopy (darkfield) and by Profilometry (WLI).

The location of the pre-existing defect (laser machined hole) is clearly visible inside the spall region. This indicates that cracks were initiated at or towards the base of the cavity and that there was significant crack growth before the actual failure occurred. Crack initiates/grows from the hole bottom and travels downward from leading and trailing edge but more deeper in trailing edges. Crack propagation happened probably in the direction normal to maximum principal stress [Ueda 1989] at close to bottom of the hole and form the cone crack propagation profile by going down (deeper) and then to surface. Due to crack growth, spall found shallow at the leading edge and deeper at the trailing edge. Deeper spall on trailing edge may be due to pressure hitting that edge. Crack propagation is almost similar to ring crack propagation as reported before [Hadfield et al. 1993a, Wang 2001, Khan 2006, Zhao 2006]. Figure 5.77 is also showing the original hole tested and post 30million stress cycles with surface wear on the track.

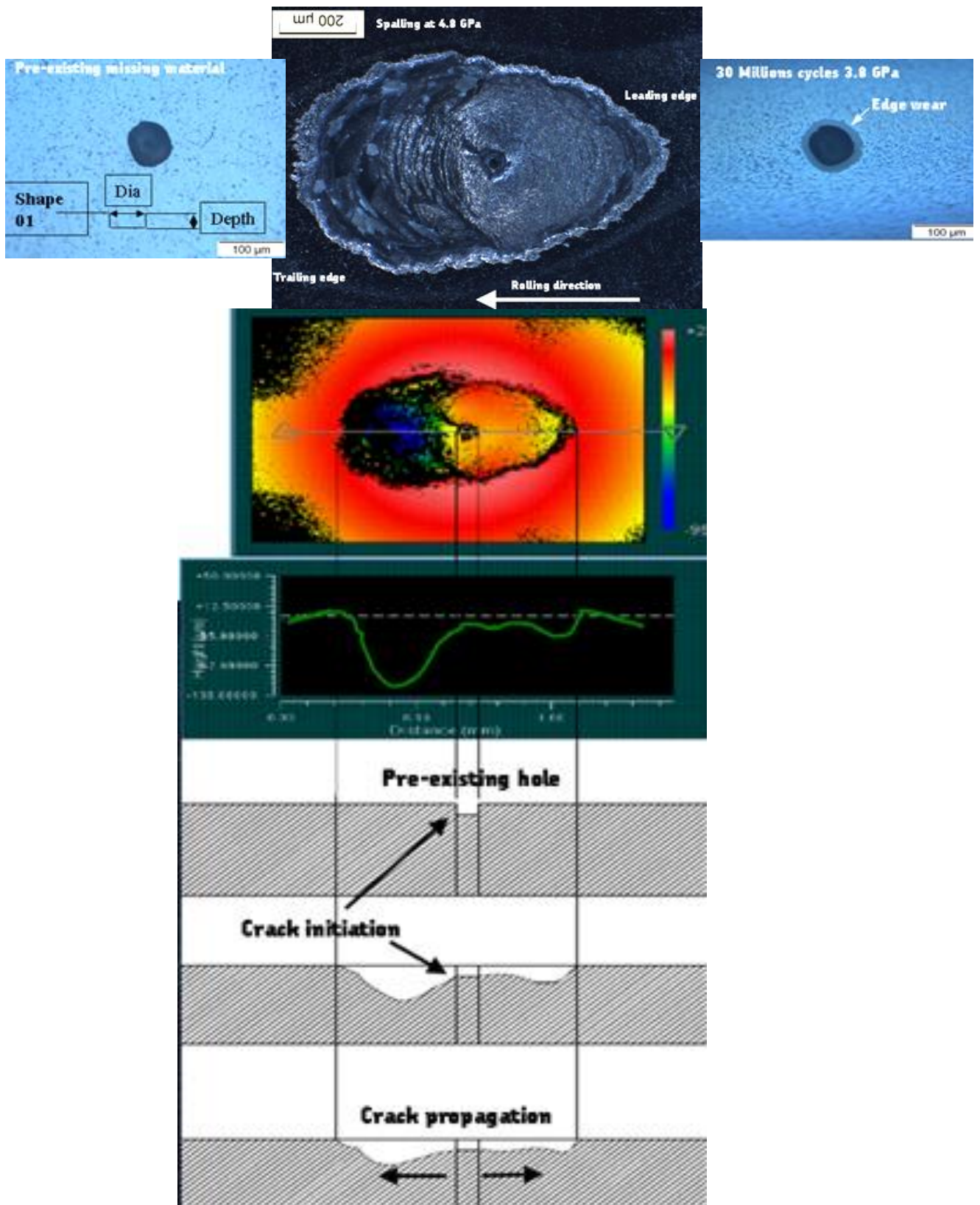


Figure 5.77: Typical spalling mechanism with Shape I profile

Some spalls were examined by cross-sectioning. A multi-step process was used to cross section the sample to explore the subsurface cracks in detail. The ball was first cut using a resin bonded diamond saw (cut-off wheel) close to the original hole and then ground, lapped and polished for examination by optical microscopy. Then the samples were processed with a fluorescent penetrant and examined under UV illumination. The next step was to grind back and the specimen to the initial hole, and re-polish and repeat the inspection. Finally another section was prepared on the other side of the hole.

Figs. 5.78 to 5.81 show sections from the spall obtained with experiment 13 (from a hole 50 μm in diameter and 30 μm deep). The first section (Figs 5.78 and 5.79) was close to the edge of the spall. On the leading side, there was only one crack at the edge of the spall but on the trailing side there was a pronounced crack angled downwards with subsidiary finer cracks extending downwards as well as a surface crack. This pattern was repeated in the sections at the edge of the hole (Fig. 5.80) and through the centre of the hole (Fig. 5.81). The angle of the large crack to the surface was 22-23 $^\circ$ with a radial depth of approx. 90 μm .

A section through the centre of a hole/spall from a large hole is shown in Figs. 5.82 and 5.83. In this case (experiment 42) the hole diameter was 100 μm and the depth 50 μm . On the trailing side, no main crack was visible as material had completely broken out. However, a number of subsidiary cracks can be seen. The spall at the trailing edge had an initial angle of 27 $^\circ$ and the radial depth was approximately 134 μm .

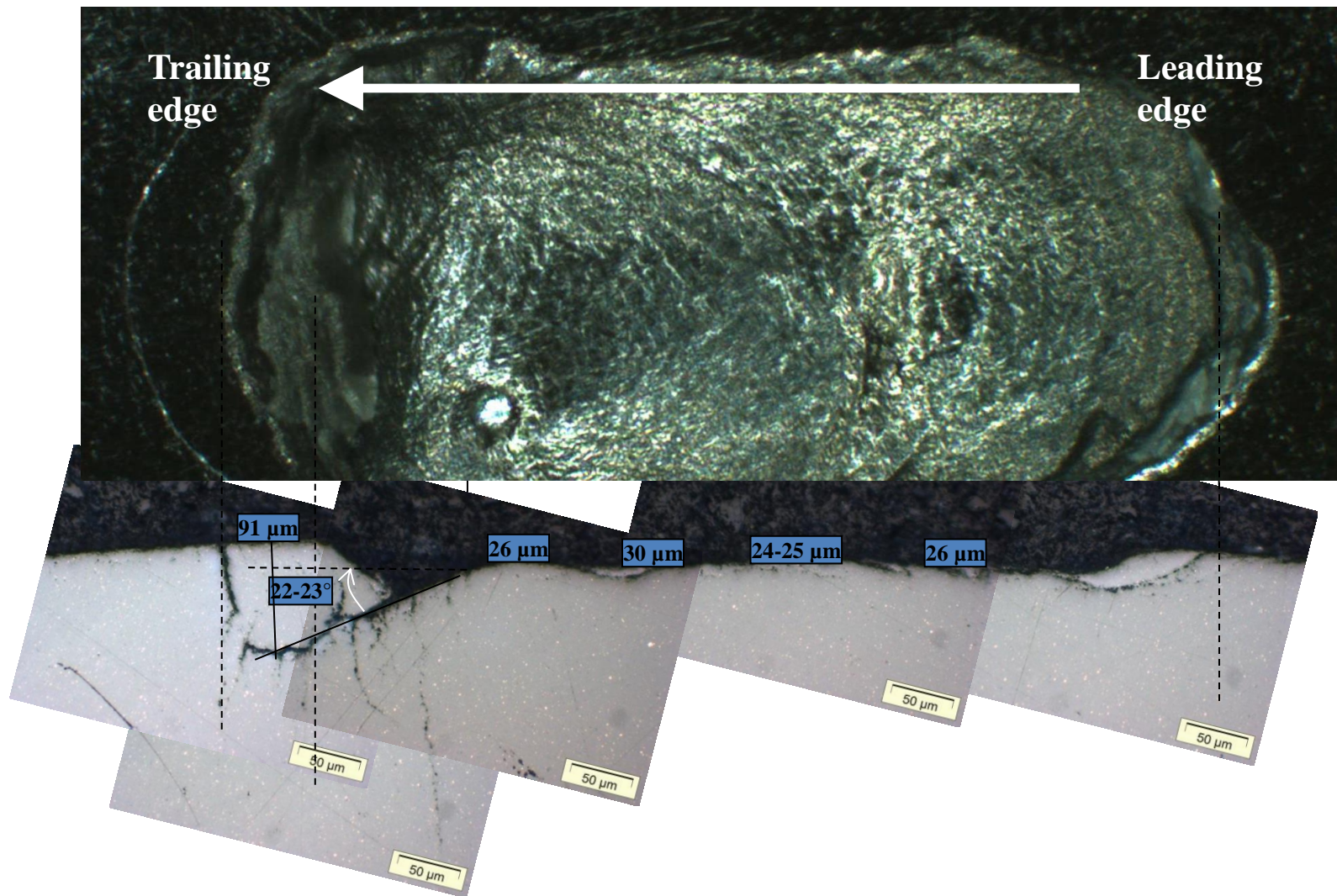


Figure 5.78: Spall analysis (exp. 13, Dia: 50μm, Depth: 30μm) of cross sectioned sample using microscopy (light illumination) - first finishing

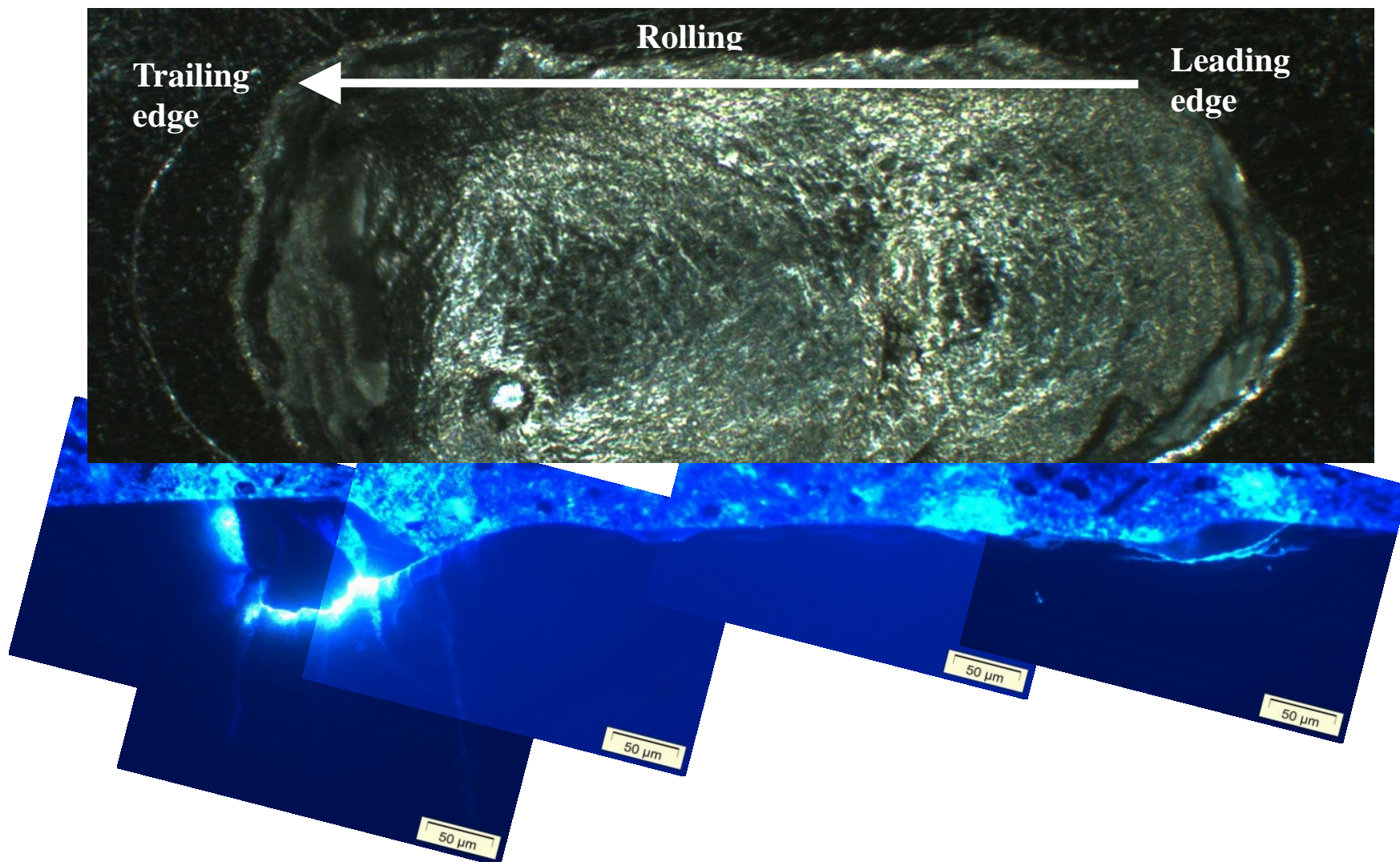


Figure 5.79: Spall analysis (exp.13, Dia: 50μm, Depth: 30μm) of cross sectioned sample using microscopy (UV illumination) - first finishing

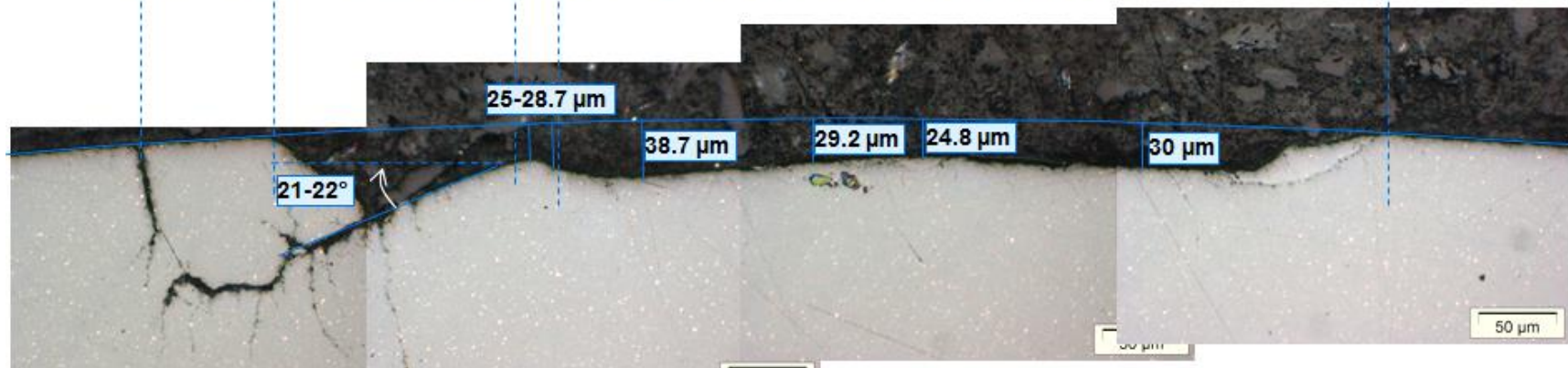
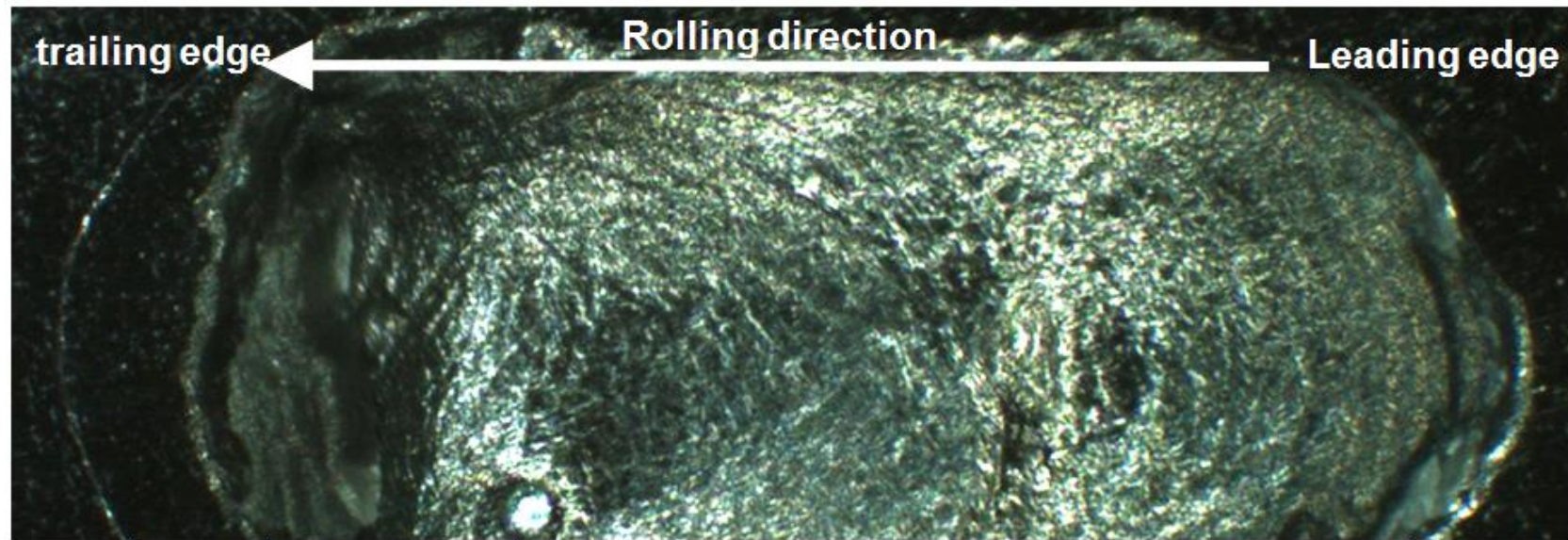


Figure 5.80: Spall analysis (exp.13, Dia: 50μm, Depth: 30μm) of cross sectioned sample using microscopy (light illumination) - second finishing

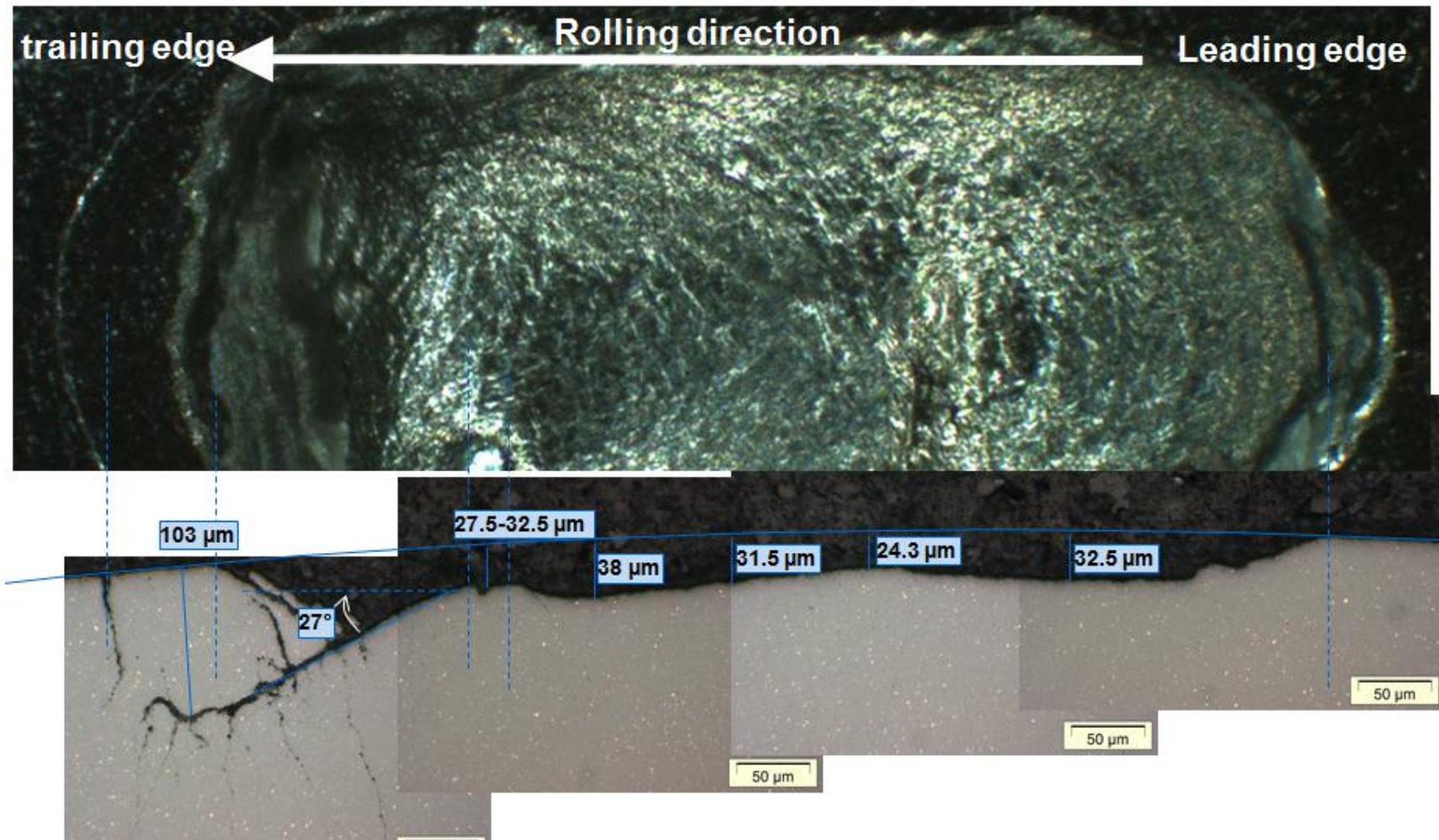


Figure 5.81: Spall analysis (exp.13, Dia: 50μm, Depth: 30μm) of cross sectioned sample using microscopy (light illumination) - 3rd finishing

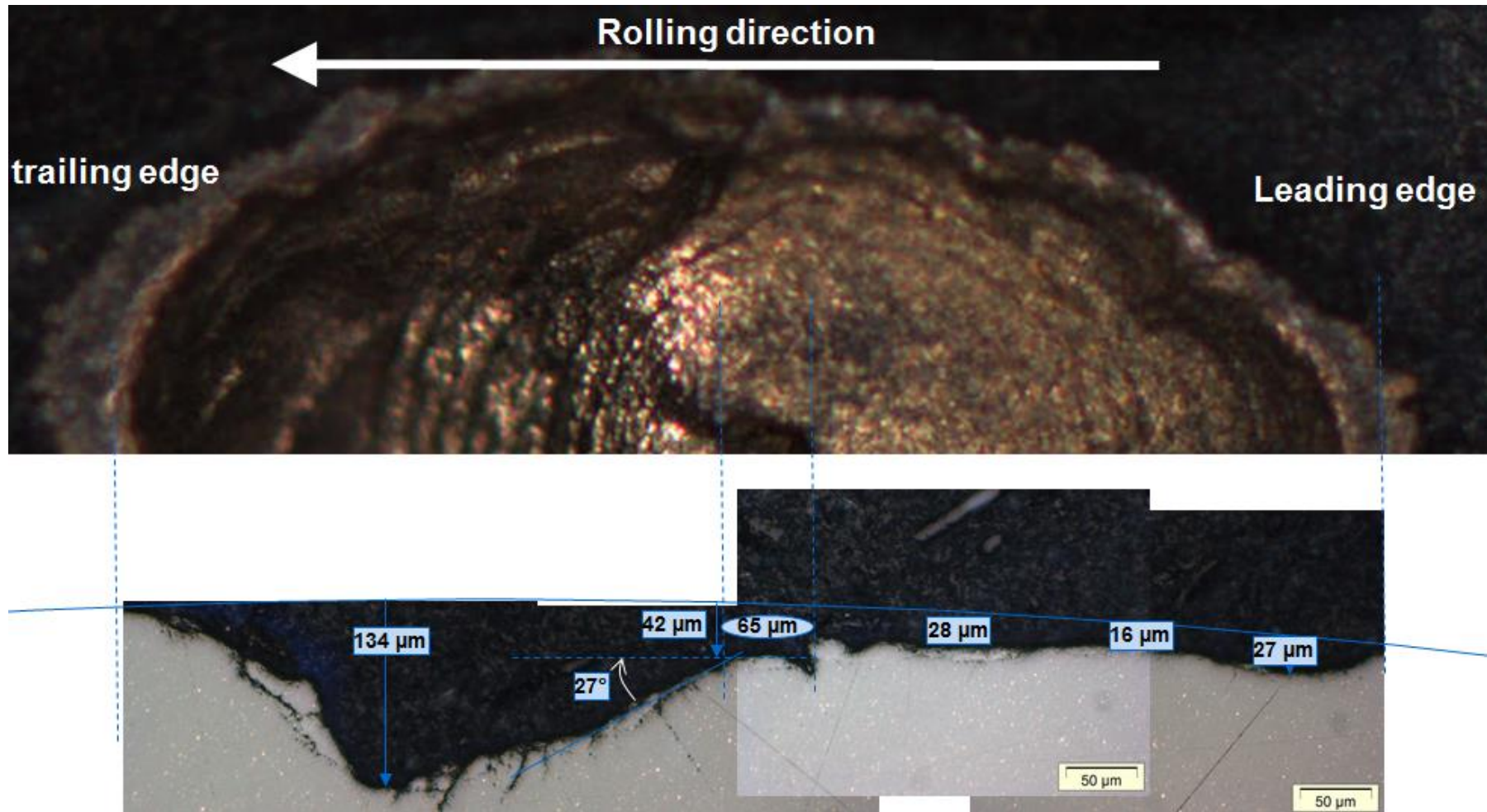


Figure 5.82: Spall analysis (exp.42, Dia: 100 μm , Depth: 50 μm) of cross sectioned sample using microscopy (light illumination) - 3rd finishing

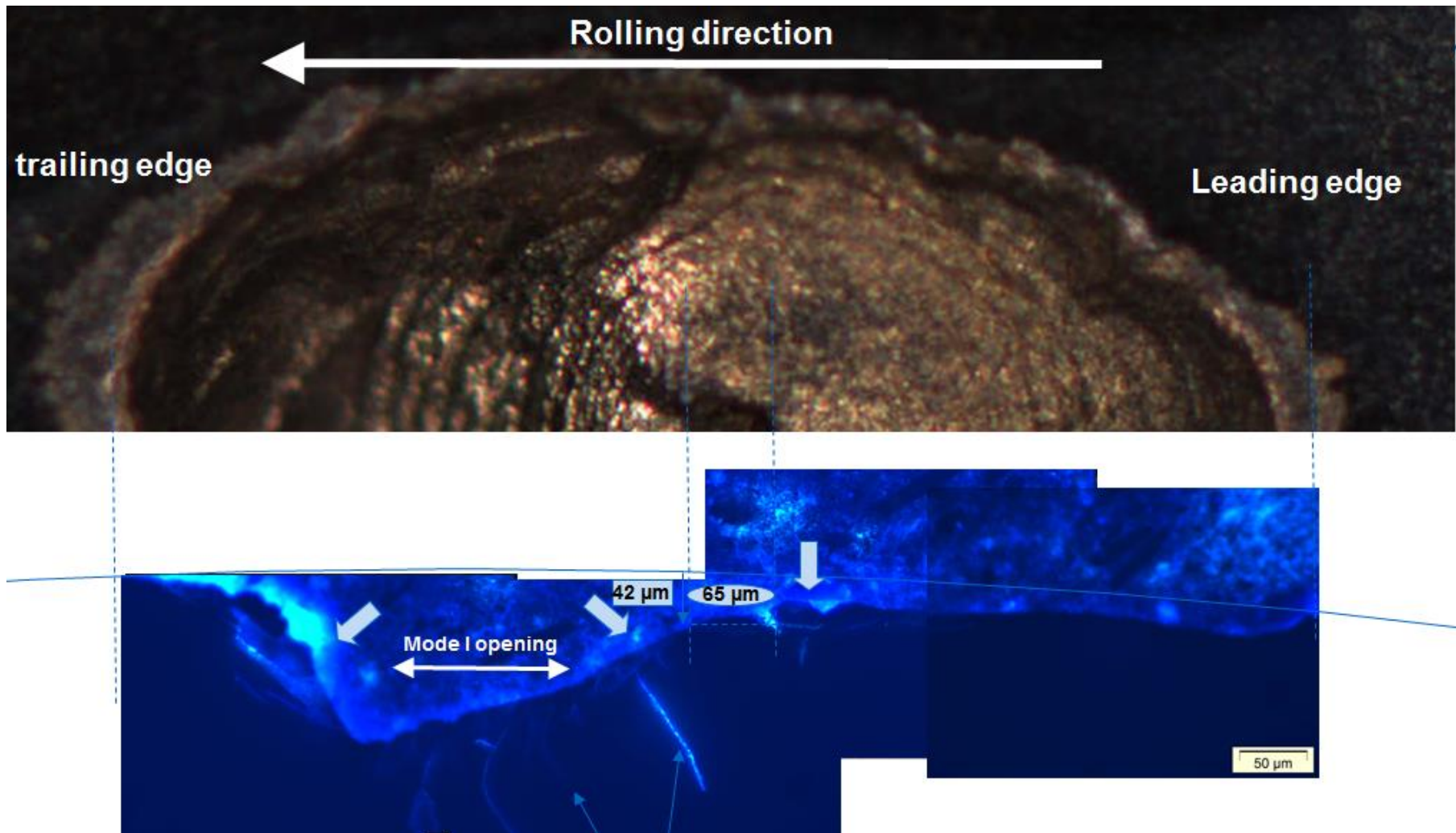


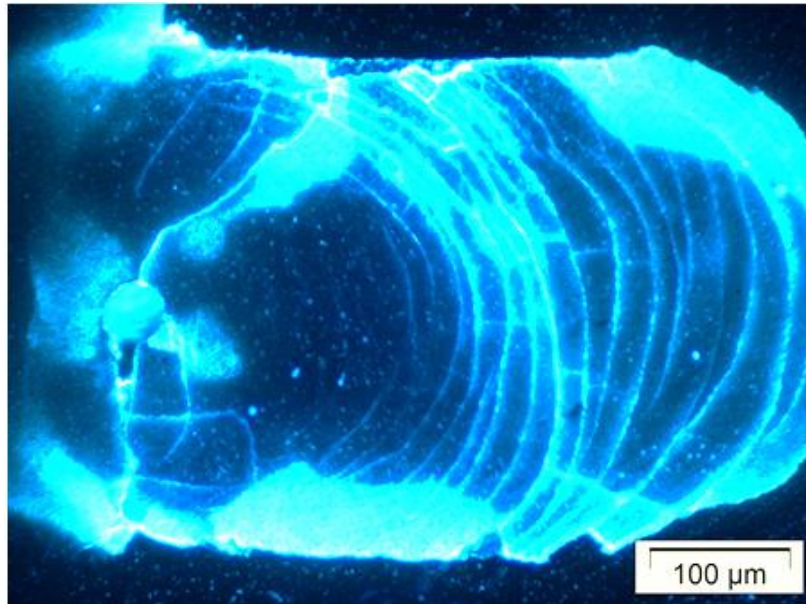
Figure 5.83: Spall analysis (exp.42, Dia: 100μm, Depth: 50μm) of cross sectioned sample using microscopy (UV illumination) - 3rd finishing

5.9.3. Incipient Spalls

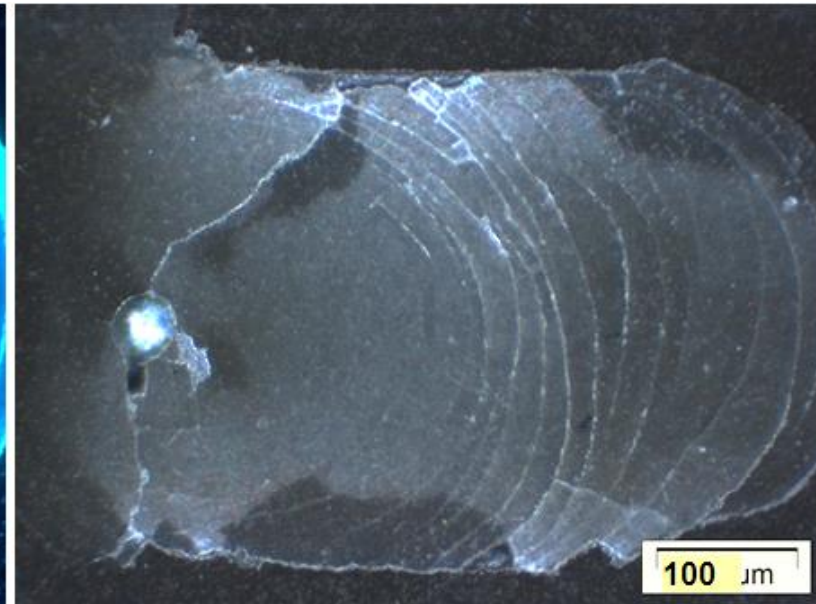
Some experiments were terminated before failure when crack networks (incipient spalls) were observed on the test balls during periodic inspections and/or when the machine was stopped by the vibration sensor due to increased friction of crack networks on the surface. An example is shown in Fig. 5.84. Some of these balls were sectioned to examine the sub-surface nature of the cracks. Figs. 5.85 to 5.88 show sections of the ball from experiment 6. These show a long sub-surface crack running parallel to the surface on the leading side (right) and a shorter but deeper crack on the trailing side (left). On the leading side cracks branch upwards to the surface. There is also crack branching both upwards and downwards from the trailing side crack.

Another incipient spall is shown in Figure 5.89. In this case there are fewer surface cracks but both the darkfield image and that with ultraviolet light indicate the presence of a sub-surface crack on the leading side. This sample also showed short cracks at the sides of the hole in a direction normal to the contact track. Sections from this ball are shown in Figs. 5.90 to 5.93. These show the shallow parallel crack on the leading side and the angled crack on the trailing side. It is interesting to note that the crack branching on the leading side first takes place at some distance from the hole (seen from the surface) and also that there is extensive crack branching in the downward direction on the trailing side.

As silicon nitride is a brittle material, therefore, this process happens quite quickly and converted into full-scaled spalls after short time of over-rolling of incipient spalls.



(a)



(b)

Figure 5.84: Surface analysis (experiment 6, Dia: 50 μ m and Depth: 20 μ m) using microscopy (a) post 50million stress cycles (UV illumination)
(b) post 50million stress cycles (dark field illumination)

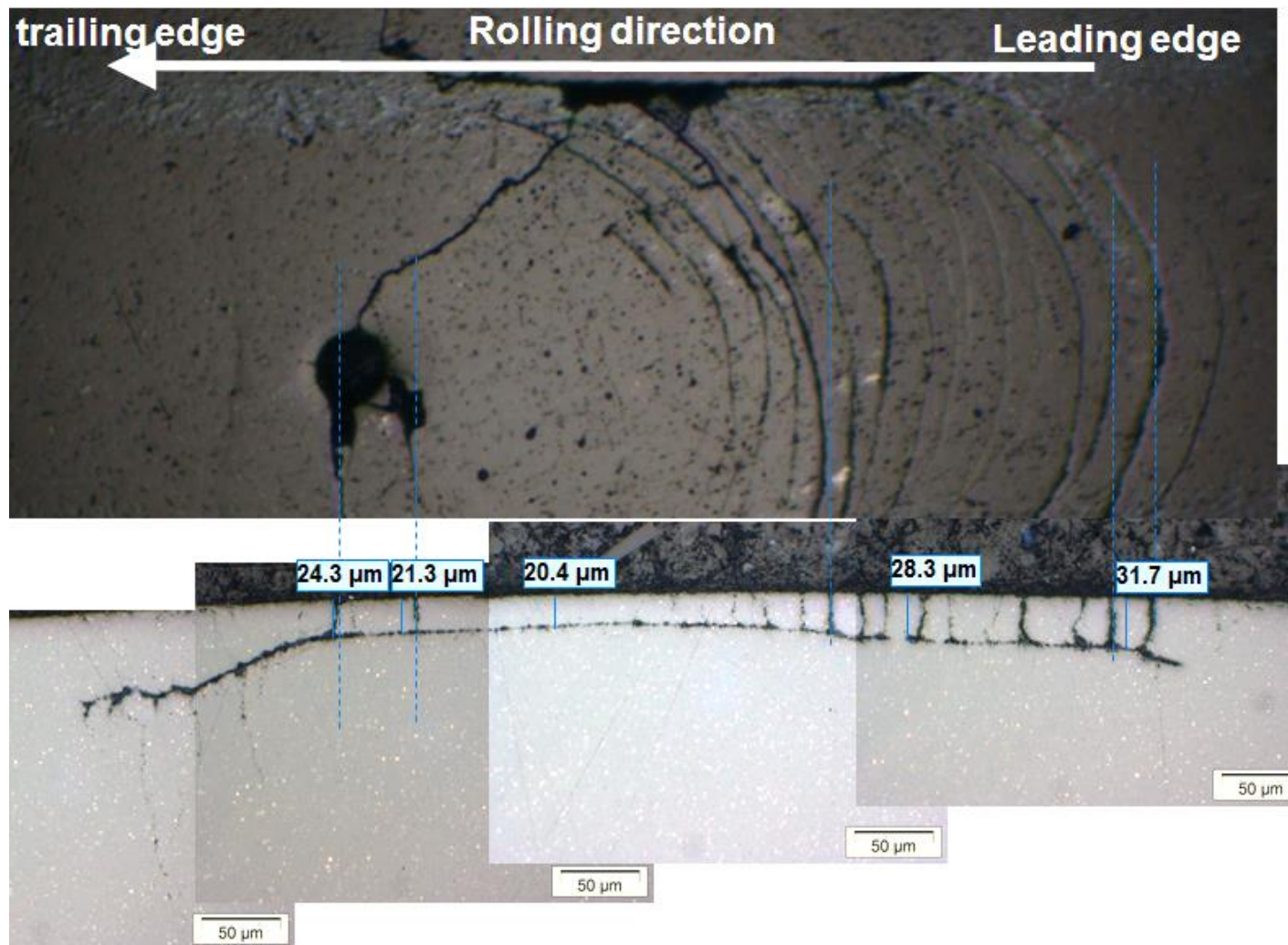


Figure 5.85: Sub-surface analysis (exp.6, Dia: 50μm, Depth: 20μm) using microscopy (light illumination) - First finishing

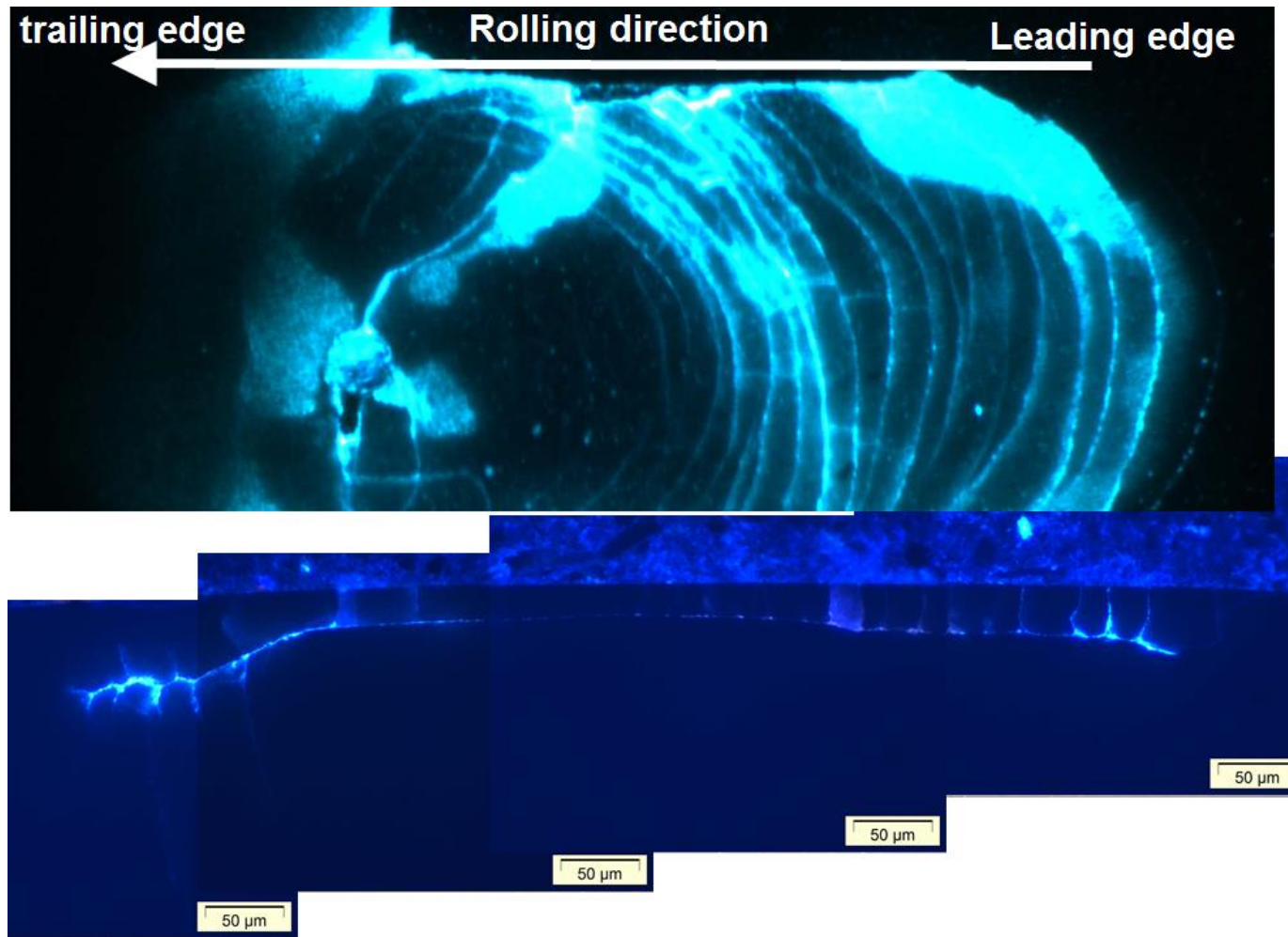


Figure 5.86: Sub-surface analysis (exp.6, Dia: 50μm, Depth: 20μm) using microscopy (UV illumination) - First finishing

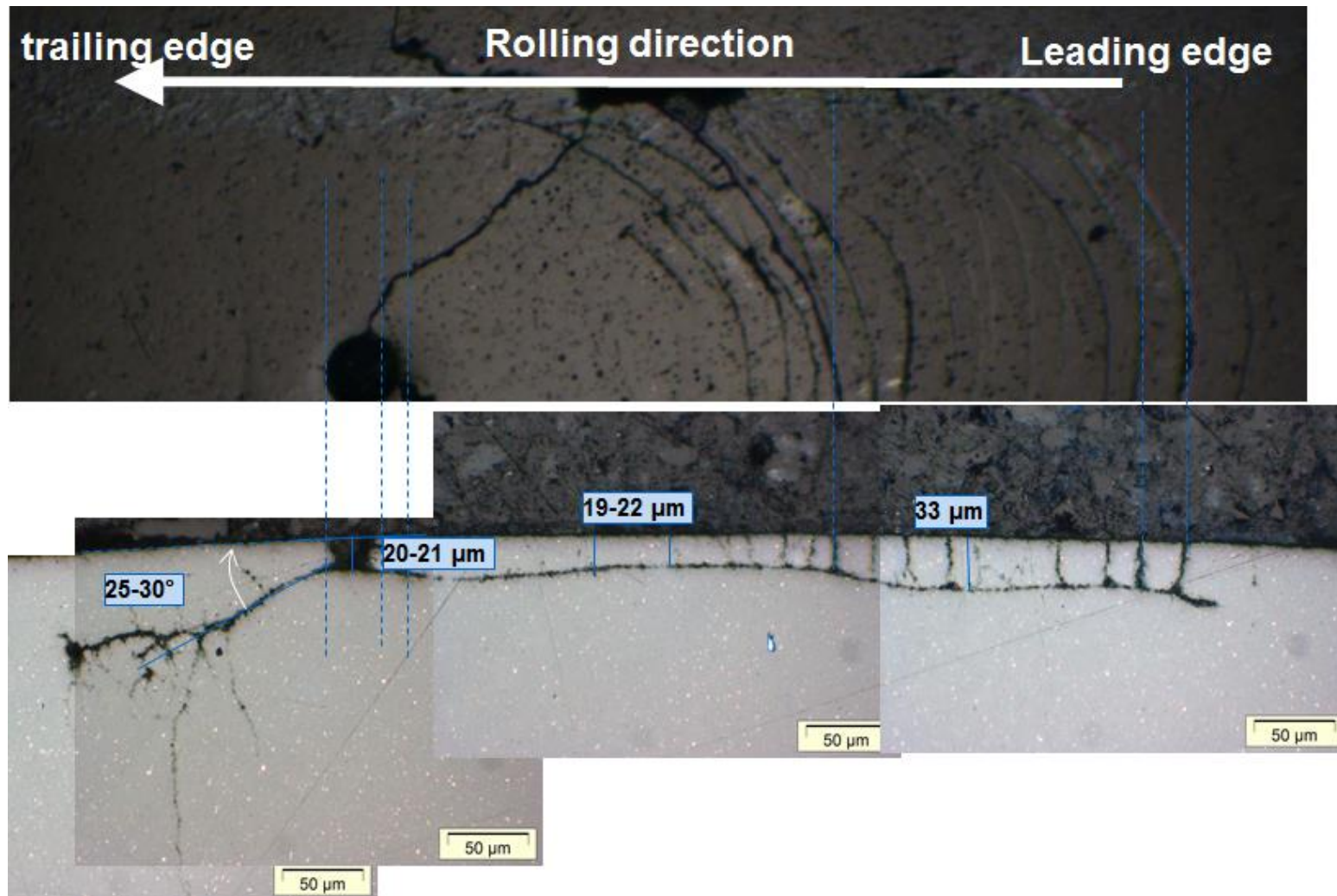


Figure 5.87: Sub-surface analysis (exp.6, Dia: 50μm, Depth: 20μm) using microscopy (light illumination) - 2nd finishing

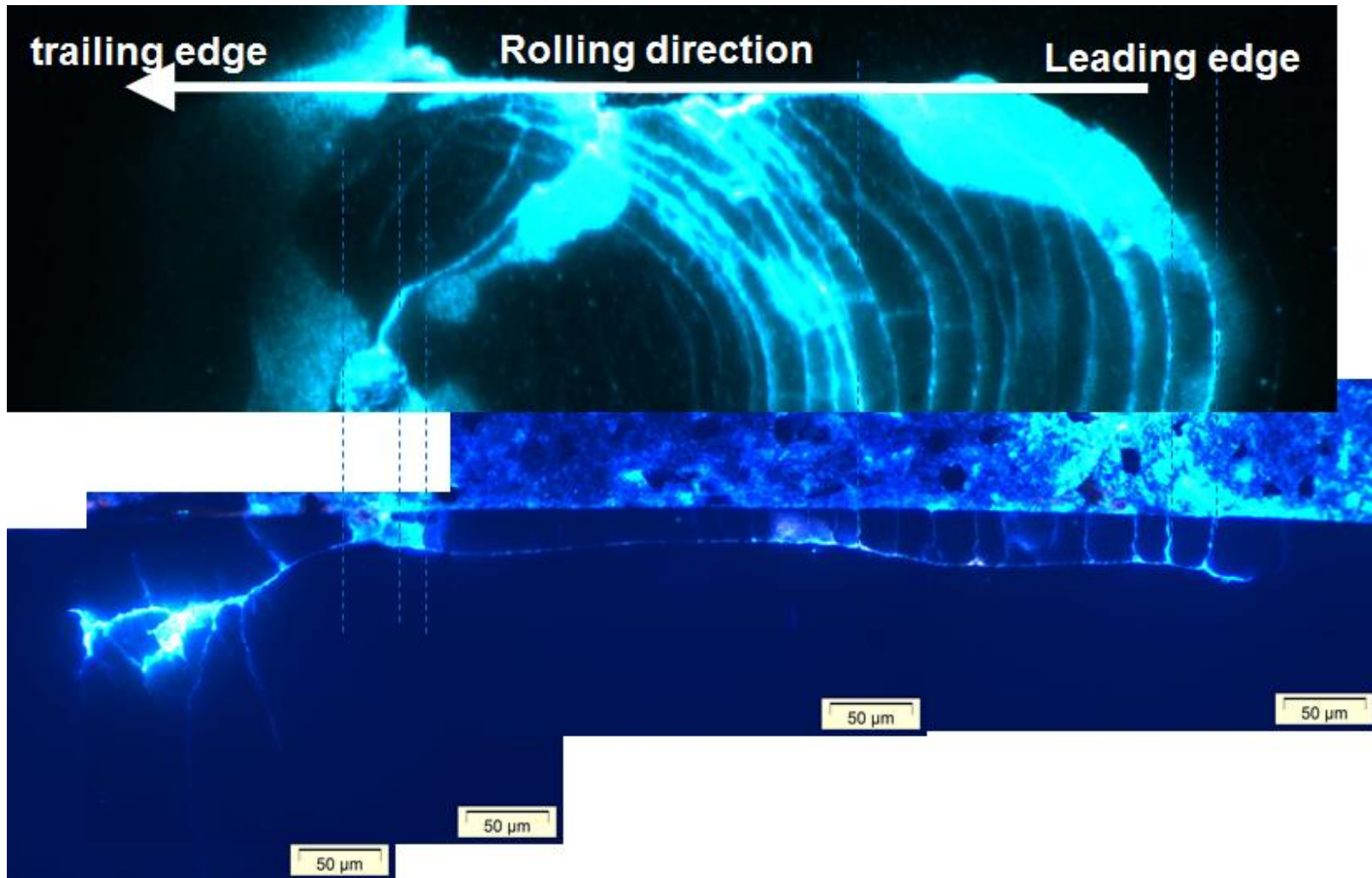
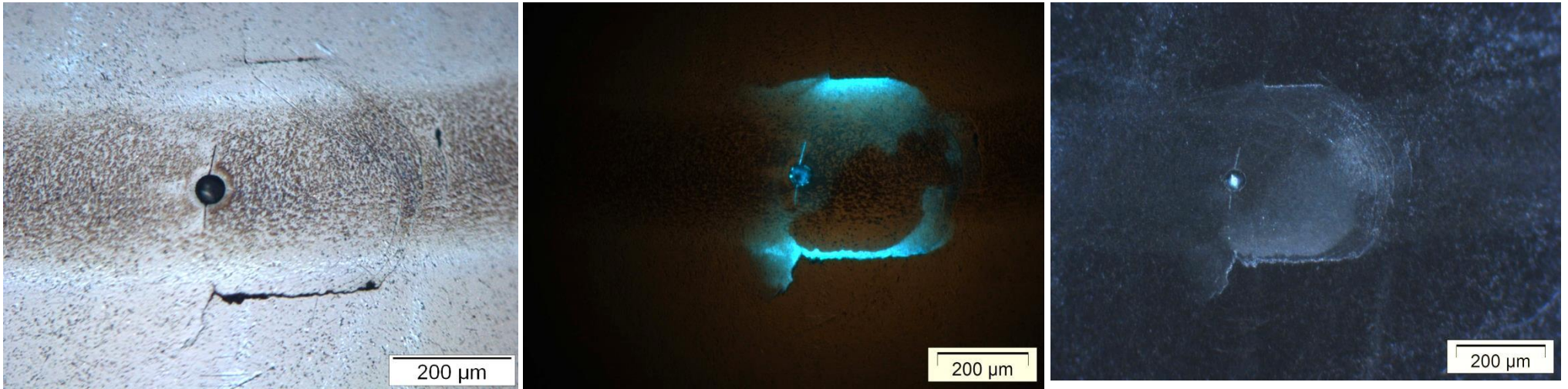


Figure 5.88: Sub-surface analysis (exp.6, Dia: 50μm, Depth: 20 μm) using microscopy (UV illumination) - 2nd finishing



(a)

(b)

(c)

Figure 5.89: Surface analysis (experiment 12, Dia: 50 μ m and Depth: 30 μ m) using microscopy (a) post-6million stress cycles (light illumination) (b) post-6million stress cycles (UV illumination) (c) post-6million stress cycles (dark field illumination)

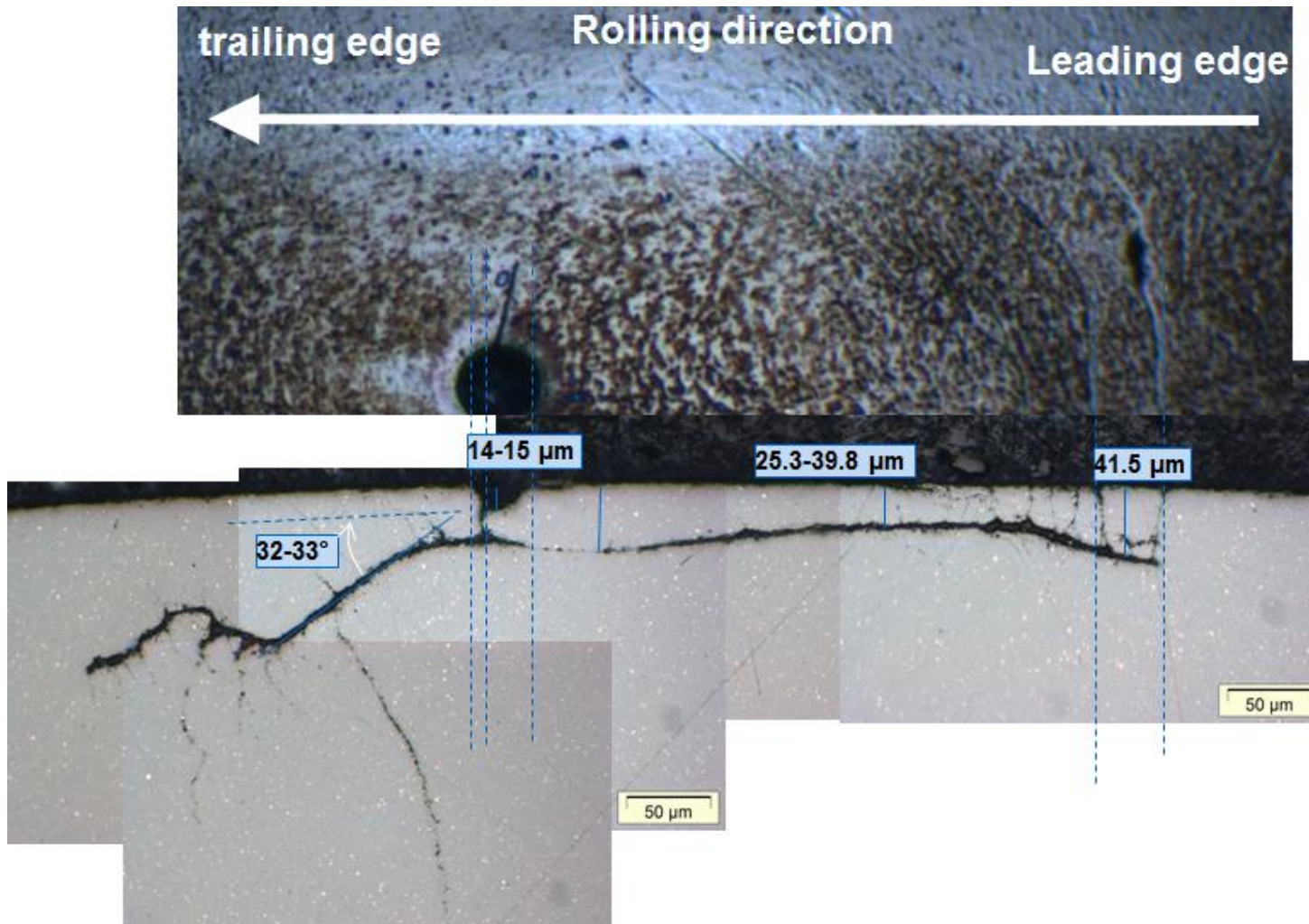


Figure 5.90: Sub-surface analysis (exp.12, Dia: 50μm, Depth: 30μm) using microscopy (light illumination) - 1st finishing

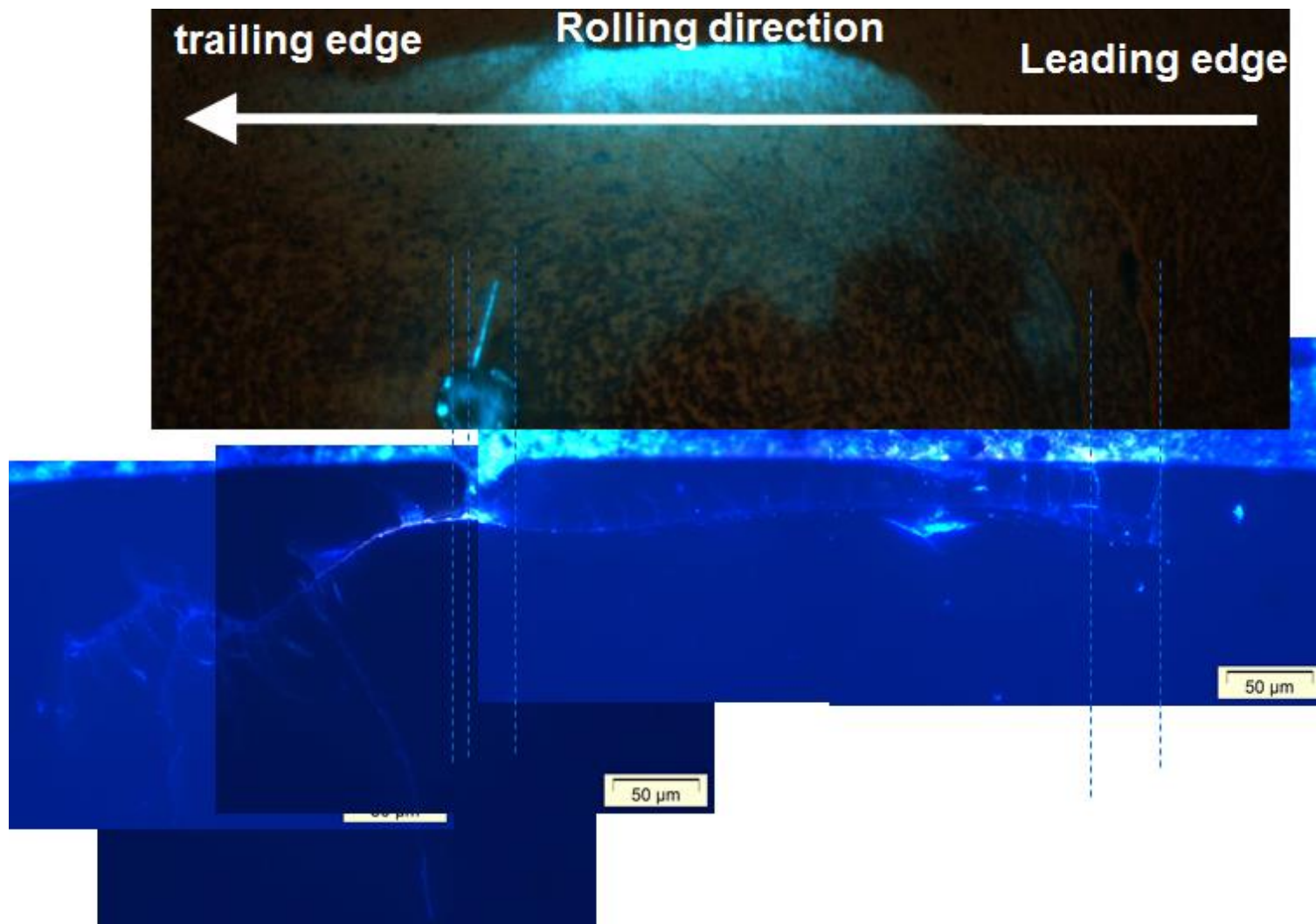


Figure 5.91: Sub-surface analysis (exp.12, Dia: 50μm, Depth: 30μm) using microscopy (UV illumination) - 1st finishing

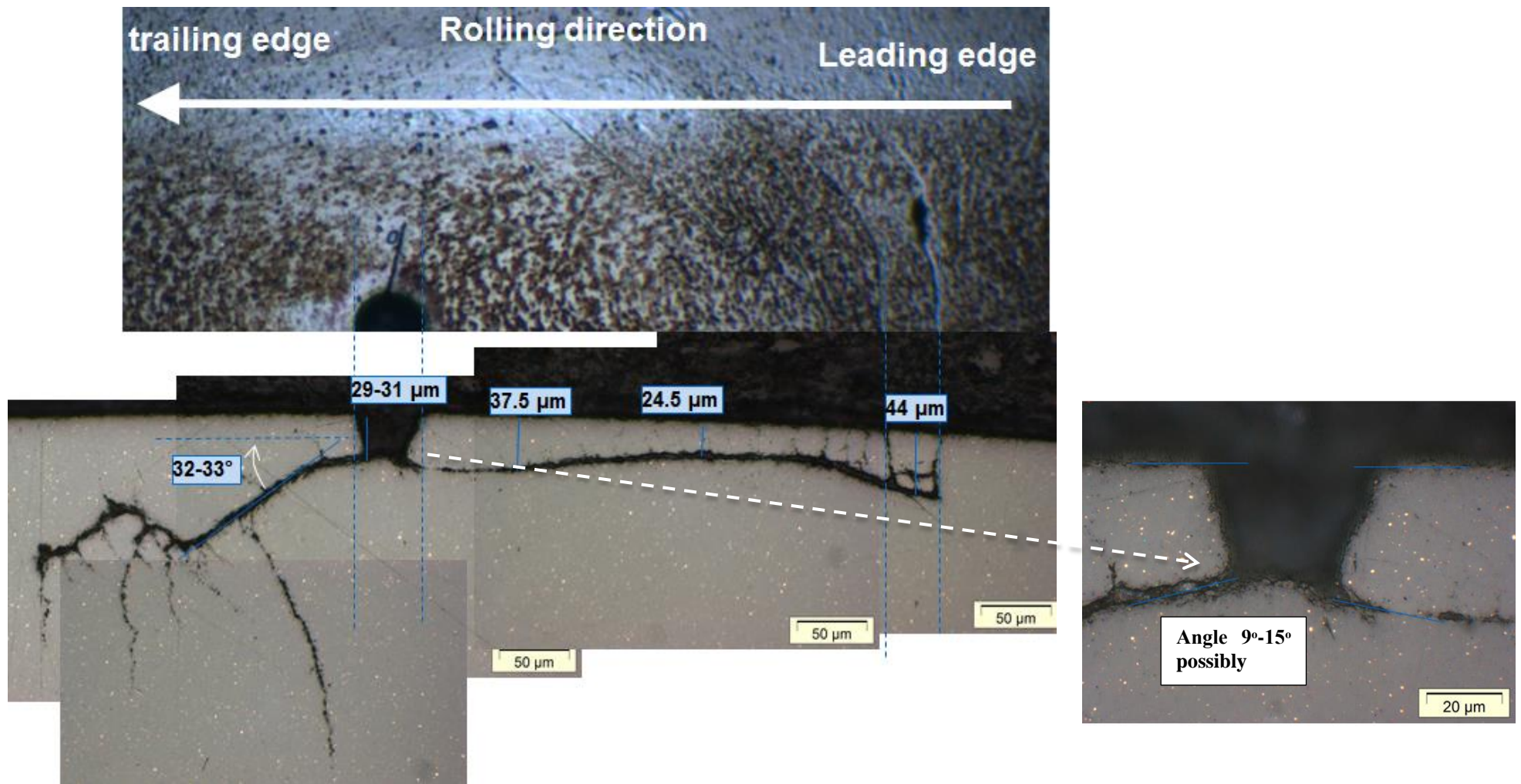


Figure 5.92: Sub-surface analysis (exp.12, Dia: 50 μm , Depth: 30 μm) using microscopy (light illumination) - 2nd finishing

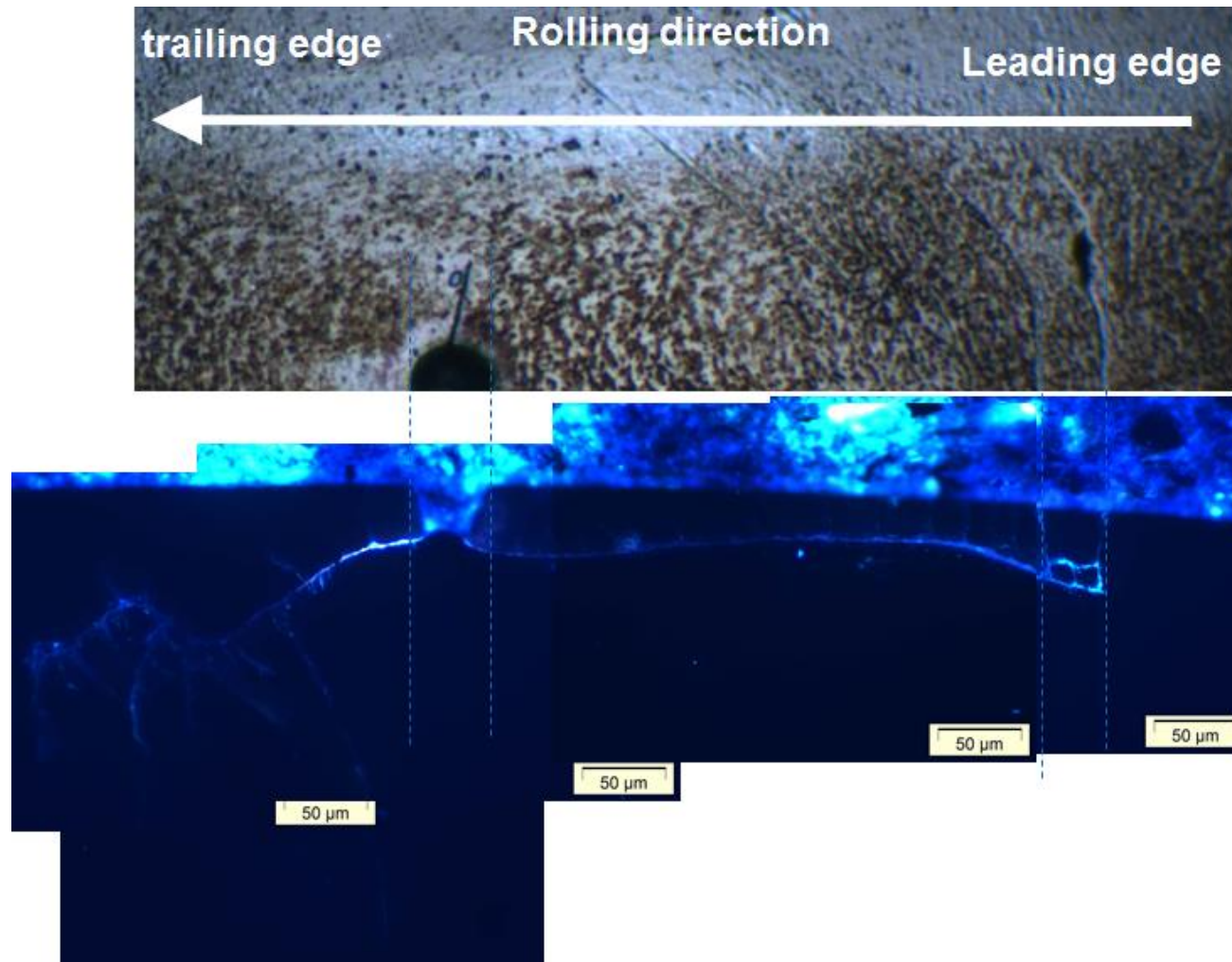


Figure 5.93: Sub-surface analysis (exp.12, Dia: 50μm, Depth: 30 μm) sample using microscopy (UV illumination) - 2nd finishing

5.9.4. Spalling Process

From the sections of unfailed balls, spalls and incipient spalls, it is possible to illustrate the progression of failure with missing material defects under rolling contact (mainly for shape I). Cracks are initiated at or close to the bottom edge of the cavity. On the leading side a crack will grow approximately parallel to the ball surface at a depth of the same order as the hole depth. From this main crack, secondary cracks branch up to the surface. The vertical cracks (branches) appearing could be related to a large weakening of the bonding of the left to right side of the missing material due to the extensive subsurface cracking, creating high tensile stresses on the missing material opposite sides [Awan et al. 2013b].

The main crack on the trailing side travels downwards at an angle of 20 – 30 degrees to the surface and is relatively short. This phenomenon is similar as reported by Yamamoto [1980] for steel rollers. From this main crack, secondary cracks form mainly branching downwards but one or two branching upwards. It cannot be determined at this stage on which side the actual spall in the form of material break-out first takes place. However, the effect is to produce a flat spall on the leading side and a smaller but deeper spall on the trailing side. A few multiple spalls were observed but this is thought to be due to over-rolling of debris from the initial spall.

The spalling process is illustrated schematically in Figs. 5.94 to 5.96 [Awan et al. 2013b].

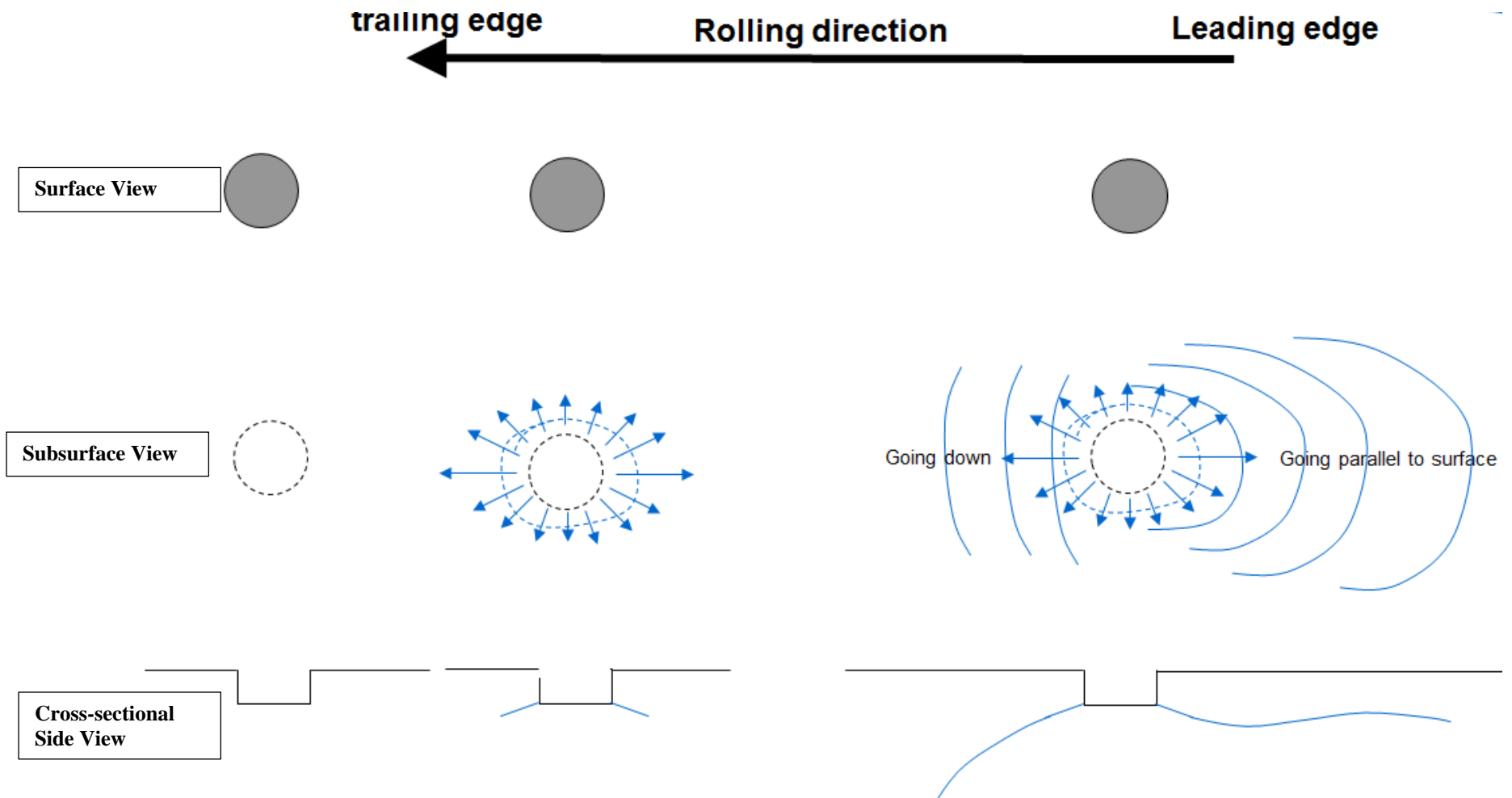


Figure 5.94: Failure mechanism schematic – Step 1 (Concluded from spalled and incipient spall samples)

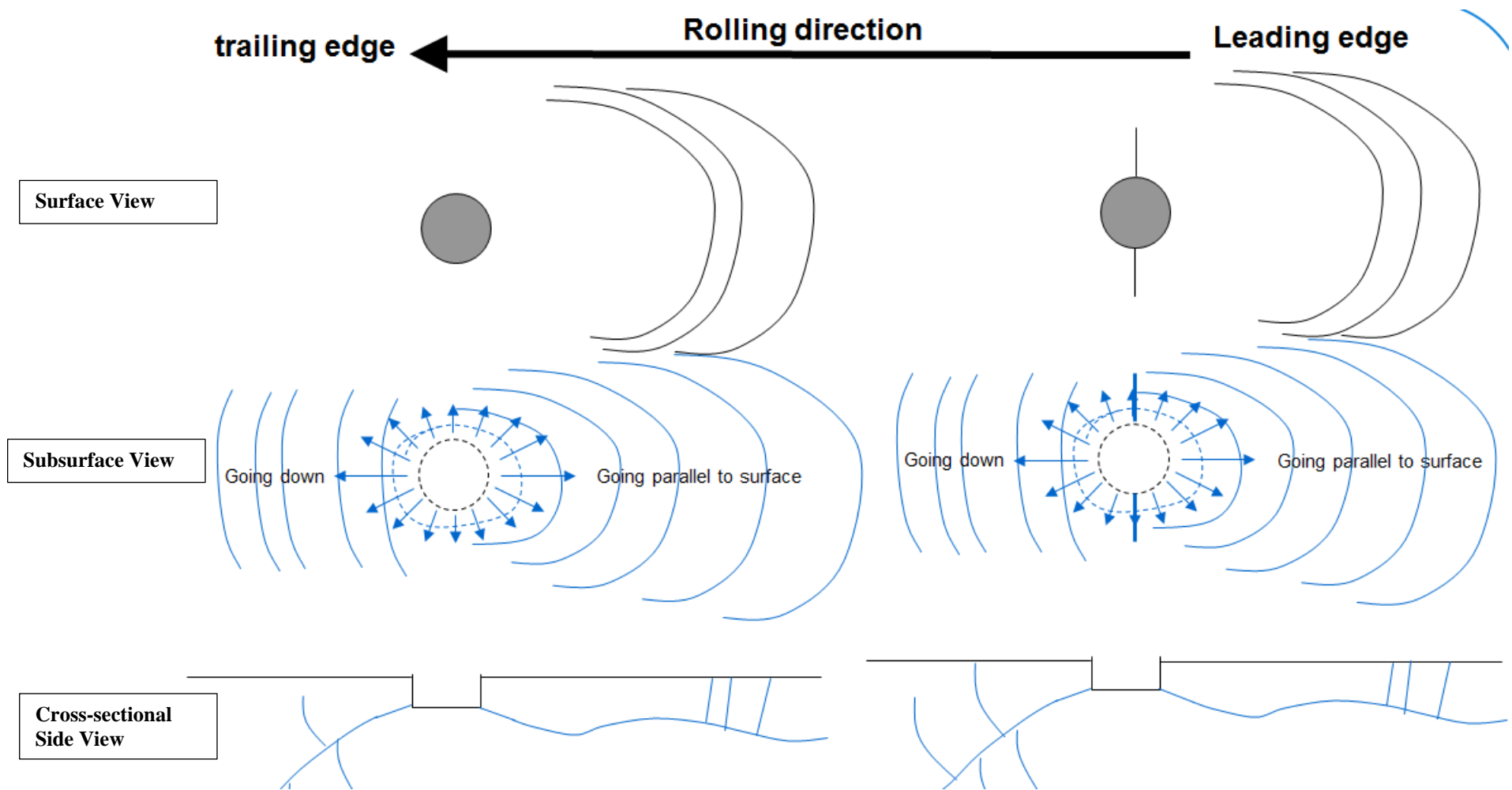


Figure 5.95: Failure mechanism schematic – Step 2

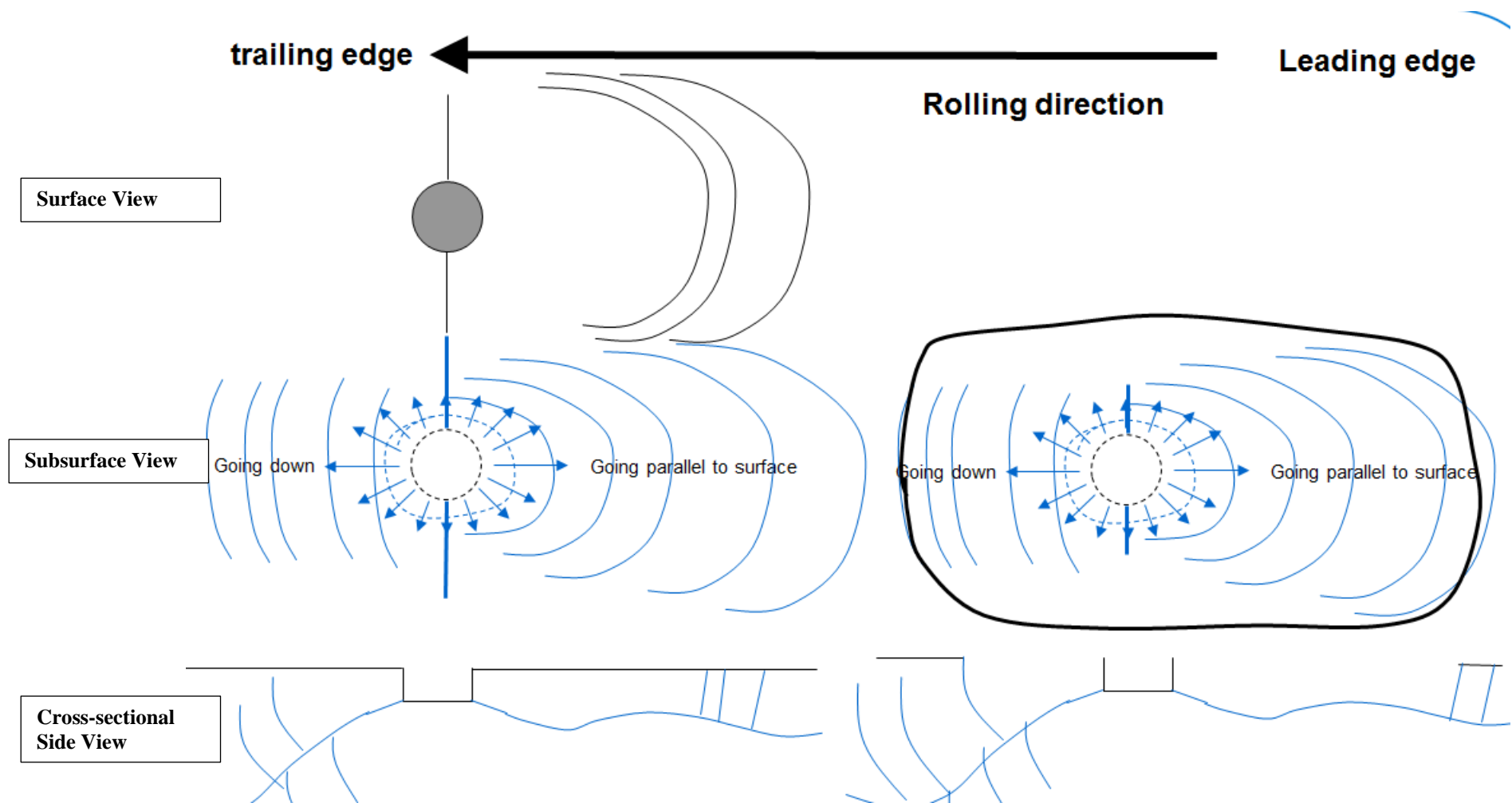


Figure 5.96: Failure mechanism schematic – Step 3

5.10. Discussion and Conclusions

Extensive experimental investigations on missing material showing the missing material dimension, shape and location along with contact pressure and orientation (in case of oblique cylindrical/shape III cavities) play important role in the performance and the life of the rolling element bearing. From these experiments, a hole of 10 μ m depth of with the smallest diameter of 50 μ m (shape 1) can be taken as tolerable under operating contact pressures of 3.8GPa-4.8GPa for up to 100 million stress cycles for class A material. However, class B material fails at these high contact pressures with the same cavity dimensions. Samples of holes having larger diameters and depths are prone to failure earlier than small diameter and shallow depths . Shape comparison was also made by conducting different experiments on similar cavity dimensions of three different shapes. It has been observed that shape III (oblique cylindrical) with adverse orientation is more prone to failure than shape I (right cylindrical) and II (conical). Similarly, shape II (conical) is least susceptible to failure than shape I and III.

Crack initiation was observed to happen from the cavity base due to maximum principal stresses (mode I) but propagation was in the direction normal to maximum principal stresses (shear stress/mode II). Crack propagation was due to shear stress/frictional effect [a similar trend was reported for flat samples - Kida et al. 2012] and it covers considerable distance parallel to the surface before turning upwards [crack grow in steel - Hills and Ashelby 1979]. Shallow and deeper cavities were found in the spall might be due to load ratio, as for small load ratio, crack goes to the surface and for large value it goes to the depth and eventually come to the surface [a similar trend was observed for steel bearing - Bower et al. 1994]. FEA study (chapter 6) has conducted to find the crack initiation location (hydrostatic pressure case) and also to find over-rolling effect on failure mechanism using 2D (Axi-symmetric and plane strain) and 3D (static and rolling) models.

5.11. Summary

In this chapter, a complete details of extensive experimental programme on artificial missing material using laser micromachining is discussed. Experiments are conducted on different shapes, depths and diameters and at range of contact pressures. Machine spindle rotational speed, bulk oil temperature and lubricant were kept constant to minimize the experimental variables and have a fair comparison at same operating conditions. Samples were taken from two different hot isostatic pressed silicon nitride materials with slightly

different material properties. Material tolerance and failure modes are determined using exhaustive experimental programme and techniques. Corrected pressure (effective contact pressure at the cavity centre) and cavity base profile were important to find material tolerance. Experiment on long slot also conducted to investigate effect of hydrostatic pressure at high contact pressure of 4.8GPa. Effect of diameter and depth of the artificial cavity on the specimen surface was investigated using experimental programme.

Chapter 6 Finite Element Modeling of Missing Material

Finite element analysis was conducted using the 2 dimensional (axi-symmetric and plane strain) and 3 dimensional models. Modeling started from axi-symmetric without defect and then with a defect. 2D (plane strain) rolling model was also generated with a defect to observe the rolling effect. 3D rolling model was then generated without considering the lubricant effect on the basis of results from 2D rolling model. High pressure lubricated rolling contact with surface cavities is an example of hydrostatic pressure applications. In this chapter, hydrostatic pressure effect is modeled using FEA software, Abaqus, for rolling contact applications to find critical location, position, depth, diameter and critical contact pressure for different sizes of the cavities.

Finite element method (FEM) or sometimes finite element analysis (FEA) is a widely used numerical analysis scheme for the solution of differential and integral equations that arise in different engineering and applied sciences fields. FEM is based on the classical variational (Rayleigh-Ritz) and weighted-residual (Galerkin, least square etc.) methods [Reddy 2004]. Many commercial softwares are available based on FEM. Abaqus is thought to be best FEA software for non-linear and contact problems due to its speciality in contact generation and good control during the solution phase.

6.1. Finite Element Modeling

As from extensive experimental programme (chapter 3), it is found that star like morphologies are converted into missing material type defect after a few million over-rolling stress cycles. Therefore, in this research work, only missing material modeling is presented. Initially, axi-symmetric models were generated with and without any missing material or hole of specific dimensions. 2D (plane strain) rolling model was also generated to compare stress field with axi-symmetric model and find the rolling effect on the stress field. 3D Model was then developed to have more realistic simulation and to compare the results with 2-dimensional model. 2D and 3D quasi-static models were developed to observe the effect of rolling on the stress field. All the models were generated using Abaqus CAE (Complete Abaqus Environment) interactive module and analyses were run using Abaqus Standard solver [ABAQUS 2012].

6.2. Model Verification

Model (axi-symmetric - without defect) was verified using Hertz theory. Contact radius was $174\mu\text{m}$ by using the model, whereas theory was calculating the radius of $172\mu\text{m}$ at contact pressure of 4.8GPa (Appendix M).

The axi-symmetric model of ball-on-ball configuration (without any hole/missing material) is shown in the Figure 6.1. The model is generated using linear quadratic axi-symmetric elements (CAX4R, Appendix Q). Loading is applied by applying displacement to get required contact pressure of 4.8GPa (used in the first instance to confirm the model). The model is constrained from the bottom and symmetry conditions are applied on the left side. Contact was defined between mating surfaces using surface to surface approach in Abaqus. Axi-symmetric model showing maximum von Mises stress lies $88\mu\text{m}$ below the surface (under the contact), similarly maximum shear stress (Tresca) is found at the depth $86\mu\text{m}$ below the contact and maximum tensile stress (maximum principal stresses) lies on the surface and outside the contact and at the distance of $196\mu\text{m}$ from the centre of the contact (Figure 6.2-6.3). All the stresses are in MPa.

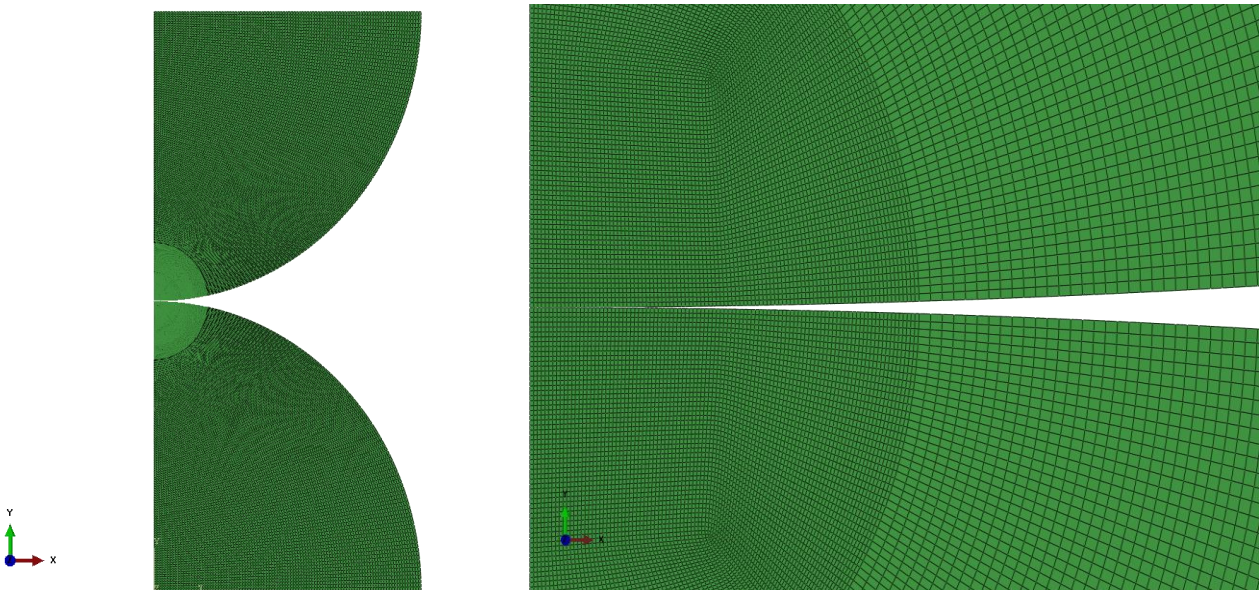


Figure 6.1: 2D Mesh for ball-on-ball (without any hole)

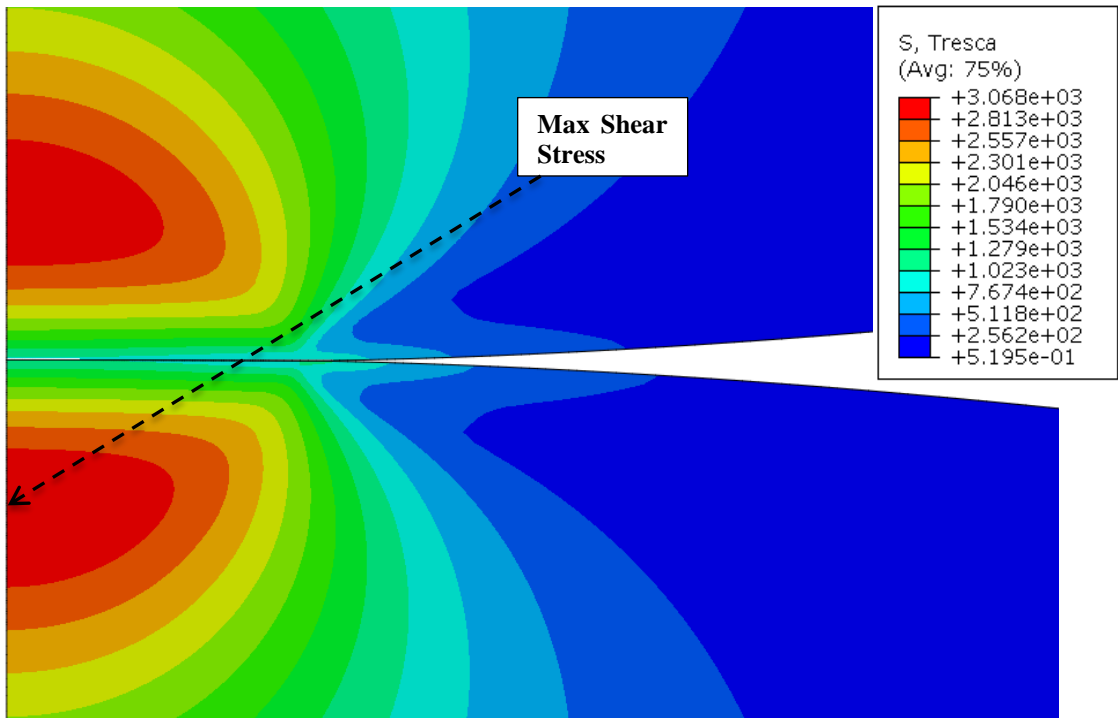


Figure 6.2: Maximum shear stress (MPa) for 2D static model ball-on-ball (without any hole)

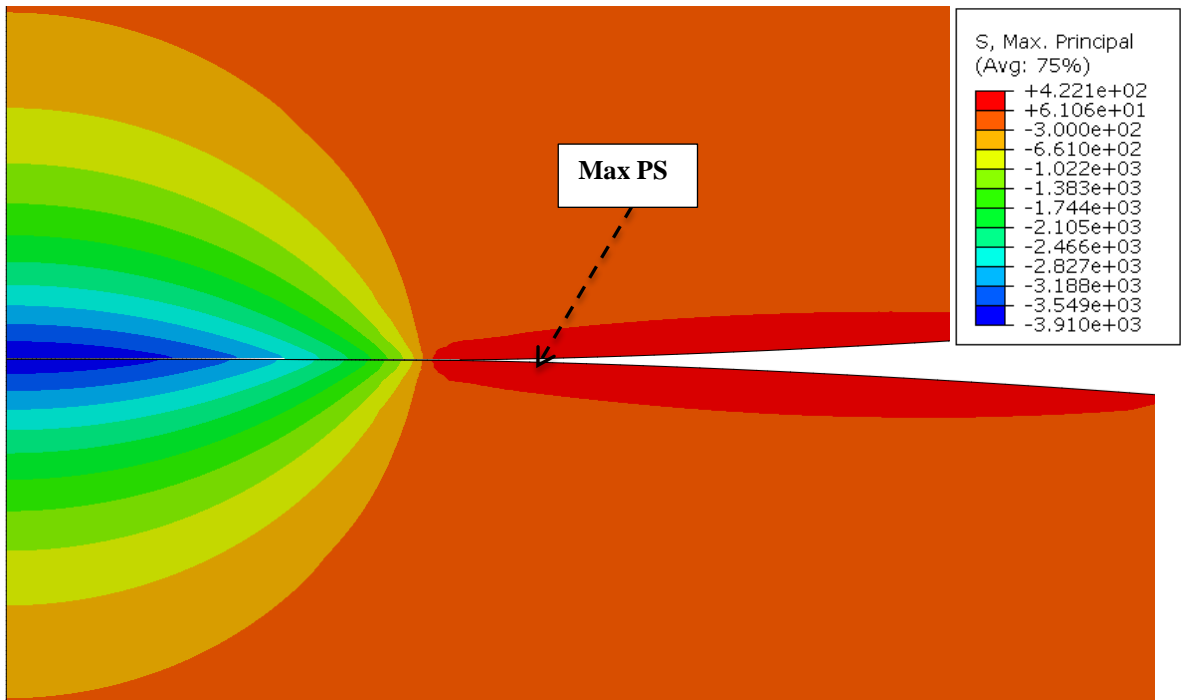


Figure 6.3: Maximum principal stress (MPa) for 2D static model ball on ball (without any hole)

An axi-symmetric model with a hole is also generated to observe the effect of indent/hole on the stress field and have more realistic modeling approach for artificially machined defect in the silicon nitride. An axisymmetric model with an indent of dimension 100 μm (diameter) and 50 μm (depth) was generated in the first case. The same vertical displacement was applied to get the stress field. A fillet was introduced on the indent corners to reduce any stress concentration. Figures 6.4-6.5 are showing maximum shear stress and maximum principal stresses in case of indent at the centre of contact. Maximum shear stress is found at 42 μm below the surface, whereas von Mises stress also having a maximum value at the depth of 42 μm below the contact surface and on the hole's inner surface. Maximum principal stress lies on the surface, outside the contact circle/radius and at a distance of around 187 μm from the centre of the contact. An almost similar stress field was found in terms of stress distribution with and without a defect/hole. Higher values of stresses are observed due to change of contact pressure distribution due to indent in the contact.

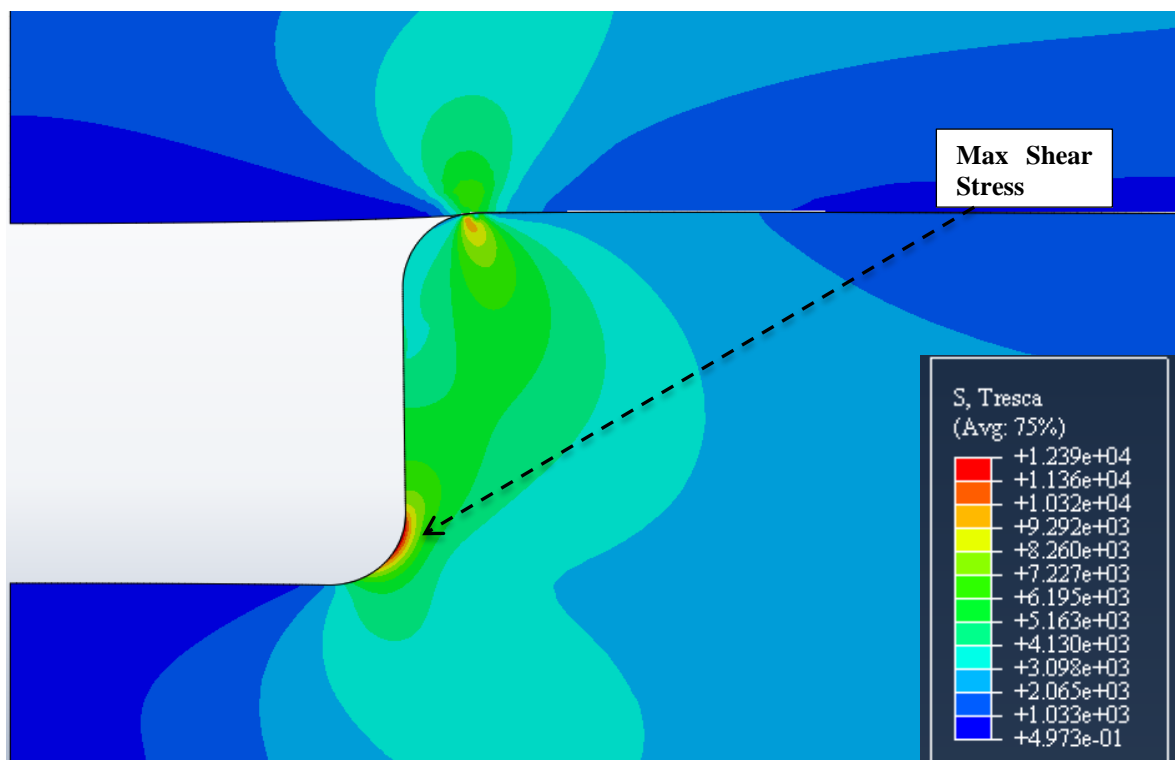


Figure 6.4: Maximum shear stress (MPa) for 2D static model ball- on-ball (with hole)

6.3. 2D Rolling Models

After applying axi-symmetric static ball-on-ball models (with and without defect), 2D rolling models were generated to observe the hole and rolling effect together in one model. The 4-node bi-linear plane strain element (CPE4R) was used for 2D rolling modeling [Appendix Q]. A finer mesh was created along the indent to have better results (Figure 6.6). Loading was applied in steps. In the first step, there was just contact between upper and lower parts. In the second step, the lower part was constrained from the base using encastre (constraints on all displacements and rotations) condition while upper part was constrained only in the x-direction and uniform displacement was applied in the downward direction (y-direction). In order to provide rotation, third step was defined where previous conditions were made inactive (suppressed) and new boundary conditions were defined.

Centre nodes of top surface of upper part were constrained in the x-direction while some displacement was applied to keep the surfaces in contact. Centre node of the base of lower part was constrained in the x and y-directions. Side nodes of top surface of the upper part were given a displacement to rotate the part in the fourth step.

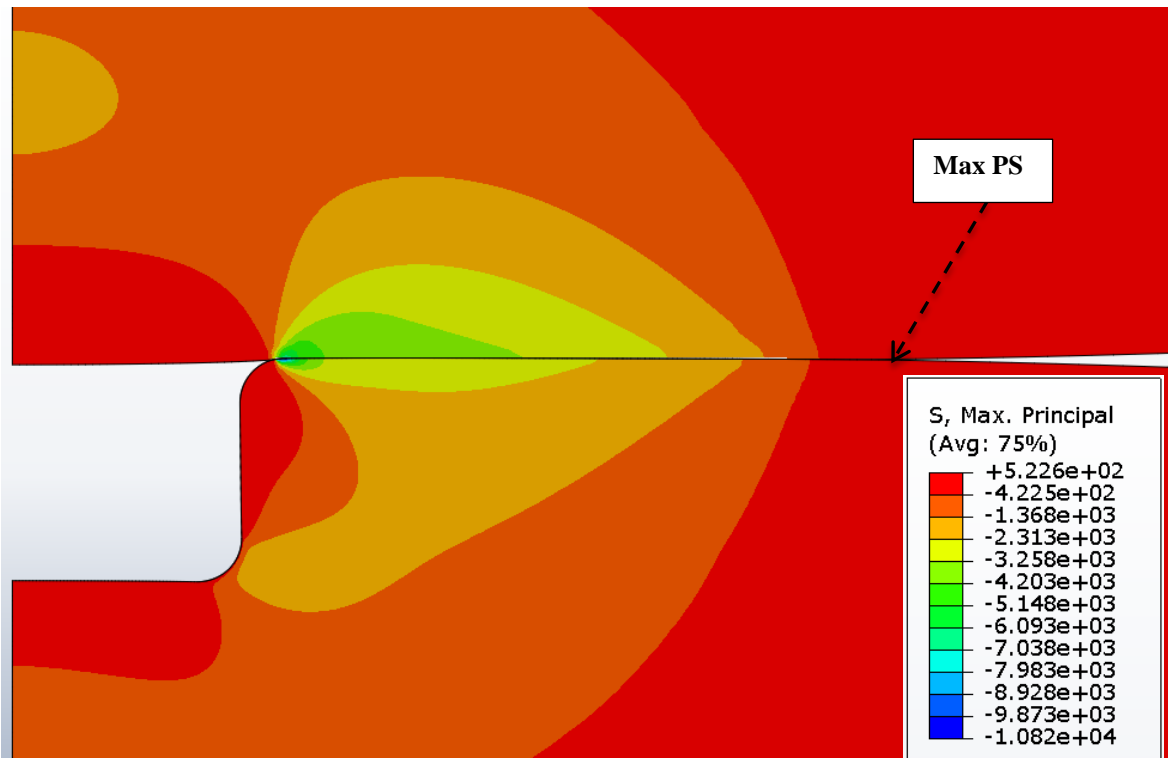


Figure 6.5: Maximum principal stress (MPa) for 2D static model ball on ball (with hole)

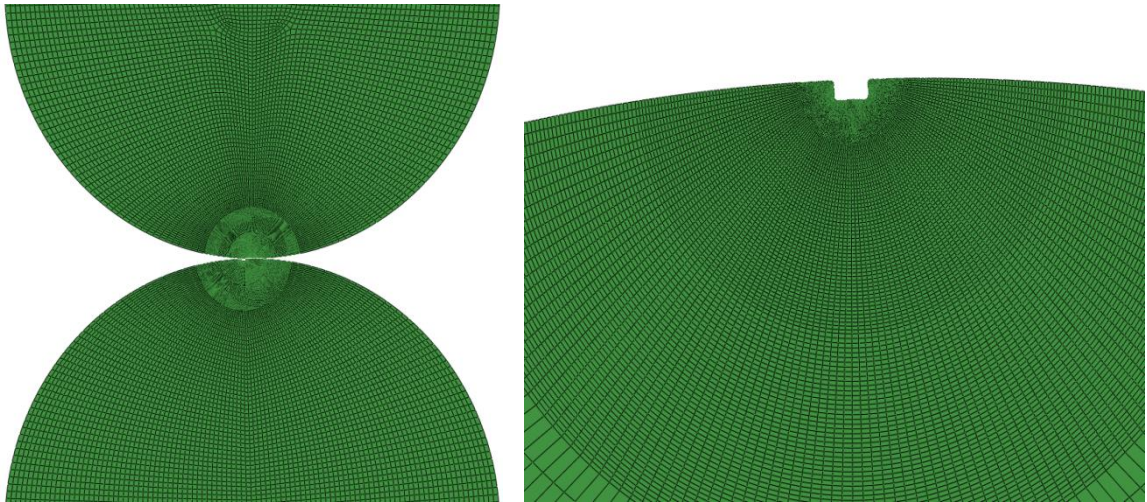


Figure 6.6: 2D Rolling model mesh for ball on ball (with hole)

Although the rolling step was further divided into 20 sub-steps to complete over-rolling, only three cases are shown for the principal stress in Figure 6.7-6.9.

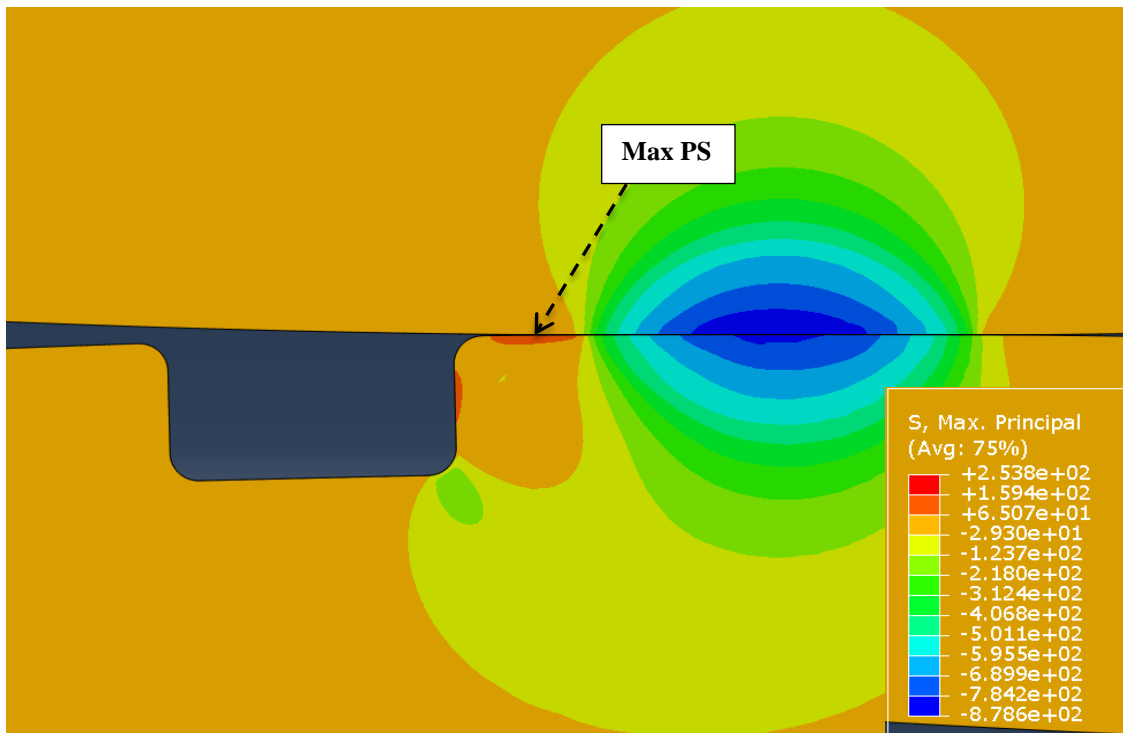


Figure 6.7: Maximum principal stress (MPa) for 2D rolling model ball on ball (with hole) - at start of rolling (indent lies outside the contact)

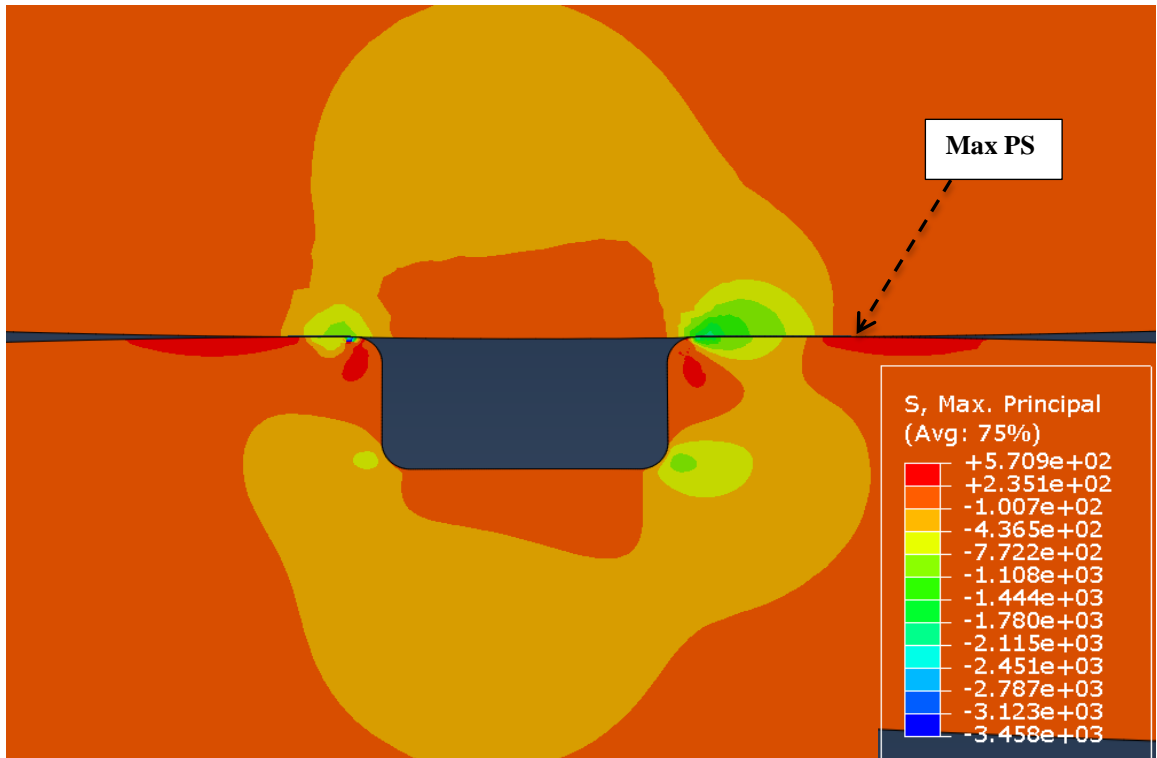


Figure 6.8: Maximum principal stress (MPa) for 2D rolling model ball on ball (with hole)
 - almost at the centre of the contact (indent lies almost centre of contact)

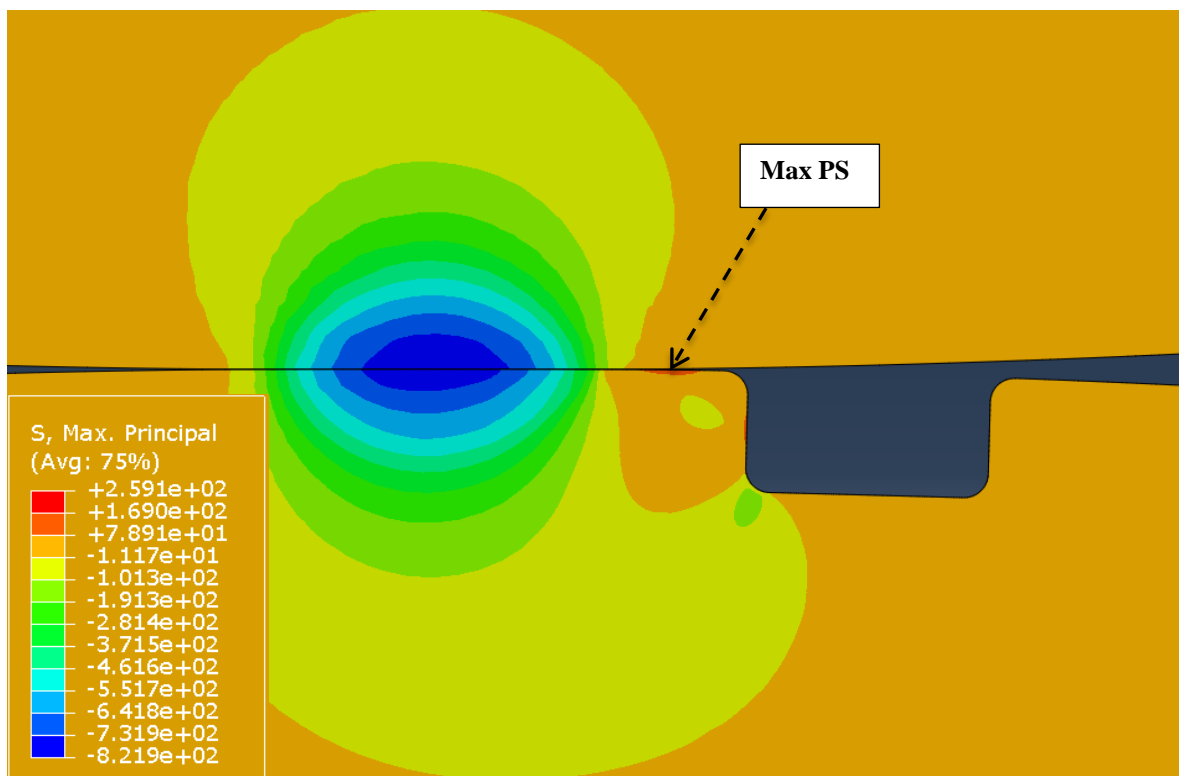


Figure 6.9: Maximum principal stress (MPa) for 2D rolling model ball-on-ball (with hole)
 - at the end of rolling (indent lies outside the contact)

Maximum principal stresses are found on the surface of the ball not at the inside of indent/hole in all cases but values considerably changed over rolling. Maximum shear stress is also found close to the surface but inside the indent; it has also very high values. The maximum value is found at one side of the indent due to eccentric loading (probably) when the contact centre was not exactly on the indent top (Figure 6.10). Static and rolling model shows that stress fields change considerably in the static and quasi-static (rolling condition), so that a full 3D model is required to fully simulate the operating conditions.

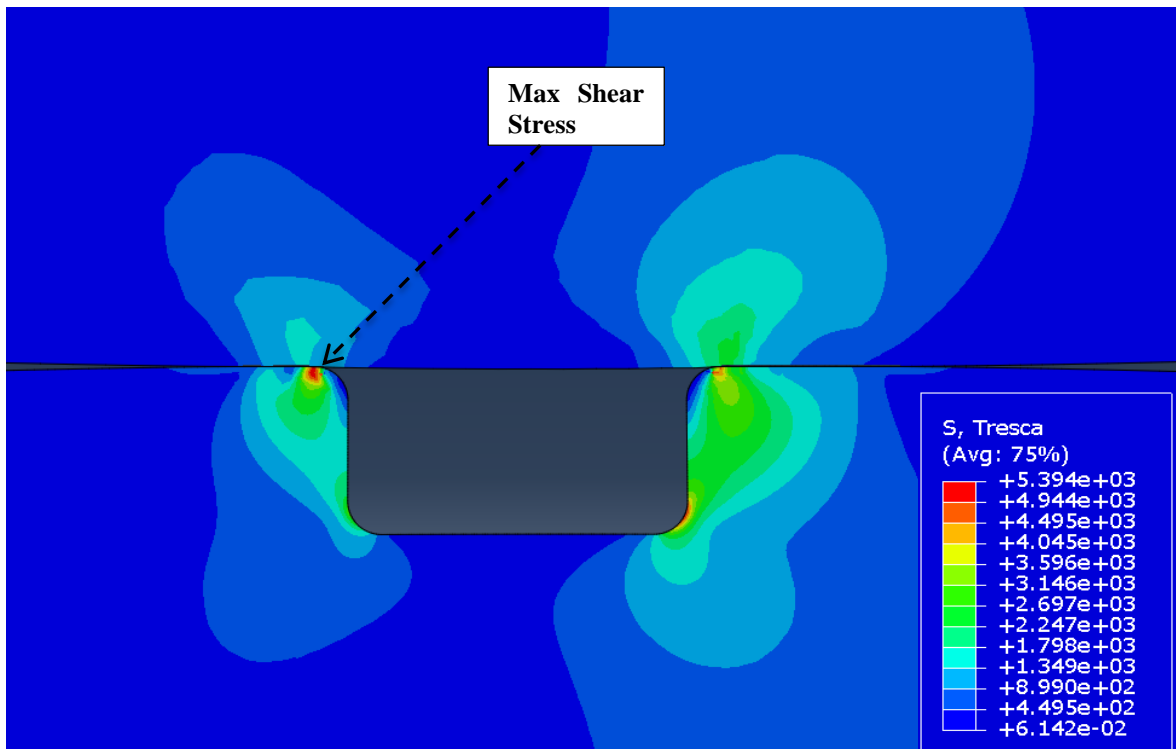


Figure 6.10: Maximum shear stress (MPa) for 2D rolling model ball on ball (with hole) - at the almost centre of contact

6.4. 3D Rolling Model

A 3D model was generated to determine the rolling effect on the stress field. The model was generated using tetrahedral elements (3D8R) [Appendix Q] in Abaqus. Finer mesh was created close to cavity to have better results and less convergence issues (Figure 6.11). Cavity size of diameter of 100 μ m and depth 50 μ m was used to analyse the 3D rolling condition under the high contact pressure of 4.8GPa.

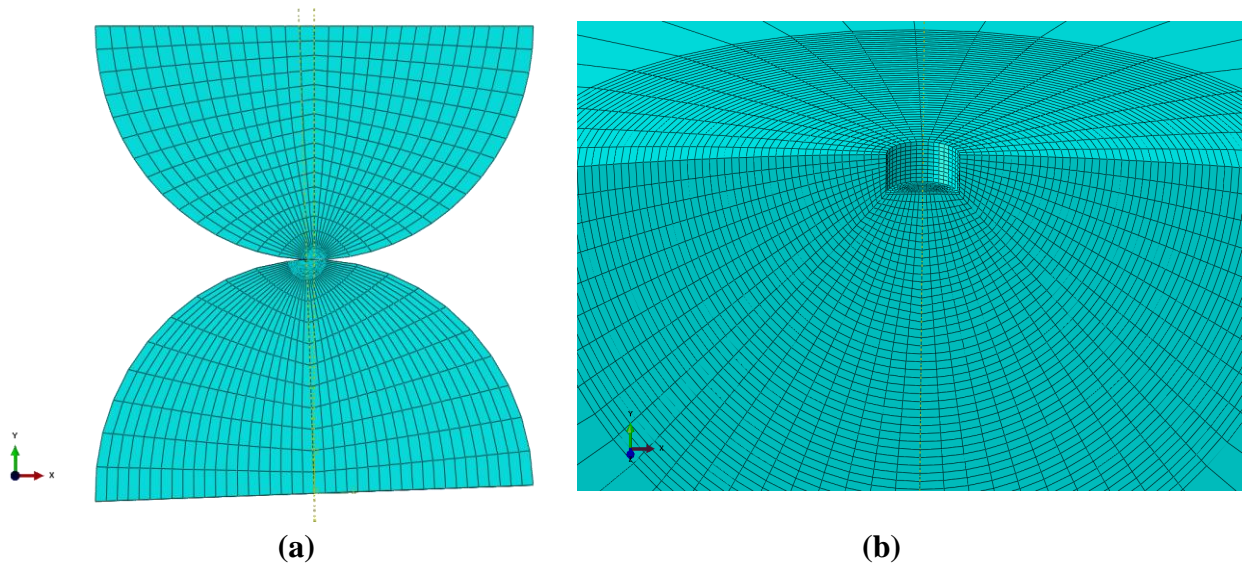


Figure 6.11: 3D Model ball on ball (with hole) (a) 3D Model mesh (b) Closer view of the mesh on the lower ball with hole of 100µm diameter and 50µm depth

The model was generated with the following boundary conditions;

- i. Symmetry condition was applied on front faces of both balls
- ii. Bottom face of lower ball constraint at early steps (during contact generation) and then only central bottom node fixed in all three translations
- iii. Downward displacement was applied on top face of upper ball in early steps and then this condition was made inactive and additional displacement was put on top central node and left corner nodes
- iv. More displacement was applied on top left node of the top ball to start rotation and then a solution was run in the final step. Twenty steps were used for the rolling solution over the indent to compare the results and find most critical scenario.

Post processing of 3D rolling analysis showed the stress field varies as ball rolls and its values increases as the contact reaches the hole. Maximum stress value was found when either the contact centre was located on the top of the hole or close to leading or trailing edge of the hole. The maximum principal stress (Fig. 6.12) lies close to leading edge when contact centre was near the trailing edge ($x/a = 1.2886$, where x = distance from contact centre to hole centre, a = contact radius) and maximum values found was 539MPa. The values of principal stresses on bottom of the hole (on the leading edge side) are also high but values at trailing edge cannot be neglected. Similarly, maximum shear stress/Tresca is located close to trailing side of the hole and it happens when the contact centre passes

almost slightly off the hole centre (Figure 6.13, and $x/a = 0.6124$) and its maximum value is 5.35GPa. Fig 6.14 shows maximum von Mises stresses having values (4.75GPa) at close to trailing edge and this happens when contact passes over the hole. So, only maximum principal stresses having maximum values when the contact centre is not located on the hole but slightly outside the hole. These results may be more useful if a parametric study can be conducted with different hole dimensions, different contact pressure ranges and friction coefficient values. The stresses mentioned above are achieved at a contact pressure of 4.8GPa and when contact centre was far away from the hole and analysis was run at friction coefficient of 0.1.

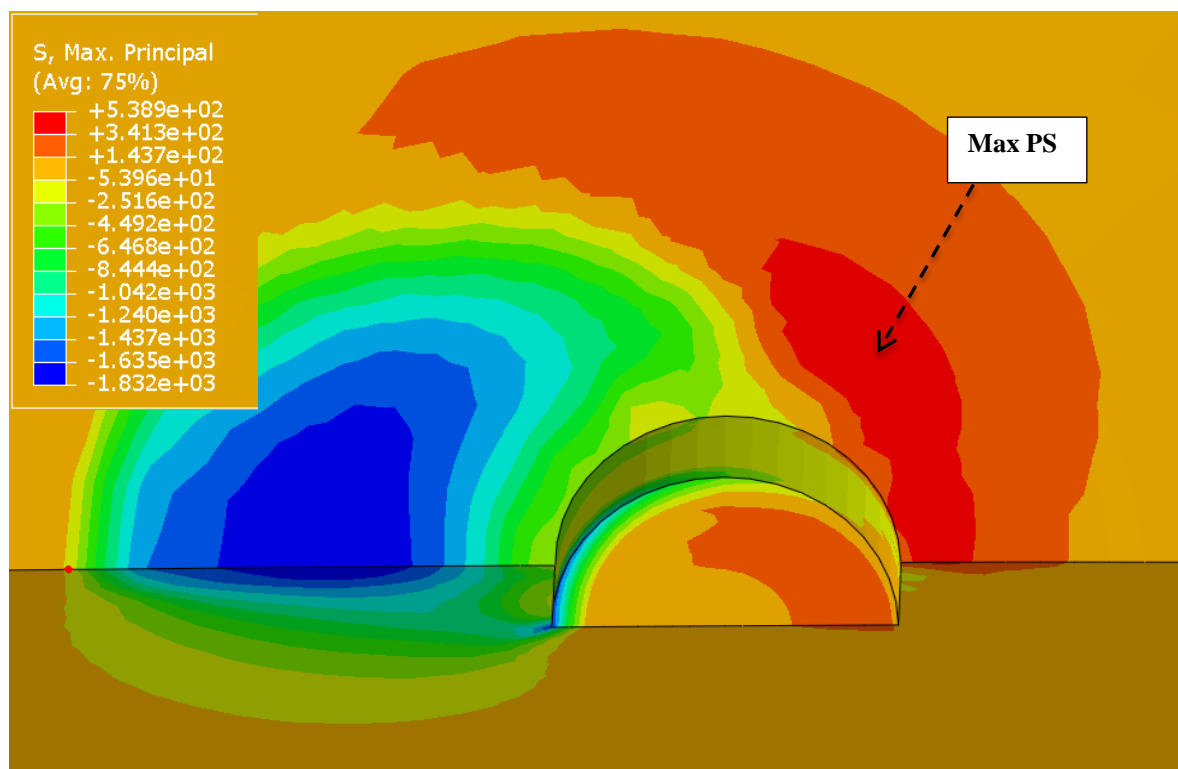


Figure 6.12: Maximum principal stress (MPa) during rolling (located close to leading edge)

Maximum shear stress (Tresca) and von Mises have almost similar profiles with maximum value located at the trailing side whereas stress values on the top side of the holes are also high enough. Figure 6.15 is showing two different scenarios i.e., when contact centre was at hole's centre and when it was outside (away) from hole to show rolling effect.

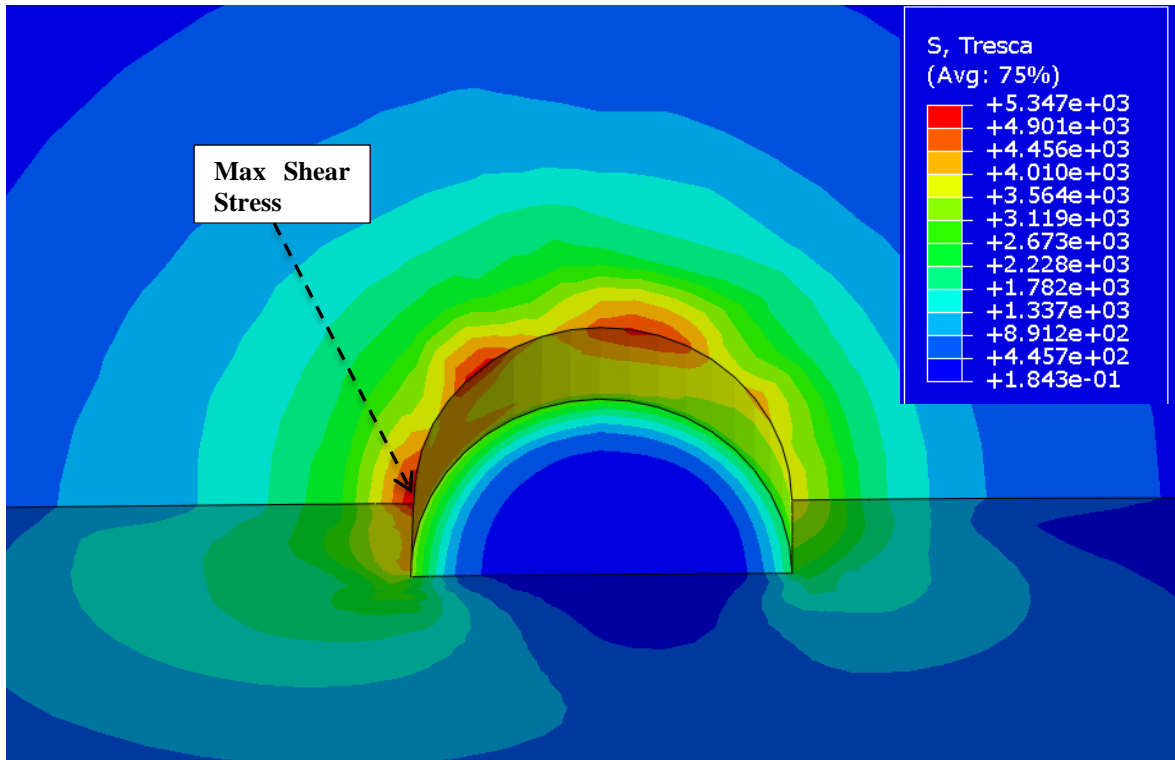


Figure 6.13: Max. shear stress (Tresca-MPa) during rolling (located close to trailing edge)

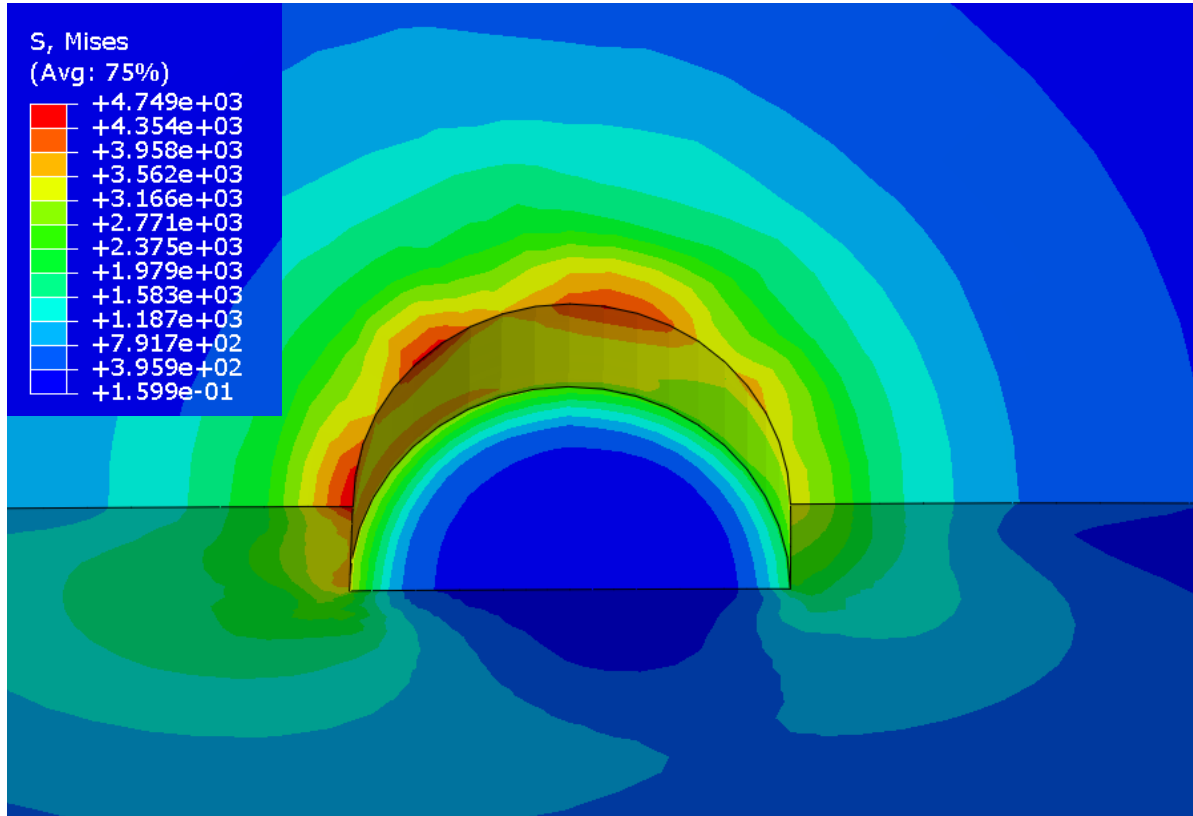


Figure 6.14: Max. von Mises stress (MPa) during rolling (located close to trailing edge)

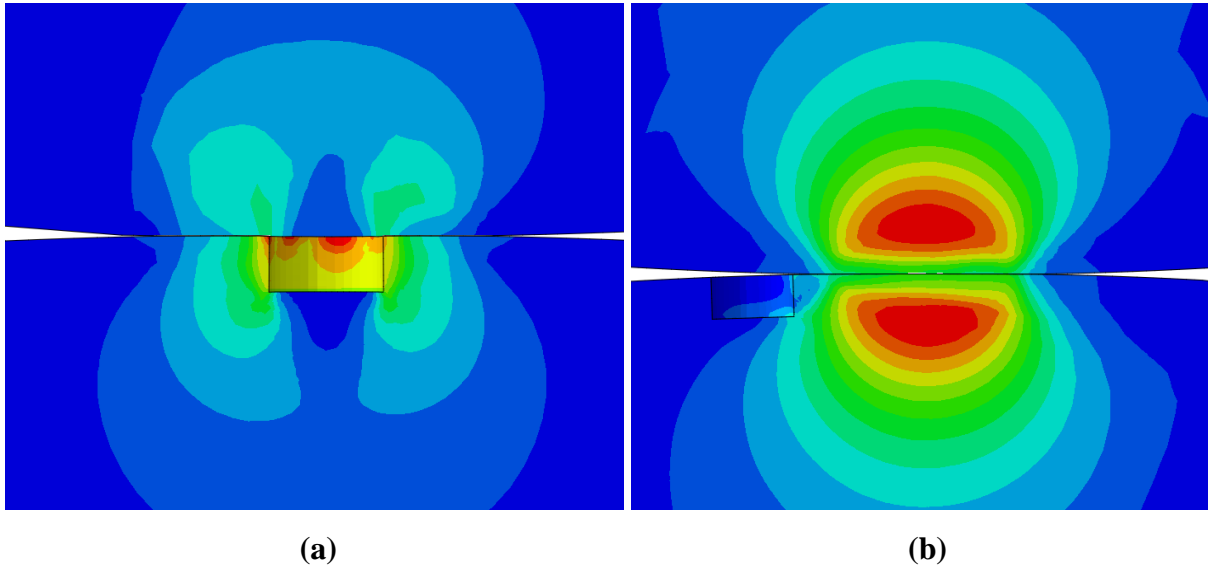


Figure 6.15: Two rolling cases (a) contact centre exactly at hole's centre (b) contact centre far away from hole

The axi-symmetric, 2D rolling and 3D rolling models have produced valuable findings and have indicated the most critical scenario (when cavity was outside the contact – based on maximum principal stress) in rolling condition. They also highlight the different ways to handle the rolling contact problem. In all of the above models, the lubrication effect was modeled by contact friction between the mating parts but the effect of trapped lubricant has not been discussed so far. In the next section (6.6), hydrostatic pressure effect due to trapped liquid in the cavity/missing material is modeled and discussed.

6.5. Hydrostatic Pressure

Hydrostatic pressure due to fluid entrapment is one of the reasons to cause failures in silicon nitride rolling elements in lubricated contact. Lubricated rolling (ball-on-ball) mechanisms can be divided into further four steps/processes;

- a. When cavity lies outside the lubricated contact, so no hydrostatic pressure applies
- b. When cavity is in the lubricated contact and fluid is filling the cavity but it is not fully filled
- c. When cavity is fully filled and sealed
- d. When fluid is coming out from the cavity and pressure is releasing

Case 'c' and 'd' are important as hydrostatic pressure can act to increase stresses and in case 'd' high pressure jet coming out from the cavity can cause erosive wear. Case 'c' is

the most critical one as it can lead to spalling failure and is considered for modeling in this section. The following assumptions are made in modeling the hydrostatic situation;

- i. Cavity is fully flooded and sealed in case ‘c’
- ii. Fluid is incompressible while solid parts are elastic

6.6. Hydrostatic Pressure Modeling in Abaqus

In commercial software, Abaqus, hydrostatic pressure modeling is done by creating the cavity and fluid/hydrostatic pressure is derived by defining fluid elements at the interface. So at the interface both fluid and solid elements are present defining solid surface of the cavity and fluid inside. In order to have a parametric study with variable cavity dimensions, an axi-symmetric approach is adopted to model the cavity. Different contact pressures are applied to investigate hydrostatic pressure effects on the stress field of a rolling element with a cavity. In the axi-symmetric case, 4-node bi-linear axi-symmetric quadrilateral elements (CAX4R) are used to model solid surface and 2-node linear axi-symmetric surface elements (SFMAX1) are used to close the cavity to have fluid cavity conditions. FAX2 elements are used to simulate fluid inside the cavity [Appendix Q]. Abaqus special fluid elements have been reported to capture entrapped fluid hydrostatic pressure in cracks [Lai et al. 2008]. Contact was defined between mating surfaces by selecting the surface to surface contact option. In Abaqus, contact can be defined in different ways; surface to node contact, node to node, surface to surface and by using specific contact elements. Similarly, fluid inside the cavity was defined by picking surface nodes/elements and assigning them axi-symmetric fluid elements. In Abaqus (hydrostatic case), cavity deformation creates hydrostatic pressure while volume remain constant. The axi-symmetric model with cavity is shown in the Figure 6.16.

6.6.1. Boundary Conditions

Boundary conditions are applied at symmetry planes, top side of the upper sphere and bottom sphere. Steps are outlined below;

1. Symmetry boundary condition is applied to the symmetry plane of the two spheres
2. Base surface of the lower sphere is fixed
3. Top surface of upper sphere is fixed along x-axis to restrain any motion in x-direction
4. Displacement on the top surface nodes is applied to get required contact pressure

6.6.2. Mesh

Mesh is important for convergence and predicting good results in the numerical study. Regular meshes were generated to get consistent results and trends. Mesh is shown in Figure 6.16.

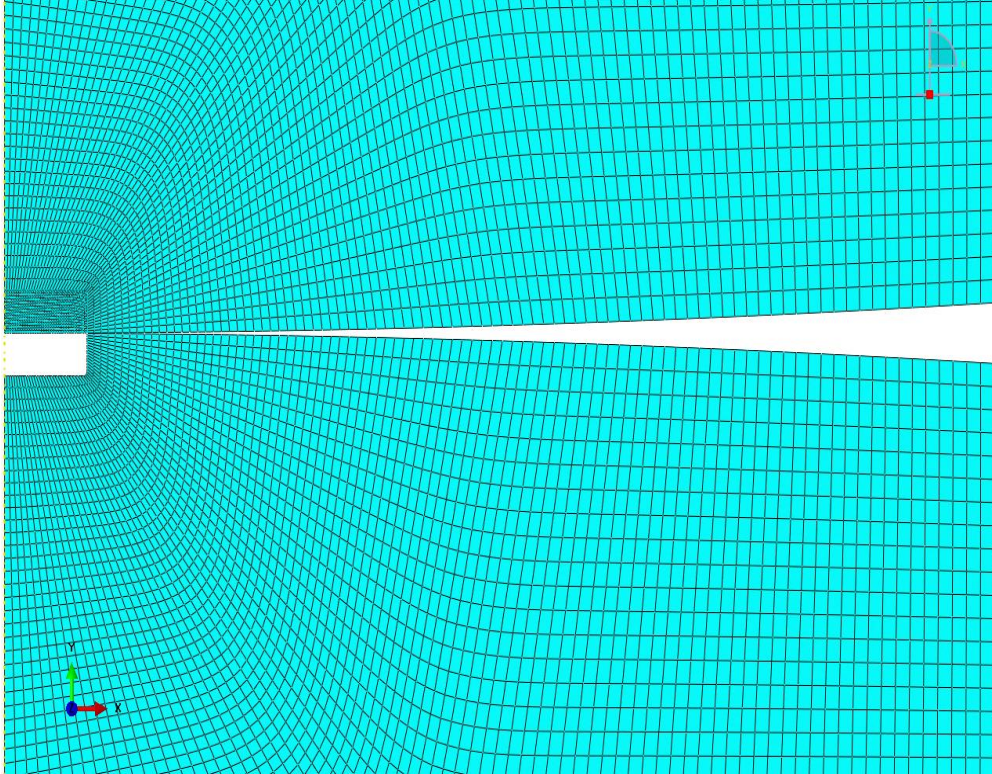


Figure 6.16: Mesh for axi-symmetric fluid cavity problem

6.6.3. Stress Field (Shape I/right cylindrical)

Stresses are calculated using FEA along hole bottom and hole top to find maximum stress area to initiate crack. As in case of FE analysis without considering hydrostatic pressure, maximum principal stresses were found outside the contact but the hydrostatic pressure case caused maximum principal stresses at the hole base corner and that has been verified experimentally using artificial missing material cavities (Chapter 5). Stresses are further discussed in the next section, Results and Discussions. Stress fields for larger diameter and shallow depth holes are shown in the Figures 6.17-6.19.

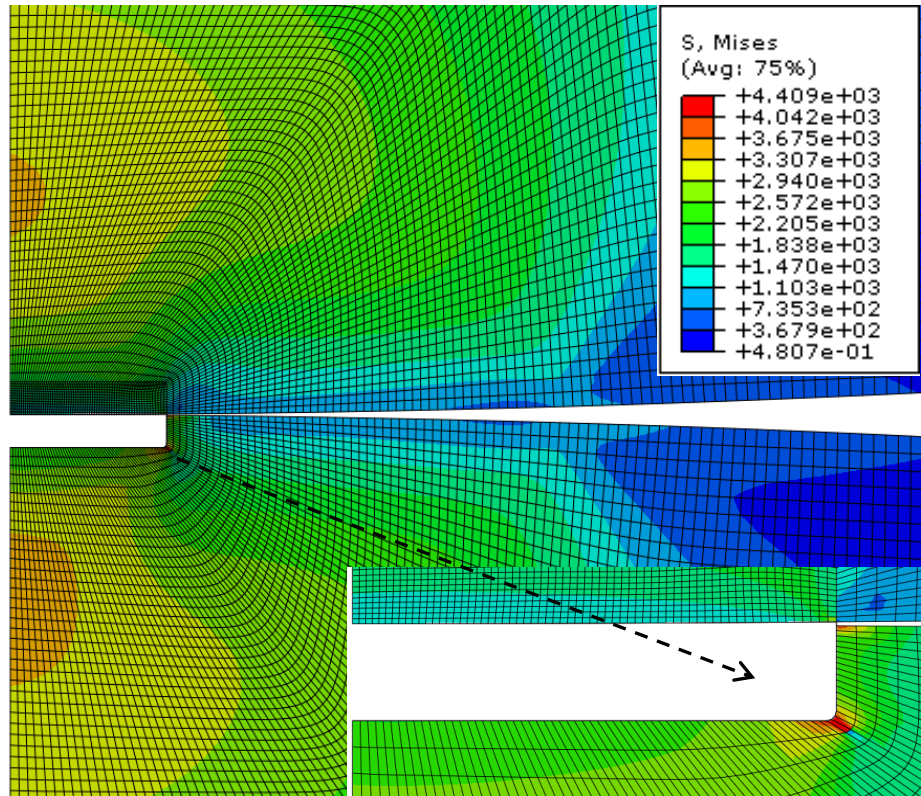


Figure 6.17: Von Mises (MPa) for larger diameter (100µm) and shallow depth (10µm)

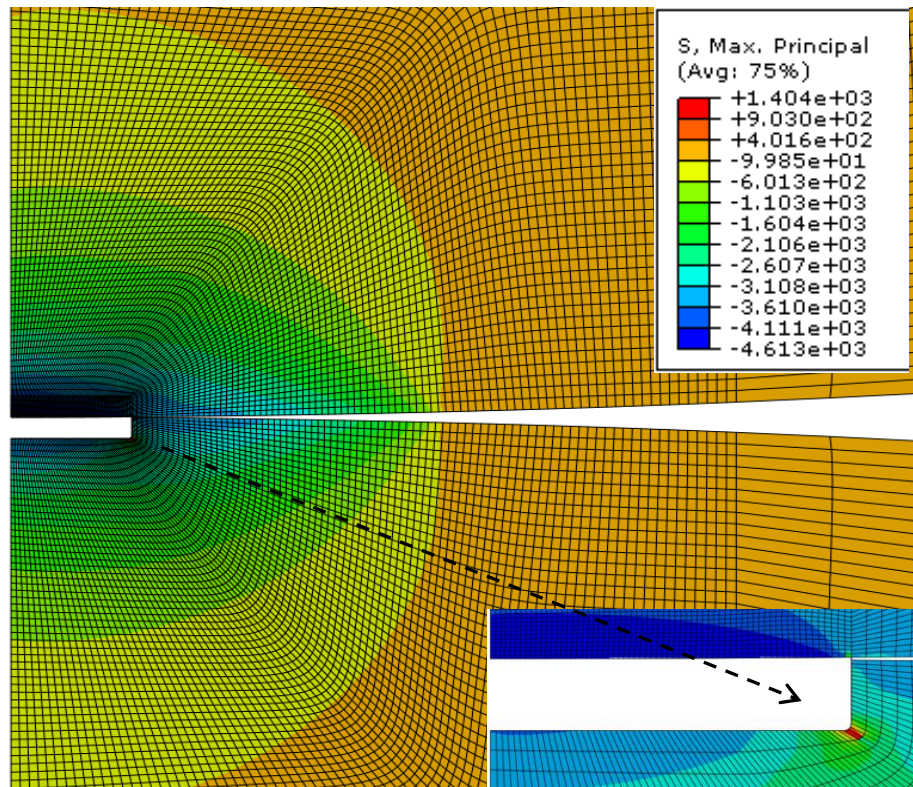


Figure 6.18: Maximum PS (MPa) for larger diameter (100µm) and shallow depth (10µm)

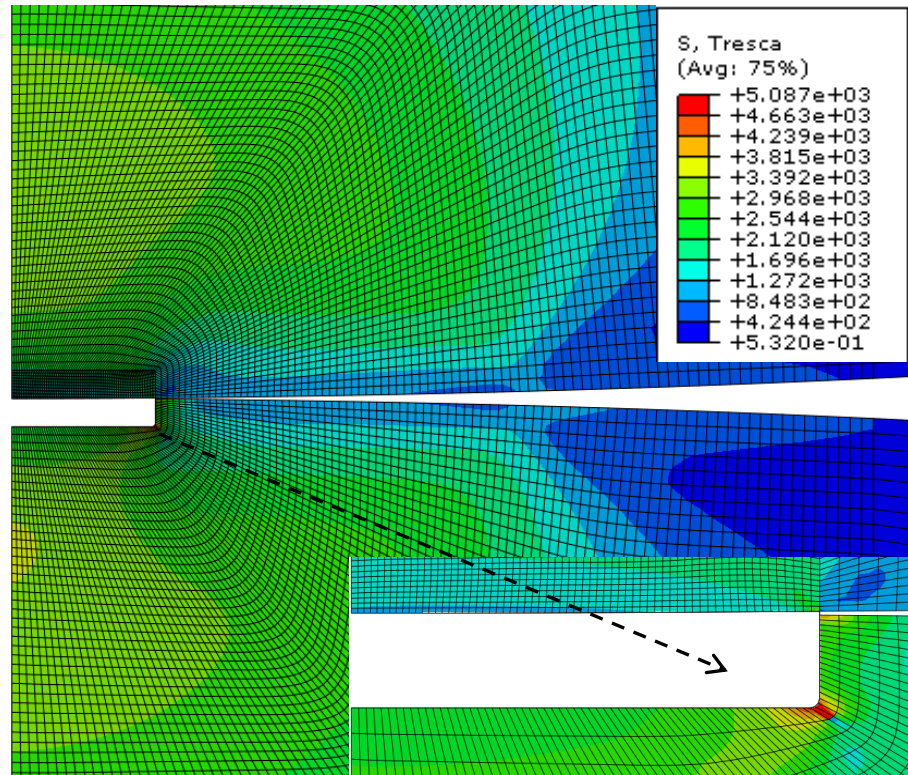


Figure 6.19: Tresca (MPa) for large diameter hole (100µm) and shallow depth (10µm)

6.6.4. Stress Field (Shape II/Conical)

Stresses (Tresca and PS) for cavities with Shape II are shown in Figures 6.20 and 6.21.

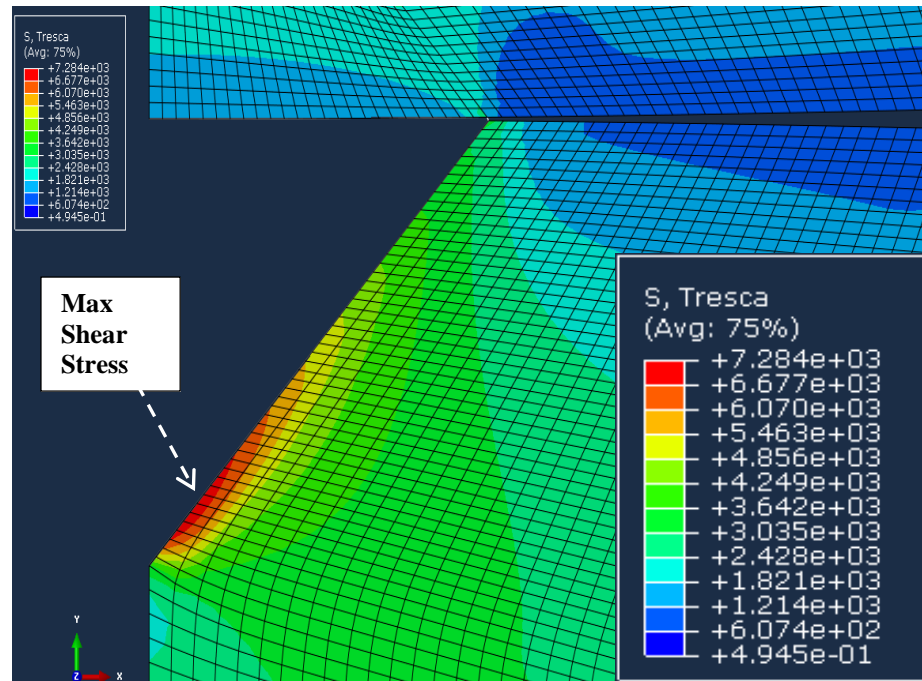


Figure 6.20: Tresca (MPa) for large diameter hole (100µm) and depth (50µm), Shape II

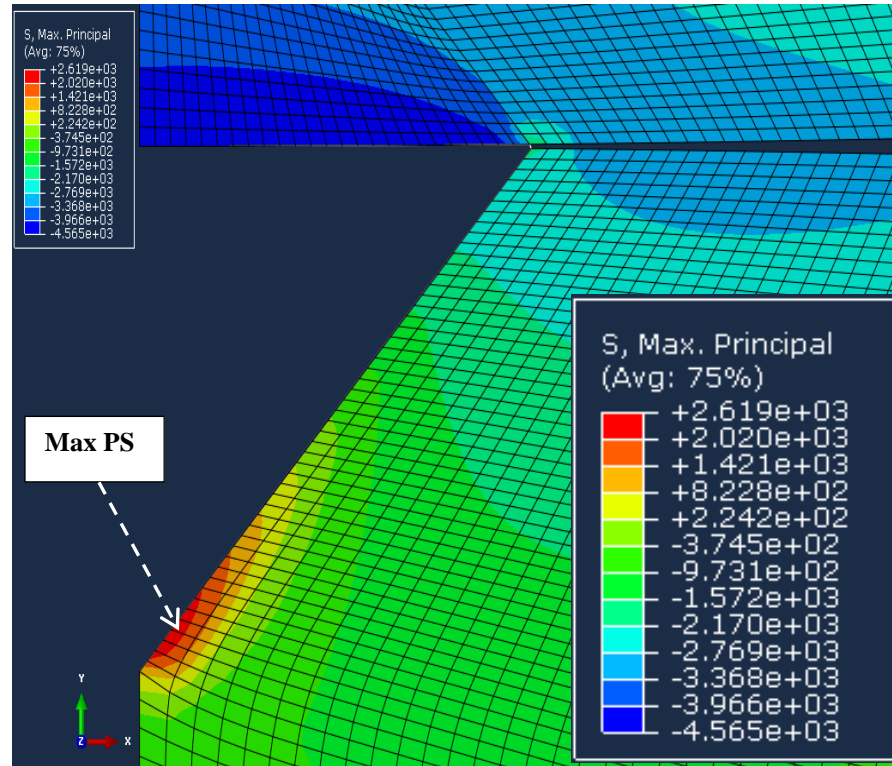


Figure 6.21: Max. PS (MPa) for large diameter hole (100µm) and depth (50µm), Shape II

6.7. Results and Discussion (Shape I/Right Cylindrical)

Stress fields are changed with fluid elements at the solid interface simulating fluid inside the cavity (fully sealed condition). Figure 6.18 shows the maximum principal stress is found at the cavity base. Results are further explained by taking stresses along the cavity base and hole top at different pressure levels and also for different cavity dimensions. For ceramic materials under passage of contact load, critical stress is assumed to be maximum tensile principal stress that material element experience due to moving contact [Chiu 1999]. It has now been well established that cracks initiated from the cavity base due to maximum tensile principal stresses and propagated in the direction normal to maximum principal stresses (shear stresses). Deeper spall cavities were found on the trailing side because of frictional effects. Figures 6.22-23 show the nodal positions for the graphs (Figures 6.24-6.33). Graphs are showing the von-Mises stress, Tresca and maximum principal stress plots for shape I type of cavities. Although corners also have stress concentration at the cavity base, maximum principal stress is always found outside the contact track or at contact base corners. These high principal stresses are responsible for initiation of the crack [Awan et al. 2014].

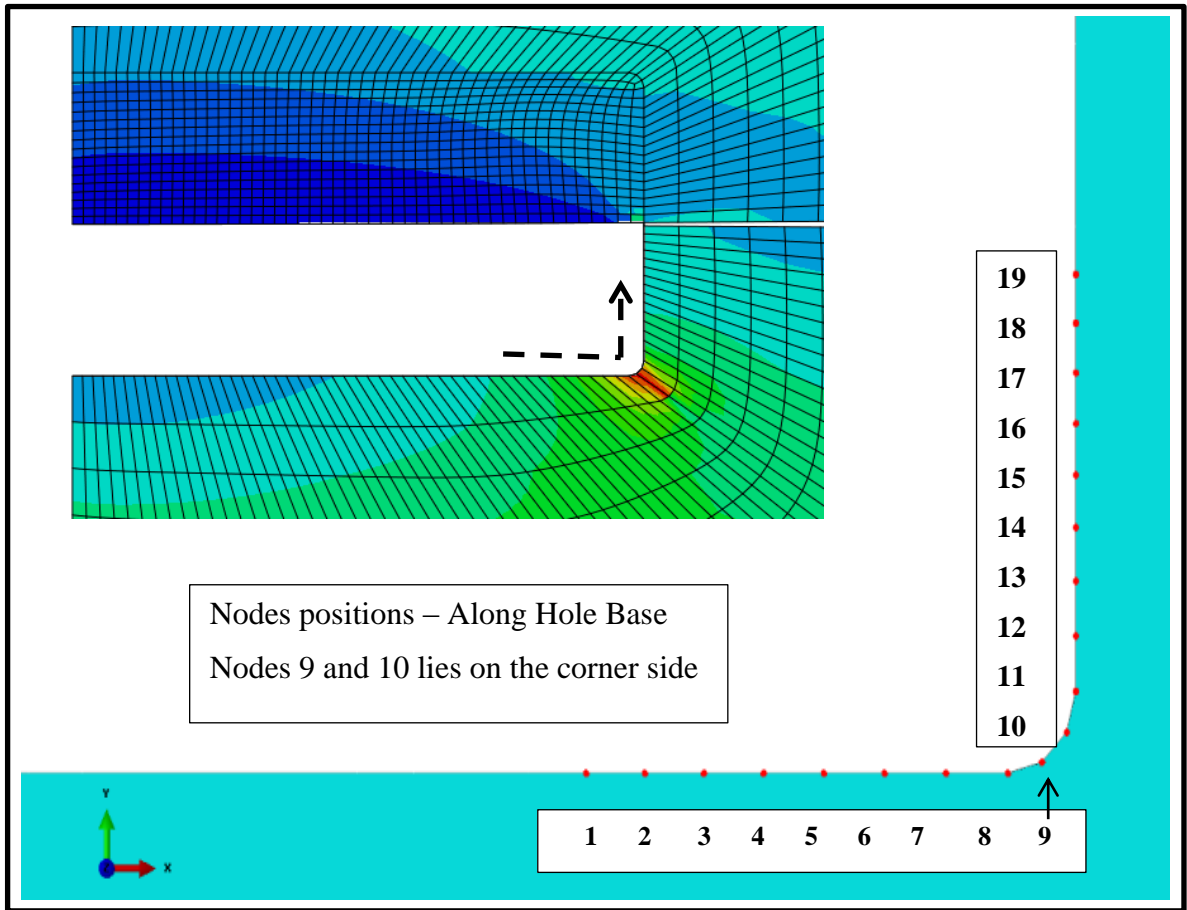


Figure 6.22: Nodal positions - along the hole base

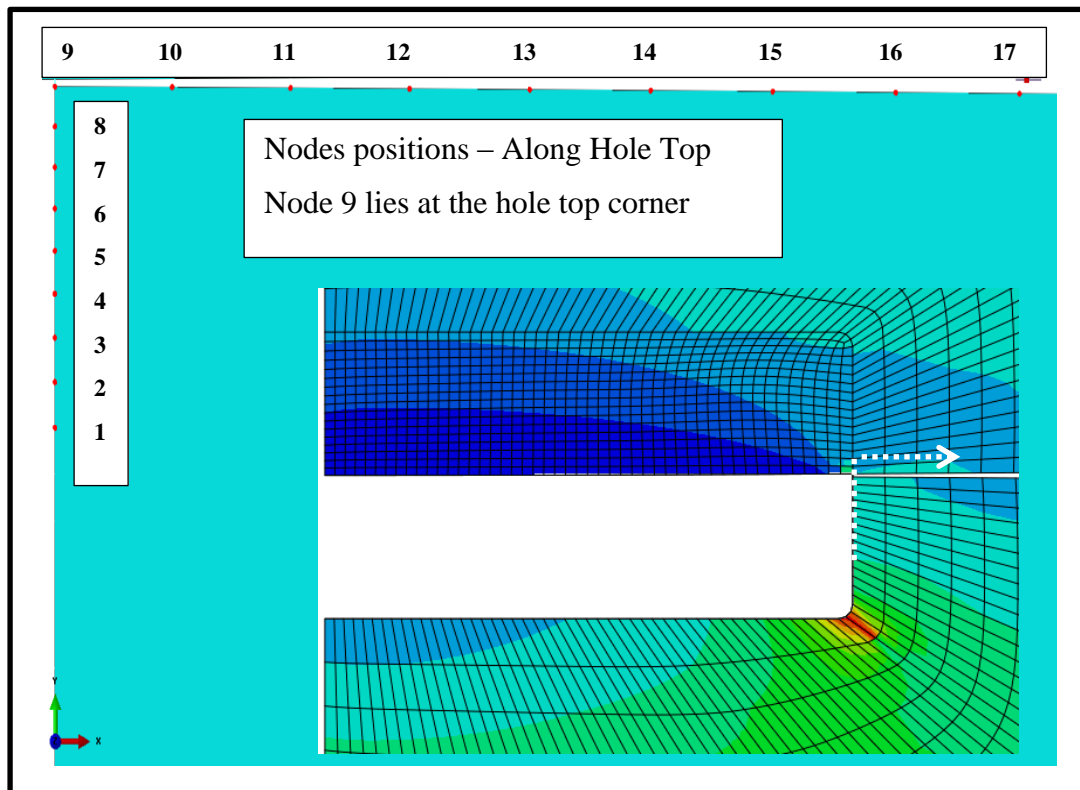


Figure 6.23: Nodal positions - along the hole top

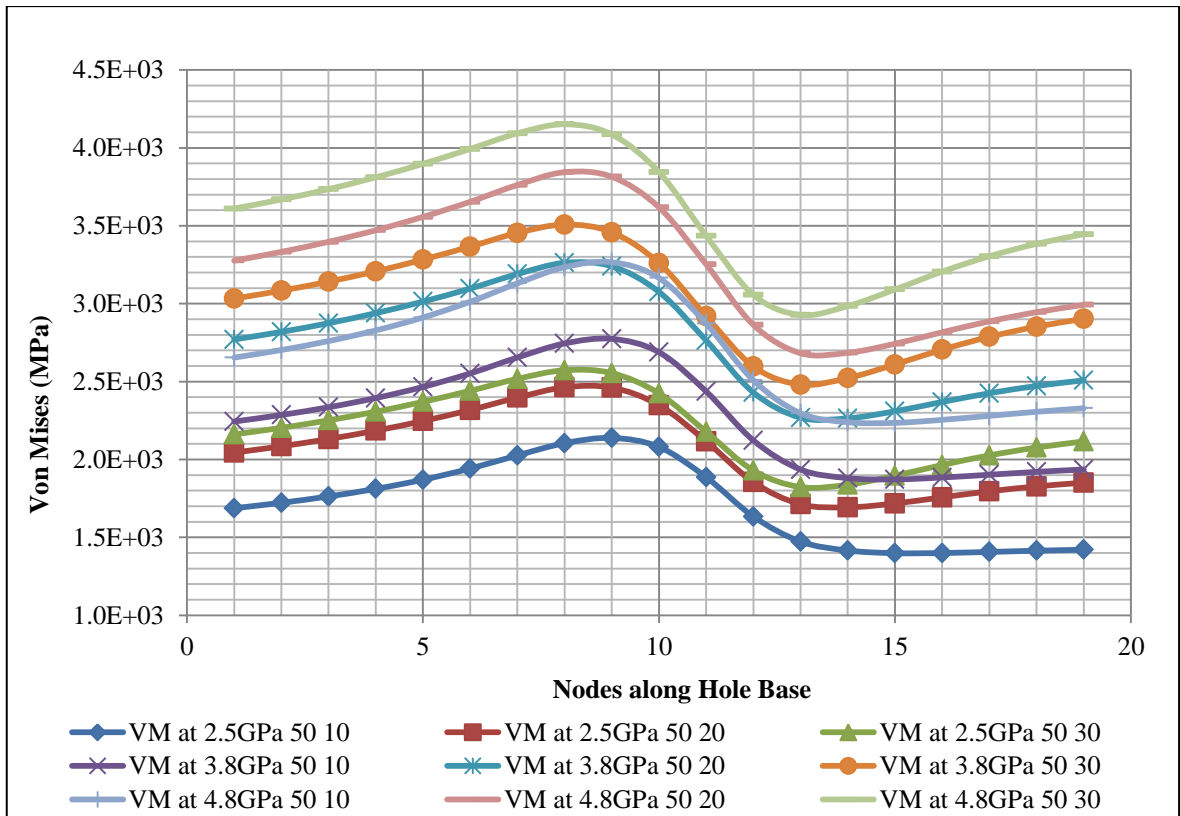


Figure 6.24: Von Mises stresses (MPa) for small diameter hole (50µm) for three depth levels – along the hole base

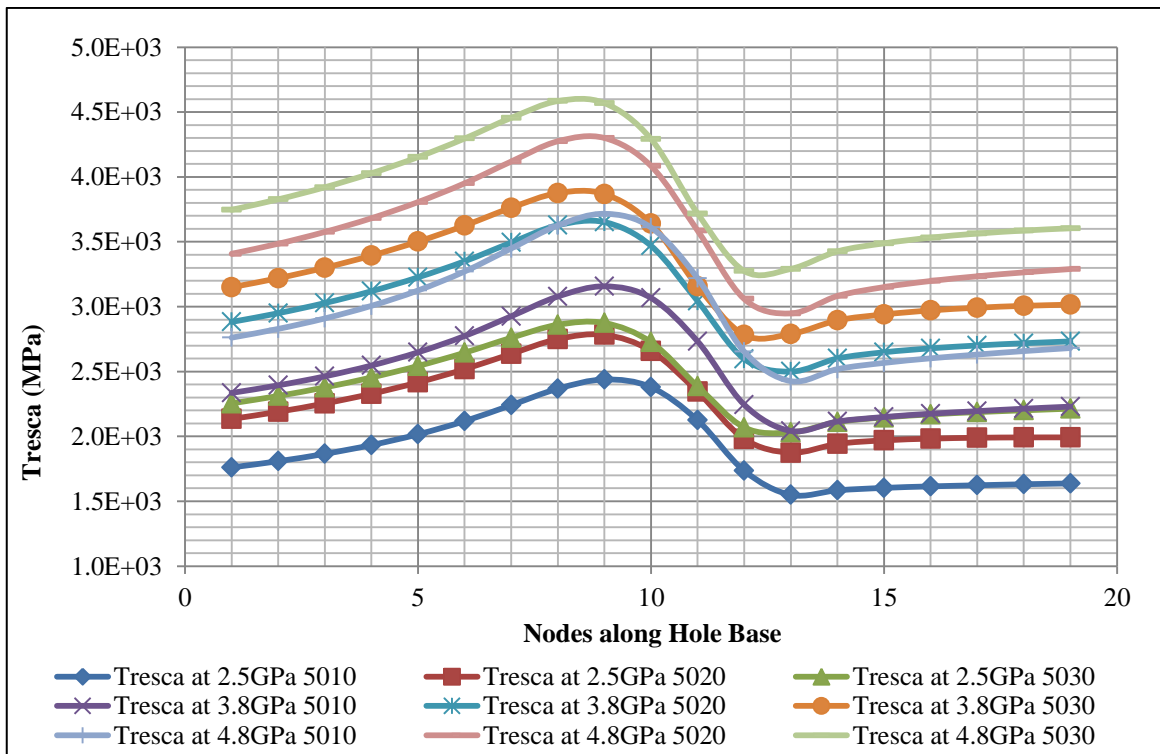


Figure 6.25: Tresca (MPa) for small diameter hole (50µm) for three depth levels – along the hole base

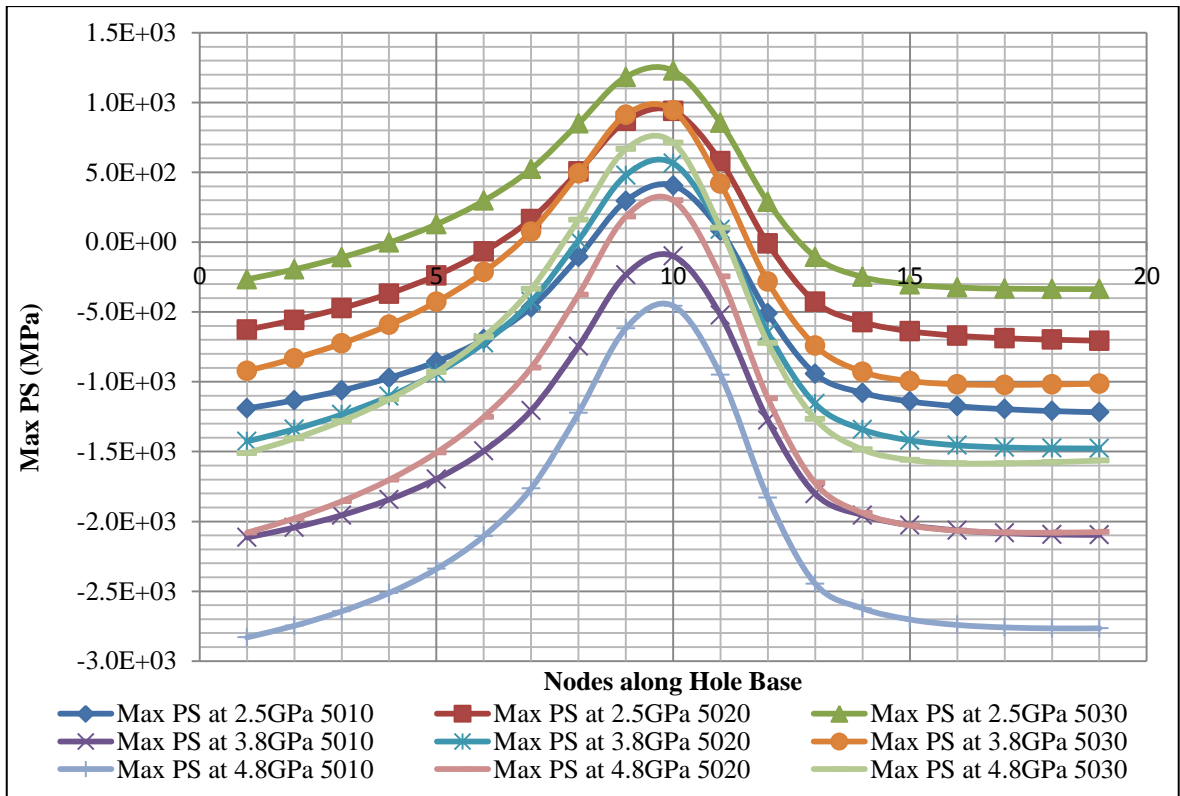


Figure 6.26: Maximum principal stresses (MPa) for small diameter hole (50 μ m) for three depth levels – along hole base

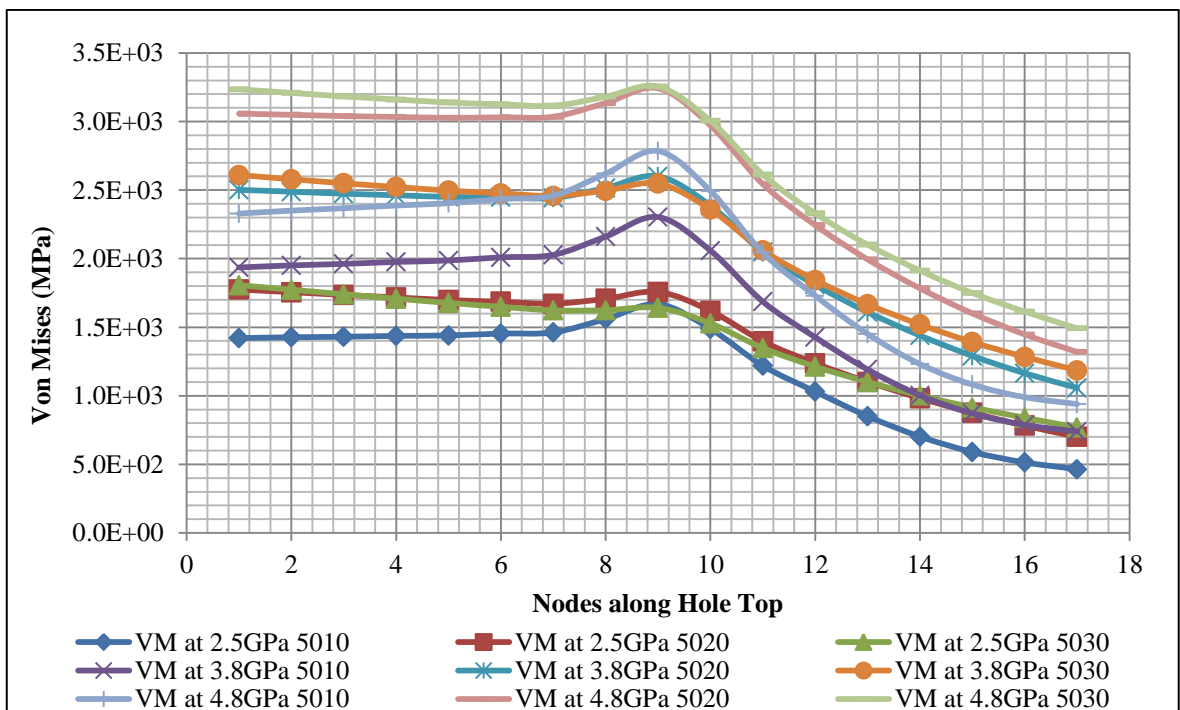


Figure 6.27: von Mises stresses (MPa) for small diameter hole (located close to cavity corner) – along hole top

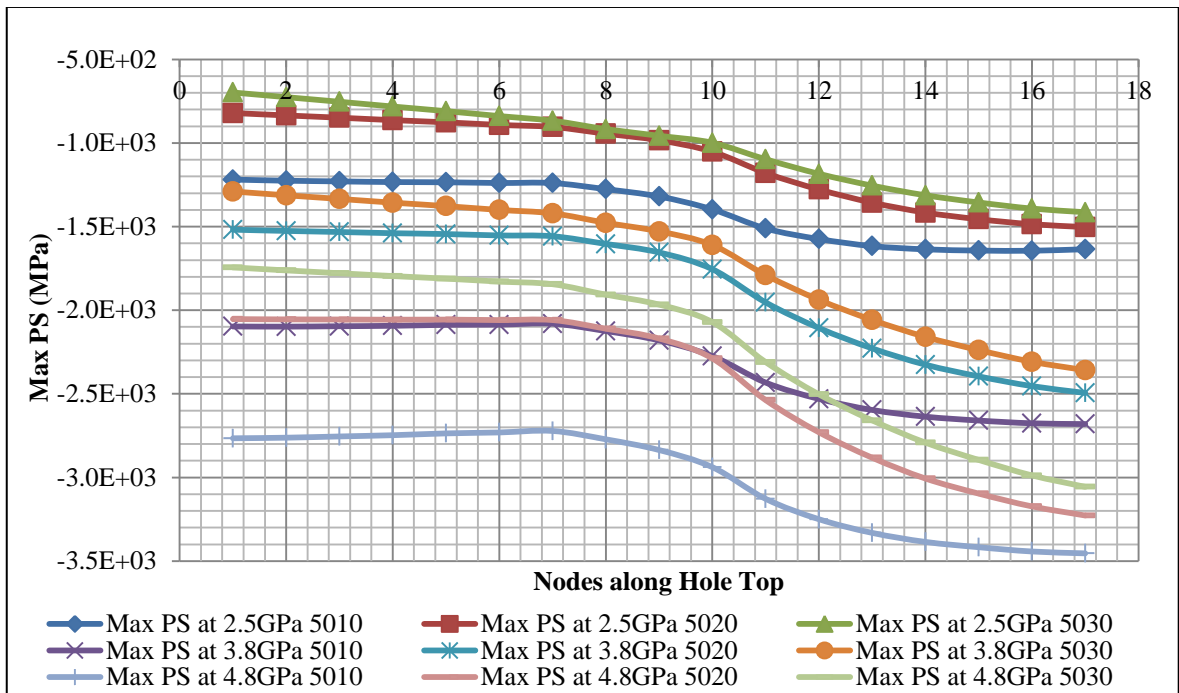


Figure 6.28: Maximum principal stresses (MPa) for small diameter hole - along hole top

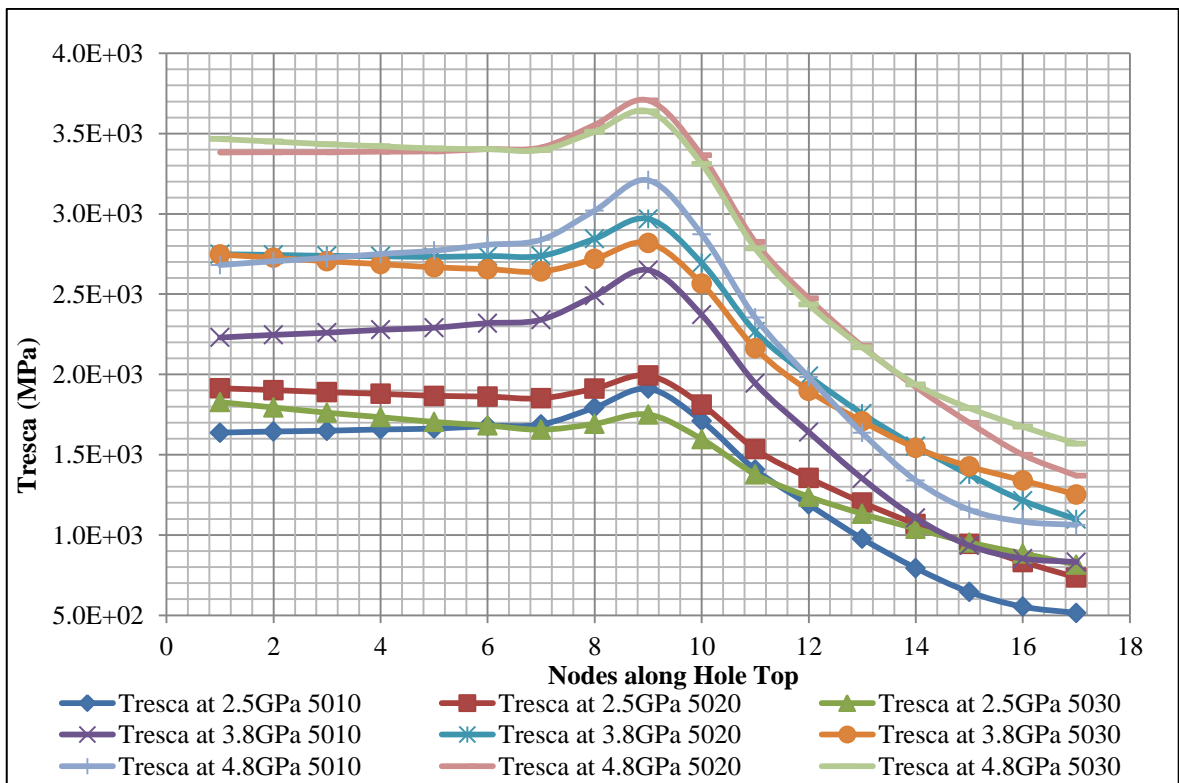


Figure 6.29: Tresca (MPa) for small diameter hole (located close to cavity corner) along hole top

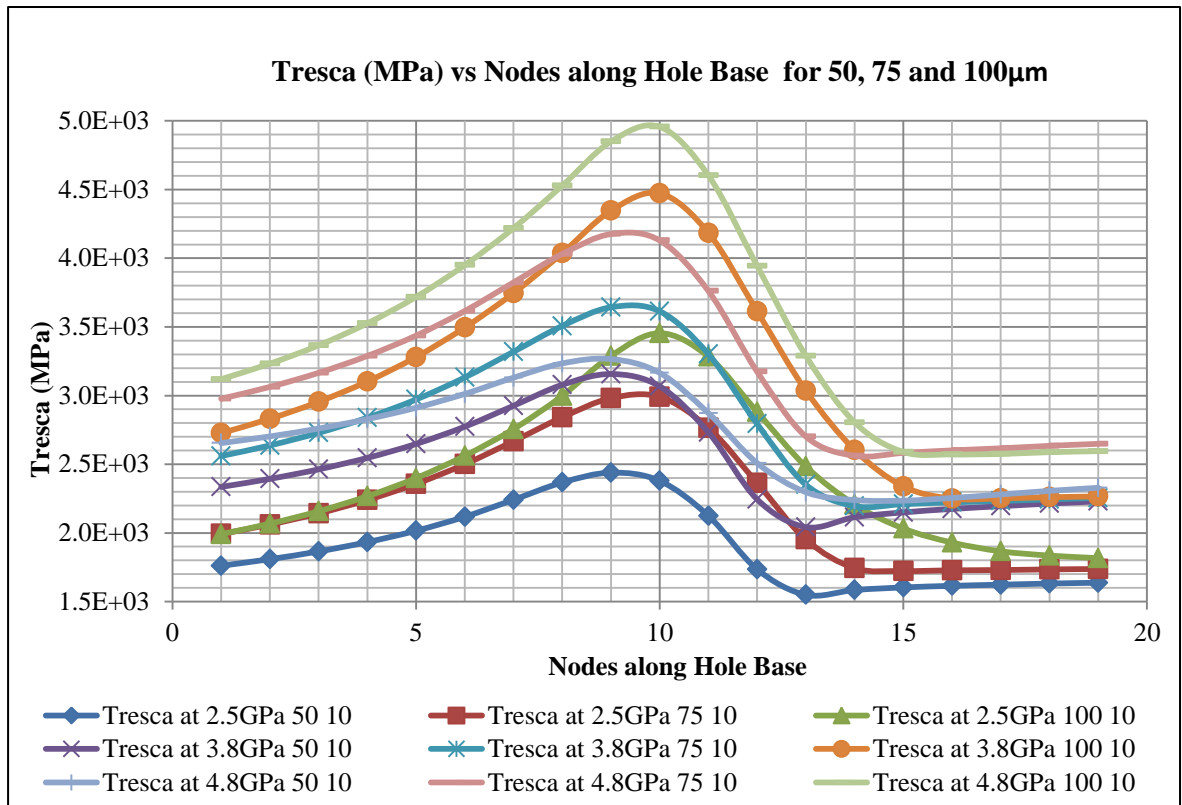


Figure 6.30: Tresca (MPa) comparison for small, medium and large diameters holes - along hole base

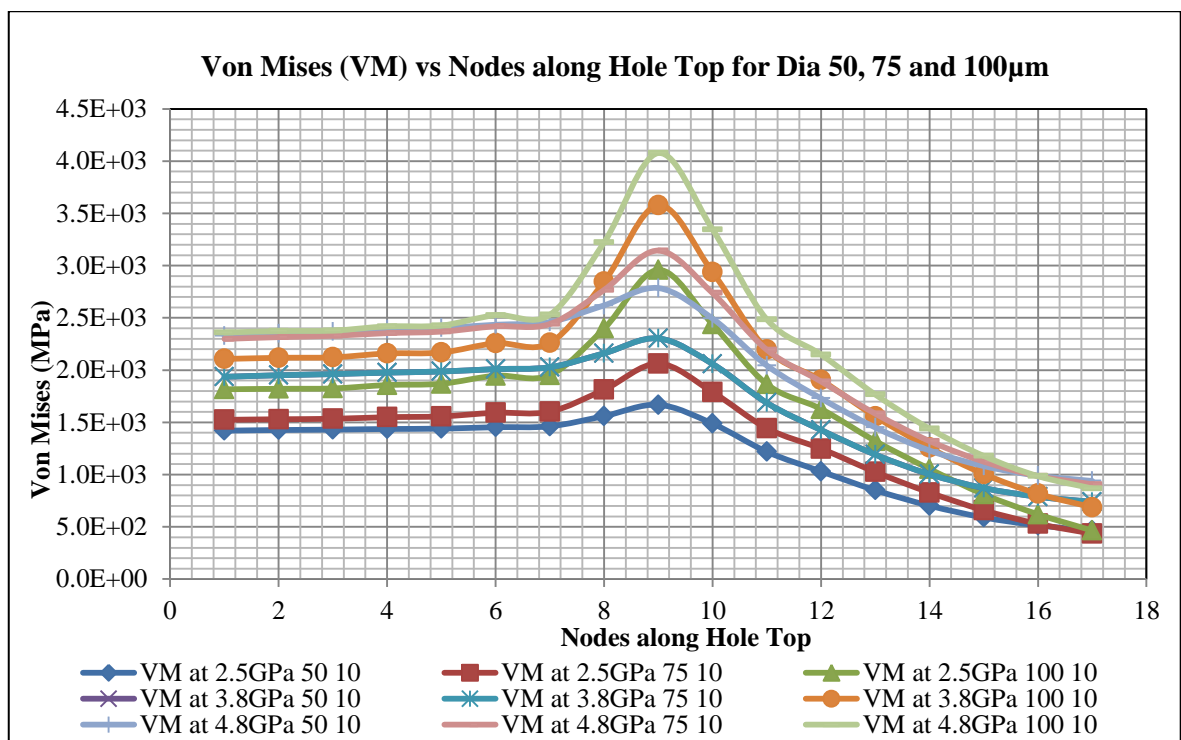


Figure 6.31: von Mises (MPa) comparison for small, medium and large diameters holes - along hole top

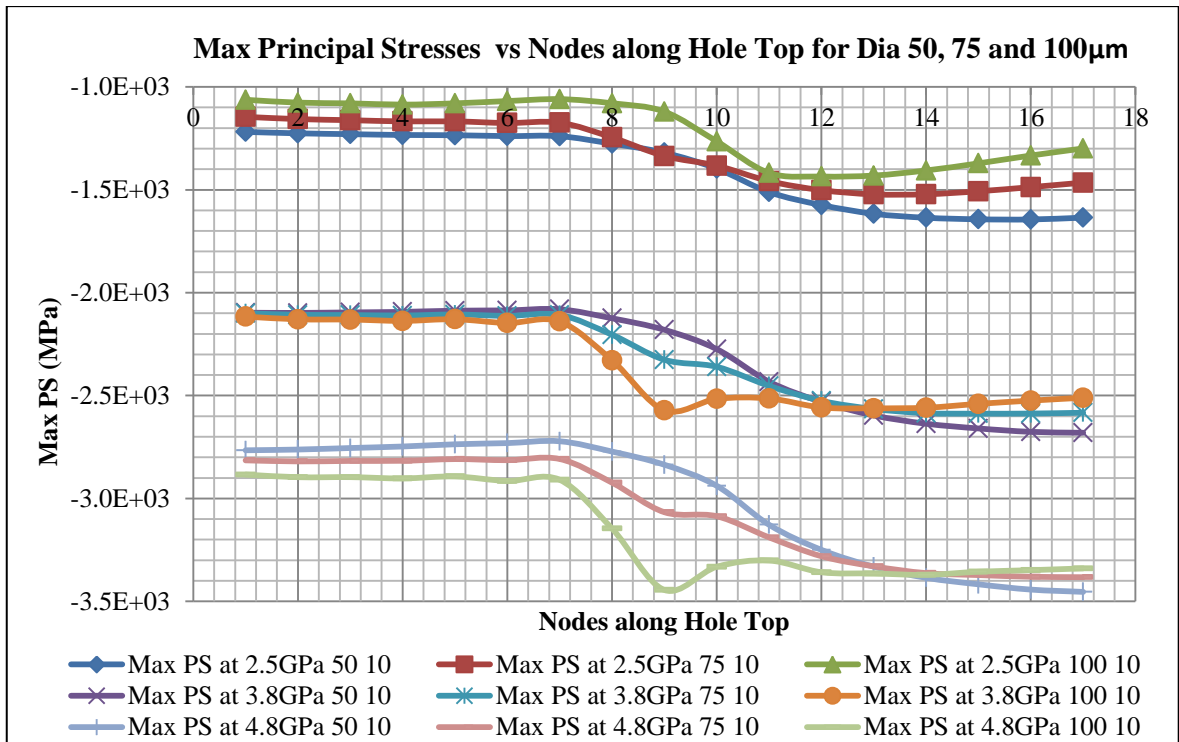


Figure 6.32: Maximum principal stresses (MPa) comparison for small, medium and large diameters holes - along hole top

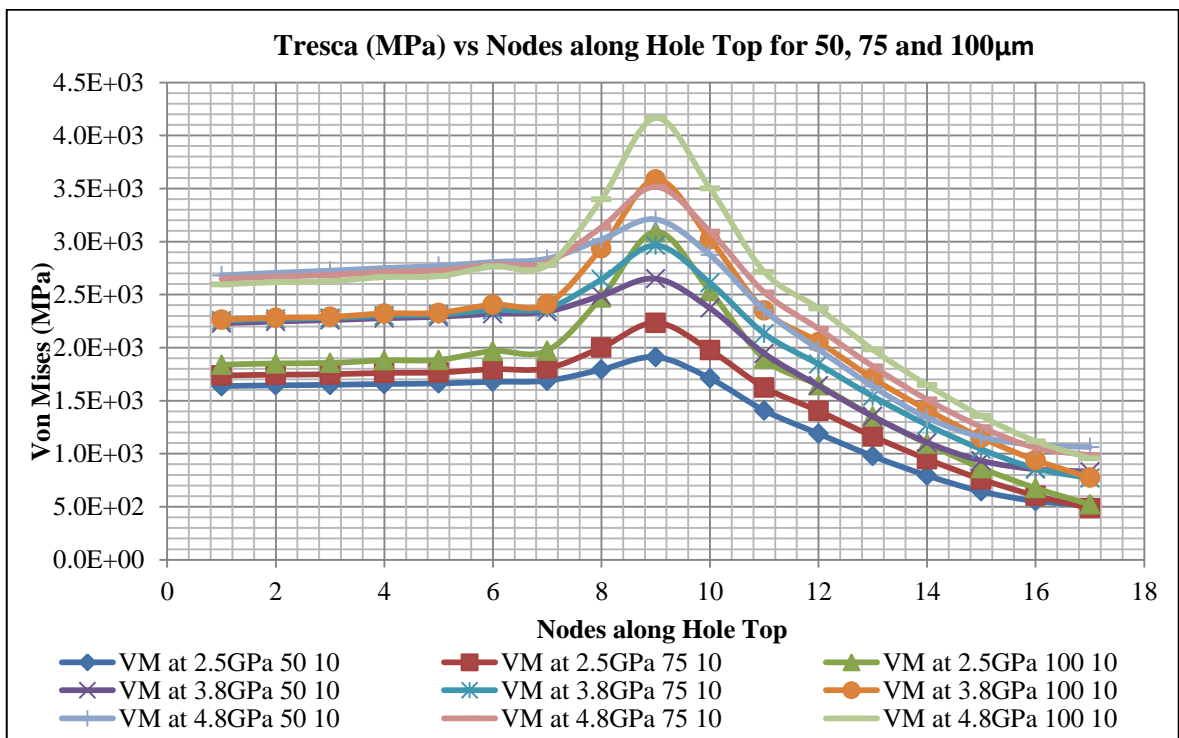


Figure 6.33: von Mises (MPa) comparison for small, medium and large diameters holes - along hole top

6.8. Results and Discussion – Shape II (Shape I vs. Shape II)

Figures 6.34-6.35 show the nodal positions for the stress field comparison for shape I (right cylindrical) and shape II (conical) holes as shown in Figure 6.36. Although Figure 6.36 indicates slightly higher stresses in case of shape II the location is not that critical and in practice very sharp pointed cavities cannot be achieved to test.

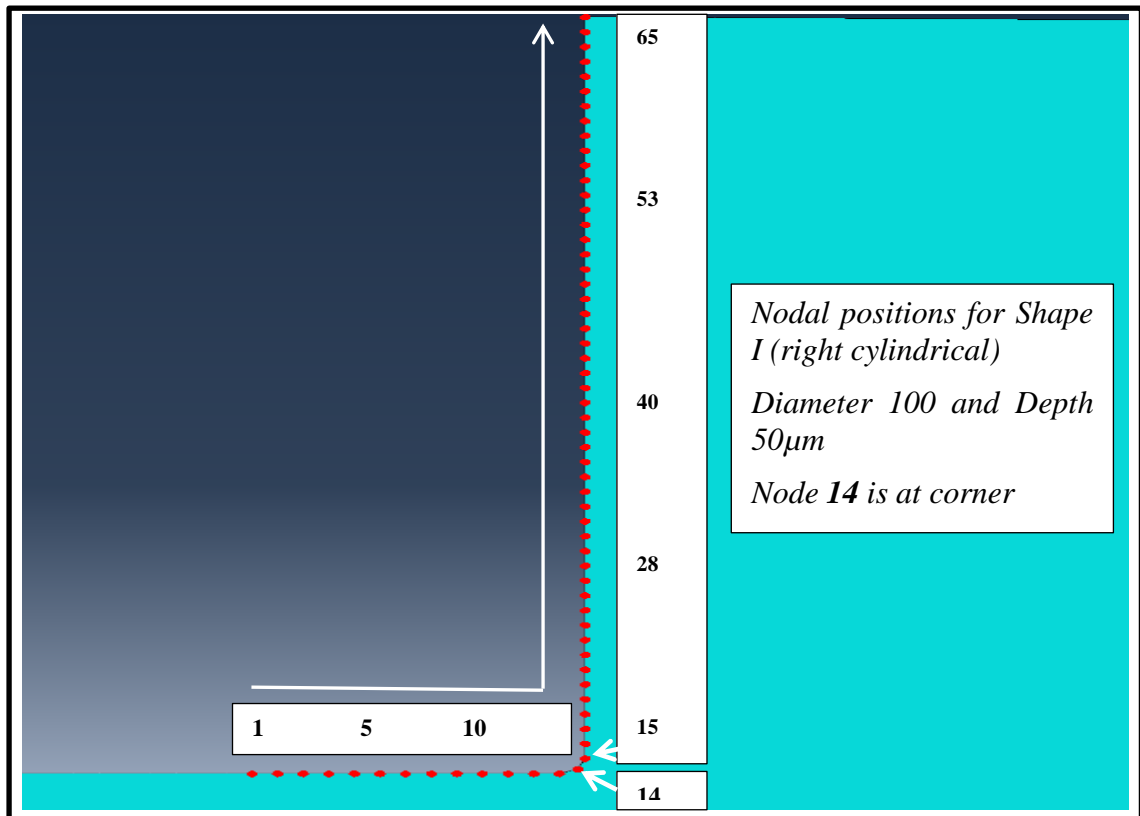


Figure 6.34: Nodal positions - along the hole base and depth – Shape I (Figure 6.36)

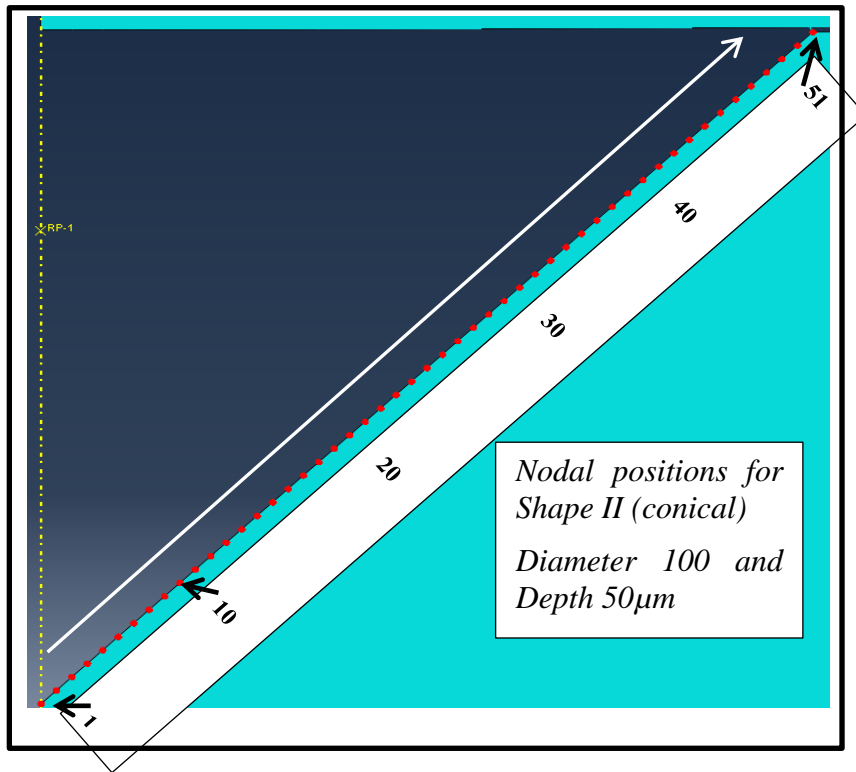


Figure 6.35: Nodal positions - along the hole depth – Shape II (Figure 6.36)

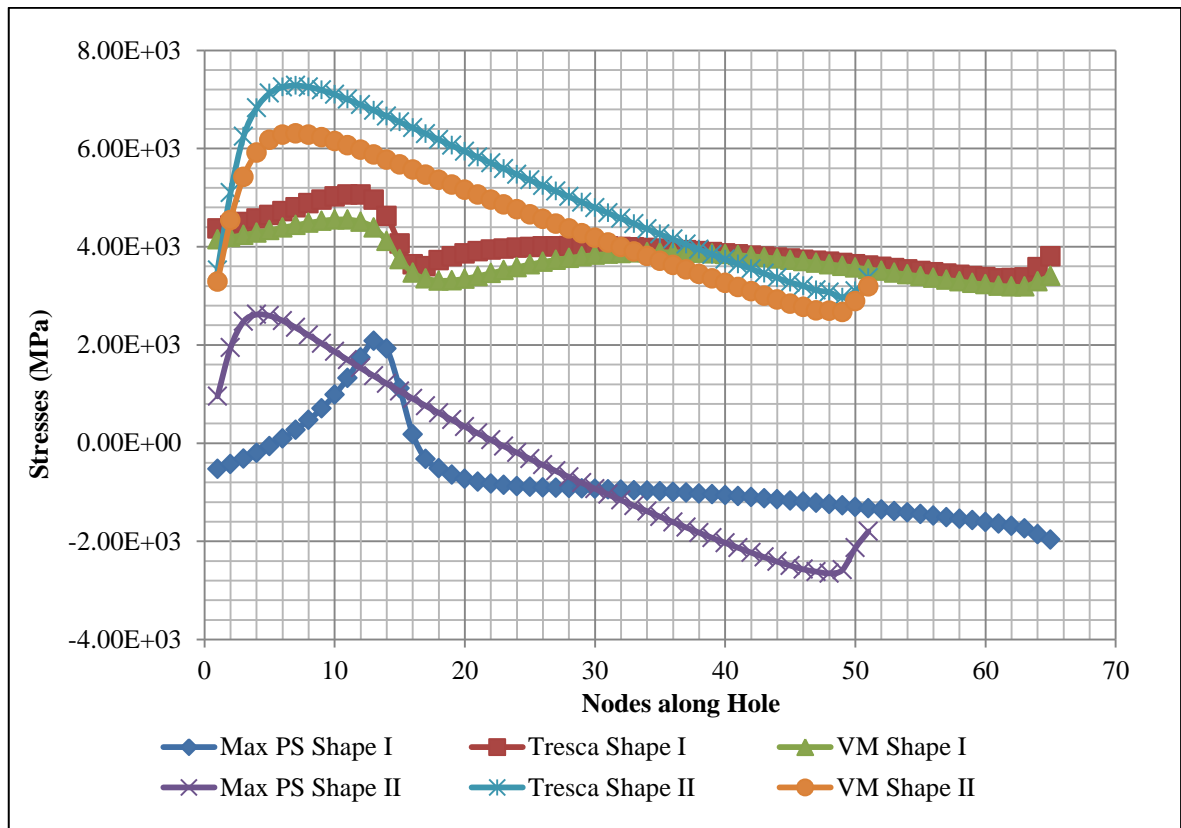


Figure 6.36: Stress field comparison for shape I and Shape II (along hole depth – Figure 6.34-6.35)

6.9. Theoretical Discussion

According to Way [1935], pit nucleation on lubricated rolling/sliding surfaces is brought by surface cracking due to oil hydraulic pressure from oil penetrated into the cracks. Extensive research has been reported based on this hypothesis. Kaneta et al. [1985], Murakami et al. [1985], Kaneta and Murakami [1987] produced theoretical and experimental studies based on hydraulic pressure concept. A similar trend has been observed in this current modeling study. Cavities shape III failed earlier due to inclined cavities/notches and this phenomenon has already been established [Kaneta and Murakami 1987]. Both surface and sub-surface entrapped liquid can initiate and propagate the cracks [Keer et al. 1982, Kudish 2002, Kudish and Burris 2004]. Entrapped fluid inside crack/cavity works as a catalyst inside the crack to convert compressive contact load into a crack opening [Balcombe 2012]. Trapped lubricant can cause high hydrostatic pressure which can propagate the crack and eventually can cause delamination failure [Hadfield and Stolarski 1994].

Based on the literature as discussed above and study conducted on different dimension cavities, it is well established that trapped fluid inside the cavities can have high hydrostatic pressure and due to this pressure, high surface tensile stresses produced. These tensile principal stresses cause the crack to initiate within silicon nitride having fully flooded cavities. High tensile principal stresses found at the (and close to) cavity base corners and these locations are susceptible for crack to initiate. Once crack was initiated in the ceramic material then it propagate fairly quickly compare to metallic fracture. Crack propagation in silicon nitride has been extensively discussed in the literature as well as in chapter 5.

6.10. Summary/Conclusions

Based on the extensive study using finite element method, following results are summarised/concluded;

1. Hydrostatic pressure effect has been successfully modeled using special elements technique. Hydrostatic pressure changed the stress field and can initiate cracks from the base of the cavities.
2. Experiments showed cracks initiating at the corner of the cavity base and propagating from it possibly under the local tensile stresses suggested by modeling
3. Shallow missing material with smaller diameter gives different stress fields and lower stresses at the cavity base corners resulting in less chances to fail
4. Both diameter and depth are important but depths are relatively more critical than diameter
5. Very deeper cavities might not give results as were expected in experiments due to less time to fill the cavity and create hydrostatic pressure scenario

FEA studies have provided similar results (trends) as were found from experiments (Chapter 5).

Chapter 7 Discussion and Conclusions

This research produced new insight into the tolerance of silicon nitride balls to surface defects under rolling contact both experimentally and numerically including the incorporation of hydrostatic pressure effects. Precise laser micro-machining was used to produce artificial cavities on the surfaces of silicon nitride balls. Star like features (small surface cracks and pits on balls) were categorised based on missing material to crack extent. Cross sectioning study highlighted crack initiation and propagation whereas replica study provided cavity base profile. In this chapter, a brief discussions of the experimental results along with FEA study is presented. Conclusions from this exhaustive study is also outlined along with design guide lines and proposed future work at the end of this chapter.

7.1. Discussion

7.1.1. Experimental Work

Surface defects including ring or C-cracks and line cracks have been discussed extensively in the past literature. In the first part of this experimental study, categorisation was made based on star to pit size/missing material part. Experiments were then conducted using different lubricants on the star features of category 1 (major star/crack and small extent of missing material part) and then of category 5 (major missing material/pit part with small extent of cracks). Some experiments were also conducted using additional categories of star features to observe the effect of pit size on the rolling contact fatigue of silicon nitride. In many cases star features were converted into shallow missing material areas after a few million stress cycles due to material flaking off. Thin mineral oil was used to conduct most of the experiments as it resulted in poorer performance compared to more viscous lubricants. Lubricant penetration effect was also observed in case of thin lubricants. The relatively high testing temperature led to a grease thinning effect and performance with grease was generally lower than with gearbox oil. Attempts were also made to artificially produce star type features as reproducible defects with some controllable pattern. Although these features could be produced but there was insufficient control of dimensions and reproducibility.

Missing material types of defect were artificially produced by precision laser micromachining with different types of shapes and cavity dimensions. Experiments were

conducted by precisely aligning defects on the silicon nitride balls within the contact path. All experiments were conducted at a high spindle speed (7500rpm), high temperature (75°C) and range of contact pressures (3.8GPa-4.8GPa). Different shapes and dimensions were tested for the main grade of silicon nitride currently used (material A) and a few samples made from an alternative grade (material B) were also tested. A well-defined failure mechanism was observed cavities/holes of right cylindrical / shape I and was also predictable for shape III (oblique cylindrical). Deeper cavities and large diameters were prone to earlier failure compared to shallow and smaller diameter cavities. Contact pressure influenced the tolerance and performance of the materials. Material A proved to have better performance and tolerance than material B. Shape assessment was conducted experimentally and it was found that shape I (right cylindrical) was more tolerable than shape III (oblique cylindrical) and shape II (conical) was more tolerable than shape I (right cylindrical).

As in fracture mechanics, stress intensities are calculated on the crack tip to compare the stress field with fracture toughness of the material. Stress intensity factor which is measure of stress intensity near the crack tip is based on many parameters including size and location of crack, sample geometry and nature, and magnitude and distribution of load.

As mode I is opening mode (high tensile stresses) and brittle materials are failed in the tensile stresses than compressive stresses. Fracture toughness of silicon nitride ($6.0\text{MPa m}^{1/2}$) is 2.5times lower than its counterpart steel ($>16.0\text{MPa m}^{1/2}$). Higher tensile stresses (stress intensity factors) causing crack to initiate and then its propagate in shearing mode (mode II).

The experiments showed a defined failure mechanism with crack initiation occurring at the corner of the cavity base and then propagation along the contact path with some branches in and outside and finally crack growth towards the surface and spalling failure. Crack initiation happens due to mode I (maximum principal stress) and propagation due to mode II (shear stresses and in the direction normal to maximum principle stresses). Friction and pressure cause a deeper spall in the trailing edge of the spall. Material tolerance and tolerable size was also defined by experimental methodology. Replica studies produced very useful results for cavity base profiles to investigate the failure mechanism.

7.1.2. FE Modeling and Analysis

FE modelling and analysis was done to find stress fields and potential failure locations based on the ball-on-ball contact scenario. The basic model was verified with Hertz theory while 2D and 3D models were generated to determine the rolling effect with a cavity in the contact. 3D static and 3D quasi- static models produced different stress fields due to over-rolling. However, the initial 3D models were generated without considering the lubricant/fluid within the contact. Over-rolling also produced high tensile stresses at the hole base when cavity lies outside the contact. Hydrostatic pressure modeling successfully produced the results for crack initiation from the cavity base due to maximum tensile principal stresses.

7.2. Conclusions

This research on performance of silicon nitride balls with surface defects in rolling contact was significant due to some novel work and techniques conducted in a three year study. For the first time, star type features were properly investigated, categorised and a tolerance study was conducted. Missing material (pits/holes on ball surface) was also extensively investigated through both experimental programme and novel numerical modeling methods using special elements. Defect tolerance in case of star features and missing material was of importance to a partner organisation to establish performance criteria for hybrid ceramic bearings and is relevant to surface quality tolerances and specifications. Conclusions of this research study according to the aims and objectives defined in Chapter 1 are as follows;

1. Star like features have been categorised on the basis of missing material/pit size. Category 1 star feature is with no/minor pit area and category 5 star with almost all pit area.
2. Star features did not lead to spalling failure under rolling contact at high contact pressures. Some minor surface damage could take place which, at worst, resulted in break-out or flaking of material - converted the star into a shallow missing material type defect. This flaking could happen after a few million stress cycles (5-10) but grow further outside the original extent of the feature for low viscosity lubricants. Lubrication had some effect on the performance of star features. Low viscosity lubricants were less effective than high viscosity lubricants due to lubricant penetration and change in crack face friction.

-
3. Laser micro-machining was used for precision machining of artificial missing material on silicon nitride ball surfaces. These cavities were produced with different diameter (50-100 μm) and depths (5-50 μm) as well as different profiles (right cylindrical, conical and oblique cylindrical) in both materials A and B.
 4. Extensive rolling contact experiments were carried out on balls with cavities to determine their effect on rolling contact performance, defect tolerances and failure modes. Class 'A' material was found to perform better than class 'B' material over a range of different operating conditions (Pressure: 3.8-4.8GPa, Speed: 7500rpm, Temperature:75°C, and different defect locations on the contact track). Premium quality material (A) can be used at higher contact load (4.8GPa) for low fatigue applications (up to 100millions) for defect size of 50 μm (diameter) and 10 μm depth. Low grade silicon nitride can only be used up to 4.5GPa for low fatigue cycles (100million stress cycles) for same defect size. Increase in the defect size (diameter and defect) reduces the defect tolerance of material (both material A and material B). Higher RCF life of material A than material B may be due to higher effective surface tensile strength and microstructure. Wider defects (75-100 μm) are not tolerable at high contact pressure (4.8GPa) with depth higher than 10 μm . Deeper cavities ($\geq 20\mu\text{m}$) cannot be used at high contact pressure with all diameter range (50-100 μm).
 5. Three shapes were tested and based on experimental work, conical cavities (shape II) performed better than those with right cylindrical/straight sides (shape I) or re-entrant angles/oblique cylindrical (shape III). Shape comparison is based on the defect tolerance at the range of operating conditions.
 6. Positioning of the defect in the contact track and the actual cavity base profile influence the performance of balls during experiment. In some cases, particularly for cavities with re-entrant angles (oblique cylindrical), replica produced a better cavity profile than white light profilometry. Cavity base profile is also found an important parameter which influences the material tolerance (both Class A and B).
 7. Spalling was the dominant failure mode observed in case of missing material (cavities) on the silicon nitride ball surface. However, some minor delamination and surface wear was also found in rolling contact experiments with both star features and missing material.

-
8. A hydrostatic pressure modeling technique was adopted to investigate the potential location and position for crack initiation based on calculated stress fields. Maximum principal stresses at the cavity base profile were spotted due to hydrostatic pressure scenario which are responsible for crack initiation in the brittle material. Failure of surface based fluid filled cavities within silicon nitride was successfully explained by numerical modeling.

7.3. Design Guidelines

Following guidelines would be recommended for use for silicon nitride as rolling element in the hybrid bearing applications;

1. Star features are tolerable for rolling contact applications for contact load/pressure up to 4.8GPa for low fatigue applications (up to 100 million stress cycles)
2. Thin lubricants are more likely to lead to localised surface deterioration compared to grease and gearbox oil
3. High quality bearing grade silicon nitride (material A) has a higher tolerance to surface defects than lower quality material (material B). Therefore material A or grades of similar quality should be used for demanding or critical applications.
4. A cavity up to 10 μ m in depth and diameter up to 50 μ m will survive rolling contact at contact pressures below 4.8GPa for up to 100 million stress cycles (Class A Material). Deeper cavities up to the same diameter can tolerate lower contact stresses.
5. Cavity profiles are important. Holes with rounded profiles are less susceptible to failure than holes with sharp corners.
6. Linear features, deep scratches or shallow gouges, are unlikely to lead directly to failure under rolling contact. However, such features could be liable to localised wear.

7.4. Future Work

Proposed future work is listed below;

- a. Although surface star feature were converting to surface missing material after few million over-rolling stress cycles for low viscosity lubricants, further study may be conducted for longer duration until getting failure to find total life of the rolling element bearing. These testing may be conducted at higher contact pressure.

-
- b. Further efforts may be made to have reproducible star pattern for testing and modeling. Natural star defect modeling is challenging as each star have almost different geometry than other star features. Reproducible star feature might help to handle this situation.
 - c. Larger diameter and deeper missing material cavities fail fairly quickly at the range of pressure defined for this research study. However, such cavities can be tested at low contact pressure. Missing material cavities might also need to test for high viscous lubricants to compare the lubrication performance.
 - d. More experiments might be needed for shape II (conical) and shape III (oblique cylindrical) type of cavities to have better comparison with shape I (right cylindrical) cavities at different contact pressure and using different lubricants. Both material A and B should be tested for shape II (conical) and shape III (oblique cylindrical) type of cavities.
 - e. Laser micro-machining might induce residual stresses in the material. Residual stresses should be measured to incorporate its effect on rolling contact fatigue life of silicon nitride material.
 - f. 3D-analysis may be conducted for missing material cavities for different shapes and dimensions. Shape III (oblique cylindrical) cavities cannot be modeled using axi-symmetric approach and hence 3D analysis might be required. Similarly, jet of lubricant coming out from the cavity as upper ball rolls further can be modeled using FEA and CFD.

...

References

- Al-Bukhaiti, M. A., Al-Hatab, K. A., Gabbert, U., 2011. The influence of high contact stresses and lubricant type on the rolling contact fatigue life and failure mode of AISI 52100 steel balls. *Emirates Journal of Engineering Research*, 16(1), 9-22.
- ABAQUS Users Manual v. 6-12, 2012. Dassault Systemes, Providence, RI, USA.
- Ahmed, R., 1998. Rolling contact fatigue of thermal spray coatings. PhD Thesis, Brunel University, UK.
- Arakere, N. K., Branch, N, Levesque, G., Svendsen, V., Forster, N. H., 2010. Rolling contact fatigue life and spall propagation of AISI M50, M50 NiL and AISI 52100, Part II: Stress Modeling. *Tribology Transactions*, 53, 42-51.
- Aramaki, H., Shoda, Y., Morishita, Y. and Sawamoto, T., 1988. The performance of ball bearings with silicon-nitride ceramic balls in high speed spindles for machine tools. *J. of Tribology*, 110, 693-698.
- Awan, A. W., Hadfield, M., Thomas, B., Vieillard, C., Cundill, R., 2013. Surface star defect tolerance assessment on finished silicon nitride balls in rolling contact. 40th Leeds-Lyon Symposium, France.
- Awan, A. W., Hadfield, M., Thomas, B., Vieillard, C., Cundill, R., 2013. An experimental investigation of rolling contact failure within silicon nitride subject to micro surface defects. 5th World Tribology Congress, Italy.
- Awan, A. W., Hadfield, M., Thomas, B., Vieillard, C., Lai, J., Kadin, Y. and Cundill, R., 2013. Modeling of surface defects in silicon nitride rolling element in lubricated rolling contact. 69th STLE Annual Meeting and Exhibition, USA.
- Balcombe, R., Fowel, M. T., Olver, A. V., Ioannides, S. and Dini, D., 2011. A coupled approach for rolling contact fatigue cracks in the hydrodynamic lubrication regime: The importance of fluid solid interactions. *Wear*, 271, 720-33.
- Bermudo, J., Osendi, M. I., Li, M. and Reece, M. J., 1997. Cyclic fatigue behaviour of silicon nitride materials. *Journal of European Ceramic Society*, 17, 1855-1860.
- Bhushan, B., Sibley, B. L., 1981. Silicon nitride rolling bearings for extreme operating conditions. *ASLE Trans.* 25 (4), 417-428.

- Bogdanski, S., 2002. A rolling contact fatigue crack driven by squeeze fluid film. *Fatigue and Fracture of Engineering Materials and Structures*, 25, 1061-1071.
- Bogdanski, S., 2005. Liquid-solid interaction at opening in rolling contact fatigue cracks. *Wear*, 258, 1273-1279.
- Bogdanski, S., Lewicki, P. and Szymaniak, M., 2005. Experimental and theoretical investigation of the phenomenon of filling the RCF crack with liquid. *Wear*, 258, 1280-1287.
- Bomidi, J. A. R., Weinzapfel, N., Sadeghi, F., Liebel, A. and Weber, J., 2013. An improved approach for 3D rolling contact fatigue simulations with microstructure topology. *Tribology Transactions*, 56(3), 385-399.
- Bormetti, E., Donzella, G. and Mazzu, A., 2002. Surface and subsurface cracks in rolling contact fatigue of hardened components. *Tribology Transactions*, 45(3), 274-283.
- Bower, A. F., 1988. The influence of crack face friction and trapped fluid on surface initiated rolling-contact fatigue cracks. *Journal of Tribology-Transactions of the ASME*, 110, 704-711.
- Bower, A. F. and Fleck, N. A., 1994. Brittle fracture under a sliding line contact. *J. Mech. Phys. Solids*, 42, 1375-1396.
- Bradshaw, K. K., 2011. Rolling contact fatigue life of hybrid bearings. MS Thesis, Howard University, USA.
- Branch, N. A., Arakere, N. K., Svendsen, V. and Forster, N. H., 2009. Stress field evolution in a ball bearing raceway fatigue spall. *Journal of ASTM International*, 7(2), DOI: 10.1520/JAI102529.
- Burrier, H. I., 1996. Optimizing the structure and properties of silicon nitride for rolling contact bearing performance. *Tribology Transactions*, 39, 276-285.
- Cann, P. M., Doner, J. P., Webster, M. N. and Wikstrom, V., 2001. Grease degradation in rolling element bearings. *Tribology Transactions*, 44:3, 399-404.
- Cento, P. and Dareing, D. W., 1999. Ceramic materials in hybrid ball bearings. *Tribology Transactions*, 42, 707-714.
- Chao, L. Y., Lakshminarayanan, R., Lyer, N., Lin, G-Y. and Shetty, D. K., 1998. Transient wear of silicon nitride in lubricated rolling contact. *Wear*, 223, 58-65.

- Cheng, W., Cheng, H. S. and Keer, L. M., 1994. Experimental investigation on rolling/sliding contact fatigue crack initiation with artificial defects. *Tribology Transactions*, 37:1, 1-12.
- Chevalier, J. and Gremillard, L., 2009. Ceramics for medical applications: A picture for the next 20 years. *Journal of European Ceramic Society*, 29, 1245-1255.
- Chiu, Y. P., 1999. An approach for fatigue cracking failure prediction of ceramic rolling elements under Hertzian loading. *Tribology Transactions*, Vol 42:2, 289-295.
- Cundill, R. T., 1997. Impact resistance of silicon nitride balls. 6th International Symposium on Ceramic Materials & Components for Engines, Arita, Japan.
- Dausinger, F., Hugel, H. and Konov, Vitali., 2003. Micromachining with ultrashort laser pulses: from basic understanding to technical applications. Proc. SPIE 5147, ALT 02 International Conference on Advanced Laser Technologies, 106.
- Dee, C. W., 1970. Silicon nitride - Tribological applications of a ceramic material. *Tribology*, 3, 89-92.
- Diab, Y., Coulon, S., Ville, F. and Flamand, L., 2003. Experimental investigations on rolling contact fatigue of dented surfaces using artificial defects: subsurface analysis. Leeds-Lyon symposium proceedings (Tribological Research and Design for Engineering Systems) 359-367.
- Fleming, J. R. and Suh, N. P., 1977. Mechanics of crack propagation in delamination wear. *Wear*, 44, 39-56.
- Fujimoto, K., Itao, H., Yamamoto, T., 1992. Effect of cracks on the contact pressure distribution. *Tribology Transactions*, 35:4, 683-695.
- Gabelli, A., Morales-Espejel, G. E. and Ioannides, E., 2008. Particle damage in hertzian contacts and life ratings of rolling bearings. *Tribology Transactions*, 51:4, 428-445.
- Glover, D., 1982. A ball-rod rolling contact fatigue tester. ASTM STP 771, Philadelphia, USA.
- Glodez, S., Potocnik, R., Flasker, J and Zafosnik, B., 2008. Numerical modelling of crack path in the lubricated rolling-sliding contact problems. *Engineering Fracture Mechanics*, 75, 880-891.

- Gloeckner, P., Sebald, W. and Bakolas, V., 2009. An approach to understanding micro-spalling in high-speed ball bearings using thermal elastohydrodynamic model. *Tribology Transactions*, 52:4, 534-543.
- Goepfert, O., Ampuero, J., Pahud, P. and Boving, H. J., 2000. Surface roughness evolution of ball bearing components. *Tribology Transactions*, 43, 275-280.
- Hamburg, G., Cowley, P. and Valori, R. 1981. Operation of an All-Ceramic Mainshaft Roller Bearing in J-402 Gas-Turbine Engine. *J. ASME, Lubrication Engineering*, 37(7), 407-415.
- Hadfield, M., 1993. Rolling Contact Fatigue of Ceramics. PhD Thesis, Brunel University, UK.
- Hadfield, M., Stolarski, T. A., Cundill, R. T. and Horton, S., 1993a. Failure modes of ceramic elements with ring-crack defects. *Tribology International*, 26, 157-164.
- Hadfield, M., Stolarski, T. A., Cundill, R. T. and Horton, S., 1993b. Failure modes of pre-cracked ceramic elements under rolling-contact. *Wear*, 169, 69-75.
- Hadfield, M., Fujinavva, G., Stolarski, T. A. and Tobe, S., 1993c. Residual stress in failed ceramic rolling-contact balls. *Ceramic International*, 19, 307-313.
- Hadfield, M. and Stolarski, T. A., 1994. Observations of delamination fatigue on pre-cracked ceramic elements in rolling-contact. *Ceramics International*, 21, 125-130.
- Hadfield, M., Tobe, S. and Stolarski, T. A., 1994. Subsurface crack investigation on delaminated ceramic elements. *Tribology International*, 27, 359-367.
- Hadfield, M. and Stolarski, T., 1995. The effect of the test machine on the failure mode in lubricated rolling contact of silicon nitride. *Tribology International*, 28:6, 377-382.
- Hadfield, M., 1998. Failure of silicon nitride rolling elements with ring crack defects. *Ceramics International*, 24, 379-386.
- Hadfield, M. and Tobe, S., 1998. Residual stress measurements of hot isostatically pressed silicon nitride rolling elements. *Ceramics International*, 24, 387-392.
- Harris, T. A., 1990. *Rolling Bearing Analysis*., John Willey & Sons.
- Hertz, H., 1882. On the contact of elastic solids.

- Hills, D. A. and Ashelby, D. W., 1979. A fracture mechanics approach to rolling contact fatigue. *Tribology International*, 12:3, 115-119.
- Ioannides, E. and Harris, T. A., 1985. A new fatigue life model for rolling bearings. *ASME Journal of Tribology*, 107, 367-378.
- Jacobson, B. O., 1991. *Rheology and Elastohydrodynamic Lubrication*. Tribology Series 19, Elsevier.
- Johnson, K. L., 1985. *Contact Mechanics*. Cambridge University Press.
- Jun, H. K., Fletcher, D. I., Jung, H. S., Lee, G. H. and Lee, D. H., 2011. Calculation of minimum crack size for growth under RCF between wheel and rail. *WIT Transactions on Engineering Sciences*, 71, 123-134.
- Kabo, E., 2002. Material defects in rolling contact fatigue-influence of overloads and defect clusters. *International Journal of Fatigue*, 24, 887-894.
- Kadin, Y. and Rychahivskyy, A. V., 2012. Modeling of surface cracks in rolling contact. *Material Science and Engineering A*, 541, 143-151.
- Kalin, M. and Vizintin, J., 2004a. A dvantages of using the ball-on-flat device in rolling-contact testing of ceramics. *Journal of Euoropean Ceramic Society*, 24, 11-15.
- Kalin, M. and Vizintin, J., 2004b. A Rolling Contact Device that uses the Ball-on-Flat Experimenting Principle. *Wear*, 256, 350-341.
- Kaneta, M., Yatsuzuka, H. and Muakami, Y., 1985. Mechanism of crack growth in lubricated rolling/slidin contact. *ASLE Transactions*, 28:3, 407-414.
- Kaneta, M. and Murakami, Y., 1987. Effects of oil hydraulic pressure on surface crack growth in rolling/sliding contact. *Tribology International*, 20:4, 210-217.
- Kang, J., 2001. *Influence of Surface Quality on the Rolling Contact Fatigue Behaviour of Ceramics*. PhD Thesis, Bournemouth University, UK.
- Kang, J., Hadfield, M. and Cundill, R. T., 2001. Rolling contact fatigue performance of HIPed Si₃N₄ with different surface roughness. *Ceramic International*, 27, 781-794.
- Kang, J., Hadfield, M. and Tobe, S., 2002. Residual stress field of HIPed silicon nitride rolling elements. *Ceramic International*, 28, 645-650.

- Kang, J. and Hadfield, M., 2003. Comparison of four-ball and five-ball rolling contact fatigue experiments on lubricated Si₃N₄/Steel contact. *Materials and Design*, 24, pp. 595-604.
- Kang, J., Hadfield, M. and Ahmed, R., 2003. The effect of material combination and surface roughness in lubricated silicon nitride/steel rolling contact fatigue. *Material and Design*, 24, 1-13.
- Karaszewski, W., 2008. The influence of oil additives on spread cracks in silicon nitride. *Tribology International*, 41, 889-895.
- Karlicek, Robert, 2011. *Advances in Laser micromachining*. JPSA Seminar, Durham, March 01, 2011.
- Karnakis, D., 2005. *Laser Micro-drilling in Industrial Applications*. Oxford Laser, UK (<http://www.designforlasermanufacture.com/assets/OLmicrodrill.pdf>)
- Keer, L. M., Bryant, M. D. and Haritos, G. K., 1982. Subsurface and surface cracking due to hertzian contact, *Journal of Applied Mechanics - Transactions of the ASME*, 105 198-205, 104, 347-351.
- Keer, L. M. and Bryant, M. D., 1983. A pitting model for rolling-contact fatigue, *Journal of Lubrication Technology-Transactions of the ASME*, 105 198-205.
- Khan, Z. A., Hadfield, M., Tobe, S. and Wang, Y., 2005. Ceramic rolling elements with ring crack defects-a residual stress approach. *Materials Science and Engineering A*, 404, 221-226.
- Khan A. Z., 2006. *Rolling Contact Wear of Hybrid Ceramic Bearings with Refrigerant Lubrication*. PhD Thesis, Bournemouth University, UK.
- Khan, Z. A., Hadfield, M., Tobe, S. and Wang, Y., 2006. Residual stress variations during rolling contact fatigue of refrigerant lubricated silicon nitride bearing elements. *Ceramics International*, 32, 751-754.
- Khan, Z. A. and Hadfield, M., 2007. Manufacturing induced residual stress influence on the rolling contact fatigue life performance of lubricated silicon nitride bearing materials. *Materials and Design*, 28, 2688-2693.

- Kida, K., Urakami, T., Yamazaki, T. and Kitamura, K., 2004. Surface crack growth of silicon nitride bearings under rolling contact fatigue. *Fatigue and Fracture of Engineering Materials and Structures*, 27, 657-668.
- Kida, K., Yoshidome, K., Yamakawa, K., Harada, H. and Oguma, N., 2006. Flaking failures originating from microholes of bearings under rolling contact fatigue. *Fatigue and Fracture of Engineering Materials and Structures*, 29, 1021-1030.
- Kida, K., Honda, T. and Santos, E. C., 2012. Mode II surface crack growth under rolling contact fatigue and cyclic shear stress in Si₃N₄. *WIT Transactions on Engineering Sciences*, 76, 175-187.
- Kim, T. W., 2003. The fatigue crack initiation life prediction based on several high-cycle fatigue criteria under spherical rolling contact. *Tribology Transactions*, 46:1, 76-82.
- Kimura, Y., Sekizawa, M., and Nitnai, A., 2002. Wear and fatigue in rolling contact. *Wear*, 253, 9-16.
- Kotzalas, M. N. and Harris, T. A., 2000. Fatigue failure and ball bearing friction. *Tribology Transactions*, 43:1, 137-143.
- Kudish, I. I., 2002. Lubricant-crack interaction, origin of pitting, and fatigue of drivers and followers. *Tribology Transactions*, 45:4, 583-594.
- Kudish, I. I., and Burris, K. W., 2004. Modeling of surface and subsurface crack behaviour under contact load in the presence of lubricant. *International Journal of Fracture*, 125, 125-147.
- Lai, J., Wang, J. and Ioannides, E., 2008. Fluid-crack interaction in lubricated rolling-sliding contact. *Proceedings of STLE/ASME Conference*, Oct 20-22, Miami, USA.
- Lawrence, C. W., Scruby, C. B., Briggs, D. A. D. and Dunhill, A., 1990. Crack detection in silicon nitride by acoustic microscopy. *NDT International*, 23(1), 1-10.
- Levesque, A. G. and Arakere, N., 2008. An investigation of partial cone cracks in silicon nitride balls. *Int. J. Solids and Structures*, 45, 6301-6315.
- Levesque, A. G., 2009. *Critical Flaw Size in Silicon Nitride Ball Bearings*, PhD Thesis, University of Florida, USA.
- Levesque, A. G. and Arakere, N., 2010a. Critical Flaw Size in Silicon Nitride Ball Bearings. *Tribology Transactions*, 53:4, 511-519.

- Levesque, A. G. and Arakere, N., 2010b. Empirical Stress Intensity Factors for Surface Cracks under Rolling Contact Fatigue. *Tribology Transactions*, 53:4, 621-629.
- Liu, Z., Sun, J. and Pei, Z., 2011. Cross-Polarization Confocal Imaging of Subsurface Flaws in Silicon Nitride. *Int. Journal of Applied Ceramic Technology*, 8:2, 411-422.
- Lube, T., 2001. Indentation crack profiles in silicon nitride. *Journal of the European Ceramic Society*, 21, 211-218.
- Lundberg, G. and Palmgren, A., 1949. Dynamic capacity of rolling bearings”, *Journal of Applied Mechanics*, 165-172.
- Mazzu, A., 2013. A numerical approach to subsurface crack propagation assessment in rolling contact. *Fat. & Fract. of Engineering Materials & Structures*, 36, 548-564.
- Mechefske, C. K. and Mathew, J., 1992. Fault detection and diagnosis in low speed rolling element bearings. *Mechanical Systems and Signal Processing*, 6:4, 309-316.
- Meijer, J., 2004. Laser beam machining (LBM), state of the art and new opportunities. *Journal of Processing Technology*, 149, 2-17.
- Melander, A., 1997. A finite element study of short cracks with different inclusion types under rolling contact fatigue load. *International Journal of Fatigue*, 19:1, 13-24.
- Miner, J. R., Dell, J., Galbato, A. T. and Ragen, M. A., 1996. F117-PW-100 Hybrid Ball Bearing Ceramic Technology Insertion. *Journal of Engineering for Gas Turbines and Power*, 118, 434-442.
- Miyazaki, H., Hyuga, H., Yoshizawa, Y., Hirao, K. and Ohji, T., 2010. Crack profiles under a vickers indent in silicon nitride ceramics with various microstructures. *Ceramics International*, 36, 173-179.
- Morals-Espejel, G. E. and Gabelli, A., 2011. The behaviour of indentation marks in rolling-sliding elastohydrodynamically lubricated contacts. *Tribology Transactions*, 54:4, 589-606.
- Morton, H.T., 1965. *Anti-friction bearings*, Ann Arbor, MI, USA.
- Mosleh, M., Bradshaw, K., Belk, J. H. and Waldrop, J.C., 2011. Fatigue failure of all-steel and steel-silicon nitride combinations. *Wear*, 271, 2471-2476.

- Mosleh, M. and Bradshaw, K., 2011. Role of component configuration in evaluation of accelerated rolling contact fatigue of ball bearings. *Wear*, 271, 2681-2686.
- Murakami, Y., Kaneta, M. and Yatsuzuka, H., 1985. Analysis of surface crack propagation in lubricated rolling contact. *ASLE Transactions*, 28:1, 60-68.
- Nakajima, A. and Mawatari, T., 2005. Rolling contact fatigue life of bearing steel rollers lubricated with low viscosity traction oil. *Life Cycle Tribology* (Paper presented at 31st Leeds Lyon Symposium, Leeds, September 7-10, 2004)
- O'Brien, M. J., de la Cruz, A. R., and Nguyen, E. A., 2011. A novel proof test for silicon nitride balls. *Journal of American Ceramic Society*, 94:2, 597-604.
- Parker, R. J. and Zaretsky, E. V., 1975. Fatigue life of high speed bearing with SiN balls. *J.Lub. Technology, Trans. ASME*, 350-357.
- Petit, S., Duquennoy, M., Ouafouh, Denuville, F., Ourak, M. and Desvaux, S., 2005. NDT of ceramic balls using high frequency ultrasonic resonance spectroscopy. *Ultrasonics*, 43, 802-810.
- Piotrowske, A. E., and O'Brien, M. J., 2006. A Novel Experiment Method to Measure the Fracture Toughness of Ceramic Balls used in Bearings. *Fatigue and Fracture of Engineering Materials and Structures*, 29, 558-572.
- Prodanov, N., Gachot, C., Rosenkranz, A., Mucklich, F. and Muser, M. H., 2013. Contact mechanics of laser-textured surfaces. *Tribology Letters*, 50, 41-48.
- Rahaman, M. N., Yao, A., Bal, B. S., Garino, J. P. and Ries, M. D., 2007. Ceramics for prosthetic hip and knee joint replacement. *J. of Americal Ceramics Soc*, 90 (3), 1965-1988.
- Raje, N. N. and Sadeghi, F., 2008. Statistical numerical modeling of sub-surface initiated spalling in bearing contacts. *IMEchE, J. Engineering Tribology, Part J*. 849-858.
- Reddy, J. N., 2004. *Mechanics of laminated plates and shells*, CRC Publishers, New York.
- Rico, J. E. F., Battez, A. H. and Cuervo, D. G., 2003. Rolling contact fatigue in lubricated contacts", *Tribology International*, 36, 35-40.
- Ringsberg, J. W. and Bergkvist, A., 2003. On propagation of short rolling contact fatigue cracks. *Fatigue and Fracture of Engineering Materials and Structures*, 26, 969-983.

- Rizvi, Nadeem and Apte, P., 2002. Developments in laser micro machining techniques. *Journal of materials processing technology*, 127:2, 206-210.
- Sadeghi, F., Jalalahmadi, B., Slack, T. S., Raje, N. and Arakere, N. K., 2009. A review of rolling contact fatigue. *Journal of Tribology*, 131/041403, 1-15.
- Slack, T. and Sadeghi, F., 2010. "Explicit finite element modeling of subsurface initiated spalling in rolling contacts", *Tribology International*, 43, 1693-1702.
- Scott, D. and Blackwell, J., 1978. The Assessment of Ball Bearing Steels of Modified Chemical Composition. *Wear*, 46, 660-663.
- Shimizu, S., 2012. A new life theory for rolling bearings-By linkage between rolling contact fatigue and structural fatigue. *Tribology Transactions*, 55:5, 558-570.
- Stolarski, T.A. and Tobe, S., 1997. Rolling Contact Induced Failures of Silicon Nitride. *Tribology Letters*, 3, 349-357.
- Suh, N. P., 1977. An overview of the delamination theory of wear. *Wear*, 44, 1-16.
- Takibayashi, H., 2001. Bearing for extreme special environments-Part 3 - Basic performance of ceramic (silicon nitride) bearings", *KOYO Engineering Journal English Edition*, 158E, 53-60.
- Tallian, T. E., 1967. On competing failure modes in rolling contact. *ASLE Transactions*, 10, 418-439.
- Tallian, T., 1969. Progress in Rolling Contact Technology. SKF Ind., Report AL690007.
- Tandon, N. and Choudhury , A., 1999. A review of vibration and accoustic measurement methods for the detection of defects in rolling element bearings. *Tribology International*, 32, 469-480.
- Tanimoto, K., Kajihara, K., and Yanai, K., 2000. Hybrid Ceramic Ball Bearings for Turbochargers. *SAE Transactions*, 109:5, 763-775.
- Taylor, D., 2007. The theory of critical distances: A new perspective in fracture mechanics", Elsevier, Oxford, UK.
- Thoma, K., Rohr, L., Rehmann, H., Roos, S. and Michler, J., 2004. Materials Failure Mechanisms of Hybrid Ball Bearings with Silicon Nitride Balls. *Tribology International*, 37, 463-471.

- Touret, R. and Wright, E. P., 1977. Rolling Contact Fatigue: Performance Experimenting of Lubricants. Papers presented at the International Symposium by Institute of Petroleum, London, October 1976, Heyden & Sons Ltd, 1977.
- Ueda, K., 1989. Contact-Stress Deformation and Fracture in Ceramics. *Jap. J. of Tribology*, 34:2, 123-131.
- Vilhena, L.M., Sedlacek, M., Podgornik, B., Vizintin, J., Babnik, A and Mozina, J., 2009. Surface texturing by pulsed Nd: YAG laser. *Tribology International*, 42, 496-1504.
- Ville, F. and Nelias, D., 1999. Early fatigue failure due to dents in EHL contacts. *Tribology Transactions*, 42:4, 795-800.
- Wang, L., Snidle, R. W. and Gu, L., 2000. Rolling contact silicon nitride bearing technology: a review of recent research. *Wear*, 246, 159-173.
- Wang, W., Hadfield, M. and Wereszczak, A. A., 2009. Surface strength of silicon nitride in relation to rolling contact performance. *Ceramic International*, 35, 3339-3345.
- Wang, W., 2010. Rolling Contact Fatigue of Silicon Nitride. PhD Thesis, Bournemouth University, UK.
- Wang, W., Hadfield, M. and Wereszczak, A. A., 2010. Surface strength of silicon nitride in relation to rolling contact performance measured on ball-on-rod and four ball testers. *Tribology International*, 43, 423-432.
- Wang Y. and Hadfield, M., 1999. Rolling contact fatigue failure modes of lubricated silicon nitride in relation to ring crack defects. *Wear*, 225-229, 1284-1292.
- Wang Y. and Hadfield, M., 2000a. The influence of ring crack location on the rolling contact fatigue failure of lubricated silicon nitride: experimental studies. *Wear*, 243, 167-174.
- Wang, Y. and Hadfield, M., 2000b. The influence of ring crack location on the rolling contact fatigue failure of lubricated silicon nitride: fracture mechanics analysis. *Wear*, 243, 157-166.
- Wang, Y., 2001. Failure Modes of Silicon Nitride Rolling Elements with Ring Crack Defects. PhD Thesis, Bournemouth University, UK.
- Wang, Y. and Hadfield, M., 2001. Ring crack propagation in silicon nitride under rolling contact. *Wear*, 250, 282-292.

- Wang, Y. and Hadfield, M., 2002. A study of line defect fatigue failure of ceramic rolling elements in rolling contacts. *Wear*, 253, 975-985.
- Wang, Y. and Hadfield, M., 2003. A mechanism for nucleating secondary fractures near a pre-existing flaw subjected to contact loading. *Wear*, 254, 597-605.
- Wang, Y. and Hadfield, M., 2003. Rolling contact fatigue of ceramics. *ASM Handbook*.
- Wang, Y. and Hadfield, M., 2004. Failure modes of ceramic rolling elements with surface crack defects. *Wear*, 256, 208-219.
- Way, S., 1935. Pitting due to rolling contact. *Journal of Applied Mechanics, Transactions of ASME*, 2, A49-A58.
- Yamamoto, T., 1980. Crack growth in lubricated rollers, in solid contact and lubrication. *ASME AMD*, 39, 223-236.
- Yu, W. K. and Harris, T. A., 2001. A new stress-based fatigue life model for ball bearings. *Tribology Transactions*, 44, 11-18.
- Zhao, P., Hadfield, M. Wang, Y. and Vieillard, C., 2004. The Influence of experiment lubricants on the rolling contact fatigue failure mechanism of silicon nitride ceramic. *Wear*, 257, 1047-1057.
- Zhao, P., 2006. Three-Dimensional Boundary Element and Experimental Analysis of Lubricated Ceramic Surface Ring Cracks in Rolling Contact. PhD Thesis, Bournemouth University, UK.
- Zhao, P., Hadfield, M. Wang, Y. and Vieillard, C., 2006a. Subsurface propagation of partial ring cracks in rolling contact: Part I. exp. studies. *Wear*, 261, 382-389.
- Zhao, P., Hadfield, M, Wang, Y and Vieillard, C., 2006b. Subsurface propagation of partial ring cracks in rolling contact: Part II. Fracture mechanics analysis. *Wear*, 261, 390-397.
- Zhou, J, Wu, G, Chen, X and Zhang, P., 2008. Rolling contact fatigue of silicon nitride bearing balls under pure rolling condition. *Journal of Shanghai University*, 12:4, 358-362.
- Zhu, D., Nanbu, T., Ren, N, Yasuda, Y. and Wang, Q. J., 2010. Model-based virtual surface texturing for concentrated conformal-contact lubrication. *Proc. IMechE Vol. 224, Part J: Journal of Engineering Tribology*, 685-696.

Bibliography

- Bogdanski, S., Olzak, M. and Stupnicki, J., 1996. Numerical stress analysis of rail rolling contact fatigue cracks. *Wear*, 191, 14-24.
- Dubey, A. K. and Yadava, V., 2008. Laser beam machining - a review. *Machine tools and manufacture*, 48, 609-628.
- Glaeser, W. A. and Shaffer, S. J., 1996. Contact fatigue. *ASME Handbook*, 19: Fatigue and Fracture, 331-336.
- Glovnea, R. P., Olver, A. V. and Spikes, H. A., 2005. Experimental investigation of the effect of speed and load on film thickness in elastohydrodynamic contact. *Tribology Transactions*, 48:3, 328-335.
- Hannes, D. and Alfredsson, B., 2011. Rolling contact fatigue crack path prediction by the asperity point load mechanism. *Engineering Fracture Mechanism*, 78, 2848-2869.
- Hartelt, M., Riesch-Oppermann, H., Schwind, T., and Kraft, O., 2011. Statistical evaluation of fatigue crack propagation from natural flaws in silicon nitride. *Journal of American Ceramic Society*, 94:10, 3480-3487.
- Jackson, A., 1981. A simple EHL film thickness equation for rolling element bearings. *ASLE Transactions*, 24:2, 147-158.
- Kang, J. and Hadfield, M., 2005. The Effect of Lapping Load in Finishing Advanced Ceramic Balls on a Novel Eccentric Lapping Machine. *IMEchE Journal of Engineering Manufacture*, 219:B, 505-513.
- Kang, J. and Hadfield, M., 2005. The Polishing Process of Advanced Ceramic Balls using a Novel Eccentric Lapping Machine. *IMEchE Journal of Engineering Manufacture*, 219:B, 493-504.
- Klaus, E. E. and Duda, J.L., 1990. Lubricated wear of silicon nitride. *Lubrication Engineering*, 47, 679-684.
- Kotzalas, M. N., 2001. A theoretical study of residual stress effects on fatigue life prediction. *Tribology Transactions*, 44:4, 609-614.
- Liu, C. R. and Choi, Y., 2008. A new methodology for predicting crack initiation life for rolling contact fatigue based on dislocation and crack propagation. *International Journal of Mechanical Sciences*, 50, 117-123.

- Lugt, P. M. and Morales-Espejel G. E., 2011. A review of elasto-hydrodynamic lubrication theory. *Tribology Transactions*, 54:3, 470-496.
- Mano, H., Yoshioka, T., Korenaga, A. and Yamamoto, T., 2000. Relationship between growth of rolling contact fatigue cracks and load distribution. *Tribology Transactions*, 43, 367-376.
- Merieux, J-S, Hurley, S., Lubrecht, A.A., and Cann, P.M., 2000. Shear-degradation of grease and base oil availability in starved EHL lubrication. *Thinning Films and Tribological Interfaces* (Elsevier), 581-587.
- Morals-Espejel, G. E. and Brizmer, V., 2011. Micropitting modelling in rolling-sliding contacts: Application to Rolling Bearings. *Tribology Transactions*, 54:4, 625-643.
- Pattabhiraman, S., Levesque, A. G., Kim, N. H., and Arakere, N. K., 2010. Uncertainty analysis for Rolling Contact Fatigue Failure Probability of Silicon Nitride Ball Bearings. *International Journal of Solids and Structures*, 45, 2543-2553.
- Querlioz, E., Ville, F., Lenon, H. and Lubrecht, T., 2007. Experimental investigations on the contact fatigue life under starved conditions. *Tribology International*, 40, 1619-1626.
- Reichenbach, G. S. and Sybiuta, W. D., 1965. An electron microscope study of rolling contact fatigue. *ASLE Transactions*, 8, 217-223.
- Ritchie, R. O., 1999. Mechanisms of fatigue crack propagation in ductile and brittle solids. *International Journal of Fracture*, 100, 55-83.
- Rosado, L., Forster, N. H., Thompson, K. L. and Cooke, J. W., 2010. Rolling contact fatigue life and spall propagation of AISI M50, M50NiL, and AISI 52100, Part I: Experimental Results. *Tribology Transactions*, 53:1, 29-41.
- Seeton, C. J., 2006. Viscosity-temperature correlation for liquids", *Tribology Letters*, 22:1, 67-78.
- Stachowiak, G. W. and Batchelor, A. W., 2014. *Engineering Tribology*. 4th Edition, Elsevier. DOI:10.1016/B978-0-12-397047-3.00019-9.
- Tuszynski, W., 2006. An effect of lubricating additives on tribochemical phenomena in a rolling steel four ball contact. *Tribology Letters*, 24:3, 207-215.

Appendices

Appendix A: *Stress Factor and Load Calculations*

Appendix A1: Stress Factor

Stress factor which is used to calculate stress cycles (for upper ball) in modified four ball machine is calculated using following equation (A.1).

$$L = Z[R_u + 2R_l] / [2(R_u + R_l)] \dots\dots\dots (A.1)$$

Where R_u = Upper ball radius = 6.35mm

R_l = Lower ball radius = 6.35mm

Z = No. of lower balls = 3

Stress Factor = L = 2.25

Appendix A2: Load calculations in Modified Four Ball Machine

Hertz contact theory [Johnson 1985] is used to calculate the contact pressure and contact radius. In the 4-ball machine, a machine spindle load (L) is applied to the top ball and from this load, contact load is calculated and then contact pressure and contact radius for the contacts with the support balls. Full contact loads calculations are given in Appendix A2 (next page).

$$\text{Contact load} = P = L/3 * \text{Cos}\phi \dots\dots\dots (A.2)$$

Where L = Machine spindle load

And ϕ = Angle in modified 4-ball machine

and contact pressure (P_0) and contact radius (a) are given by;

$$P_0 = [6PE^*]^2]^{1/3} / [\pi^3 R^*]^2]^{1/3} \dots\dots\dots (A.3)$$

$$a = [3PR^*/4E^*]^{1/3} \dots\dots\dots (A.4)$$

Load Calculations

		L = Spindle Load		P = Contact Load = (L/3*Cos(φ))		τ_{max} = Max. Shear Stress = 1/3(P)		1/3(P_o) at depth of 0.638a		
		φ = Angle = 35.3° in Modified Four Machine				max σ_t = Max. Tensile Stress = ((1-2*ν)*P_o)/3 (at rad "a")				
		P_o = Max Compressive Stre				$1/\pi[\{(6*P*E'^2)^{1/3}/R'^2/3]$				
		E' = Effective Elastic Constant = [{{1-(ν1)²}/E1} + {{1-(ν2)²}/E2}]⁻¹								
		E' = 136.869E09 For Ceramic Steel Combination								
		R' = Relative Radius = [{{1/(R1)}+{{1/(R2)}}]⁻¹				a = Contact Rad = Contact Diminsion = ((3*P*R')/4*E')^{1/3}				
		R' = 3.175mm by taking R1 = R2 = 6.35mm								
S.No	φ	Cos(φ)	L (N)	P (N)	P _o in Pa	P _o in GPa	a (μm)	Max τ (MPa)	Max σ _t (MPa)	Max τ Depth(μm)
1	35.3deg	0.816	184	75.15	3000906973	3.001	109.34	1000.30	440.13	69.76
2	35.3deg	0.816	224	91.49	3204271186	3.204	116.75	1068.09	469.96	74.49
3	35.3deg	0.816	245	100.06	3301428934	3.301	120.29	1100.48	484.21	76.74
4	35.3deg	0.816	268	109.46	3401664855	3.402	123.94	1133.89	498.91	79.07
5	35.3deg	0.816	292	119.26	3500318329	3.500	127.54	1166.77	513.38	81.37
6	35.3deg	0.816	318	129.88	3601269573	3.601	131.21	1200.42	528.19	83.71
7	35.3deg	0.816	374	152.75	3801343590	3.801	138.50	1267.11	557.53	88.37
8	35.3deg	0.816	436	178.07	4000756210	4.001	145.77	1333.59	586.78	93.00
9	35.3deg	0.816	505	206.26	4201558206	4.202	153.09	1400.52	616.23	97.67
10	35.3deg	0.816	542	221.37	4301761752	4.302	156.74	1433.92	630.93	100.00
11	35.3deg	0.816	580	236.89	4400032890	4.400	160.32	1466.68	645.34	102.28
12	35.3deg	0.816	621	253.63	4501360459	4.501	164.01	1500.45	660.20	104.64
13	35.3deg	0.816	663	270.79	4600634881	4.601	167.63	1533.54	674.76	106.95
14	35.3deg	0.816	707	288.76	4700236704	4.700	171.26	1566.75	689.37	109.26
15	35.3deg	0.816	753	307.55	4800040669	4.800	174.89	1600.01	704.01	111.58
16	35.3deg	0.816	802	327.56	4901978263	4.902	178.61	1633.99	718.96	113.95
17	35.3deg	0.816	852	347.98	5001801547	5.002	182.24	1667.27	733.60	116.27
18	35.3deg	0.816	958	391.27	5201178532	5.201	189.51	1733.73	762.84	120.91
19	35.3deg	0.816	1133	462.75	5500344546	5.500	200.41	1833.45	806.72	127.86
20	35.3deg	0.816	1472	601.21	6001813946	6.002	218.68	2000.60	880.27	139.52
21	35.3deg	0.816	1870	763.76	6500206104	6.500	236.84	2166.74	953.36	151.10
22	35.3deg	0.816	2340	955.72	7004630177	7.005	255.22	2334.88	1027.35	162.83
23	35.3deg	0.816	2873	1173.41	7500527374	7.501	273.28	2500.18	1100.08	174.36

Appendix B: Calibration for TE92HS

TE92CAL/COMPEND2000

Calibration

Certificate

TE92 Microprocessor Controlled Rotary Tribometer

Serial No. TE92/8699

Phoenix Tribology Ltd

Woodham House

Whitway

Newbury

RG20 9LF

England

Phone: 44 (0) 1635 276064

Fax: 44 (0) 8707 877017

E-mail: info@phoenix-tribology.com

Web Site: www.phoenix-tribology.com

This is to certify that the above unit has been Calibrated in accordance with our standard procedures and conforms to the specification. Calibration covers:

Thermocouple inputs, linearity and scale.
West controller input, linearity and scale.
Speed, actual value and display, linearity and scale.
Friction transducers & amplifier, linearity and scale.
Load-cell transducer & amplifier, linearity and scale.
HS SLIM & associated amplifiers, linearity and scale.

CALIBRATION EQUIPEMNT

Multimeter, test leads & Probes
Thermocouple simulator
Optical tachometer and reflective tape
Loadcell

Serial Number
14400367
3075
2015652
078687

Signed 
David Willmont
For and on behalf of

Date 3rd February 2011

Appendix C : Replica Technical Data, Selection and Specifications

TECHNICAL DATA	RepliSet	RepliFix
Viscosity of uncured compound	Very low (F-types) Low (T-types)	High
Detail reproduction	Down to 0.1 µm	Down to 5 µm
Shrinkage	Negligible	Negligible
Tear strength	15-20 kN/m ²	Low
Hardness	30 Shore A	76 Shore A
Temperature range for the surface to be examined	-10°C to + 180°C (14°F to + 356°F)	0°C to + 150°C (32°F to + 302°F)
Life span of the finished replica	Practically indefinite	Practically indefinite

Selection of Compound

Surface facing	Temperature of surface	Working life	Recommended compound
Horizontal, sloping	> 20°C	Normal	RepliSet-F5
		Short	RepliSet-F1/GF1
	< 20°C	Normal	
Vertical, overhead	> 20°C	Normal	RepliSet-T3
		Short	RepliSet-T1/GT1
	< 20°C	Normal	

SPECIFICATIONS	Cat.No.	Cat.No.
<p>RepliSet Replication system for non-destructive testing of a microstructure or a 3D structure. Fast curing two-part silicon rubber compound for flexible high-resolution 3D replicas. For the 50 ml system, the hand-operated dispensing gun (40900066) and the static mixing nozzles (40900088) are used in combination with the 50 ml cartridges. For the 265 ml system, the hand-operated dispensing gun (40900065) and the static-mixing nozzles (40900056) are used in combination with the 265 ml cartridges.</p>		
<p>RepliSet-F1 Particularly useful for replicating horizontal or sloping surfaces in low temperature conditions or where rapid results are required. Fluid rapid curing compound with working life of 0.5-1 min. and curing time of 4 min. at 25°C (77°F).</p>		
1 cartridge of 50 ml	40900069	
5 cartridges of 50 ml	40900047	
2 cartridges of 265 ml	40900051	
<p>RepliSet-F5 General-purpose material. Particularly useful for replicating horizontal or sloping surfaces in normal or high temperature conditions. Fluid fast curing compound with working life of 5 min. and curing time of 18 min. at 25°C (77°F).</p>		
1 cartridge of 50 ml	40900068	
5 cartridges of 50 ml	40900046	
2 cartridges of 265 ml	40900050	
<p>RepliSet-T1 Particularly useful for replicating vertical or overhead surfaces in low temperature conditions or where rapid results are required. Thixotropic rapid curing compound with working life of 0.5 - 1 min. and curing time of 4 min. at 25°C (77°F).</p>		
1 cartridge of 50 ml	40900071	
5 cartridges of 50 ml	40900049	
2 cartridges of 265 ml	40900053	
<p>RepliSet-T3 General-purpose material. Particularly useful for replicating vertical or overhead surfaces in normal or high temperature conditions. Thixotropic fast curing compound with working life of 3 min. and curing time of 10 min. at 25°C (77°F).</p>		
1 cartridge of 50 ml	40900070	
5 cartridges of 50 ml	40900048	
2 cartridges of 265 ml	40900052	
<p>RepliSet-GF1 Replication system especially for comparator macroscopy and metrology. Particularly useful for replicating horizontal or sloping surfaces and filling holes. Fluid rapid curing compound with working life of 0.5-1 min. and curing time of 4 min. at 25°C (77°F).</p>		
1 cartridge of 50 ml	40900078	
5 cartridges of 50 ml	40900076	
<p>RepliSet-GT1 Replication system especially for comparator macroscopy and metrology. Particularly useful for replicating vertical or overhead surfaces. Thixotropic rapid curing compound with working life of 0.5-1 min. and curing time of 4 min. at 25°C (77°F)</p>		
1 cartridge of 50 ml	40900079	
5 cartridges of 50 ml	40900077	
<p>RepliFix Specially formulated hand mixed fast curing two-part silicone rubber. Bonds to RepliSet. Particularly useful in combination with RepliSet for producing a rigid backing. It can be used directly for moulding of surface shape for profile measurement.</p>		
<p>RepliFix-2 For low temperature conditions or where rapid results are required. Working life of 2-3 min. and curing time of 10 min. at 25°C (77°F). 500 g</p>		40900084
<p>RepliFix-20 For high temperature conditions or for taking replicas of complicated geometry or large areas. Working life of 20 min. and curing time of 60 min. at 25°C (77°F). 500 g</p>		40900086
ACCESSORIES		
Dispensing Gun		
Hand-operated dispensing gun.		
For 50 ml cartridges		40900066
For 265 ml cartridges		40900065
Static-mixing Nozzles		
For RepliSet replication compound in		
50 ml cartridges, 35 pcs.		40900088
265 ml cartridges, 10 pcs.		40900056
Nozzle Tips		
For replicating flat surfaces. Fishtail spreaders, 10 mm width. To be mounted on 50 ml static-mixing nozzle (40900088). 30 pcs.		40900089
For replicating small holes. Luer needle, 1 mm dia., 30 mm long. To be mounted on 50 ml static-mixing nozzle (40900088). 10 pcs.		40900060
For replicating larger holes. Flexible hose, 6 mm dia., 100 mm long. To be mounted on 50 ml static-mixing nozzle (40900088) 10 pcs.		40900061
Backing Slides		
A flexible plastic slide, which bonds to the replica and ensures a flat back to the replica. For levelling of replicas to assist microscopic examination, as dimensional support for metrology and for well-ordered labelling, transport and storage of RepliSet replicas. 26 x 76 x 1 mm. 50 pcs.		40900087
Backing Paper		
Bonds to the replica and facilitates labelling, handling and the levelling of replicas to assist microscopic examination. 60 x 70 mm. 100 pcs.		40900062
A4 (210 x 297 mm). 10 pcs.		40900063
Case for RepliSet 50 ml System		
Aluminium carrying case with room for all necessities for field applications. The content is ordered separately. L x d x h = 445 x 155 x 330 mm		40900067

Appendix D: *Conductive Silver Paint – Technical Details*



Conductive Silver Paint

AGG3790

Description:

The air-dry silvers are used to make non-conductive surfaces electrically and thermally conductive. They can be used in circuit repair or as RF shielding materials. Most can be brushed, sprayed or dipped. These materials will cure at room temperature in 16-20 hours or in 30 minutes at 120-200°C. A heat gun will cure the material in seconds. The conductivity of the film can be increased by repeated application of layers.

Key Benefits:

- *Electrically and thermally conductive*
- *Curable at room temperature*
- *Brush applicator cap*
- *High adhesion to most materials*
- *Solvent resistant*

Processing Notes:

- *Surfaces do not have to be prepared prior to application.*
- *Materials will adhere to polymer (phenolic) boards, ceramic, glass, metal, plastic and fiberglass.*

Curing Conditions: *Colloidal Silver will cure at room temperature in 16-20 hours or in 30 minutes at 120-200°C. A heat gun will cure the material in seconds.*

% Solids: *60% ± 1% Ag*

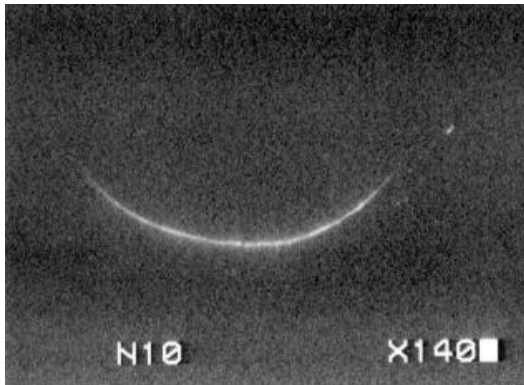
Sheet Resistance: *0.02 - 0.05 ohms/sq/mil (25µm)*

Thinner: *G3791 - Diluent for G3790 silver paint*

Shelf Life: *6 months; material should be jar rolled at 1-6 rev/hr. Avoid exposure to extreme temperatures.*

Storage: *Store in a dry location at 5-30°C. Allow paint to come to room temperature prior to opening. Mix thoroughly before using*

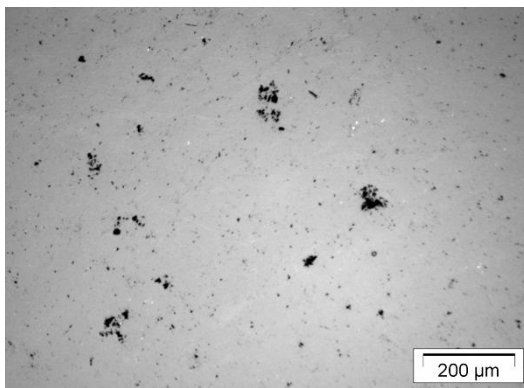
Appendix E: *Typical Surface Defects in Silicon Nitride*



C-crack



Surface star feature

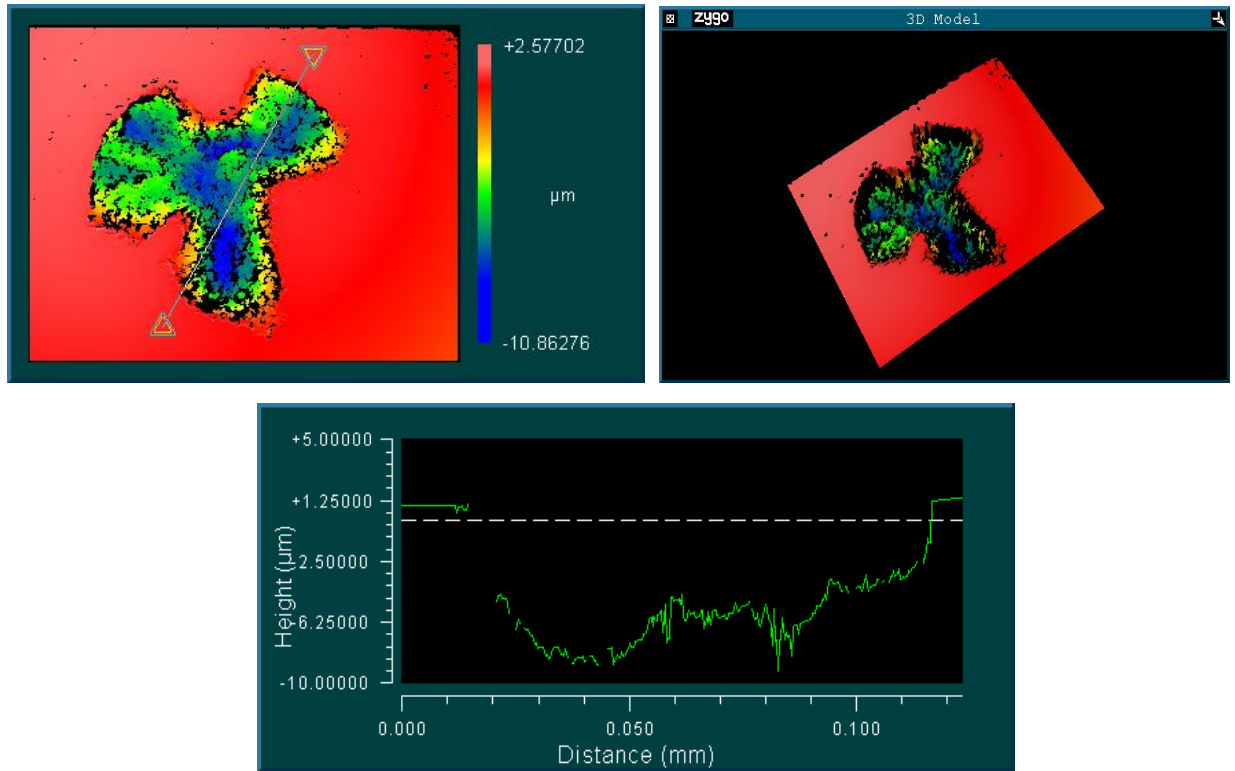


Missing material

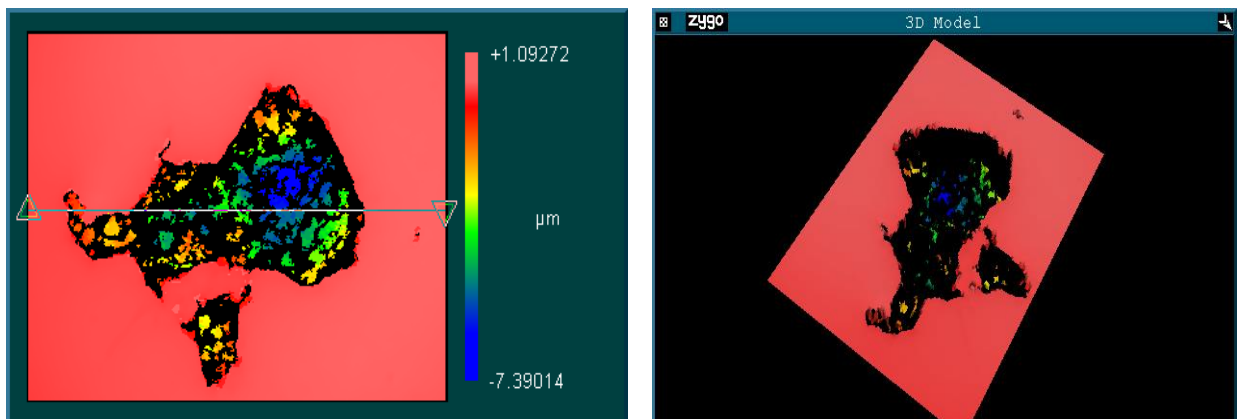


Contact Mark

Appendix F: Missing material (natural) shapes and depth



Natural Star with major missing material with depth up to $9\mu\text{m}$ (Cat. 5)



Natural Star with major missing material with depth up to $7\mu\text{m}$ (Cat. 5)

Appendix G: *Minimum Film Thickness*

Minimum film thickness is estimated by famous Hamrock and Dowson equation (G.1) as below [Hadfield 1993, Wang 2001];

$$H_{\min} = 3.63 U^{0.68} G^{0.49} W^{-0.073} (1 - e^{-0.68k}) \dots\dots\dots(G.1)$$

Where U, G, W and k are dimensionless parameters for speed, materials, load and ellipticity respectively. i.e.,

$$G = \xi E^* , \quad k = \left[\frac{R_y}{R_x} \right] , \quad U = \left[\frac{\eta_0 u}{E^* R_x} \right] , \quad W = \left[\frac{P}{E^* R_x^2} \right]$$

Where

ξ = Pressure viscosity (N-sec/m²)

E^* = Effective modulus of elasticity (N/m²)

R_x = Effective radius in x (motion) direction (m)

R_y = Effective radius in y (motion) direction (m)

P = Total load (N)

Appendix H: Calculations for Diamond Tip Removal in Vickers Indentation

Vickers indentation was used to create indentation and hence star like feature in silicon nitride material

In order to create star like indent on silicon nitride surfaces, following steps were taken to create indentation

1. Specimen was placed in the chuck and required load was applied (pressed)
2. Time duration was 15sec (normally 10-20sec)
3. A circle was drawn of 1-2mm around the indent using permanent marker with the help of microscope eyepiece
4. Indent depth was measured using optical microscopy and interferometry. Theoretical calculations were done to confirm the indent depth.

Following cross corner distances found using 1kg_f, 5kg_f and 10kg_f.

1kg_f = 30μm, 5kg_f = 74μm and 10kg_f = 140μm

In order to get reasonable star like indent feature, it was decided that to remove the tip off of indenter and to have flat face rather than sharp tip, following calculations were made;

Cross corner distance = 74μm, to have cross crack distance = 140 μm

As Vickers has Opposite faces angle = 136°

Using Sin Law for half triangle (Right Angle Triangle)

$$\frac{H}{\sin 22^\circ} = \frac{37}{\sin 68^\circ} \text{ where } H = \text{Distance from tip to remove}$$

Where 37μm is half cross corner distance and 68° is half opposite faces angle to have half triangle.

H = 14.94 ≈ 15 μm (maximum depth)

But practically Vickers indent is calculated using formula

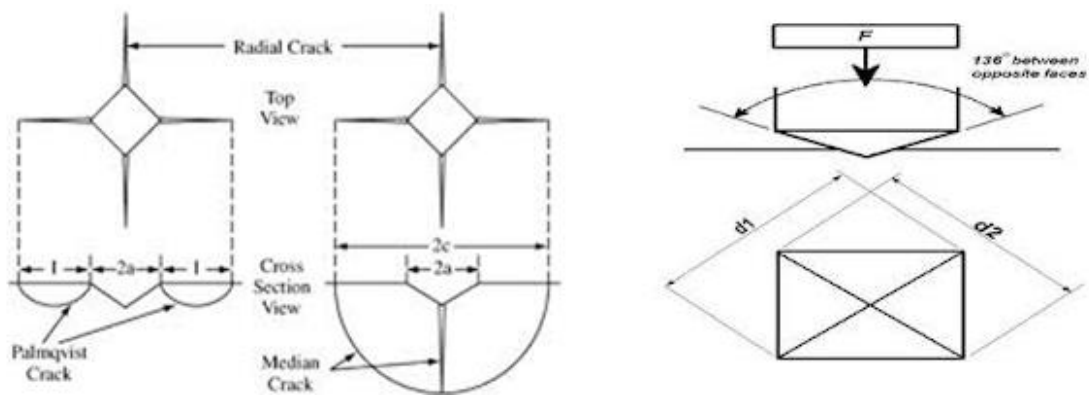
$$h = b/7.006$$

Where b = cross corner distance = 0.074mm (74μm)

h = 0.01056mm = 10.56μm (which was almost upper limit of nature star features)

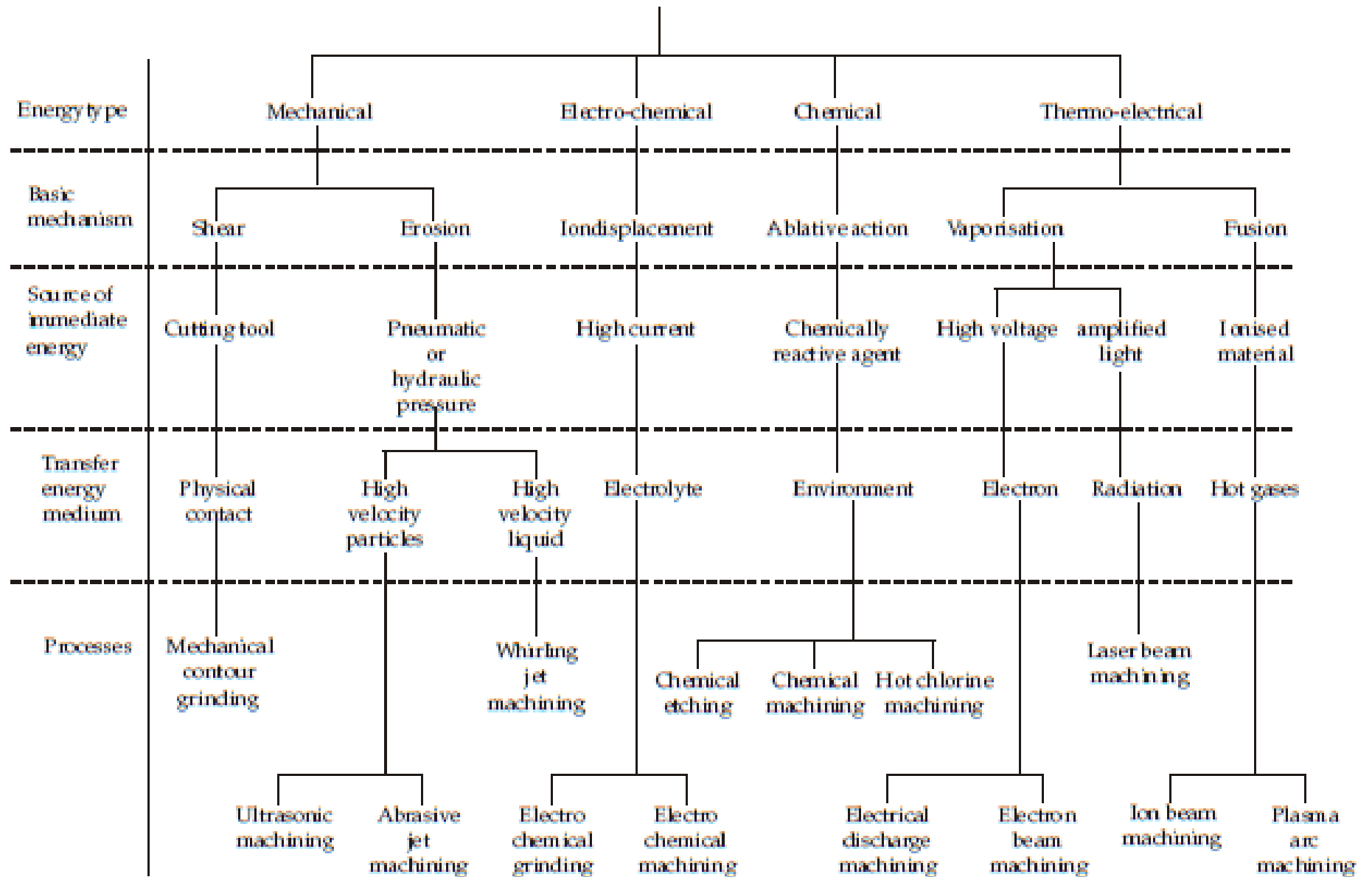


Vickers indenter used to create indent in the silicon nitride surface



Indent/crack generation using Vickers indentation

Appendix I: *Non-Conventional Machining Classifications*



Appendix J: Laser micromachining in Silicon Nitride

Appendix J1: Details of holes machined into Material A test balls

S.No	Ball ID	Shape	Diam (μm)	Depth (μm)	S.No	Ball ID	Shape	Diam (μm)	Depth (μm)
1	01	I	100	50	36	46	I	100	20
2	02	I	75	30	37	47	I	100	20
3	03	I	50	10	38	48	I	100	20
4	04	II	50	5	39	49	I	100	20
5	05	II	100	50	40	50	I	100	20
6	06	II	75	30	41	51	I	100	30
7	07	II	50	10	42	52	I	100	30
8	08	III	100	50	43	53	I	100	30
9	09	III	75	30	44	54	I	100	30
10	10	III	50	10	45	55	I	100	30
11	11	I	100	10	46	56	I	75	10
12	12	I	75	10	47	57	I	75	10
13	13	I	100	20	48	58	I	75	10
14	14	I	75	20	49	59	I	75	10
15	15	I	50	20	50	60	I	75	10
16	16	I	50	30	51	61	I	75	20
17	21	I	50	30	52	62	I	75	20
18	22	I	50	30	53	63	I	75	20
19	24	I	50	30	54	64	I	75	20
20	25	I	50	30	55	65	I	75	20
21	26	I	50	20	56	66	I	75	30
22	27	I	50	20	57	67	I	75	30
23	28	I	50	20	58	68	I	75	30
24	29	I	50	20	59	69	I	75	30
25	30	I	50	20	60	70	I	75	30
26	31	I	50	10	61	71	I	50	20
27	32	I	50	10	62	72	I	50	20
28	33	I	50	10	63	73	I	50	30
29	34	I	50	10	64	74	I	50	30

S.No	Ball ID	Shape	Diam (μm)	Depth (μm)	S.No	Ball ID	Shape	Diam (μm)	Depth (μm)
30	35	I	50	10	65	75	I	75	5
31	41	I	100	10	66	76	I	75	5
32	42	I	100	10	67	77	I	75	5
33	43	I	100	10	68	78	I	100	5
34	44	I	100	10	69	79	I	100	5
35	45	I	100	10	70	80	I	100	5

Appendix J2: Details of holes machined into Material B balls

S.No	Ball ID	Cavity Dimensions (μm)	Cavity Shape
1	<i>B01</i>	Diameter: 50 Depth: 10	Shape I
2	<i>B02</i>	Diameter: 50 Depth: 10	Shape I
3	<i>B03</i>	Diameter: 50 Depth: 10	Shape I
4	<i>B04</i>	Diameter: 50 Depth: 20	Shape I
5	<i>B05</i>	Diameter: 50 Depth: 20	Shape I
6	<i>B06</i>	Diameter: 50 Depth: 20	Shape I
7	<i>B07</i>	Diameter: 50 Depth: 30	Shape I
8	<i>B08</i>	Diameter: 50 Depth: 30	Shape I
9	<i>B09</i>	Diameter: 50 Depth: 30	Shape I

Appendix J3: Dimensions and shapes of laser machined slots on nitride balls (Material A)

S.No	Ball ID	Slot Dimensions (μm)	Profile/Shape
1	<i>S01</i>	Width: 100 Depth: 10	Shape I
2	<i>S02</i>	Width: 75 Depth: 7	Shape I
3	<i>S03</i>	Width: 50 Depth: 4	Shape I
4	<i>S04</i>	Width: 100 Depth: 10	Shape I
5	<i>S05</i>	Width: 100 Depth: 10	Shape II
6	<i>S06</i>	Width: 75 Depth: 7	Shape II
7	<i>S07</i>	Width: 50 Depth: 4	Shape II
8	<i>S08</i>	Width: 100 Depth: 10	Shape III
9	<i>S09</i>	Width: 75 Depth: 7	Shape III
10	<i>S10</i>	Width: 50 Depth: 4	Shape III

Appendix K: Additional Features of CPA Series Micro Workstations

Other features of CPA Series UMW

Pulse width:	< 150 fs
Wavelength:	775 nm
TBWP:	< 1.4 x transform limit (sech ²)
Polarization:	Linear, horizontal
Aspect Ratio:	100:1
Transverse mode:	TEM ₀₀
Energy stability:	< 1% rms
Beam diameter (FWHM):	4 – 6 mm
Beam divergence:	<100 micro radians

Additional Output Options:

Amplifier pump laser:	Up to 10 mJ/pulse at circa 200 ns pulse width at 532 nm
Oscillator wavelength:	Average power output > 10 mW at 1550 nm or > 3 mW at 775 nm at nominal repetition rate of 30 MHz

Picosecond Option for CPA-2101:

Pulse energy:	> 0.6 mJ at rep. rates \leq 1 kHz Linewidth: < 8 cm ⁻¹
TBWP:	< 1.2 x transform limit (Gaussian)

Physical Dimensions:

Laser head:	48" L x 20" W x 12" H
Power supply:	28" H x 23" W x 38" D

Utility Requirements:

Electric:	110 VAC, 60 or 50 Hz, 10 A and 208 VAC, 60 or 50 Hz, 40 A
Water:	Tap water 4 gpm, 15-20°C, 30-50 psi

CPA-2101 UMW having the following performance parameters

Nanosecond (Option):

Pulse Energy: >0.8 mJ at repetition rates \leq 1 kHz

Pulse Width: <150 fs

TBWP: <1.4 x transform limit (sech²)

Pico second (Option):

Pulse energy: > 0.6 mJ at repetition rates. 1 kHz.

Linewidth: < 8 cm⁻¹

TBWP: < 1.2 x transform limit (Gaussian)

Additional output options2:

Oscillator wavelength: Average power output > 10 mW, at 1550 nm

or > 3 mW at 775 nm at nominal repetition rate of 30 MHz

Amplifier pump laser: up to 10 mJ/pulse at circa 200 ns pulse width
at 532 nm.

General:

Wavelength: 775 nm

Transverse mode: TEM₀₀

M₂: < 1.5

Rep. Rate: User-adjustable up to 1 kHz

Polarization: Linear, horizontal

Energy stability: < 1% rms

Beam diameter: 4.6 mm

Beam divergence: < 100 microradians

Physical Dimensions:

Laser head: 48 • h L x 20 • h W x 12 • h H

Power supply: 28 • h H x 23 • h W x 38 • h D

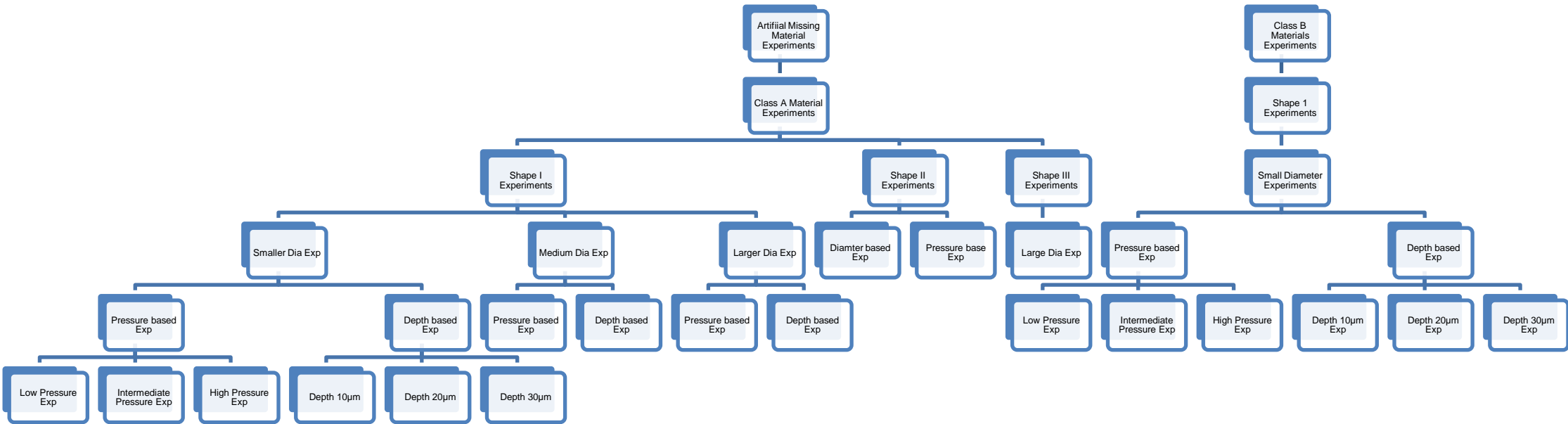
Utility Requirements:

Electric: 110 VAC, 60 or 50 Hz, 10 A and

208 VAC, 60 or 50 Hz, 40 A

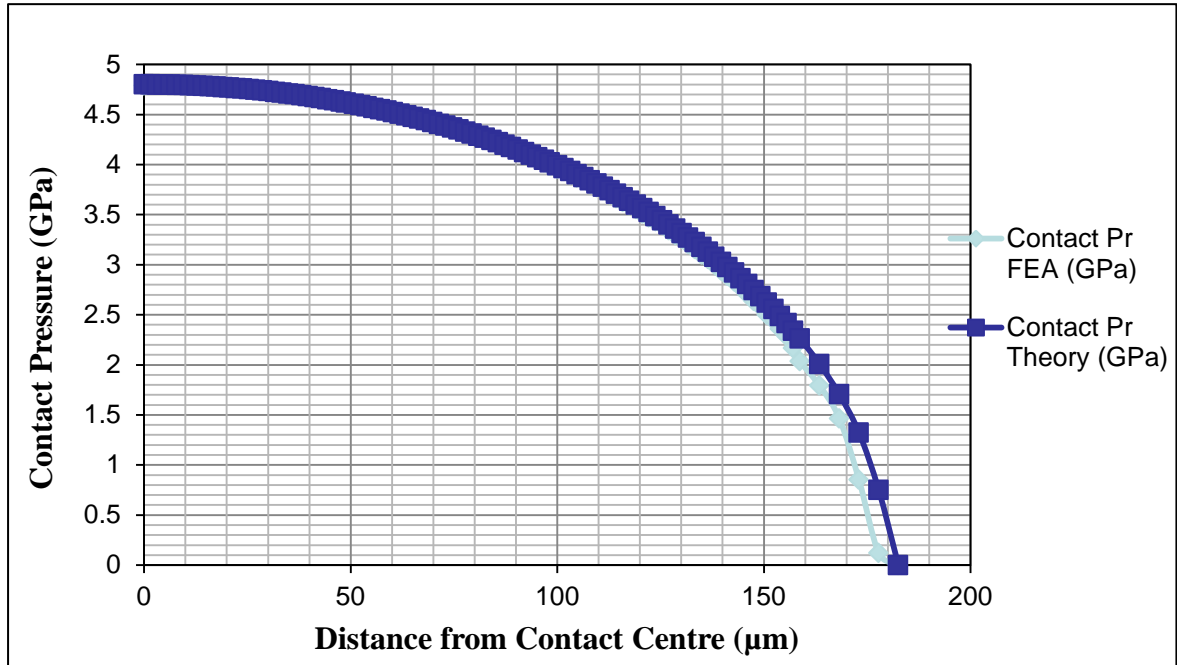
Water: Tap water, 4 gpm, 15-20oC, 30-50 psi

Appendix L: Missing Material Experiments Classifications

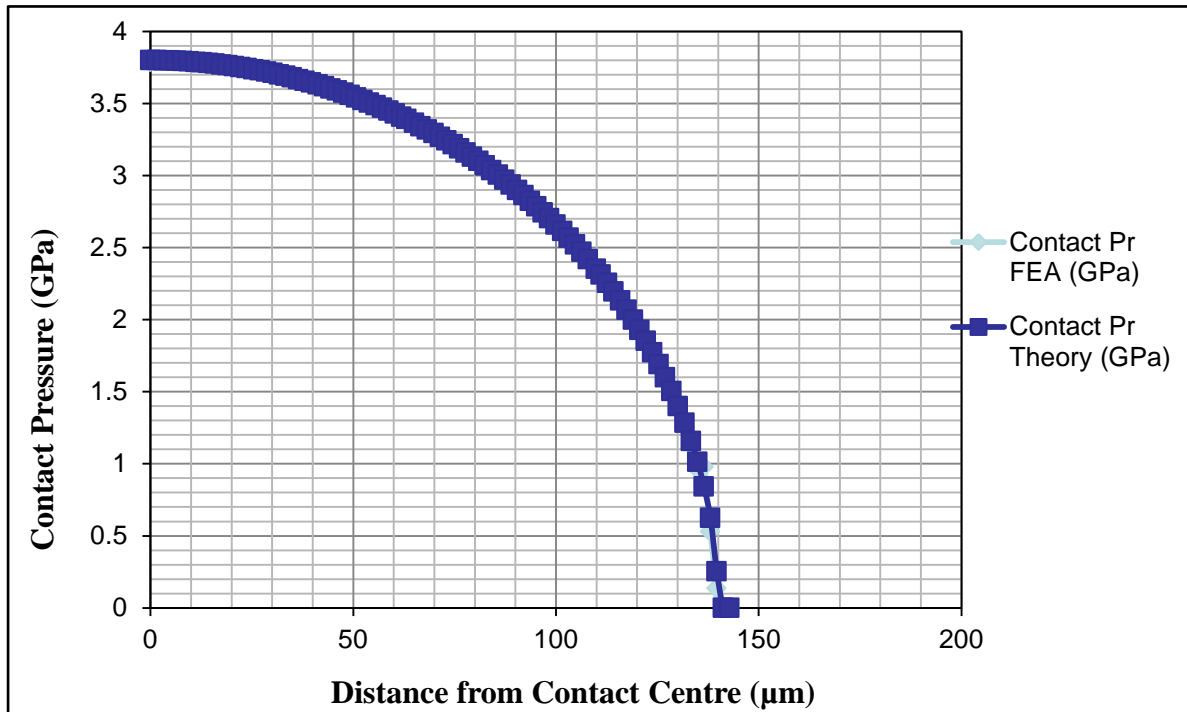


Appendix M: Contact Pressure variation from contact centre

Contact Pressure Variation For 4.8GPa



Contact Pressure Variation For 3.8GPa



Appendix N: Tables for Corrected pressure

Appendix N1: Corrected contact pressures – Small (50µm diameter) holes

Exp. ID	Ball ID	Applied Pressure	Corrected Pressure	Hole Depth	Outcome
<i>Exp. 01</i>	B03H01	4.8GPa	3.44GPa	10µm	<i>Completed</i>
<i>Exp. 02</i>	B03H02	4.8GPa	4.15GPa	10µm	<i>Completed</i>
<i>Exp. 03</i>	B31H01	4.8GPa	4.79GPa	10µm	<i>Completed</i>
<i>Exp. 04</i>	B26H01	4.8GPa	4.68GPa	20µm	<i>Failed</i>
<i>Exp. 05</i>	B27H01	4.8GPa	3.99GPa	20µm	<i>Stopped</i>
<i>Exp. 06</i>	B28H01	4.8GPa	4.68GPa	20µm	<i>Stopped</i>
<i>Exp. 07</i>	B29H01	4.8GPa	4.8GPa	20µm	<i>Failed</i>
<i>Exp. 08</i>	B29H02	4.8GPa	4.65GPa	20µm	<i>Failed</i>
<i>Exp. 09</i>	B30H01	3.8GPa	2.9GPa	20µm	<i>Completed</i>
<i>Exp. 10</i>	B21H01	3.8GPa	3.75GPa	30µm	<i>Completed</i>
<i>Exp. 11</i>	B22H01	3.8GPa	3.79GPa	30µm	<i>Completed</i>
<i>Exp. 12</i>	B23H01	4.8GPa	4.8GPa	30µm	<i>Stopped</i>
<i>Exp. 13</i>	B23H02	4.8GPa	3.44GPa	30µm	<i>Failed</i>
<i>Exp. 14</i>	B21H02	4.8GPa	3.75GPa	30µm	<i>Completed</i>
<i>Exp. 15</i>	B22H02	4.8GPa	4.28GPa	30µm	<i>Failed</i>
<i>Exp. 16</i>	B26H02	4.5GPa	4.03GPa	20µm	<i>Completed</i>
<i>Exp. 17</i>	B30H02	4.5GPa	4.45GPa	20µm	<i>Failed</i>
<i>Exp. 18</i>	B24H01	4.5GPa	3.2GPa	30µm	<i>Completed</i>
<i>Exp. 19</i>	B24H02	4.5GPa	4.31GPa	30µm	<i>Completed</i>
<i>Exp. 20</i>	B25H01	4.5GPa	3.09GPa	30µm	<i>Completed</i>
<i>Exp. 21</i>	B15H01	4.8GPa	4.28GPa	20µm	<i>Failed</i>
<i>Exp. 22</i>	B15H02	3.8GPa	3.75GPa	20µm	<i>Failed</i>

Appendix N2: Corrected contact pressures – Medium (75µm diameter) holes

Exp. ID	Ball ID	Applied Pressure	Corrected Pressure	Hole Depth	Outcome
<i>Exp. 23</i>	B56H01	3.8GPa	3.54GPa	10µm	<i>Completed</i>
<i>Exp. 24</i>	B56H02	3.8GPa	3.28GPa	10µm	<i>Failed</i>
<i>Exp. 25</i>	B57H01	3.8GPa	3.7GPa	10µm	<i>Completed</i>
<i>Exp. 26</i>	B57H02	3.8GPa	3.75GPa	10µm	<i>Failed</i>
<i>Exp. 27</i>	B75H01	4.8GPa	4.44GPa	5µm	<i>Completed</i>
<i>Exp. 28</i>	B75H02	4.8GPa	2.55GPa	5µm	<i>Completed</i>
<i>Exp. 29</i>	B02H01	3.8GPa	3.8GPa	30µm	<i>Completed</i>
<i>Exp. 30</i>	B02H02	4.8GPa	3.85GPa	30µm	<i>Failed</i>

Appendix N3: Corrected contact pressures – Large (100µm diameter) holes

Exp. ID	Ball ID	Applied Pressure	Corrected Pressure	Hole Depth	Outcome
<i>Exp. 31</i>	B41H01	4.8GPa	3.2GPa	10µm	<i>Failed</i>
<i>Exp. 32</i>	B42H01	4.8GPa	4.31GPa	10µm	<i>Failed</i>
<i>Exp. 33</i>	B41H02	3.8GPa	3.09GPa	10µm	<i>Failed</i>
<i>Exp. 34</i>	B42H02	3.8GPa	2.78GPa	10µm	<i>Failed</i>
<i>Exp. 35</i>	B78H01	4.8GPa	4.42GPa	5µm	<i>Completed</i>
<i>Exp. 36</i>	B78H02	4.8GPa	4.37GPa	5µm	<i>Failed</i>
<i>Exp. 37</i>	B79H01	4.5GPa	3.93GPa	5µm	<i>Completed</i>

Appendix N4: Corrected contact pressures – Material B Small holes (50µm diameter)

Exp. ID	Ball ID	Applied Pressure	Corrected Pressure	Hole Depth	Outcome
<i>Exp. B1</i>	BB01H01	4.8GPa	4.47GPa	10µm	<i>Failed</i>
<i>Exp. B2</i>	BB01H02	4.8GPa	3.78GPa	10µm	<i>Completed</i>
<i>Exp. B3</i>	BB02H01	4.5GPa	4.49GPa	10µm	<i>Completed</i>
<i>Exp. B4</i>	BB02H02	4.5GPa	2.84GPa	10µm	<i>Completed</i>
<i>Exp. B5</i>	BB04H01	4.5GPa	4.38GPa	20µm	<i>Failed</i>
<i>Exp. B6</i>	BB05H01	4.2GPa	4.0GPa	20µm	<i>Failed</i>
<i>Exp. B7</i>	BB06H01	3.8GPa	3.5GPa	20µm	<i>Failed</i>
<i>Exp. B8</i>	BB07H01	3.8GPa	3.71GPa	30µm	<i>Failed/Stopped</i>

Appendix N5: Corrected contact pressures – Profile Shape II

Exp. ID	Ball ID	Profile Shape	Applied Pressure	Corrected Pressure	Hole Dimensions	Outcome
Exp. 39	B07H01	II	4.8GPa	1.2GPa	Dia: 50µm, Depth: 10µm	<i>Completed</i>
Exp. 40	B06H01	II	4.8GPa	1.95GPa	Dia: 75µm, Depth: 30µm	<i>Completed</i>

Appendix N6: Corrected contact pressures – Profile shape experiments

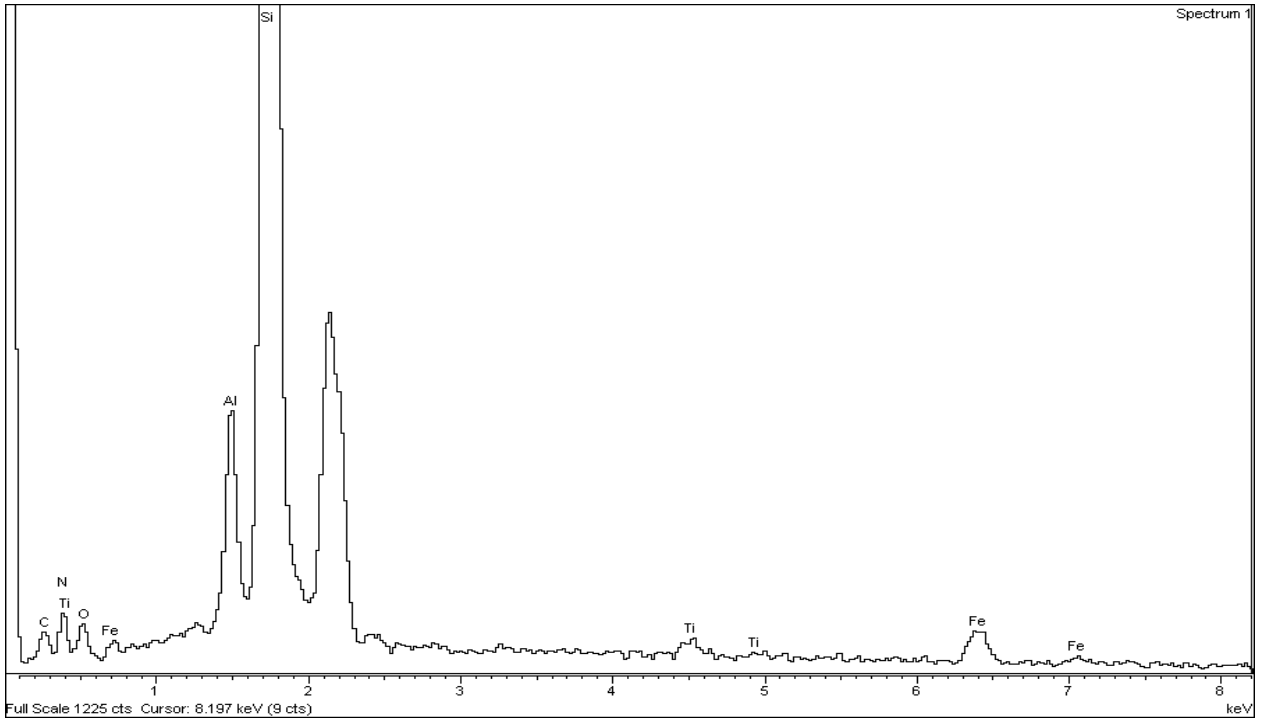
Exp. ID	Ball ID	Profile Shape	Applied Pressure	Corrected Pressure	Hole Dimensions	Outcome
Exp. 41	S1B2H1	I	3.8GPa	1.93GPa	Dia: 100µm	<i>Completed</i>
			4.8GPa	3.56GPa	Depth: 50µm	<i>Failed</i>
Exp. 42	S1B2H2	I	4.8GPa	4.78GPa	Dia: 100µm Depth: 50µm	<i>Failed</i>
Exp. 43	S2B1H1	II	3.8GPa	3.98GPa	Dia: 100µm	<i>Completed</i>
			4.8GPa		Depth: 50µm	
Exp. 44	S2B1H2	II	4.8GPa	3.75GPa	Dia: 100µm Depth: 50µm	<i>Completed</i>
Exp. 45	S3B1H1	III	3.8GPa	NA	Dia: 100µm Depth: 50µm	<i>Failed</i>
Exp. 46	S3B1H2	III	3.8GPa	NA	Dia: 100µm Depth: 50µm	<i>Failed</i>

Appendix O: *EDS Analysis of Silicon Nitride Ball*

(Laser Machined SiN sample - RCF Experiment 1)

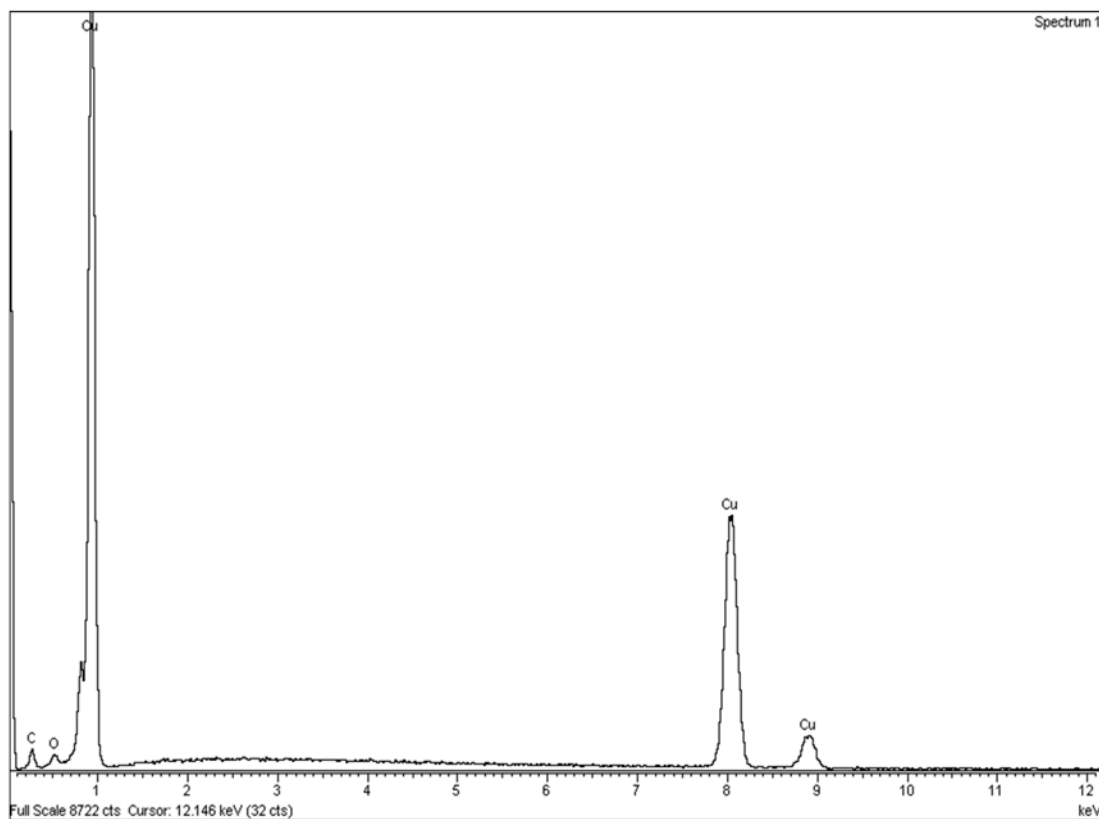
27046

11/1/2011 1:03:09 PM



Comment:

Appendix P: Calibration for SEM EDS



Element	Line	Quant	Area	Sigma	Fit index
	Noise 1	No	69705.3	1682.8	14.4
	Noise 2	No	-83384.4	5275.4	14.9
	Noise 3	No	66371.6	3870.3	14.9
C	K_SERIES	Yes	1398.5	88.5	8.8
O	K_SERIES	Yes	862.0	97.0	1.1
Co	K_SERIES	Yes	-66.6	98.1	3.1
Co	L_SERIES	No	1024.8	311.4	14.7
Cu	K_SERIES	Yes	55237.2	400.3	3.3
Cu	L_SERIES	No	87211.8	569.4	17.3



Appendix Q : *Finite Elements used in Missing Material Modeling*

- CAX4R:** Axi-symmetric 4-node element (reduced integration)
- CPEAR:** 4 node bilinear plane strain element (reduced integration)
- SFMAX1:** 2-node linear surface element
- FAX2:** 2-Node axi-symmetric fluid element
- C3D8R:** 3-D 8-node solid element